Establishing a genetic and exogenous toolbox for studying multiple stages of vertebrate development *in vivo*

Thesis by

William P. Dempsey

In Partial Fulfillment of the Requirements

for the Degree of

Doctor of Philosophy

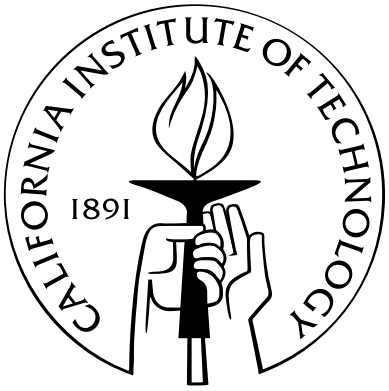

California Institute of Technology

Pasadena, California

2012

(Defended May 17, 2012)

for Corey

Acknowledgements

I would like to acknowledge everyone who has helped me! I would say that it makes sense to start with my high school mentor and physics teacher, Dr. Larry Dodd — his constant encouragement and confidence in my abilities had a huge part in setting the foundation for my eventual path to graduate school. Some people who I have kept up with and have helped support me from as early as middle and high school are three of my best friends, William Misek, Matt Gallivan, and Kenneth Shaw. I have to thank Will especially for his entertaining daily instant messaging conversations with me during my time at Caltech, quoting "The Simpsons", sending me link after link to keep me amused, etc. I am glad to have maintained such a strong friendship with these guys for so long.

Next, I would like to thank my mentors at the Johns Hopkins University, where I did my Bachelor's and Master's work. Prof. Konstantinos Konstantopoulos in the Chemical Engineering department was the first JHU professor to see my potential when I was in his Transport Phenomena II course, and I am thankful to have "cut my teeth" on research in his lab. I thank Prof. Goutsias, my Master's advisor, for so much: he pushed me to learn and apply a variety of math principles and modeling techniques as thoroughly as I could — always willing to be there for me, and always expecting nothing less than the best out of me. I feel absolutely honored to have been able to work so closely with these professors during my time in Baltimore. I would like to thank Prof. Eric Young, a professor of Biomedical Engineering at JHU, for his advice and support as well.

I have many people to thank here at Caltech. I would like to thank my graduate student col-

leagues for their friendship and for the fun conversations that I have had with them during my time here, especially Nakul Reddy, Geoffrey Lovely, Indira Wu, Jonathan Sternberg, Cindy Chiu, Alborz Mahdavi, and Sungwook Woo. Rahul Deb has been my buddy ever since we roomed together here at Caltech, and I thank him for his consistent friendship as well as for the zany adventures we have had in California, New York, and abroad. I look forward to keeping in touch with all of these guys as we all slowly go our separate ways after graduate school.

Other colleagues at Caltech that I would like to thank for all of their advice and friendship include my fellow "Fraserland" lab-mates and collaborators. I would like to thank Periklis Pantazis, my closest collaborator, for all of his support and advice; working with him has been a joy, and I look forward to our continued collaborations in the future. I am especially grateful to Le Trinh and Thai Truong for always being there to provide me with guidance, advice, assistance, and a critical eye for my research. Jelena Čulić-Viskota and Nathan Hodas have been fantastic to work with, and I wish them continued success outside of graduate school. I would, of course, like to thank my advisor, Scott E. Fraser. His positive attitude, expertise, knowledge, and (sometimes quite "out there") suggestions were always a great help in steering my research in the right direction. Prof. Rob Phillips has also played a mentoring role for me at Caltech, and I truly appreciate his wisdom as I wrap up my graduate work. I would also like to thank my other thesis committee members, Prof. Morteza Gharib and Prof. Changhuei Yang, for their support for me during my time here. I thank Andres Collazo and the House Research Institute for allowing me access to their laser scanning microscope facility during my time at Caltech.

I want to thank my family, especially my parents, William and Nicolina Dempsey, for their unwavering and boundless support throughout my life. Additionally, I thank my brother, Christopher Dempsey, for always having a witty, sarcastic comment in his pocket to make me laugh, and for being a tremendous friend and scientific colleague.

Last, but never least, I want to thank Corey McCullough — my love, my girlfriend, and my partner in life for the past eight wonderful years. She is unfailingly there for me and makes me smile. What else is there to say?

You guys mean everything to me.

Abstract

Understanding of cell behavior during vertebrate development and repair has been greatly facilitated by advances in biological imaging. Importantly, more powerful tools to generate contrast within the tissue make *in vivo* analyses of these processes in time and space more tractable. Here, I present my efforts to develop and refine an imaging toolbox to study *in vivo* cell shape, dynamics, structure, and behavior in the zebrafish vertebrate model system. Mosaic analysis and targeted photoconversion illuminate fine morphological details as cells migrate during gastrulation, revealing cell connections that span several cell diameters across the embryo. These intercellular bridges link cells between lineage boundaries and allow cells to share membrane components on a developmentally relevant time scale. The PhOTO zebrafish transgenic lines combine the strengths of sparse and global cell labeling to monitor cell dynamics and morphology at any stage in the lifetime of the zebrafish. I demonstrate targeted and instantaneous sparse cell tracking in the context of global cell behavior in the embryo, and I also isolate a subset of slowly dividing cells populating a regenerating adult tail fin. Combining fluorescence and endogenous second harmonic generation (SHG) imaging as a tool to study early muscle structure and organization within whole zebrafish muscle compartments uncovers the source of vernier-patterned signal in highly ordered myosin arrays. Instead of being physical distortions in muscle sarcomeres, these patterns may result from an optical artifact of SHG imaging, since comparable signal is not visible in both the SHG and fluorescence channels. To complement the aforementioned genetic labeling and endogenous contrast tools, barium titanate SHG

nanoprobes — exogenous and nontoxic SHG-capable nanomaterial tags — are refined for cell labeling in the zebrafish. Silane functionalization acts as a platform for further surface modifications, including: multistep chemical additions, non-reactive surface coating modifications, and antibody linkages for cell targeting applications. The power of each of these tools lies in their compatibility with one another: combining the fluorescence and SHG contrast approaches described here may enable high-resolution imaging at a variety of developmental stages to appreciate the multifaceted cell behaviors governing vertebrate developmental programs more completely.

Contents

List of Figures

Chapter 1

Introduction

1.1 Fluorescence as a powerful tool to probe biological problems

Advancements in fluorescence, a process involving absorption and emission of light in often tight spectral frequency bands (see Fig. 1.1A), have resulted in monumental steps being made toward more effective monitoring of living cells in biological samples with high contrast[1]. Since the cloning of the green fluorescent protein (GFP) from the jellyfish *Aequorea victoria* [2], an assortment of genetically encoded fluorescent protein (FP) tags have been developed to enable multicolor imaging of cells and cell components (e.g., proteins), some of which are described in [3]. The growing number and continued engineering of optical tags have improved the study of biology, with applications in embryonic development [4, 5, 6, 7], protein function/behavior [8, 9, 10, 11, 12, 13, 14, 15], complex regeneration [16, 17, 18, 19, 20], and cancer progression [21, 22, 23, 24, 25].

1.1.1 Photomodulatable FPs and their advantages in biological imaging

A variety of improved, multicolor FPs have been established since the first applications of GFP [3], leading to the development of FPs that can change their fluorescence spectra as a result of an external perturbation — certain wavelengths of light, in this case. Photoconvertible, photoactivatable, and

[1]Much of the text and the figures in this chapter were first reported in a review published in *Bioessays*, which was a written collaboration between Scott E. Fraser, Periklis Pantazis, and myself [1].

photoswitchable FPs have revolutionized the field of molecular imaging, with applications in cell culture [26, 27], *in vivo* studies [14, 28], and even super-resolution microscopy [29, 30]. Photoconvertible proteins are advantageous for long-term confocal imaging experiments (e.g., cell tracking, cell fate analyses, etc.), because their pre-converted state is readily visible, unlike photoactivatable fluorophores. Moreover, their photoconverted state lasts until the protein is degraded within the cell, unlike photoswitchable fluorophores. Several transgenic lines have been developed to take advantage of photoconvertible proteins in early developmental imaging applications. For example, two transgenic lines have been reported that take advantage of certain photoconvertible proteins, specifically Kaede [31] in zebrafish and KikGR [32] in mice. These lines are useful for photoconversion studies involving cytoplasmic labeling, such as the recent study monitoring trigeminal ganglion development in zebrafish [33]. Many photoconvertible proteins have monomeric variants — this property is essential for protein fusion studies [26, 34, 35, 36] and any studies requiring close co-localization of proteins, as with Förster Resonance Energy Transfer (FRET) analysis [37].

mDendra2, a monomeric ('m') protein derived from *Dendronephthya sp.* [38], normally fluoresces green, with a peak excitation and emission at 492 nm and 505 nm, respectively. However, after exposure to $\sim$ 405 nm light, a histidine cleavage event within the backbone of the mDendra2 chromophore red-shifts the excitation/emission profile, resulting in peak excitation and emission of 555 nm and 571 nm, respectively [39]. Importantly, photoconversion of restricted volumes with high spatio-temporal resolution in mDendra2 expressing cells is possible using standard confocal microscopy [26, 36]. Thus, selecting a subset of cells of interest from an entire labeled population can be achieved without requiring a cell-specific promoter. These properties make mDendra2 an ideal FP for long-term imaging of both converted and unconverted fusion proteins in cells and tissues. This particular photoconvertible protein plays an integral role in the experiments performed in Chapters 2 and 3 of this thesis.

1.1.2 Multicistronic gene expression and potential use in FP labeling

2A coding sequences, discovered in picoRNAviruses such as foot-and-mouth disease virus (FMDV), have been used to genetically encode the translation of multiple proteins from a single DNA sequence [40]. Viral *2A* sequences placed between coding sequences of two proteins on a bicistronic template have been shown to undergo self-mediated protein cleavage during translation, most likely due to a momentary pause, release, and continuation mechanism of translation at the ribosome, which results in the generation of two independent proteins [41]. Unlike internal ribosomal entry sites (IRESs), *2A* sequence processing at the ribosome results in the production of proteins at a 1:1 stoichiometric ratio, and certain *2A* fragments, such as the 20 amino acid *Thosea asigna* virus (TaV) *2A*, have high cleavage efficiency *in vitro* [42].

These viral sequences can be taken advantage of to separate two or more FP coding regions (or other protein sequences) on a single plasmid for genome insertion, ultimately generating transgenic lines with stoichiometric multicistronic expression. Previously, *2A*-mediated cleavage of bicistronic proteins fused to a variety of non-photomodulatable FPs have been used to visualize cellular compartments in different transgenic lines (e.g., in zebrafish [43] and mice [44]). Alternate recent applications of multicistronic FP labeling are wide-ranging — for example, in neurophysiology [45], immunology [46], gene therapy [47], and cancer [48, 49] — though for this thesis, we will focus on multicistronic expression of compartmentalized FPs, specifically in Chapter 3.

1.1.3 Zebrafish: an attractive vertebrate model system for FP labeling experiments

Model organisms enable researchers to tease apart underlying fundamental biological mechanisms (e.g., cell cycle, disease progression, etc.) in a rigorous manner. Historically, model organisms have been chosen across the five kingdoms of living organisms, often in the hopes of gaining biological insight into the human condition — perception and cognition, sleep cycle, and aging to name a few

— and many of these living systems have been chosen due to their close relation to humans on the branches of the phylogenetic tree [50].

Out of the wide assortment of model organisms, the zebrafish (*Danio rerio*) is perhaps one of the most appealing from an imaging perspective. Most importantly in this regard, this vertebrate is small ($<$ 1 mm thick, up to a few mm long) and mostly transparent throughout the major early stages of development, even while the major body compartments are differentiating and organizing [51]. Additionally, zebrafish: (1) produce embryos that are externally fertilized in clutches sometimes numbering near 100, (2) can be raised and maintained cheaply as compared to higher-order vertebrates, (3) reach sexual maturity by around 3 months of age, (4) have a well-characterized genome, (5) have appreciable molecular and anatomical similarity to humans, and (6) can be used to model disease progression [52]. In addition to studies manipulating the wild type (WT) condition, the establishment of zebrafish transgenics in the late 1980s [53] has primed this model organism for FP-labeling studies. In this thesis, I will take advantage of the zebrafish model system predominately, though I will briefly touch on moving into studies of mice towards the end of Chapter 5.

1.2 Biological imaging as a means to probe cell behaviors with high resolution

Powerful microscope systems for *in vivo* optical imaging complement improvements in the fluorescence toolbox. Confocal laser scanning microscopy (CLSM) is a technique using a scanned, focused laser to image fluorescent labels within biological samples (demonstrated in [54]). The laser focus is translated across the sample to achieve a two-dimensional (2D) reconstruction of a single 'optical section' of the material (e.g., a piece of tissue or a whole organism). By repeating these scans through the depth, full three-dimensional (3D) reconstructions of the material are possible. Note

that for CLSM, out-of-focus light is still absorbed by the tissue above and below the plane of focus, leading to out-of-focus photon emission. To prevent this signal from being directed to the detector, a pinhole is positioned with respect to the excitation focus and can be adjusted so that (mainly) light from the focus is allowed through [55].

A similar method of imaging, called two-photon laser scanning microscopy (TPLSM), uses a pulsed, 2-photon (2P) laser source to excite fluorescent labels mostly within the focal volume of a biological sample. The confinement of fluorescence within the focal volume when using 2P lasers stems from the fact that simultaneous interaction of two photons with the fluorescent material is a necessary requirement for absorption. As a result, the probability of two photons being absorbed within the focus is orders of magnitude higher than outside of this small volume [56]. Using TPLSM, a pinhole is not necessary, though it has been shown to improve resolution, as compared to CLSM experiments [56]. Importantly, 2P illumination in the near infrared regime penetrates deeply into biological samples and excites a variety of fluorophores (such as GFP) [13].

1.2.1 Using biological imaging to study early development in vertebrates

During early development, extensive migratory events, signaling, and cell divisions shape the vertebrate embryo, resulting in a stereotypic organization of the general body plan[2]. Major imaging-based efforts have attempted to dissect how these cellular processes lead to the patterning of specialized tissue compartments within the vertebrate system [58, 59]. Lineage tracing — the process of tracking a cell and its progeny in space and time as it moves from an early to a specified state — provides an overall picture of the coordinated events required to set up or repair a whole organism. Two major considerations are required for this tracking strategy: first, a precise, indelible mark must be placed within cells of interest at an early stage of development; and second, after sufficient time,

[2]Note that much of the text in Sections 1.2.1 and 1.2.2 was first reported in a recent publication in *PLoS ONE* in collaboration with Scott E. Fraser and Periklis Pantazis, where I was first author [57].

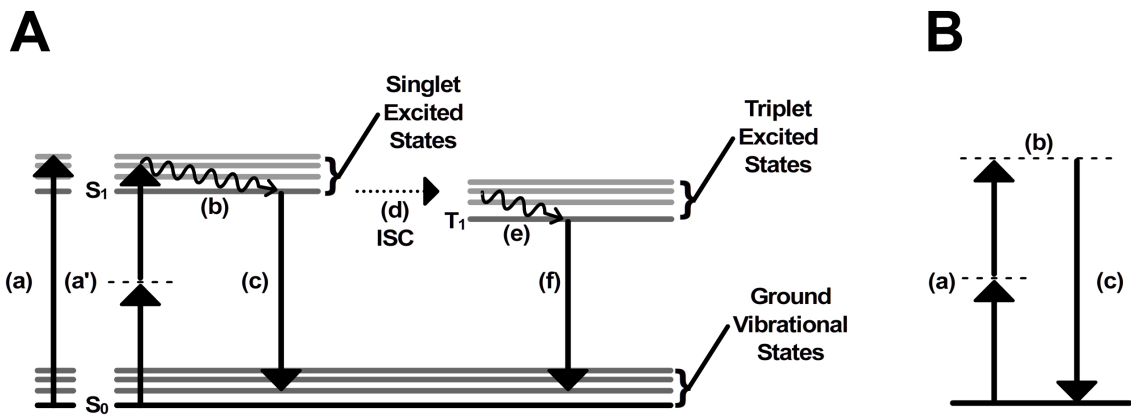

Figure 1.1: **The principles of single-photon excited fluorescence (SPEF), two-photon excited fluorescence (TPEF) and second harmonic generation (SHG)**. (A) SPEF and TPEF. Either (a) one photon (with frequency ω_1) or (a') near-simultaneous two photons (with frequency $\omega_{1'}$) striking a fluorescent material within its excitation spectrum may be absorbed, driving electrons from a ground vibrational state (S_0) to one of many singlet excited state energy levels. (b) Due to Kasha's Rule, a rapid vibrational relaxation to the first singlet state (S_1) — also known as the fluorescent state — must occur. (c) The lifetime in S_1 is $\sim$ 5 ns and can be followed by relaxation to any one of the ground vibrational states (as low as S_0) by the release of a photon with lower energy than the single photon or two combined photons ($\omega_{SPEF} < \omega_1$ and $\omega_{TPEF} < 2\omega_{1'}$), or (d) the relaxation can be followed by less likely interstate conversion (ISC) to spin-forbidden triplet excited states. (e) Relaxation to the first triplet excited state (T_1) occurs. (f) After a waiting period on the order of milliseconds to seconds, a relaxation to a ground state occurs, releasing a so-called "phosphorescence" photon ($\omega_{Phos} < \omega_1$ and $\omega_{Phos} < 2\omega_{1'}$). During this waiting period in the T_1 state, the molecule remains dark without fluorescing, which is seen in a continuous imaging time-lapse as blinking. (B) SHG. (a) Two photons (with frequency ω_2) simultaneously striking a highly ordered, noncentrosymmetric material may induce (b) a virtual energy state transition that lasts only as long as the illuminating pulse ($\sim$ 1 fs), resulting in (c) rapid relaxation to S_0 and the release of a photon of exactly twice the energy ($\omega_{SHG} = 2\omega_2$) of the incoming photons. Note that this virtual energy state occurs without the absorption of a photon, though at frequencies close to the singlet states, resonance enhancement of SHG can occur. As a consequence, SHG is a coherent process, and the photon normally proceeds in the same direction as the incoming illumination. (This figure is reproduced from [1].)

the final location of labeled cells and their progeny must be scored accurately [60]. Thus, techniques capable of monitoring long-term behavior (i.e., movements as well as morphology) in precise cell locations are key to tease out the timing and cellular events controlling general cell fate decisions *in vivo*.

Most techniques for lineage tracing can be split into two general categories, (1) sparse/partial and (2) global cell labeling and tracking. Sparse cell labeling methodologies include traditional lineage tracing analyses involving early stage dye injection (e.g., fluorescein, etc.), followed by fixed sample analysis or live cell tracking after sufficient developmental time [60]. More recent sparse labeling modalities take advantage of genetically encoded means for generating random transgenic mosaics expressing cell-targeted fluorescent proteins (FPs) — for example, using random gene insertion events [61, 62], drug induced recombination [63, 64] or heat shock promoters [65]. Other partial cell labeling techniques revolve around tissue specific promoter driven FP expression to isolate only cells in a particular tissue of interest [33, 66, 17, 19, 18]. The second variety, global cell labeling, is most often achieved by ubiquitous nuclear FP expression driven by constitutive promoter sequences [5, 7, 67].

These two techniques have opposing benefits and disadvantages that limit their effectiveness as lineage tracing tools. Sparse/partial methods simplify the tracking problem by focusing solely on cells of interest, though the data lacks context with other cell types in a given tissue environment. Additionally, lineage tracing using exogenous labels (e.g., vital dyes, fluorescein) requires invasive administration, and labeling cellular positions at early developmental stages is imprecise, at best [60]. Even though mosaic approaches — where a fraction of cells are labeled — can result in sparse FP expression, labeling a specific subset of interest is sometimes impractical due to the fact that the process is random, especially if labeling of a certain cell type is desired (e.g., cells of a certain lineage as in [62]). Tissue-specific promoter approaches may be limited by the fact that these labels

are often expressed only late in embryogenesis (i.e., when the tissue compartment matures), so imaging the early cells that eventually become a part of these compartments is impossible using a tissue-specific promoter. There is also an inherent inefficiency in the use of tissue-specific promoters for lineage tracing analysis — in order to analyze each and every cell-type in an organism, a different tissue-specific promoter-driven construct/transgenic line would need to be created and imaged for each cell type.

In contrast, global methods supply cell behavior data in context to every cell in the organism at the expense of requiring sophisticated volumetric imaging and algorithms for cell segmentation and tracking. Additionally, if only a small subset of cells need to be analyzed for tracking/tracing, whole embryo segmentation and analysis is inefficient and overly complicated. Recent whole-embryo labeling studies tend to focus on nuclear tracking [5, 7, 67], while ignoring important morphological changes during development [68], which is a limitation that will be addressed in Chapters 2 and 3.

1.2.2 Imaging to understand epimorphic tissue regeneration

Similar attention in the bioimaging community has been paid to regeneration of fully differentiated tissue compartments after trauma, termed epimorphic tissue regeneration, which is a process that requires complex cell events, including migration, signaling, division, and even de-differentiation [16]. This process can be somehow likened to development in that de-dedifferentiated cells in a so-called blastema are organized to reform the multiple tissue types in an organ by particular signaling molecules (e.g., fibroblast growth factor (FGF) [20], retinoic acid [69], etc.); an interesting contrast is that, in regeneration, de-differentiated cells retain memory of their previous lineage as well as positional information — there is a predictable limit to the growth of the tissue [70]. Perhaps the most elegant studies of regeneration have been performed in *Ambystoma mexicanum* (the axolotl salamander) [70]. However, a lack of genetic tools in this model system has forced researchers to

resort to laborious and invasive cell/tissue transplantations to create partial labeling, and their methods often involve fixation and sectioning, preventing live analysis of this process [71]. Currently, zebrafish are the only vertebrate model system that can follow the process of regeneration using real time imaging [16]. This is due to the fact that lineage tracing tools for the study of complex adult tissue regeneration had not been established previously (as mentioned in [66]). Our recent publication attempts to address this need [57], which is a major focus of Chapter 3.

1.3 Second harmonic generation microscopy

1.3.1 Limitations of fluorescence-based imaging approaches

Fluorescence has many advantageous properties: a set of spectrally-separable probes can be chosen to label different cell types in a given tissue, fluorescent signal can have high signal over background, and TPEF enables deep penetration into biological samples [3, 11, 13]. However, the photophysical properties that govern fluorescence are the source of several important limitations for *in vivo* biological imaging applications. These limitations — especially dye bleaching (damage associated with the absorptive process) and blinking (fluctuating 'on' and 'off' states of an individual fluorescent tag) — are presented in [72] (also discussed in [55]).

These factors can limit one's ability to distinguish and separate signal from fluorescently labeled biological molecules within the sample being imaged. An additional concern is that in order to have appreciable signal above background-level autofluorescence in a tissue, fluorophores must emit a substantial number of photons [72]. Ramping the laser power or slowing laser scanning to get stronger fluorescent signal decreases temporal resolution, can destroy the material being imaged, and can bleach the fluorescent probe [72].

1.3.2 Second harmonic generation as a compatible optical phenomenon to fluorescence

A mechanism that has a compatible optical signature to fluorescence while circumventing many of the aforementioned limitations of fluorescent probes is second harmonic generation (SHG). The nonlinear process of SHG is illustrated in Fig. 1.1B. Two photons at frequency ω can contact certain asymmetric materials (specifically, noncentrosymmetric materials), combine, and produce a new single photon with twice the frequency, 2ω, of the two incident photons [73, 74]. The result of this interaction of light with matter can be specified by the following induced polarization $P(\omega)$ (dipole moment per unit volume) equation, which is expanded as a power series of the electric field amplitude, $\mathbf{E}(\omega)$, of the incoming laser:

$$P(\omega) = \chi^{(1)}\,\mathbf{E}(\omega) + \chi^{(2)}\,\mathbf{E}^2(\omega) + \chi^{(3)}\,\mathbf{E}^3(\omega) + \ldots \quad .$$

Here, $\chi^{(1)}$ is the linear susceptibility, $\chi^{(2)}$ is the second-order susceptibility, and $\chi^{(3)}$ is the third-order susceptibility, etc. The first term corresponds to linear optical responses: absorption, scattering, and reflection of light. SHG as well as sum frequency generation processes are the result of the nonlinear second-order susceptibility term. An example of a process governed by the third term is third harmonic generation (THG). One important consideration is that $\chi^{(2)}$ vanishes for all centrosymmetric materials (e.g., crystals with cubic crystal lattices) except at their surface, where there is a natural asymmetry [75]. The first observation of SHG was reported in a quartz crystal by Franken et al. [76], shortly after the demonstration of the first working laser in 1960 by Maiman [77].

Since SHG requires two photons to interact with an SHG-capable material almost simultaneously (as in TPEF), visualization of the signal from this process does not require a pinhole aperture to constrain out of focus SHG events — resulting signal is only appreciable within the focal volume. Interestingly, SHG contrasts with TPEF in that the energy transition is a “virtual transition”,

which means that there is no vibrational relaxation or interstate conversion (see Fig. 1.1B). The non-absorptive nature of the SHG process is what gives it such attractive properties (e.g., no blinking or bleaching).

1.3.3 Applications of SHG microscopy

An important consideration for SHG is that this process requires optical coherence for efficient signal production. This means that in order for SHG signal to be substantial at the detector, the outgoing waves generated by different molecules within an SHG-capable material should be in phase, resulting in signal enhancement by constructive interference (see Fig. 1.2A) [73]. Importantly, this 'phase-matching' principle only occurs when the generated and illuminating photons have matching velocity. Additionally, the signal is mainly forward-directed (unlike isotropic fluorescence signal), so transmitted detection within a conventional TPLSM system is often essential [78, 79]. Interestingly, both fluorescence and SHG in thicker tissue can scatter a portion of forward-directed signal backward, allowing for epi-detection, which is taken advantage of in certain studies (e.g., [80]).

Non-biological applications for SHG include the use of this principle: to achieve frequency conversion of lasers [81] and to describe surface properties of various materials [82]. Biological microscopy with SHG was first used to image the polarization of collagen fibers in the rat-tail tendon [83], which has been suggested to be an SHG-capable material due to the organization of its outer shell [84]. One clinically relevant application took advantage of collagen's SHG-capable properties to evaluate the effect of molecular therapeutics on tumor growth after pharmacological intervention [22]. SHG imaging microscopy has also been used to visualize sarcomeric components in muscles, clearly revealing myosin band striation patterns without the use of any fluorescent dye [85]. SHG signal is sensitive to the structural state of the myosin motors *in vivo* [86], so functional imaging promises to have great potential as an early diagnostic readout for pathological muscle

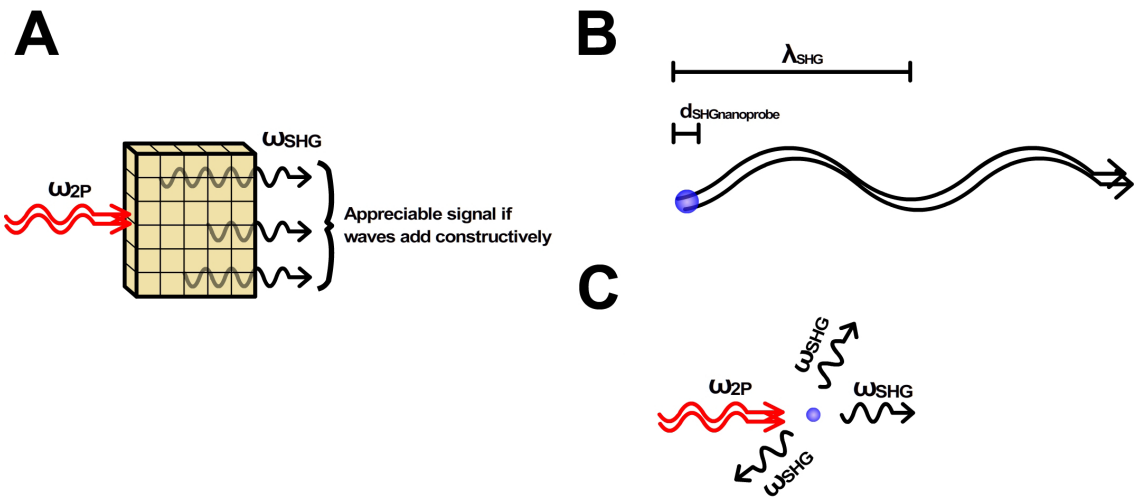

Figure 1.2: **SHG in bulk material versus nanoparticles**. (A) In a bulk SHG-capable material, two photons of frequency ω_{2P} (in red) may simultaneously strike a highly ordered, noncentrosymmetric material. Appreciable SHG signal at frequency $\omega_{SHG} = 2\omega_{2P}$ (in black) will only occur if the resulting SHG signal moves at the same velocity of the incident photons in the material, resulting in constructive interference. This constructive interference is a consequence of the so-called phase-matching condition of SHG. (B) In contrast, SHG nanoprobes (blue sphere) do not require a phase-matching condition for appreciable signal. Since the diameter of the nanoparticles is small with respect to the wavelength of incident light and the wavelength of the SHG signal ($d_{SHGnanoprobe} \ll \lambda_{SHG}$ and $d_{SHGnanoprobe} \ll \lambda_{2P}$), SHG scattered from anywhere in the material will be at approximately the same phase (in black). (C) As a consequence, when 2 photons of frequency ω_{2P} (in red) simultaneously strike the SHG nanoprobes, SHG at $\omega_{SHG} = 2\omega_{2P}$ (in black) is scattered in multiple directions. These cartoons are not to scale. Note too that the SHG waves drawn in this image are for illustrative purposes only and do not represent precise directions for multi-directed signal. (This figure is reproduced from [1].)

conditions (e.g., muscle dystrophy). An interesting feature of endogenous SHG from the skeletal muscles of fixed, intact zebrafish will be probed in Chapter 4. For completeness, other endogenous structures known to generate appreciable SHG signal are microtubules in mitotic spindles [85, 87] and cellulose [88].

In addition to SHG imaging of endogenous structures, exogenous markers, when carefully designed and properly organized, can produce detectable SHG signal. Cell membranes that have been labeled with asymmetric styryl or porphyrin dyes [89, 90, 91, 92, 93] produce an SHG signal that is sensitive to membrane potential. This observation could be explained by the idea that the effective $\chi^{(2)}$ could change in the presence of an applied electric field, which can modify SHG intensity [73]. Because of this electro-optic mechanism, SHG imaging may become a practical approach for optical recordings of membrane potential [94].

1.3.4 SHG nanoprobes as exogenous contrast agents for biological imaging

Recent exogenous markers that have gained attention in the imaging field, called SHG nanoprobes, are SHG-capable nanomaterials. SHG nanoprobes have been used for biological *in vitro* [95, 96, 97, 98] and more recently *in vivo* imaging [72]. SHG properties for a variety of crystals have been reported, including $BaTiO_3$ [97, 99, 100], ZnO [95, 101], $Fe(IO_3)_3$ [98, 102], $KTiOPO_4$ [103, 104, 105, 106], $Sr_{0.6}Ba_{0.4}Nb_2O_6$ [107], $KNbO_3$ [108], and $PbTiO_3$ [100]. In addition, an overview of previously performed material characterizations since the introduction of SHG in 1961 was put together by Nikogosyan [109]. These (and potentially other) materials could possibly function as SHG nanoprobe labels.

SHG was first applied *in vivo* by Pantazis et al. [72]. In this study, $\sim$ 30 nm tetragonal $BaTiO_3$ was selected as an SHG-capable tag with great potential because of its bright SHG signal even at non-tissue-damaging 2P illumination intensities [72]. SHG signal spectra from the SHG nanoprobes

have attractive features for deep-tissue *in vivo* imaging. First, small bandwidth emission filters can be placed before the detector, since the full-width half maximum (FWHM) spectral bandwidth of SHG is narrow ($\sim$ 5 nm) [72]. Emission from fluorescent dyes, fluorescent nanocrystals — including nanodiamonds [110, 111, 112], quantum dots [113] as well as non-blinking quantum dots [114] — or genetically encoded fluorescent proteins, on the other hand, have a much wider spectral bandwidth and do not depend on the bandwidth of the illuminating beam. This photophysical phenomenon can be explained by Kasha's rule, where incident photons may be absorbed at any range of higher excited states. Following absorption, fluorescence photons are always released solely during the energy transition from the lowest singlet state (S_1) down to any one of the ground vibrational states (S_0) [115] (see Fig. 1.1A). Thus, the spectral bandwidth is dictated by the energy bandgap (i.e., the spacing between ground and singlet states) of the material, and the difference between the frequency of absorption and emission peaks in fluorescence is called the Stokes shift. Note that SHG is an example of an anti-Stokes shift of photons, where scattered photons end up at a higher frequency than the incoming beam.

Unlike SHG signal propagation from bulk materials, including SHG signal from biological protein arrays, SHG nanoprobes scatter signal in many directions (see Fig. 1.2). Though this may seem contradictory considering the coherent nature of SHG, this multi-directional signal can be attributed to the small size of the SHG nanoprobes themselves. Since these particles are smaller than the wavelength of the incoming illumination photon, SHG produced anywhere in the nanocrystal will always be approximately in phase, allowing the scattering to proceed in multiple directions [116, 117] (see Fig. 1.2B, C). As a result, the signal from SHG nanoprobes — like the isotropic signal from fluorescent probes — can be visualized in the preferred epi-detection arrangement of conventional microscope systems [72]. $BaTiO_3$ nanoprobe functionalization and *in vivo* imaging will be covered extensively in Chapter 5.

1.4 Overview of the following chapters

In this thesis, I will describe how I have created, used, and refined a varied set of tools for probing vertebrate development and epimorphic tissue regeneration in the zebrafish. In this regard, I cannot move forward without mentioning the many collaborators who have worked with me to achieve my goals. I will mention each again in the chapters ahead, but I wish to preempt the main data-containing chapters of this thesis to touch on the collaborative spirit and expertise that enabled me to take on the projects detailed here. I will list in which chapters each have contributed, more-or-less based on chapter order: of course, Scott E. Fraser (Chapters 2–5), my Principal Investigator at Caltech and an Anna L. Rosen Professor of Biology and Professor of Bioengineering, whose experience spans a wide variety of disciplines; Periklis Pantazis (Chapters 2–5), a former biochemistry postdoctoral scholar in the lab who is now an Assistant Professor at ETH Zürich in Switzerland; Luca Caneparo (Chapter 2), a former biology postdoctoral scholar in the lab; Nathan Hodas (Chapter 4), a former physics graduate student in the lab who is now a postdoctoral scholar at the Information Sciences Institute at the University of Southern California; Christopher Dempsey (Section 5.1), a former Caltech undergraduate student who is now a graduate student at Rice University; Jelena Čulić-Viskota (Chapter 5), a chemical engineering graduate student in the laboratory of Mark Davis at Caltech; Gregor Adams (Section 5.2.7), an Assistant Professor of Cell and Neurobiology at the University of Southern California; and Sapna Shah (Section 5.2.7), a current graduate student in Gregor Adams' lab.

As an overview, my interests span the life stages of the vertebrate system, starting from the early stages of development (especially gastrulation and early segmentation) and moving into adult-related issues (especially epimorphic tissue regeneration). Chapter 2 discusses the use of a photo-convertible protein-driven mosaic analysis tool to highlight membrane morphology in the zebrafish

embryo. In Chapter 3, I developed a transgenic tool, combining multicistronic FP expression and photomodulation, to enable global and targeted sparse lineage tracing in early development as well as during epimorphic tissue regeneration processes in the zebrafish. Chapter 4 focuses on using endogenous SHG in the zebrafish skeletal musculature to tease out the meaning of an interesting SHG-mediated "optical illusion". I present my efforts to refine the SHG nanoprobe exogenous labeling tool for use in an *in vivo* system in Chapter 5. And finally, I try to link each of these tools together in my perspectives chapter, Chapter 6.

Chapter 2

Mosaic fluorescent photoconvertible protein expression illuminates intercellular bridges between cells within the developing zebrafish embryo

2.1 Introduction

Inspired by the groundbreaking four-dimensional analysis of the cell divisions and migratory patterns within the early zebrafish embryo by Keller et al. [5], my colleagues and I strove to find a tool to dissect additional information from cells during early development. Clearly, data concerning cell motility, velocity, and division may be extracted and characterized *in vivo* using tracked FP-tagged nuclei alone [5, 7, 67]. However, dramatic cell shape and morphological changes also occur during dynamic early developmental processes (especially during gastrulation [118]). Indeed, extensive dynamic membrane events — such as the cell extensions (e.g., filapodia) that are seen during cell migration (during involution, for example) and morphological changes (e.g., as cells intercalate during epiboly) — are hallmarks of cell behavior during the proper formation of the vertebrate body plan during gastrulation [68].

For nearly two decades, fluorescence-based biological imaging has enabled extensive characterizations of the organization and migration of cells within the zebrafish blastoderm, and these

approaches generated generalized fate maps linking early cell progeny to eventual tissue identity [60]. Surprisingly, few studies have been performed to analyze the shape of individual cells in the developing zebrafish embryo [119, 120]. Of these, the morphology — including blebbing, filapodia, and pseudopodia — of the hypoblast cells, which give rise to the endodermal and mesodermal cell lineages, was most often examined [68, 121, 122]. These characteristic membrane features are thought to enable the hypoblast to migrate and position themselves correctly within the developing embryo after involution at the blastoderm margin [122]. The epiblast layer, which gives rise to ectodermal tissue, has been thought to be a relatively homogenous pseudostratified epithelium, especially paraxially during later stage epiboly [51]. Cytoplasmic fluorescent labeling has suggested that the epiblast cells are less motile and have a far simpler morphology than the hypoblast cells beneath [122, 123].

As mentioned, ubiquitous nuclear labeling by the use of an FP-histone fusion tag [5] is a possible way to track cells over long periods of time without resorting to sparse labeling techniques. In contrast, cell morphology can only be appreciated by labeling cytoplasmic or membrane components. Ubiquitous FP labeling of the cytoplasm in an *in vivo* context results in the absence of morphological contrast: in most cases, cells usually cannot be segmented and visualized independently from one another at all (Fig. 2.1A). On the other hand, cell boundaries can be isolated with high fidelity when using ubiquitous membrane FP labeling techniques (Fig. 2.1B,C), because there is increased fluorescence at the border between neighboring cells relative to the negligible fluorescence seen internally within each cell, resulting in a high-contrast view of the cell periphery. However, small-scale membrane characteristics (e.g., filapodia or other membrane extensions) of each individual cell cannot be appreciated with ubiquitous labeling of membranes, since the highlighted membrane boundaries appear as a continuous meshwork. Cellular projections into the extracellular matrix between cells would just be seen as part of the fluorescence of the membrane boundaries

themselves.

Previous studies have overcome the limitation of ubiquitous fluorescent labeling to visualize cell morphology using invasive single blastomere injections [4, 68] or cell isolation/transplantation [124], usually relying upon cytoplasmic labeling of cells. Targeted sparse labeling can also be achieved by expressing a ubiquitous photomodulatable FP and then selecting a cell or set of cells of interest specifically using targeted illumination, as described in the introduction. An alternative technique for sparse labeling that allows for targeted subcellular localization of FPs includes what we will refer to as fluorescent mosaicism. We define this kind of mosaicism as the incorporation of an FP label into only a subset of the total number of cells of an intact embryo by means of random gene insertion.

In the case of the zebrafish model system, this can be most commonly achieved by the following co-injection at the zygote stage of development (Fig. 2.3A): (1) plasmid DNA encoding a particular FP of interest driven by some constitutive promoter (e.g., β-actin [125]) and flanked by transposable elements and (2) mRNA from a different species' transposase enzyme that recognizes the transposable elements flanking the gene to be inserted [126]. At some stage of development, cells that inherited both plasmid DNA and transposase mRNA from the zygote injection may translate the transposase mRNA. This newly translated transposase will randomly insert the gene encoding the FP of interest into the genome of that particular cell. If the insertion is in an area that can be actively transcribed, the FP will be expressed in that particular cell. The extent of labeling (i.e., more or less sparse) can be tuned by the concentration of DNA and mRNA that is injected — keeping in mind, of course, that over-injection may disrupt proper embryo development.

Normally, these transposase-mediated gene insertions are used as a means-to-an-end in that researchers screen for germline transmission of the gene insertion so that a transgenic zebrafish line can be generated [126, 125, 127]. An undervalued use for mosaics generated from this technique

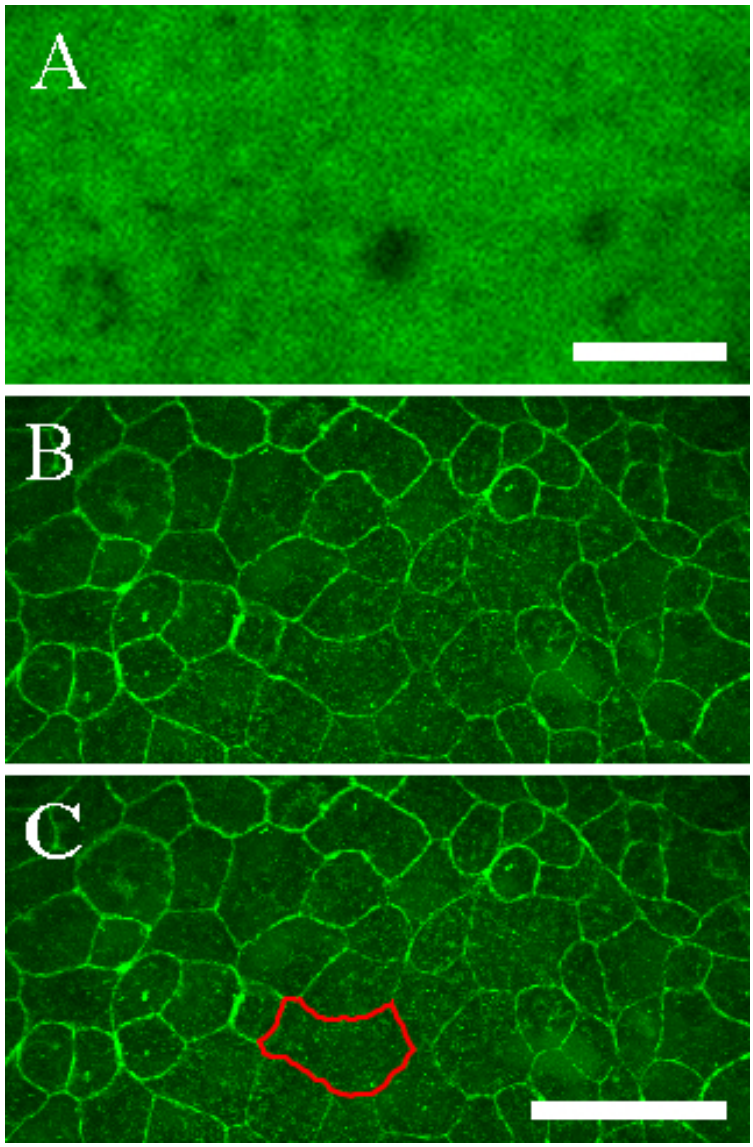

Figure 2.1: **The disadvantages of ubiquitous FP labeling *in vivo***. (A) This panel shows a single optical section of a portion of the developing neural plate within a live, 3-somite stage zebrafish embryo. It is difficult to distinguish cell boundaries with ubiquitous cytoplasmic mDendra2 labeling, since the cells are tightly packed in this developing tissue system. Note that wide gaps in the fluorescence may be extracellular spaces within the embryo, which is the only way to appreciate that there is more than one cell in the field at all. (B,C) These panels show a single optical section of labeled enveloping layer cells just ventral to the animal pole of the developing $\sim$ 75% epiboly embryo. (B) Cell boundaries can be seen with high contrast when cells are labeled with membrane-targeted mDendra2 (described in the results section). (C) These boundaries can be used to segment the cell, as with this exemplary boundary segmentation using the magnetic lasso tool in Adobe Photoshop CS3. However, this stage of development is characterized by dramatic cell morphology changes, which cannot be appreciated with ubiquitous labeling, since small-scale cell extensions cannot be extracted from the fluorescence in the cell boundaries. Scale bars: 25 μm (A), 100 μm (B,C)

is to study the sparse collections of cells themselves (which we call a 'mosaic analysis' approach), especially when considering the application of studying cell morphology. My colleagues and I hoped that sparse membrane labeling using this genetic mosaic strategy would enable us to examine the complex membrane morphology of individual cells *in vivo*.

This chapter focuses on my efforts in collaboration with Luca Caneparo, Periklis Pantazis, and Scott E. Fraser to develop and apply this genetic mosaic labeling tool to characterize zebrafish cell morphology during early development with high contrast. Much of the data and text found in this chapter was first reported in our publication in *PLoS ONE* in May of 2011 [61]. Here, we examined a mosaic subset of membrane-targeted photoconvertible FP-labeled cells within developing zebrafish embryos and discovered that certain epiblast cells have unique membrane domains that link cells across substantial distances. This finding is in sharp contrast with the aforementioned assertion that epiblast cells seem to function as a simple migrating epithelium, and our results demonstrate the power of mosaic, photoconvertible FP labeling in an embryo-wide context.

2.2 Results

2.2.1 Generating mosaic embryos to visualize membrane morphology *in vivo*

In order to probe the membrane dynamics and behavior of early stage zebrafish embryos in a mosaic manner, we took advantage of a plasmid (called pMTB) designed by a former postdoctoral student in the lab, Sean Megason. This plasmid allows efficient constitutive expression of a protein of choice within all cells of the zebrafish embryo. To achieve membrane-targeted FP labeling, two identical lipid anchor recognition sequences [37, 128] were added in frame upstream of the sequence for the unaltered monomeric, photoconvertible FP *mDendra2* [26]. The expressed protein from this construct, which is anchored on the cytoplasmic side of the cell plasma membrane (Fig. 2.2), will

be referred to as memb-Dendra2.

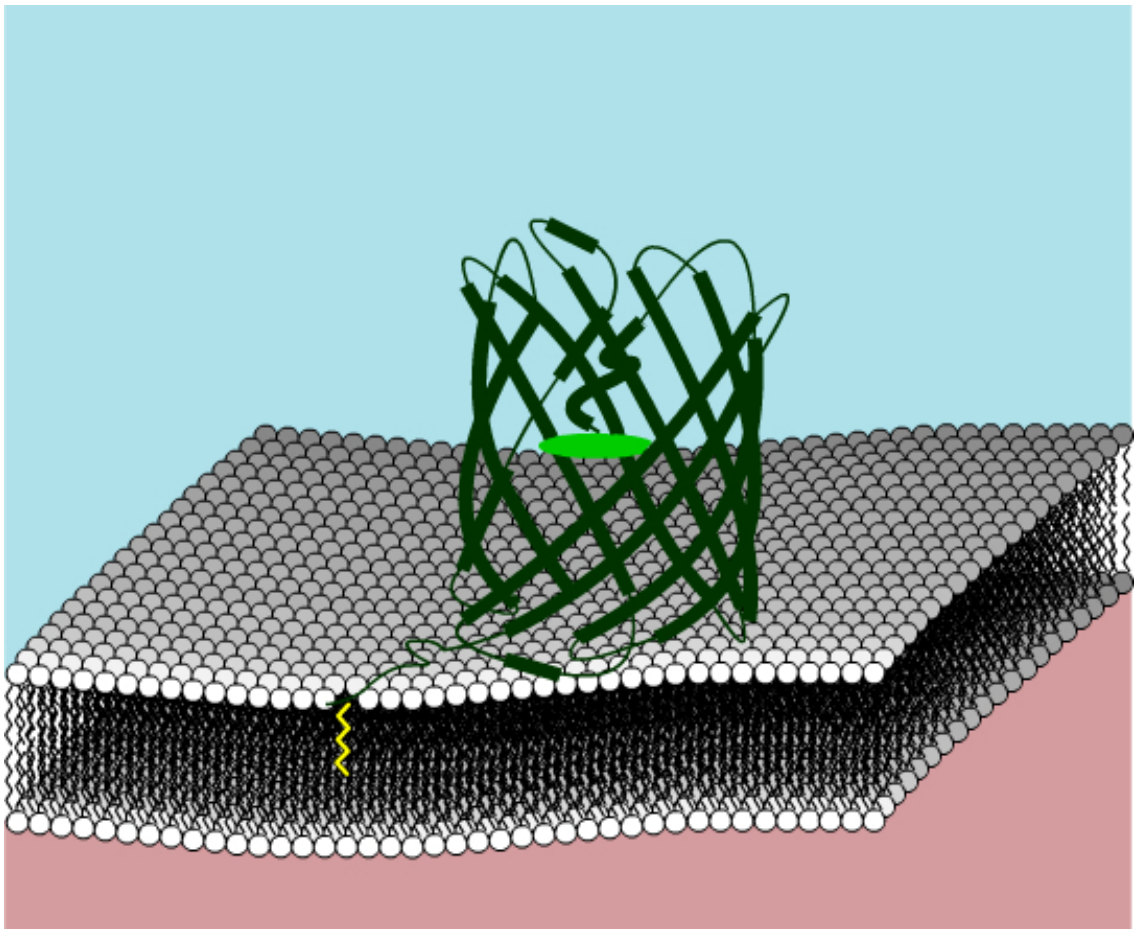

Figure 2.2: **memb-Dendra2 labels the plasma membrane**. This is a simplified cartoon (not to scale) representation of the memb-Dendra2 (structure in dark green, with the chromophore at the center of the β-barrel represented as a light green ellipse) protein anchored to the plasma membrane of a cell. Post-translational lipid modifications (represented by a jagged yellow line) due to the lipid anchor recognition sequences [37] cause the FP to be localized to the inner leaflet of the plasma membrane. The cytoplasm is labeled light blue while the extracellular matrix is labeled in pink.

Since Tol2-mediated transposition into the zebrafish genome most often occurs only after the midblastula transition [62], we typically started our analyses late into the blastula period or during the gastrula period of zebrafish development. By the gastrula period of development, the lateral aspects of the embryo away from the periphery can be simplified into three clear individual cell layers, the so-called enveloping layer (EVL), the epiblast layer, and the hypoblast layer, mentioned

previously (Fig. 2.3B). The leading edges of the epibolic movements of cells across the yolk ball and the dorsal aspect become slightly more complicated, in that there is a cellular thickening due to continued involution, convergence, and extension movements, but these three cell layers are still maintained within the embryo [68]. A typical mosaic embryo at the beginning of the gastrula period following zygote stage injections can be seen in Fig. 2.3C. Right away, we noticed long (many cell diameters in length) cytoplasmic filaments across wide stretches of the developing embryo. These filaments are most-likely not related to neural progenitors, since the neural differentiation program has not initiated this early in development, so we investigated these filaments more closely.

2.2.2 Examination of long cellular membrane extensions that exist within the epiblast layer

Focusing in on each of the different layers of embryonic tissue using high-resolution, 3D confocal imaging, we determined that these membrane extensions only appeared in the epiblast layer (Fig. 2.3D). Though the hypoblast layer had short (less than 1 cell diameter) membrane protrusions, no long membrane fibers were observed. Viewing the long membrane structures using high-resolution confocal microscopy, we determined that these long membrane filaments were protruding out from cells. Additionally, we approximated that nearly 20% of epiblast cells within the gastrula embryo have these long membrane extensions.

We were curious as to why these strikingly long membrane protrusions have not been described before in zebrafish embryos. First, we wanted to make sure that these long extensions were not an artifact of memb-Dendra2 overexpression. In unlabeled, WT zebrafish embryos, we used differential interference contrast (DIC) microscopy to enable us to see long membrane projections within the epiblast layer, seemingly linking cells together (Fig. 2.3E). We explore this possibility of cellular connections later in the study. These membrane projections are difficult to find using DIC

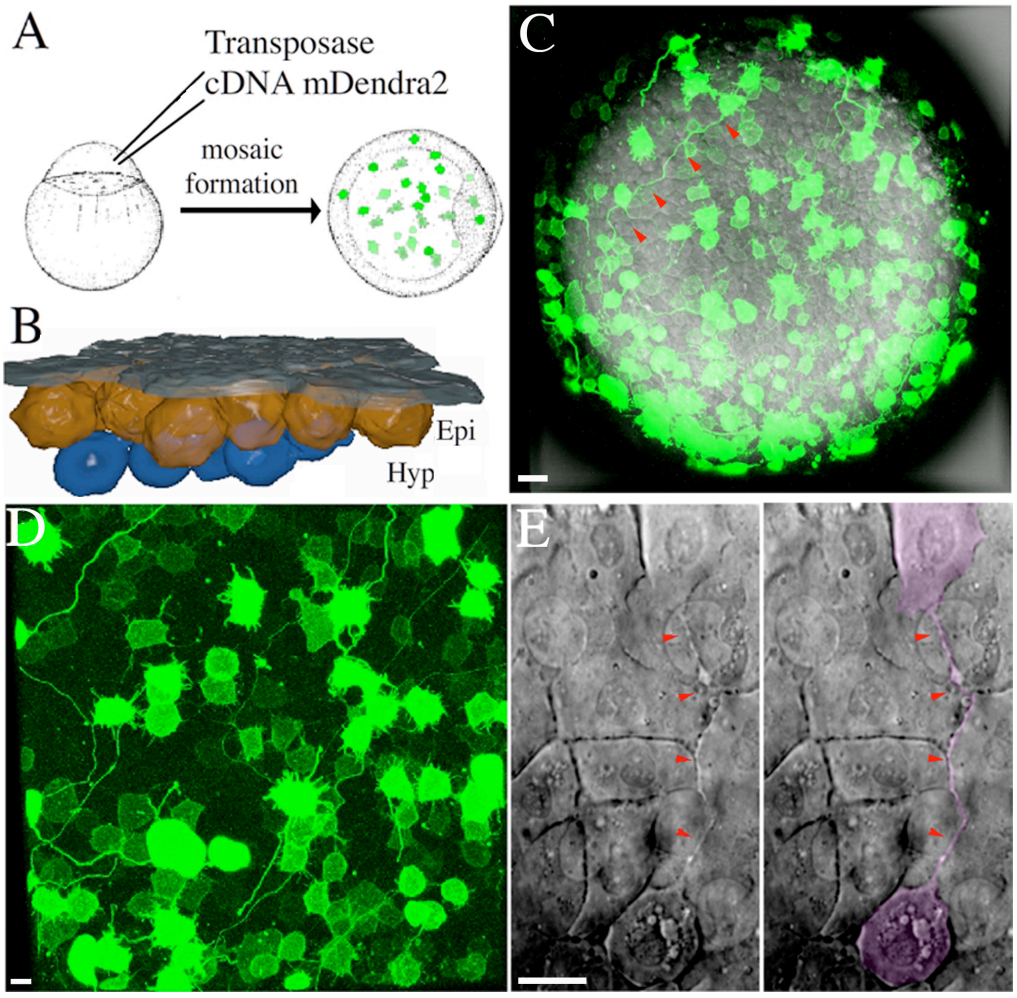

Figure 2.3: **Generating fluorescent mosaic embryos for the analysis of membrane morphology in the developing embryo**. (A) This is a simplified cartoon depicting how fluorescent mosaic embryos are generated (modified from [51]). Co-injection of pMTB plasmid DNA encoding an FP of interest and *Tol2* transposase mRNA using a glass micropipette into a zygote stage embryo (left) results in the generation of an embryo with mosaic fluorescent protein expression (right). (B) This panel depicts a 3D rendering (not to scale) of a portion of the paraxial aspect of an idealized mid-gastrula zebrafish embryo. Three cell layers can be seen atop the yolk syncytial layer and yolk cell of the zebrafish embryo at this stage (each one cell layer thick, in this portion of the embryo). Large cells in the EVL surround the blastodisc, covering the epiblast (ectodermal fate) and hypoblast (mesoderm and endodermal fate) layers, which are separated by the so-called Brachet's cleft as a result of involution [51]. (C) This is an animal pole view of a merged bright-field and confocal fluorescence image of a fluorescent memb-Dendra2 mosaic embryo at the onset of gastrulation. (D) This is a zoomed in portion of the fluorescence channel from the epiblast layer of the embryo in C, where long membrane extensions are clearly visible, emanating from individual cells. (E) DIC image of a WT embryo where a clear long (greater than 3 cell diameters) membrane extension can be seen intercalating between cells in the epiblast layer (red arrowheads), seemingly linking two cells together. The right panel highlights the intercellular bridge and the connected cells in magenta. (This figure is reproduced from [61].) Scale bars: 20 μm (C–E)

microscopy alone; we were only able to identify them, because we knew what we were seeking, giving a reason for why these projections have not been noticed previously.

We also generated a cytoplasmically localized mDendra2 fluorescent mosaic using a pMTB plasmid containing just the *mDendra2* sequence alone, without upstream post-translational modification sequences. In mosaic embryos resulting from co-injection of this plasmid with transposase mRNA, we no longer see long membrane projections at all; only short projections remain visible in these embryos (Fig. 2.4A, arrowheads). Thus, the longest membrane extensions that are present in the epiblast layer may contain very little — if any — cytoplasm. This could be why cytoplasmically labeled mosaics (from, e.g., dye label fate mapping experiments [68, 124]) were unable to resolve these projections previously.

We next considered whether these membrane projections are only present during a particular time window of development and that we were lucky enough to catch them when we first analyzed these mosaics at the onset of gastrulation. However, it soon became clear that these membrane extensions were visible as late as the bud (Fig. 2.4B) and the 3 somite (Fig. 2.4C) stages of development, which are time points after the completion of gastrulation. Indeed, individual extensions are often maintained throughout the gastrula period into early segmentation (Video A.1.1), and long extensions can be seen in mosaic embryos even at the 10 somite stage (Video A.1.2), approximately 14 hpf and nearly 10 hours after the onset of gastrulation. Interestingly, as development proceeds, longer membrane extensions transition from being somewhat tortuous in structure to becoming much more straight (compare projections in Fig. 2.3D and Fig. 2.4C). Additionally, these extensions often fragment and disintegrate following the gastrula period (Video A.1.2).

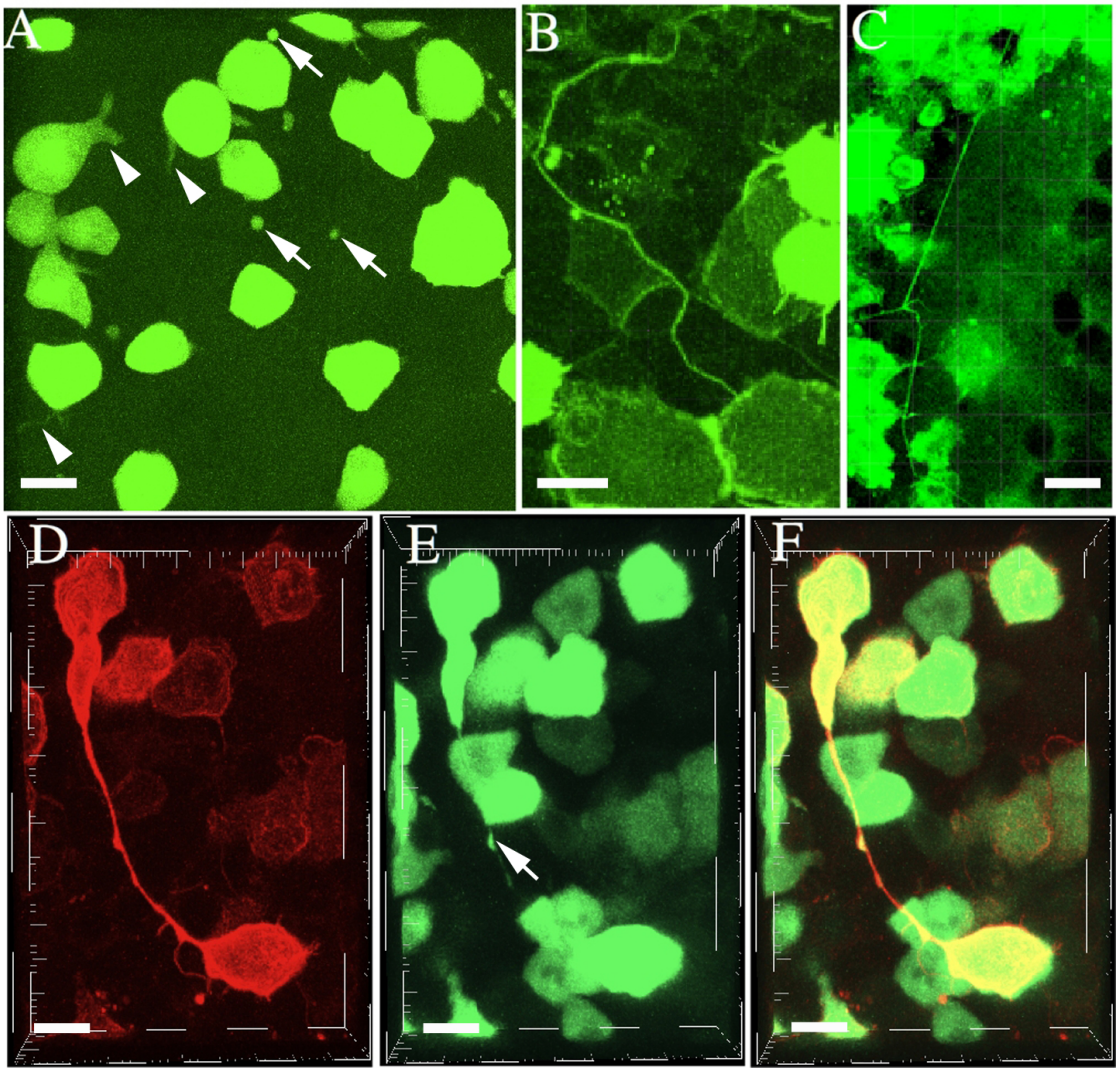

Figure 2.4: **Long membranous extensions contain little cytoplasm and last throughout gastrulation**. Each of these panels shows an animal pole view of an early gastrula embryo. (A) This first panel shows an embryo following zygote stage injections of cytoplasmic *mDendra2* DNA in the pMTB plasmid and *Tol2* mRNA. The long cellular extensions cannot be visualized with mosaic cytoplasmic FP labeling; only short membrane extensions can be seen (arrowheads). Interestingly, small high-intensity regions with mDendra2 fluorescence could be seen outside of cells (arrows, potentially similar to the arrow in D), which could be cytoplasmic contents of these long membrane extensions. (B, C) These long extensions can also be seen later in development, for example, during the (B) bud and (C) 3 somite stages of development. Later in development, these membrane projections seem to become straighter and thinner. (D–F) Co-injection of pMTB plasmid DNA encoding membrane-targeted *mCherry* [129] and an *EGFP-β-actin* fusion with *Tol2* mRNA enables visualization of the (D) membrane projections (red fluorescence) as well as (E) labeled cytoskeletal components (green fluorescence). (F) Some EGFP-β-actin can be seen throughout the membrane extension, especially within a central region where the diameter is slightly increased (arrow in D). (This figure is reproduced from [61].) Scale bars: 20 μm

2.2.3 The membrane extensions bridge cells together across the embryo

As mentioned previously, we had early evidence from our fluorescent mosaics and DIC analysis that these long membrane projections somehow linked two cells together. So, we decided to explore the possibility that these extensions act as cell connections and how cells that are linked might be related. Initially, we visualized gastrula period embryos and could not determine how these structures formed and linked cells.

We initially postulated that these thin cellular extensions may somehow be related to the so-called cytonemes seen during *Drosophila melanogaster* wing imaginal disc development, where in culture, cytonemes protruding from anterior flank cells seem to elongate and eventually come into contact with chemoattractant-producing central cells of the imaginal disc [130]. Additionally, the extensions seen in the zebrafish gastrula are similar to cytonemes in that they are thin (less than 1 μm in diameter) and extend many cell diameters across the developing embryo. We had already discovered from our cytoplasmic mDendra2 mosaic (Fig. 2.4A) that the cytoplasmic contents were either negligible or were made up of a particular protein that somehow excluded the free mDendra2 from the interior. Since cytonemes seem to arise due to the polymerization of actin and not tubulin, we developed a co-injection mosaic strategy to try to visualize β-actin within these membrane filaments. We co-injected two pMTB plasmid constructs with transposase mRNA in this test: one of the pMTB plasmids encoded a membrane-targeted mCherry [129] FP, while the other included the coding region for a fusion of EGFP (Clontech) with β-actin. However, we only saw β-actin within thicker cellular extensions (Fig. 2.4D–F); we could not resolve cytoplasmic components in thinner extensions (as in later stages, like in Fig. 2.4B, C). Interestingly, some of these membrane extensions are thicker regionally (Fig. 2.4E, arrow), and cytoplasmic contents sit in a bolus within these structures. It is possible that patches of cytoplasm seen in the cytoplasmic mDendra2 mosaic (2.4A, arrows) could be explained by attributing them to being a part of portions of these membrane

extensions.

Since we could not immediately rule out that these were cytoneme-like cellular processes linking cells together, we decided to look earlier than the gastrula stage in an attempt to witness the formation of one of these cellular connections in the developing embryo. Using four-dimensional (4D) confocal imaging (3D plus time), we discovered that the formation of these membrane projections is dramatically different than cytonemes in *Drosophila*. Starting in the late blastula period ($\sim$ 4–5 hpf), a subset of cells undergoing mitosis do not fully complete cytokinesis. As the daughter cells migrate apart from one another, a thin membrane tether — presumably in the space between cell boundaries as cells intercalate, as seen in Fig. 2.3E — is maintained between them (Fig. 2.5A, Video A.1.3). Indeed, these membrane extensions always connect two separate epiblast cells within the embryo (arrowheads Fig. 2.5B). These cell extensions are physical links between daughter cells that often span distances of many cell diameters across the embryo for several hours during development (Fig. 2.5C, C'), and we will hereafter refer to these as intercellular bridges. Thus, intercellular bridges represent a new class of membrane extensions that are unique as compared to already characterized long membrane extensions such as cytonemes in *Drosophila* [130] or even filapodial protrusions seen during sea urchin development [131].

2.2.4 Intercellular bridges link vastly separated cells across territorial boundaries

With a newfound understanding that these intercellular bridges link daughter cells, we wished to analyze how these daughter cells distribute within the embryo. Since the cells can remain linked throughout gastrulation, they must be able to maintain the connection even when undergoing normal morphogenetic movements, such as radial intercalation. Additionally, we observed that linked cells can still undergo normal oriented cell division [132, 133] during gastrulation (Video A.1.4). By the shield stage of gastrulation, dorsal-ventral patterning has been established, and — soon after — pri-

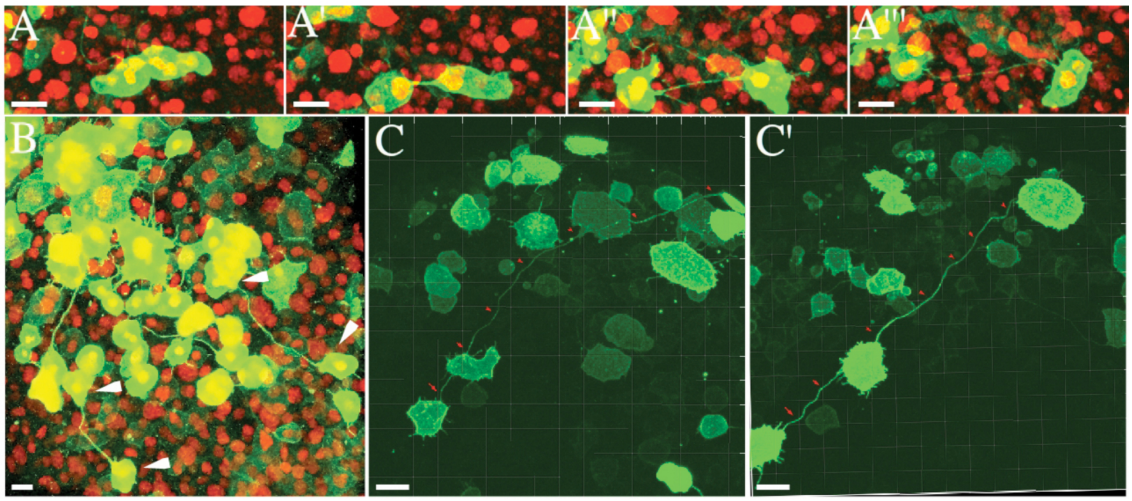

Figure 2.5: **Intercellular bridges are formed during cell division and can persist throughout gastrulation**. (A–A''') These images are successive time-points from a time-lapse confocal imaging experiment (see Video A.1.3), viewing mosaic memb-Dendra2-labeled cells near the animal pole of a late blastula stage embryo. The long membrane extensions seen in all of the images thus far link two cells and presumably arise after incomplete cell division, where cytokinesis does not fully separate the cells. The two daughter cells maintain a connection as unlabeled cells intercalate between them. Nuclear labeling was achieved by means of a histone 2B (H2B) fusion to mCherry [129]. mRNA encoding *H2B-mCherry* was co-injected with plasmid *memb-Dendra2* DNA and *Tol2* mRNA at the zygote stage. This nuclear marker enabled us to ensure that these so-called intercellular bridges did in fact link two daughter cells. (B) This is an animal pole view of a similarly injected embryo as in A during gastrulation. Pairs of cells linked by an intercellular bridge (green cells, arrows) are seen within a sea of nuclear-labeled cells (red). (C, C') Successive time points of animal pole view from Video A.1.1, showing that even long intercellular bridges linking 2 cells (red arrowheads) can persist for over an hour, from (C) the middle to (C') the end of gastrulation. (This figure is reproduced from [61].) Scale bars: 20 μm (A–C')

mary neural specification begins in the epiblast layer, forming an anterior neural border towards the animal pole of the embryo, separating neural and non-neural fated cells [134]. By mid-gastrula, we see that, although the anterior neural border has been established, cells connected by intercellular bridges may be linked across territorial boundaries. Interestingly, superimposing 30 cell pairs of intercellular bridges from 20 different embryos, we discovered that there is no obvious orientation for the cells linked by intercellular bridges (Fig. 2.6A): some cells adhered to territorial boundaries, certain cells are connected between neural and non-neural territories, and others link cells on opposite lateral sides of the developing embryo.

Concentrating on the late gastrula period, we analyzed 51 intercellular bridges in 38 independent embryos and calculated that their average length was approximately 215 μm (Fig. 2.6B, C), an order of magnitude longer than pseudopodial projections, which rarely extended past a cell diameter or two ($\sim$ 20–25 μm). Intercellular bridge diameter normally ranged from 1 μm in late blastula, early gastrula periods to diffraction-limited ($\sim$ 200 nm) by the end of gastrulation. Assuming that a membrane tether of length 215 μm between two cells during late gastrulation is a cylindrical lipid bilayer with a diameter of 0.5 μm, we can estimate the surface area to be approximately 338 μm^2. The surface area of an epiblast cell at the same period of development can be approximated to be 1260 μm^2, assuming the cell is a sphere of radius 20 μm. Thus, even with a conservative estimate, these intercellular bridges are made up of as much membrane as 25–40% of the total membrane of an individual cell.

2.2.5 Membrane-associated proteins can be shared between cells linked by intercellular bridges

Since these intercellular bridges are maintained membrane connections between cells that are far apart within the embryo, we wondered whether membrane components could be shuttled between

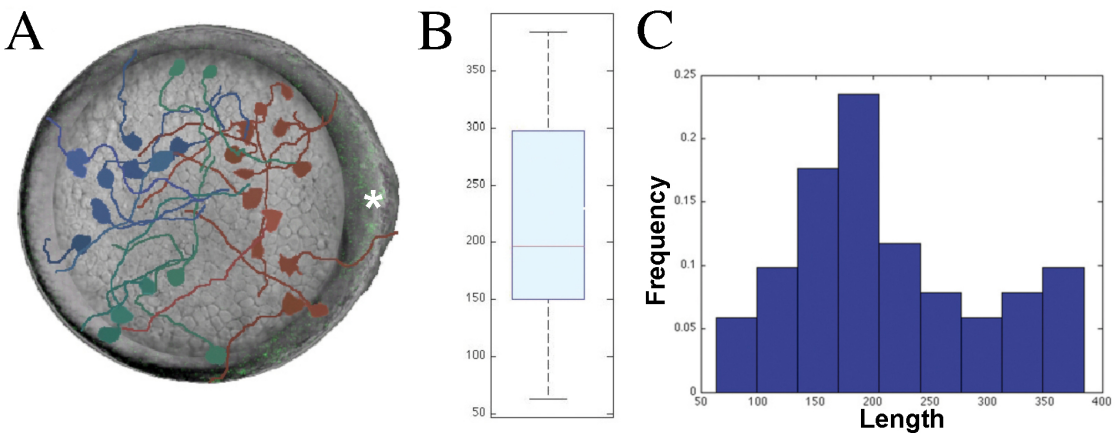

Figure 2.6: **Intercellular bridges lengthen significantly during gastrulation and link cells across territorial boundaries**.(A) This image shows an overlay of intercellular bridge-connected cells on an idealized embryo (grayscale) during the middle of gastrulation. The idealized embryo is in an animal pole view, with the dorsal aspect depicted on the right-hand side of the image (asterisk). In addition to cells linked within the a particular fated region, intercellular bridges link cells across cellular boundaries, including cells between neural (red) and non-neural (blue) territories. Additionally, some cells are connected across the different lateral sides of the embryo (green). (B) This boxplot indicates the spread of the length of intercellular bridges at the middle of gastrulation. The average length is ~ 215 μm, the median is depicted by the red line, and the dotted line bars display the extreme values of the length distribution. (C) The data from E plotted as a histogram, to show the heavy-tailed (for longer lengths) distribution of intercellular bridge lengths. (This figure is reproduced from [61].)

linked cells in a developmentally relevant time window. Specifically, could membrane components move from one linked cell to the other within the $\sim$ 5 hour period of gastrulation? To answer this question, we utilized the photoconvertible property of memb-Dendra2. Photoconversion can be used to further isolate individual cells within the embryo beyond the level of random mosaicism alone, but we wished to take this targeted fluorescence switch one step further. We hypothesized that if one cell (which we will Cell 1) is photoconverted from an intercellular bridge-linked pair, the photoconverted memb-Dendra2 pool in Cell 1 should eventually be distributed across the intercellular bridge into the unconverted cell (which we will call Cell 2) by lateral diffusion or by some active shuttling process.

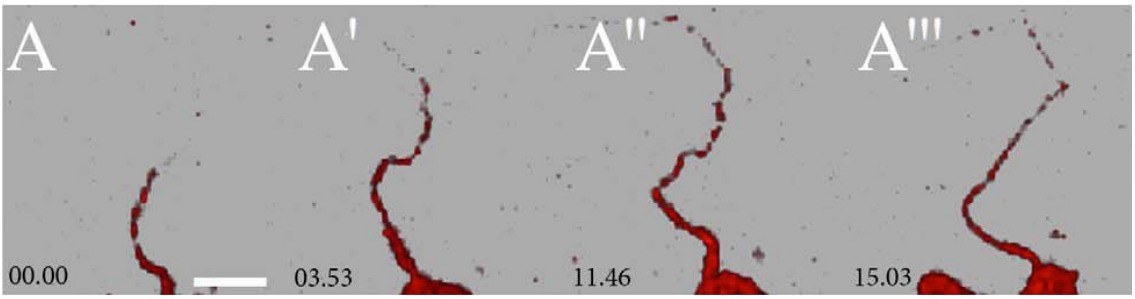

Figure 2.7: **Membrane contents can move along the intercellular bridges**. (A–A"') These are successive images from a confocal time-lapse of an animal pole mounted, gastrula period embryo. One of two memb-Dendra2 expressing cells linked by an intercellular bridge was photoconverted, and the migration of photoconverted memb-Dendra2 was monitored in time and space. Thus, membrane-associated proteins can progress into the thin intercellular bridges. (This figure is reproduced from [61]). Time-stamps: min.sec. Scale bar: 10 μm

As expected, photoconversion of Cell 1 leads to the progression of photoconverted memb-Dendra2 along the length of the intercellular bridge, and this transfer can be visualized in 4D with confocal microscopy (Fig. 2.7). Note that in all cases, photoconverted fluorescence moved from Cell 1 out onto the intercellular bridge, and in this case, we quantified the extent of memb-Dendra2 movement within a 50 min time window. We estimated that photoconverted memb-Dendra2 can move as far as 100 μm in 30 min, though we can attribute some of this apparent motion as further

elongation of the intercellular bridge, as the cells still move during the quantification period. Importantly, we were able to see photoconverted memb-Dendra2 move all the way from Cell 1 to Cell 2 in several cases (Fig. 2.8), most often when the intercellular bridges had larger diameters connecting nearby cells. Longer and thinner bridges often had a slower rate of memb-Dendra2 transfer (for example, taking nearly 18 minutes to traverse approximately 22 μm, Fig. 2.9 and Video A.1.5).

2.3 Discussion

2.3.1 Genetic mosaicism and photoconvertible proteins can be used together to reveal morphological changes within the developing embryo

In the study, we created genetic mosaic embryos, highlighting a random subset of cell membranes in the three major cell layers. Although short filapodial projections can be seen in both the epiblast and hypoblast cells as cells proceed with normal morphogenetic movements (e.g., involution, convergence, and extension [51, 68]), a fraction of cells within the epiblast layer that divide during the late blastula period and maintain a membranous link between them. These intercellular bridges narrow as more cells intercalate between the daughters, but surprisingly, they are often maintained throughout gastrulation, suggesting that these membranous tethers are more than just an anomaly of division. Since cells are constantly intercalating and migrating during the highly dynamic period of gastrulation, it might be expected that weak membrane linkages would be torn apart soon after the division event. By the late gastrula period, the average length of an intercellular bridge is approximately ten cell diameters in length and often just above the diffraction limit in diameter, yet these cells remain connected and each daughter can even divide normally. Thus, genetic mosaicism is a powerful tool to illuminate complex cell morphology early in development, providing actual shape-related context to the dramatic cell movements seen in fate mapping and nuclear tracking

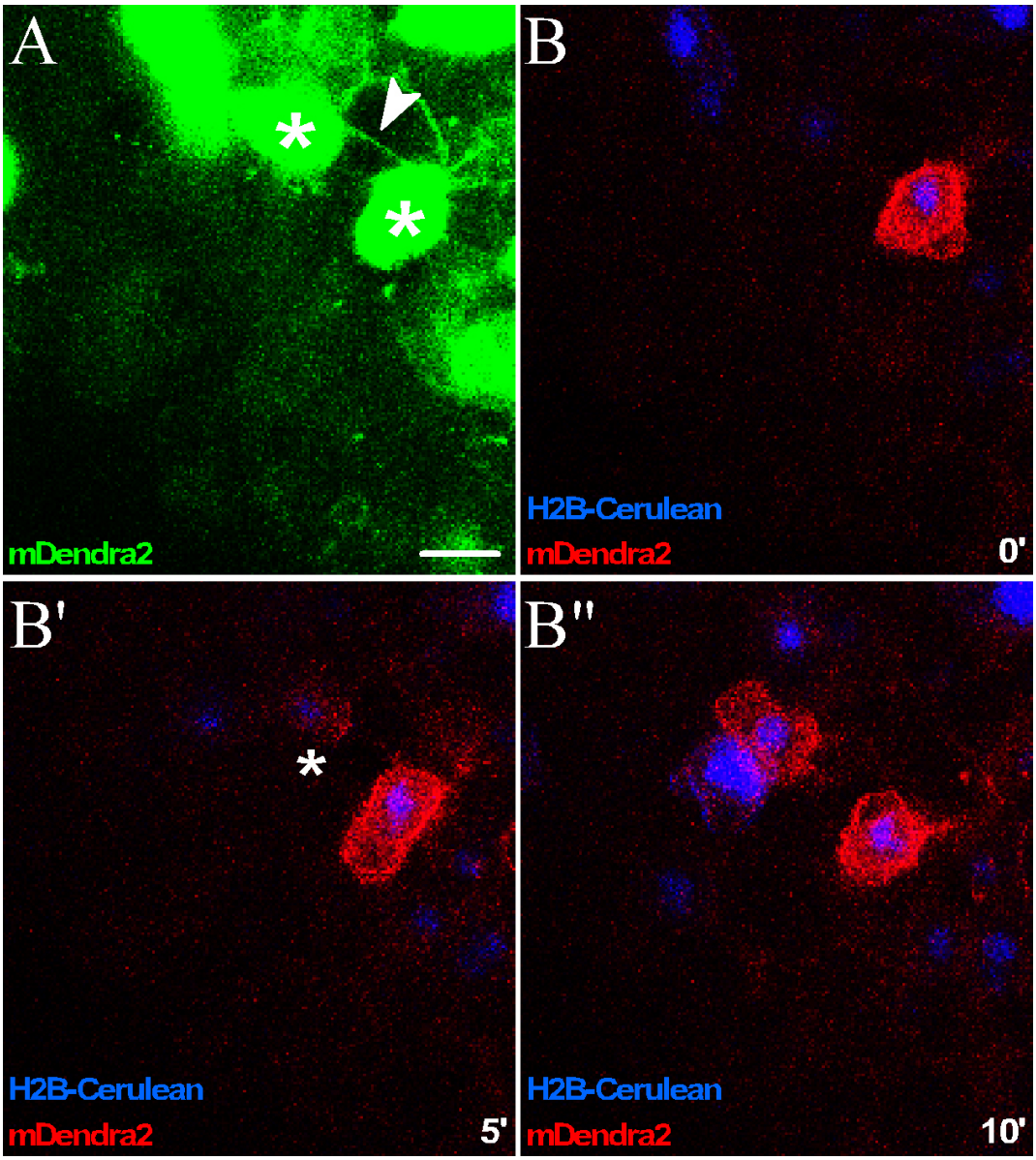

Figure 2.8: **Cells linked by intercellular bridges can share membrane associated protein components**. These panels depict mosaic memb-Dendra2-labeled cells in the animal pole of an early gastrula stage embryo. (A) The unconverted memb-Dendra2 channel shows two cells (asterisks) linked by an intercellular bridge. Cell 1 is the rightmost cell, which is photoconverted at time t = 0, and Cell 2 is the leftmost cell of the pair. (B–B") Merged image of the photoconverted memb-Dendra2 channel (red) and a nuclear-labeled channel (blue). The nuclear label in this case comes from pMTB plasmid DNA including the coding region of an H2B fusion with the FP Cerulean [135], which was co-injected with the usual *memb-Dendra2* DNA/*Tol2* mRNA solution at the zygote stage. (B) Immediately after photoconversion of Cell 1, only Cell 1 has red membrane localized fluorescence. (B') After 5 minutes, photoconverted memb-Dendra2 can be seen in Cell 1 and Cell 2 (asterisk). (B") After 10 minutes, photoconverted memb-Dendra2 is seen throughout the plasma membrane in both Cell 1 and Cell 2. Scale bar: $\sim 20\ \mu$m

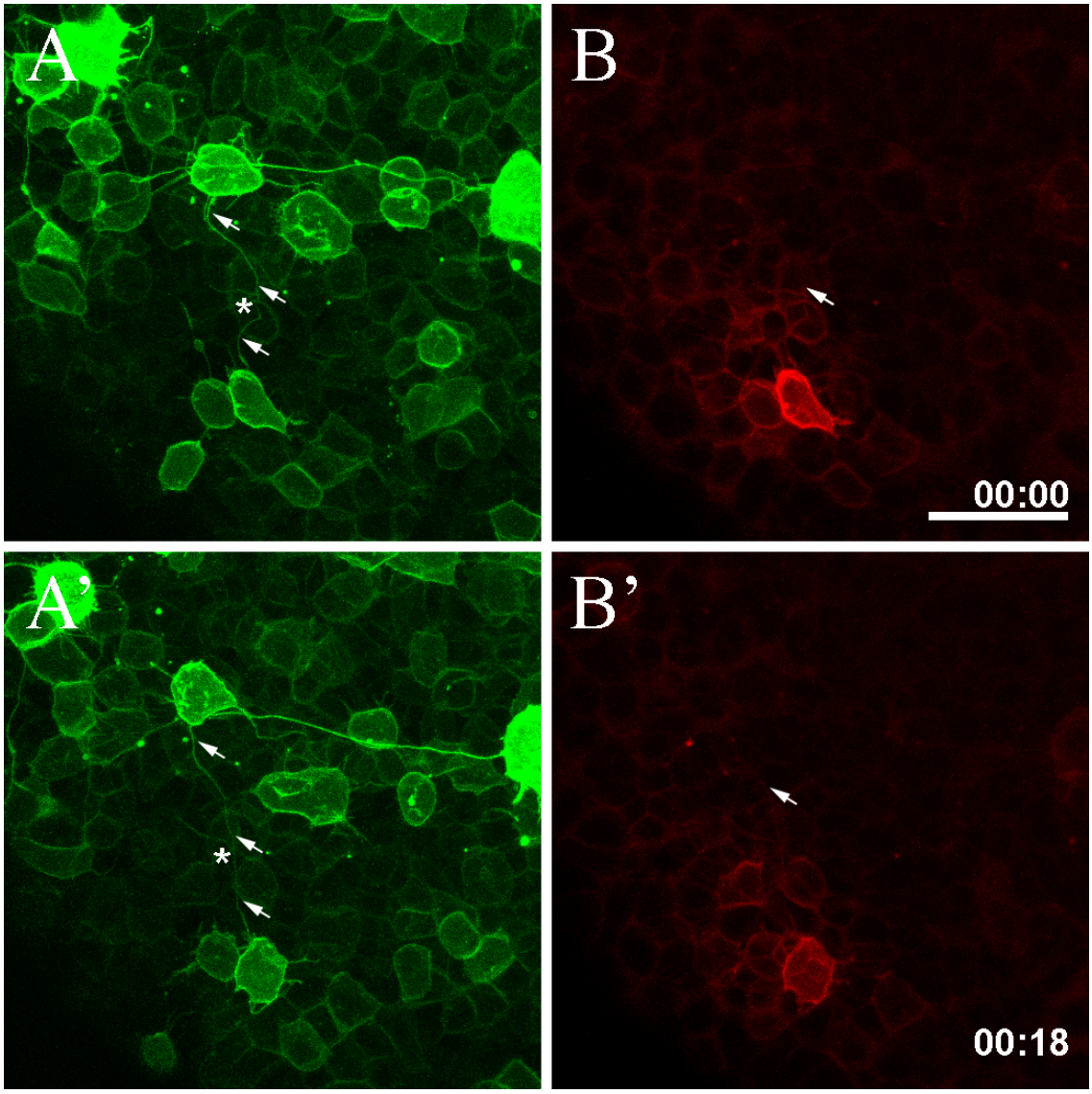

Figure 2.9: **Thinner intercellular bridges exhibit slow memb-Dendra2 transport**. These are successive images from a confocal time-lapse imaging session of an animal pole mounted mosaic memb-Dendra2 embryo during early gastrulation (see Video A.1.5). (A, A') The unconverted memb-Dendra2 channel illuminates two cells linked by an intercellular bridge (arrows) at 0 min and at 18 min of imaging. The bottom cell of the pair is the cell that is photoconverted. This particular intercellular bridge seems to have a bifurcation point, which has unknown origin. (B, B') The photoconverted memb-Dendra2 channel shows that the leading edge of the photoconverted protein along the intercellular bridge (arrow) moves slowly in this thin intercellular bridge, requiring 18 minutes to move ~ 22 μm. Scale bar: 50 μm

studies.

Taking sparse labeling one step further, we took advantage of membrane-targeted photoconvertible FP mDendra2 to enable isolation down to the level of individual cells within the sparse labeled mosaic embryo for further high-contrast observation. Although we determined that the cytoplasm is negligible in thinner intercellular bridges, targeted photoconversion gave us the means to determine whether cells linked by intercellular bridges could share membrane components between them on a physiologically relevant time scale. We determined approximate protein kinetics (apparent lateral protein movement rates) of memb-Dendra2 transport into the intercellular bridge, and found that the rate of protein transport along the intercellular bridge could be as rapid as around 3 μm per minute. This, in conjunction with the finding that a photoconverted memb-Dendra pool can be shuttled from one connected cell to the other suggests that membrane communication can occur within the early developmental period. Clearly, the combination of genetic mosaicism and targeted photoconversion can be a powerful tool for tracing cellular morphology as well as protein kinetics in a living embryo zebrafish embryo in 4D.

2.3.2 Intercellular bridges in the zebrafish gastrula are unique in length and cytoplasmic content

Intercellular bridges in the zebrafish embryo differ from many other previously reported long membranous structures. Unlike cytonemes, axon growth cones, sea urchin filapodia and other filamentous membrane projections (reviewed in [136]), intercellular bridges form between two cells as a result of incomplete cytokinesis. Thus, their formation and persistence is not likely driven by chemoattractants, which is true for these other membranous fibers. Like the long cellular projections emanating from single cells, intercellular bridges contain at least actin within the early phases of their creation, when the diameter of these tethers can be as thick as 1 μm. However, cytoplasmic

components seem to be absent in thinner intercellular bridges, especially by the mid to late gastrula period. In addition, unlike these other cell projections, intercellular bridges have no particular orientation within the embryo as they can link cells spanning across territorial boundaries within the embryo. Importantly, this lack of orientation in intercellular bridge formation is not unexpected, since the axes of division during the blastula stage are not related to future tissue lineage [68, 119]. Importantly, studies of these other long membranous structures could be enhanced using our fluorescent mosaic technique — especially using membrane-targeted and photoconvertible FPs — since visualizing the thinnest of these filamentous projections is difficult when there are too many other fluorescent cells nearby [130].

Intercellular bridges in the zebrafish gastrula are also distinct from other described intercellular bridges from previous studies. In cell culture, short (10–30 μm) intercellular bridges have been described and have been shown to share even cytoplasmic contents [137]. However, since these cell culture experiments focus on immortalized cell lines, they may not reflect true cell-cell behavior such as is seen *in vivo* in the zebrafish. For example, the intercellular connections in cell culture may not get as long because there are not significant morphogenetic movements driving the cells further and further apart.

Intercellular bridges between germ cells in the developing testis have been studied for decades and have been thought to play a role in compensating for genetic imbalances that could be possible after switching to a haploid genetic paradigm after meiosis [138]. In contrast to intercellular bridges, germ cell linkages are much wider in diameter, are much shorter, and connect more than one cell together. Additionally, the idea of compensating for genetic imbalance does not fit in the context of the developing embryo. However, since mechanisms for incomplete cytokinesis may be conserved between these systems, understanding germ cell intercellular bridges could give insight into how embryonic intercellular bridges are formed.

A study of the deep cells within medaka teleost embryos described short ($\sim$ 30 μm) intercellular connections [139]. Interestingly, this result suggests that the intercellular bridges are at least conserved within teleost fish embryos, since these cells were fixed and dissociated from the blastoderm before being visualized. It is possible that the intercellular bridges that we have seen in the mid to late gastrula period were also present in these fish, but these longer, more fragile intercellular bridges may have been severed during the dissociation process. Thus, our mosaic analysis technique is clearly a robust method for visualizing cell shape in a whole embryo context that maintains fragile cellular connections and processes. Ultimately, perhaps the closest relatives to the intercellular bridges discovered in this study may be found in studies of chick embryogenesis [140] and neurulation [141], where longer intercellular connections were described, which suggests that intercellular bridges might be conserved in other vertebrates in addition to teleost fish.

2.3.3 Are intercellular bridges conserved in vertebrates during early development?

One major open question is whether these intercellular bridges are conserved across vertebrates. Currently, studies of the mouse gastrula using genetic mosaicism is made difficult by the lack of optical transparency within these embryos. However, one of two methods could be used to overcome these limitations. Since we now know where (the epiblast layer) and when (late blastula, early gastrula) to look for these structures at least in the zebrafish, we can perform cryosectioning and scanning electron microscopy to ascertain whether these structures exist in other vertebrate embryos, as was performed in the chick system several decades ago [140]. This particular endeavor may be assisted by recent advances in high-throughput field emission scanning electron microscopy [142]. The major advantage of this method is that embryos from many different vertebrate species can be analyzed without the necessity for genetic tools that are prevalent in just a few model organisms (e.g., mice, zebrafish, and chick)

Alternatively, fluorescence-based approaches — such as a membrane-targeted fluorescent mosaic similar to the one used in this study or so-called brainbow organisms [143, 144, 145] — could be considered for species where genetic toolboxes exist. In this case, embryos can be fixed and then treated with newly developed tissue clearing agents [146], which provide superior optical transparency during imaging. The major disadvantage to either of these methods is that they require fixed samples, which precludes the study of individual intercellular bridges in time as well as space. However, if these membrane connections are found to be a conserved morphological feature across multiple vertebrate species, future advances in microscopy (enabling deeper penetration by further red-shifted pulsed lasers, for example) will hopefully provide the necessary tools to visualize this complex membrane morphological feature in time.

2.3.4 Hypotheses regarding the potential function of intercellular bridges in the developing embryo

Since we were able to show that cytoplasm is present within early, thicker intercellular bridges and that membrane proteins can be shuttled between connected cells, an obvious possible function for these intercellular bridges is to act as a channel to share cell components between the daughter cells. Intercellular bridges between immortalized cell lines can share cytoplasmic protein contents [137], and cells connected by tunneling nanotubes have been shown to share organelles [147], retroviruses [148], and immune surface receptors [149]. The idea of sharing subcellular proteins, nucleic acids, organelles, and membrane proteins is also consistent with previous studies of intercellular bridges between germ cells [138], cells in the chick gastrula [140], and squid embryo cells [150] in a tissue-wide context.

This possibility is attractive when considering one time-lapse analysis of the intercellular bridges in particular (Fig. 2.10 and Video A.1.6). In this time-lapse, two cells in the middle of gastrula-

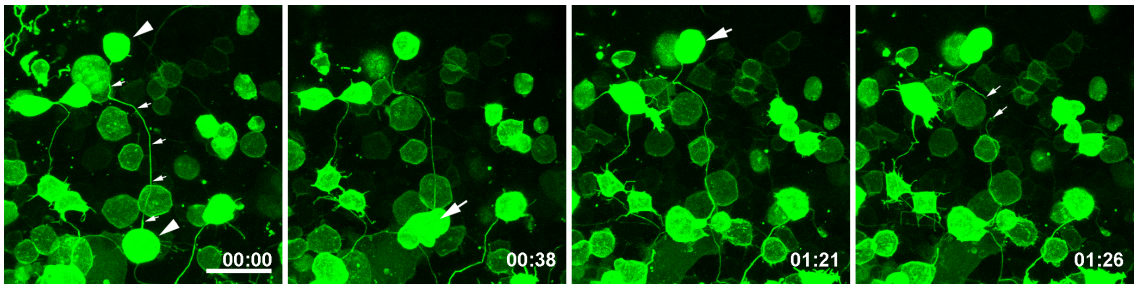

Figure 2.10: **Cell division events may be communicated by the intercellular bridges**. These panels depict successive images from a confocal time-lapse of an animal pole mounted mosaic memb-Dendra2 embryo during the middle of gastrulation (see Video A.1.6). Two cells (arrowheads, left panel) are linked by an intercellular bridge (arrows, left panel). 38 minutes after the start of the time-lapse, the lower connected cell begins to divide (arrow, middle left panel). 43 minutes later, the upper connected cell begins to divide (arrow, middle right panel). This division event is followed by the destruction of the intercellular bridge shortly thereafter (arrows, right panel). Since membrane components can be shared during the gastrula period, perhaps the membrane tethers are maintained to relay cell division information between daughter cells separated by large distances. Note that low power illumination was used to visualize this intercellular bridge, so it seems unlikely that these division events were induced by photodamage from the laser. Scale bar: 50 μm

tion are linked by an intercellular bridge that is approximately 145 μm in length and approximately 0.8 μm in diameter. At a certain point in the time-lapse, one of the cells (Cell 1) divides and the intercellular bridge is maintained between one of the daughter cells of this division and the other original connected cell (Cell 2). 43 minutes later, Cell 2 also begins to divide. Finally, as Cell 2 continues to divide, the intercellular bridge breaks, even though there is no visible tension in the intercellular bridge (the cells do not seem to be pulling apart from one another significantly during the entire time-lapse). Additionally, since all of the labeled cells in the time-lapse seem to be relatively stationary within this portion of the animal pole, it seems unlikely that an unlabeled migratory cell caused the intercellular bridge to break coincidentally. Considering that our fastest rate of photoconverted memb-Dendra2 transfer within an intercellular bridge was approximately 3 μm per minute, it is possible that cell division information was carried from one cell to the other within the $\sim$ 40 minute interval between cell divisions ($\frac{145\mu m}{3\frac{\mu m}{min}} \approx 48$ min). Interestingly, this idea that cues are sent between connected cells to enable cell cycle synchrony is also postulated for germ cell

intercellular bridges [138].

The finding that a few of these intercellular bridges may remain even during the segmentation period is intriguing: dramatic cell specification events, including the first neuron specification and axonal pathfinding events, are already underway during this period of development [51]. This observation may explain why hypoblast cells may not exhibit the same intercellular connections: almost immediately after gastrulation, major mesodermal and endodermal specification events take place, and early body rudiments can already be seen within an hour or so after gastrulation. Sharing of cytoplasmic or membrane between cells of different mesodermal or endodermal fates would not likely favor the proper development of the organism, since conflicting differentiation programs might be shared between the two cells.

Alternatively, intercellular bridges may provide mechanical support to the developing embryo during gastrulation. This possibility is strengthened by the following observations: (1) cells linked by intercellular bridges create a meshwork within the blastoderm with no particular orientation and (2) these membrane connections are maintained throughout the gastrula period. This mesh may provide support to the blastoderm as the yolk is enveloped by coordinated, dramatic morphogenetic movements. The lifetime of intercellular bridges seems to be characterized by an early phase, where cytoskeletal contents such as actin are present inside, and a later phase, where the bridges seem to be mostly membrane. Perhaps early on, when a full meshwork of intercellular bridges has not been established and cells are still close together, cytoskeletal elements may provide support and may keep these connections from breaking as cells rapidly intercalate within the epiblast layer. Later, once a more complete mesh is established, the membrane alone may be enough to maintain mechanical support. A possible analogy to this later stage might be that a bundle of twigs is much more difficult to break than one twig by itself.

In the future, tests of the function of these intercellular bridges will hopefully be able to de-

termine whether these two alternatives are mutually exclusive or somehow work in tandem. For example, perhaps early on, the intercellular bridges allow cells to communicate, while later in the gastrula period they just provide mechanical support to the embryo. Functional tests for cell-cell communication can be performed by labeling certain cytoplasmic components with photoconvertible proteins, such as mitochondria, transcription factors, or particular cell surface receptors. Additionally, expression of relevant signaling molecules (e.g., FGF, BMP, or Wnt [58]) may be taken advantage of to see whether the frequency, length, or persistence of intercellular bridges can be affected during development. Targeted destruction of intercellular bridges by focused laser ablation [6] may allow us to tease out whether this membrane meshwork plays a mechanical role in the zebrafish gastrula. Clearly, the use of a photoconvertible fluorescent mosaic approach has revealed a novel structure during zebrafish development in an *in vivo* context, and further characterizations of membrane morphology as well as protein dynamics in general (perhaps using a modified approach as in [14]) may also be explored using this powerful tool.

2.4 Materials and methods

2.4.1 Zebrafish husbandry

Zebrafish were maintained in an in-house colony, and the wild-type crosses, zygote stage injections, and raising before imaging (i.e., at 28°C in 30x Danieau solution [4]) were performed as previously described [151].

2.4.2 Subcloning

The pMTB donor plasmid contains a β-actin minimal promoter flanked by minimal *Tol2* transposase [126] *cis* sequences, which enable coding region transposition into the zebrafish genome

by the transposase enzyme [152, 153]. This excision and insertion into the somatic genome of zebrafish cells usually occurs within a few hours of developmental time post injection [62]. Plasmid constructs were generated by inserting the coding region of the following FPs within the pMTB vector with proper subcloning (e.g., the proper choice of restriction sites, such as ClaI and BamHI in the pMTB vector): the photoconvertible FP mDendra2 [26], the red FP mCherry [129], and the cyan FP Cerulean [135]. The following elements were also incorporated upstream of the 5' coding regions of the FPs in certain cases: 2 repeats of the lipid anchor myristoylation and palmitoylation secquences from Lyn kinase (MGCIKSKRKDNLNDDE) to label the plasma membrane (referred to here as "memb") as previously described [37] and the H2B protein sequence as previously described [154]. The following pMTB constructs were created: *pMTB memb-Dendra2*, *pMTB mDendra2*, *pMTB memb-mCherry*, *pMTB H2B-mCherry*, and *pMTB H2B-Cerulean*. The fusion constructs were created using polymerase chain reaction primer extension and subcloning into the donor vector pMTB. The *pMTB EGFP-β-actin* fusion construct was generated by subcloning the PCR products from the *pEGFP-β-actin* vector (Clontech) into the transposon donor vector pMTB (ClaI and SnaBI restriction sites, in this case).

2.4.3 Imaging and mDendra2 photoconversion

To prepare for imaging, embryos were placed in 1% low melting point agarose (Invitrogen) within Lab-Tek 2-well imaging chambers with #1 coverslip bottoms (Nalge Nunc International). The embryos were oriented such that their animal pole was nearest the coverslip bottom. Live 4D images were obtained with an LD C-Apochromat 40x magnification/1.1 NA water objective (Zeiss) on a Zeiss LSM 5 exciter or a Zeiss LSM 710 confocal microscope. Regions of interest were selected around target cells for photoconversion, where intense 40 sec exposure to 405 nm light caused the shift in the absorption/emission spectrum of mDendra2 [26].

2.4.4 Image processing

Images were processed using Adobe Photoshop CS3 (Adobe Systems). The length of individual intercellular bridges was quantified in 3D using Imaris (Bitplane AG). Analyses of the images (e.g., characterizing the orientation of the cells connected by intercellular bridges) were also performed in Imaris (Bitplane AG) as well as ImageJ (NIH).

Chapter 3

PhOTO zebrafish: A genetic tool enabling *in vivo* lineage tracing during early development and adult tissue regeneration

3.1 Introduction

While working on the project to study intercellular bridges, my colleagues and I realized that we could extend the genetic technique that we applied for the intracellular bridges to generate a powerful tool to combine global and sparse/partial labeling approaches for lineage tracing. Since extensive migratory events, morphological changes, and cell divisions coordinated by cell signaling drive complex vertebrate patterning events during both embryonic development [58] as well as during epimorphic tissue regeneration [16], we wanted to develop our lineage tracing tool to: (1) combine the strengths of both varieties of lineage tracing and (2) enable studies of cell dynamics and morphology throughout the zebrafish lifetime.

A variety of lessons learned from the literature and from our previous efforts helped us create this particular tool. First, we learned from the intracellular bridges effort that nuclear labeling is not only a useful tool for cell tracking as in previous studies [5, 7, 67], but nuclear labeling also provided us with a context for the membrane dynamics of tethered cells. With the H2B-FP fusion,

we were able to verify that intracellular bridges form after a cell division event, watching the phases of mitosis in the nucleus (as in [154]) while monitoring the incomplete cell division itself using the membrane label. Thus, we determined that combined nuclear and membrane labeling would be ideal to extract dynamic and morphological data from target cells within the zebrafish.

However — though it is a subtle point — our previous mosaic analysis approach could not achieve this multicompartment labeling feat easily. Co-injection of two different appropriate DNA plasmids (one encoding a membrane-targeted FP and one encoding a nuclear-targeted FP) with transposase mRNA does not guarantee that both FP fusion constructs will be inserted into the same cell, and even if they are, there is no guarantee that each would be inserted into the somatic genome in a region that would allow efficient expression. As a result, only a subset of cells in a mosaic embryo would have both the membrane and nucleus labeled. Additionally, only a subset of embryos would transmit both genes through the germline [155], so establishing a transgenic line with adequate expression of each of the FPs would be inefficient, at best. Instead, we determined that the most effective way to label both compartments with different FPs was to put each of the FP fusions in one bicistronic construct, separated by a highly efficiently cleavable *2A* sequence [42].

Using the photoconvertible property of mDendra2, we could instantaneously select out any cell of choice for closer analysis. We realized that if we could harness this targeting ability down to the level of a single cell, we would have a labeling tool akin to those seen in early dye injection and tracking experiments in the zebrafish [68, 4]. Only, in this case, the labeling would be non-invasive, and there could be precise control in choosing the cell of interest, since the indelible mark (i.e., the photoconversion) could be made on a high-resolution confocal microscope setup at high magnification, if necessary. Ubiquitous, constitutive promoter driven mDendra2-fusion labels would be of great advantage over mosaic labeling in this lineage tracing tool for two reasons: (1) global photoconvertible FP labeling would enable us to choose any cell at any stage in time to target

and follow with high signal over background and (2) the remaining unconverted signal would act as a global label that could also be monitored in parallel.

Next, we wanted the tool to be able to track cells at any stage in the lifetime of the fish. In order to have consistent long-term FP labeling, we cannot rely on mRNA injections from the coding region of the bicistronic plasmid, which will eventually be degraded and will not be replaced. So, a stable gene insertion of the bicistronic FP coding region driven by a constitutive promoter would be desirable to achieve FP expression throughout the lifetime of the fish. Targeting by photoconversion would allow us to have a promoter-independent means for selecting cells of interest, so constitutive FP expression would be ideal in this lineage tracing tool.

Finally, we knew that we should choose the FPs in this bicistronic coding region so that we could have three spectrally separable colors in the two-protein sequence. This is because the mDendra2 fusion label already has two distinct spectra to take into account, the green unconverted global population of labeled cells, and the targeted, red photoconverted population. To be safe, the second FP in the bicistronic sequence should not overlap with either of the mDendra2 spectra. As a corollary to this particular constraint, we wished to be able to target both nuclei and membranes using the photoconvertible property of mDendra2; to accomplish this, two bicistronic FP expressing transgenic lines would need to be created with opposite compartmental (nuclear and membrane) FP targeting.

Here, I will describe a set of transgenic zebrafish lines that we named PhOTO (Photoconvertible Optical Tracking Of), which meets the challenges of long-term lineage tracing in both early development as well as adult epimorphic tissue regeneration. This work to develop this tool was performed in collaboration with Periklis Pantazis and Scott E. Fraser, and much of the text and data from this chapter was first reported in a publication in *PLoS ONE* [57], in which I was the lead author. The transgenic lines described here combine the benefits of global and sparse imaging approaches for

lineage analysis. Whole organism imaging and tracking is enhanced by the multicompartment (nuclear and membrane) expression of spectrally distinct FPs from a single coding sequence, providing better accuracy for segmentation and tracking of cells *in vivo*. Additionally, with the aid of optically induced photoconversion, long-lasting sparse cell labeling is easily achieved, allowing high signal-to-noise tracking of a subset of cells in space and time at any point during the lifetime of the zebrafish.

3.2 Results

3.2.1 Establishing the PhOTO-N and PhOTO-M transgenic lines

In order to best address the requirements for long-term imaging of complex vertebrate development and regeneration, we constructed the PhOTO vector (Fig. 3.1A), which allows for constitutive β*-actin2* [125] driven expression of two FPs — green-to-red photoconvertible mDendra2 [26] and the blue FP Cerulean [135] — targeted to either (1) the nucleus of the cell by means of an H2B fusion or (2) the membrane ("memb") via a palmitoylation and myristoylation fatty acid substrate sequence included at the N-terminus of the protein [37]. Self-cleavage of a highly efficient *Thosea asigna* virus (TaV) *2A* sequence between the two FPs at the ribosome separates the two proteins to their respective target locations within the cell at a 1:1 stoichiometric ratio [42]. Two stable transgenic lines (*Tg(*β*actin2:memb-Cerulean-2A-H2B-Dendra2)*^{pw1} and *Tg(*β*actin2:memb-Dendra2-2A-H2B-Cerulean)*^{pw2}) were established after Tol2-mediated [126] genome integration (Fig. 3.1B). PhOTO-N zebrafish constitutively express H2B-Dendra2 to label all nuclei and memb-Cerulean to label all membranes, and the complementary PhOTO-M zebrafish line expresses H2B-Cerulean and memb-Dendra2. Efficient cleavage and proper FP localization were verified by western blot (Fig. 3.2) and confocal microscopy (Fig. 3.3, 3.4). Founders were established for each line

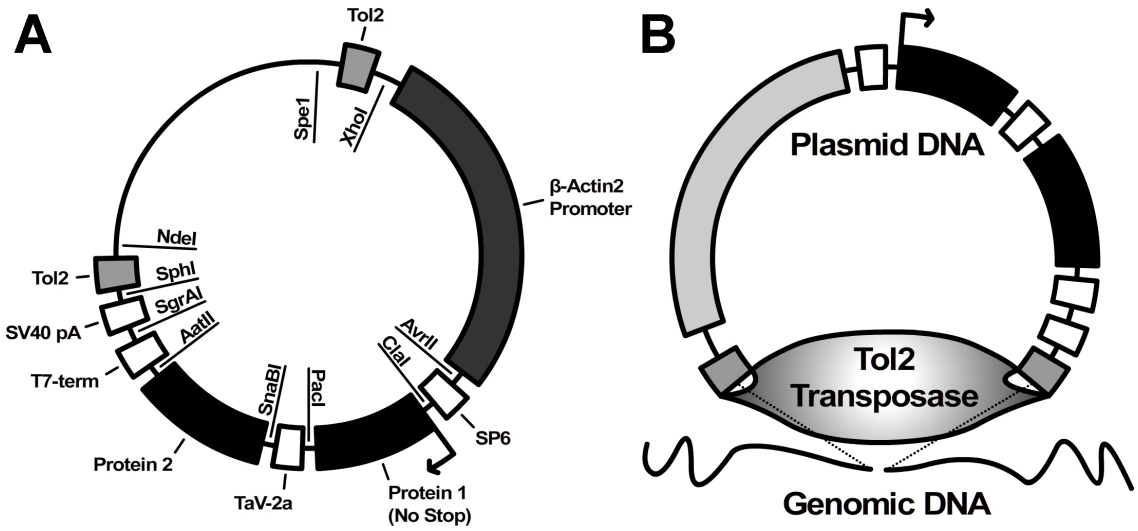

Figure 3.1: **The PhOTO vector, which enables bicistronic, targeted FP expression for multi-scale cell tracking**. (A) Depicted is a schematic of the general PhOTO vector. The major components of the vector, including the promoter, the TaV *2A* sequence, the *Tol2* transposable elements, and the FP coding region locations are indicated on the outside of the plasmid circle. Each vector was designed such that each of the components (e.g., the promoter, the FPs, etc.) may be easily switched out for alternate protein fusions, etc., using the listed restriction enzymes (inside the circle) and an appropriate subcloning procedure. The sizes of the blocked regions indicating coding sequences are not to scale. (Panel A is reproduced from [57].) (B) To generate a transgenic line, this DNA plasmid is co-injected at the zygote stage along with mRNA encoding the Tol2 transposase. At some point in early development (usually starting at the midblastula transition [62]), expressed Tol2 can randomly excise the coding region within the plasmid upon recognition of the transposable elements and insert this gene sequence randomly into the somatic genome of the embryonic cells (depending on the amount of injected protein, this can occur more than once). If the gene insertion does not disrupt the function of the genomic region that it is inserted into (e.g., it is not inserted into an exon of another gene), the FPs encoded in the PhOTO coding region may be expressed. If some of the cells that have this genomic insertion eventually become germ cells, the gene insertion may be propagated to the next generation.

(7 for PhOTO-N; 5 for PhOTO-M), and only offspring with ubiquitous, bright FP expression in all cells were considered for this analysis.

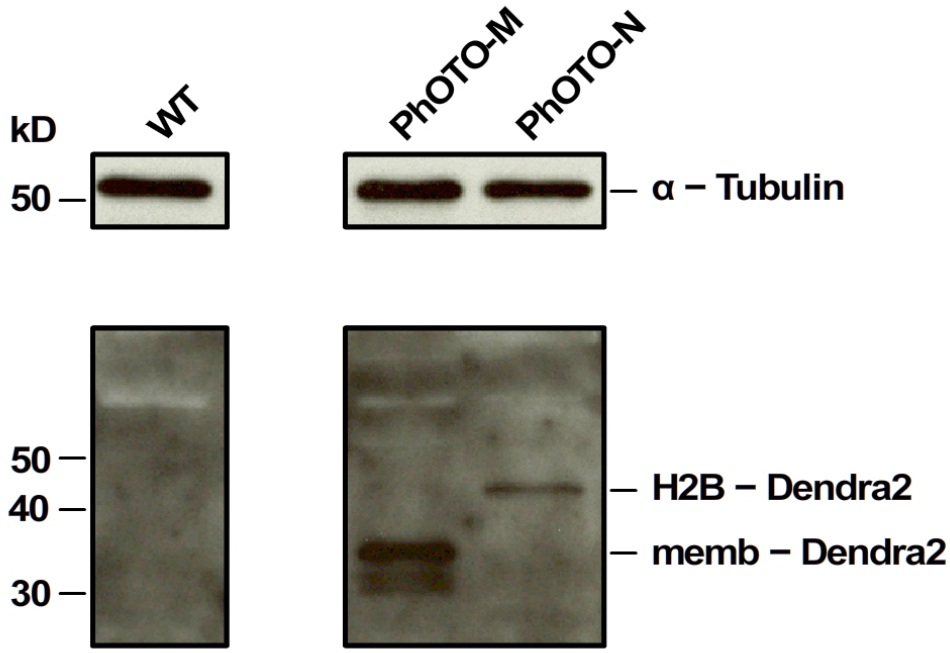

Figure 3.2: **Efficient TaV *2A*-mediated protein cleavage in the PhOTO zebrafish lines**. Western blot analysis of each PhOTO line: lane (1) WT (2) PhOTO-M (3) PhOTO-N. The membrane was probed for mDendra2 as well as α-Tubulin (loading control, upper blot). No mDendra2 was seen in the WT (lane 1), and each PhOTO lane had the mDendra2 protein at approximately the molecular weight expected from the particular fusion protein. Note that for lane 2, two bands are present, reflecting the heterogeneity of post-translational palmitoylation/myristoylation additions. Efficient protein cleavage as a result of the TaV *2A* sequence was confirmed by the lack of an un-cleaved product within the two PhOTO lanes (absence of a band above 50 kDa in the lower blot). (This figure is reproduced from [57].)

3.2.2 PhOTO-N enables precise nuclear tracking during early development

Since nuclear tracking has become standard practice for developmental lineage tracing [5, 7, 67], we illustrated the simplicity of targeting down to the level of a single cell during the dynamic period of gastrulation in the PhOTO-N line (Fig. 3.5 and Videos A.2.1, A.2.2). Our approach only requires

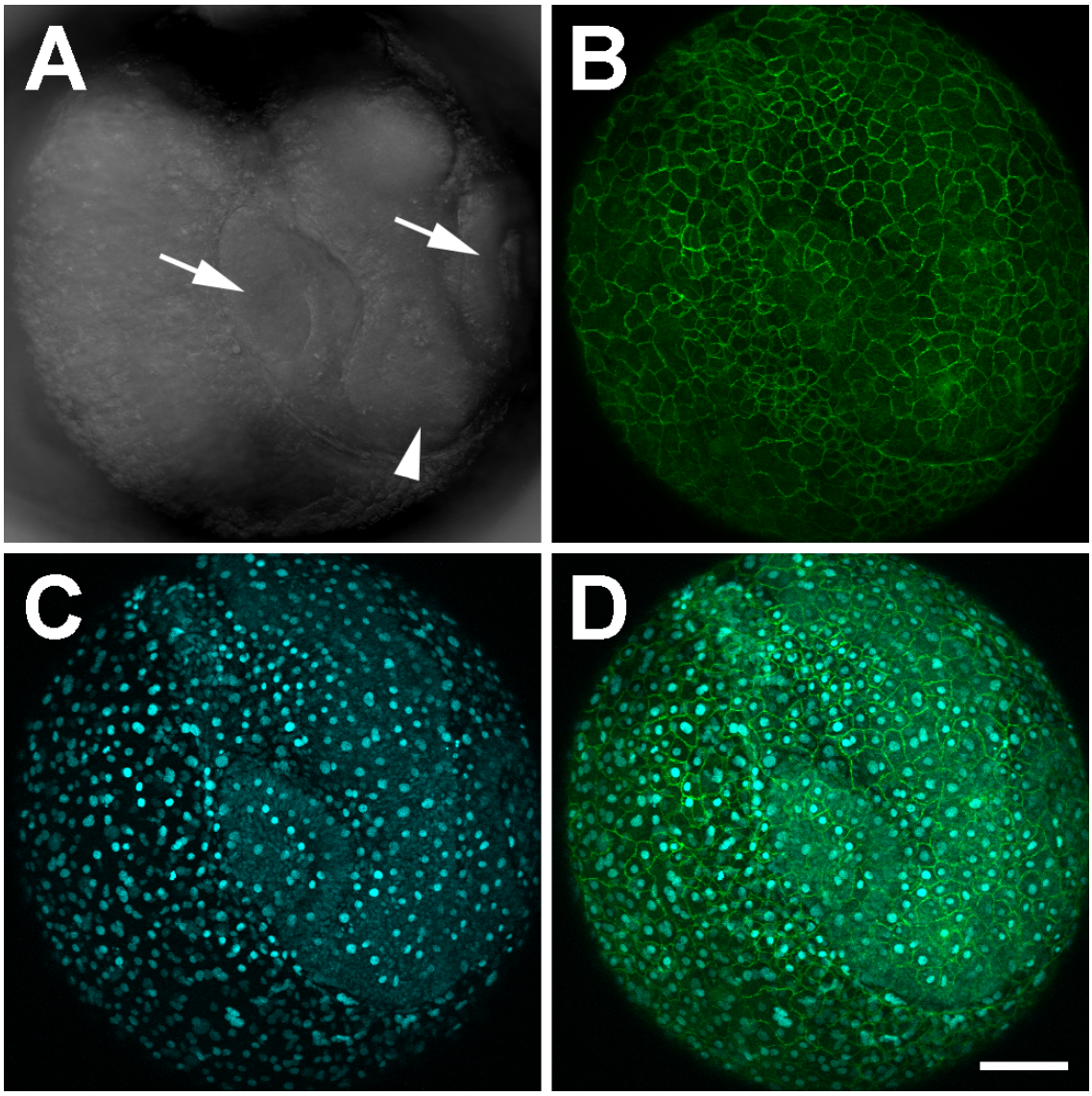

Figure 3.3: **PhOTO-M transgenic zebrafish express ubiquitous nuclear Cerulean and memb-Dendra2 labels**. Representative heterozygous PhOTO-M expression in an 18–19 hpf F1 transgenic zebrafish embryo. (A) The bright field channel, showing the anterior mounting of the embryo. Notice the eye rudiments (arrows) and the developing forebrain (arrowhead). In the PhOTO-M line, membranes are labeled with (B) memb-Dendra2 (green) and nuclei are labeled with (C) H2B-Cerulean (blue). (D) A merged image of B and C, showing the co-expression of the two FP fusion proteins in all cells. Scale bar: 100 μm

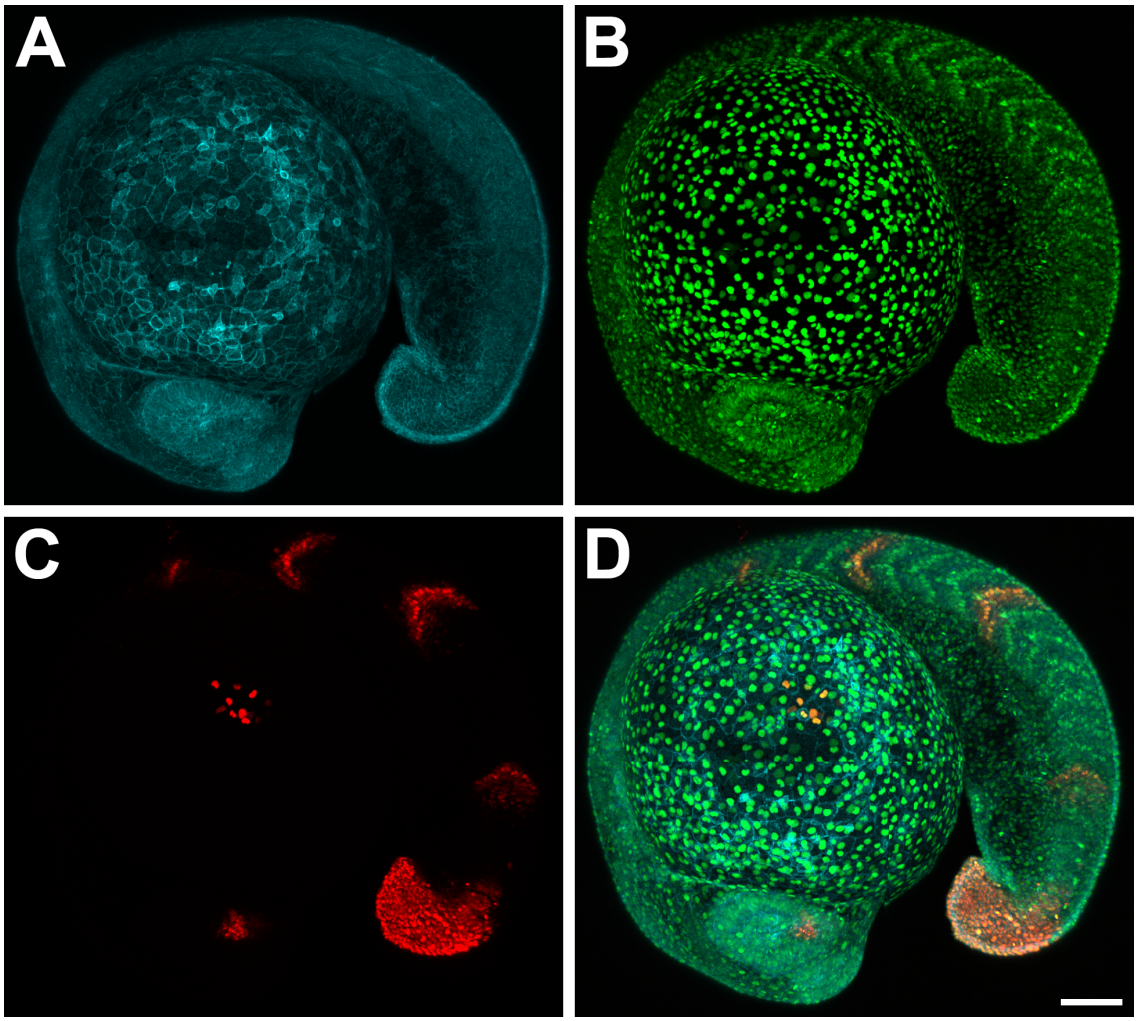

Figure 3.4: **Demonstrating the targeted photoconversion of cells in a PhOTO-N transgenic zebrafish embryo**. Representative heterozygous PhOTO-N expression in an 18–19 hpf F1 transgenic zebrafish embryo. In the PhOTO-N line, membranes are labeled with (A) memb-Cerulean (blue), nuclei are labeled with (B) unconverted H2B-Dendra2 (green), and targeted photoconversion can be used to isolate nuclei in the (C) photoconverted H2B-Dendra2 (red) channel. In this case, we highlighted cells in 4 somites, the tip of the tail, a subset of cells in the eye, and a subset of cells atop the yolk. (D) A merged image of all three colors. (This figure is reproduced from [57].) Scale bar: 100 μm

semi-automated image analysis (see materials and methods), and we segmented and tracked the photoconverted H2B-Dendra2 nuclei in time through $\sim$ 6 hours of development. Simultaneous collection of memb-Cerulean and unconverted nuclear H2B-Dendra2 fluorescence data from all surrounding cells gives context to the behavior of the photoconverted nuclei.

3.2.3 PhOTO-M highlights the dynamics of cell membranes and nuclei during early development

To extend lineage tracing beyond the level of nuclei alone, we utilized the PhOTO-M line to capture a condensed, high-resolution view of cell dynamics at the membrane level (Fig. 3.6 and Videos A.2.3, A.2.4). Although gross membrane morphological changes (e.g., total cell volume changes) in all cells are visible in the unconverted memb-Dendra2 channel, small-scale membrane dynamics of cells within the embryo can be appreciated only in a sparsely labeled environment such as in the segmented (see materials and methods) photoconverted memb-Dendra2 channel, where short membrane extensions can be seen to reach out as the cells crawl across the surface of the embryo. We also used the photoconverted membranes as visible boundaries to segment the H2B-Cerulean-labeled nuclei within these cells, allowing us to distinguish cell division events (arrowheads in Fig. 3.6C) and cell migration into the field of view (arrow in Fig. 3.6C) with high precision. Photoconverted membranes are still visible above background greater than 20 hours after photoconversion in different cell types (Fig. 3.7), ensuring the documentation of membrane behavior throughout early embryogenesis as well as during major tissue specification events later in development.

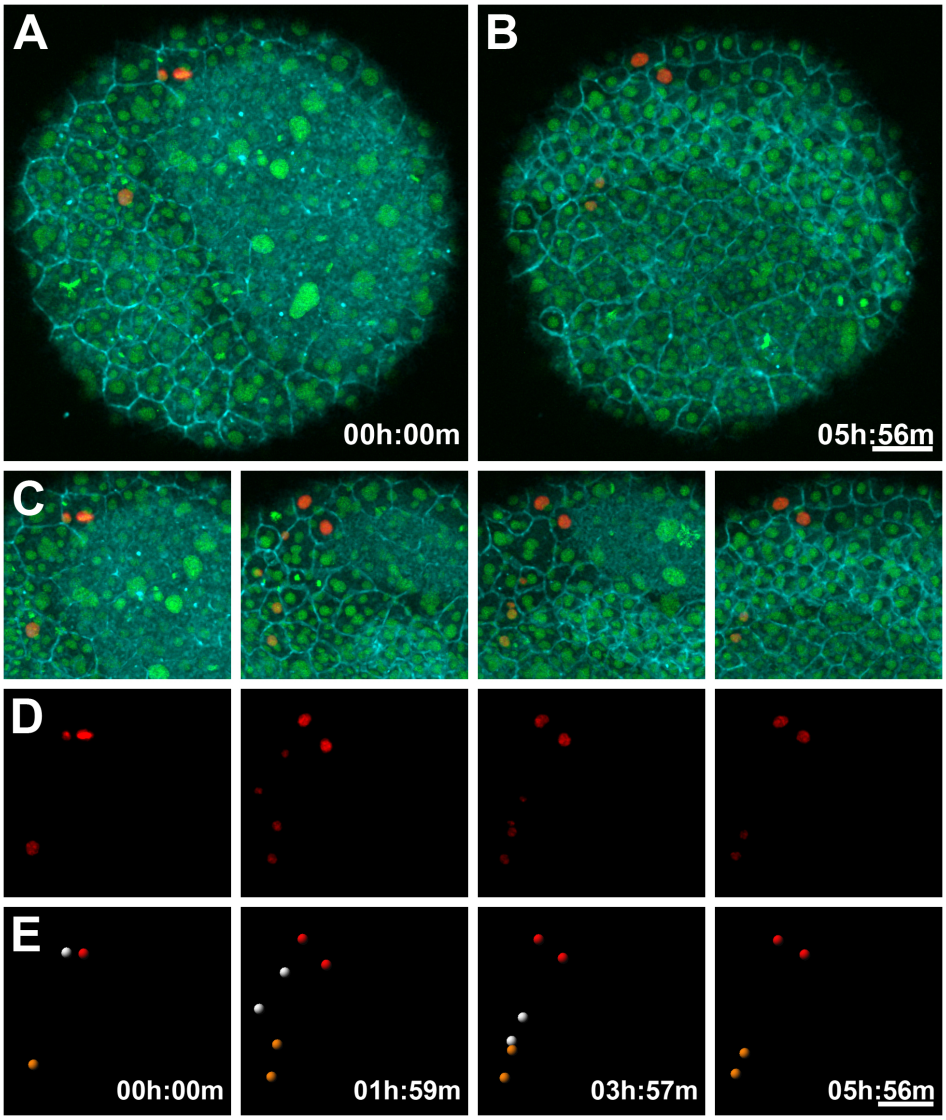

Figure 3.5: **Targeted individual nuclear photoconversion and segmentation in a PhOTO-N zebrafish during gastrulation**. Animal pole view maximum intensity projection (MIP) images of the first 10.5 μm (in depth from the animal pole) of an $\sim$ 6 hour time-lapse of a heterozygote F1 PhOTO-N zebrafish from late gastrulation ($>$ 80% epiboly) until early segmentation. (A) Merged MIP of the first frame of the time-lapse, showing memb-Cerulean (blue) and both unconverted (green) and segmented photoconverted (red) H2B-Dendra2. (B) Merged MIP image of the final time frame of the time-lapse. (C) Zoomed in MIP areas at four different time-points of the merged fluorescence images as a reference for the photoconverted images seen in panels D and E. (D) Intensity images from segmented photoconverted nuclei (red) for the same 4 time points as the merged image in panel C. (E) Segmented nuclei from the intensity images from panel D. Two enveloping layer (EVL) cells are photoconverted (the orange and red spheres) as well as an epiblast cell (the white sphere). Each cell undergoes a single cell division during the course of the time-lapse. Note that the epiblast cells move beneath the field of view in the last frame, due to the development of the head during early segmentation. (This figure is reproduced from [57].) Scale bars: 50 μm

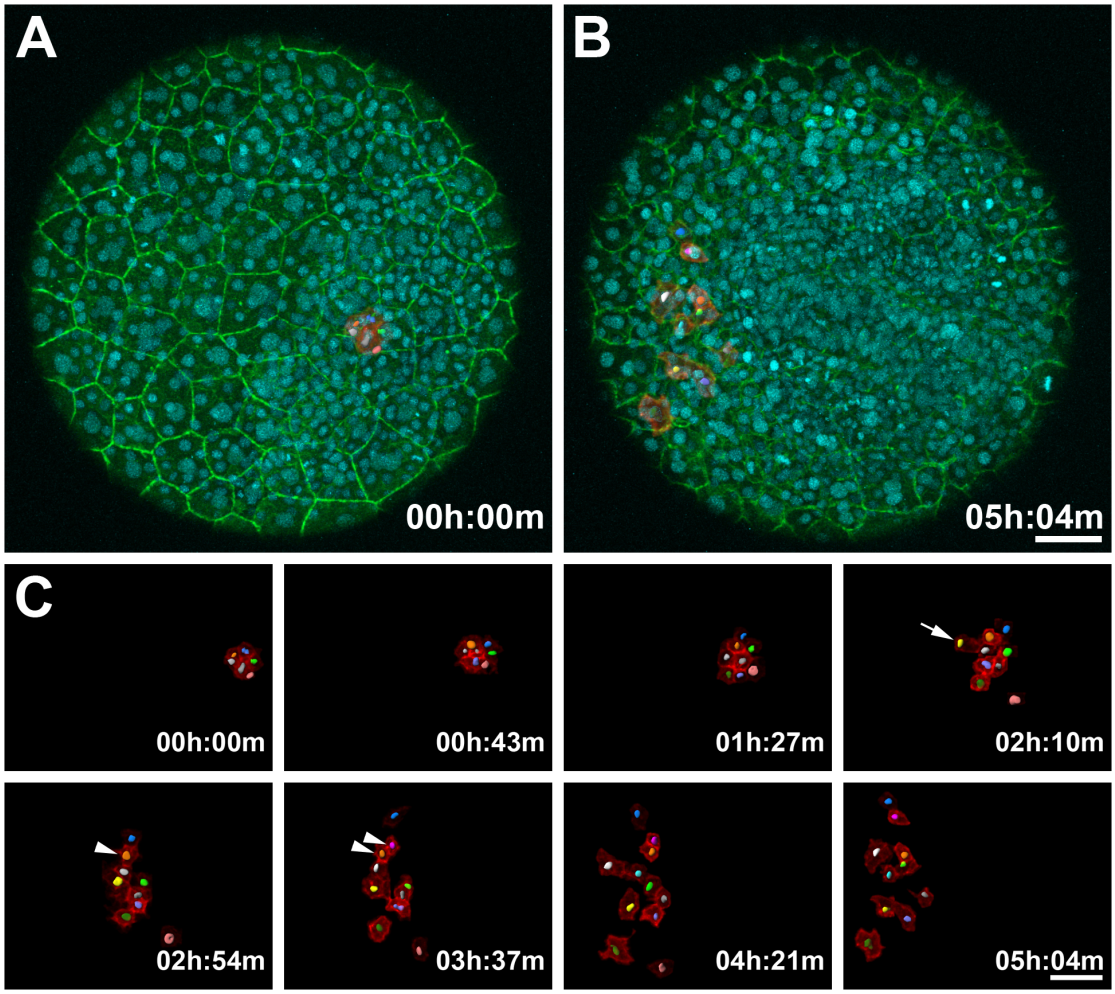

Figure 3.6: **Monitoring dynamic membrane movements and tracking nuclei in a PhOTO-M zebrafish during gastrulation**. Animal pole view MIP images of the first 21 μm (in depth) of an $\sim$ 5 hour time-lapse of a heterozygote F1 PhOTO-M zebrafish from late gastrulation ($>$ 80% epiboly) until early segmentation. (A) Merged MIP of the first frame of the time-lapse, showing unconverted (green) memb-Dendra2, segmented photoconverted (red) memb-Dendra2, and H2B-Cerulean-labeled (blue) nuclei as well as segmented H2B-Cerulean nuclei (multi-colored surfaces in the photoconverted cells). (B) Merged MIP image of the final frame of the time-lapse. (C) Zoomed MIP images of segmented, photoconverted, and migrating memb-Dendra2 intensity data (red) and segmented H2B-Cerulean nuclei (multi-colored surfaces) at 8 different time-points. H2B-Cerulean was segmented using the surrounding membranes as a guide in three dimensions. Cells are migrating in front of the developing head and move apart laterally. Arrowheads depict a cell division event and the arrow depicts a cell moving into the field of view from below. Note that a few overlying enveloping layer (EVL) cells were photoconverted in addition to the tracked cells, but since these remained stationary throughout the time-lapse, they were neglected when performing semi-automated membrane segmentation of the data. (This figure is reproduced from [57].) Scale bars: 50 μm

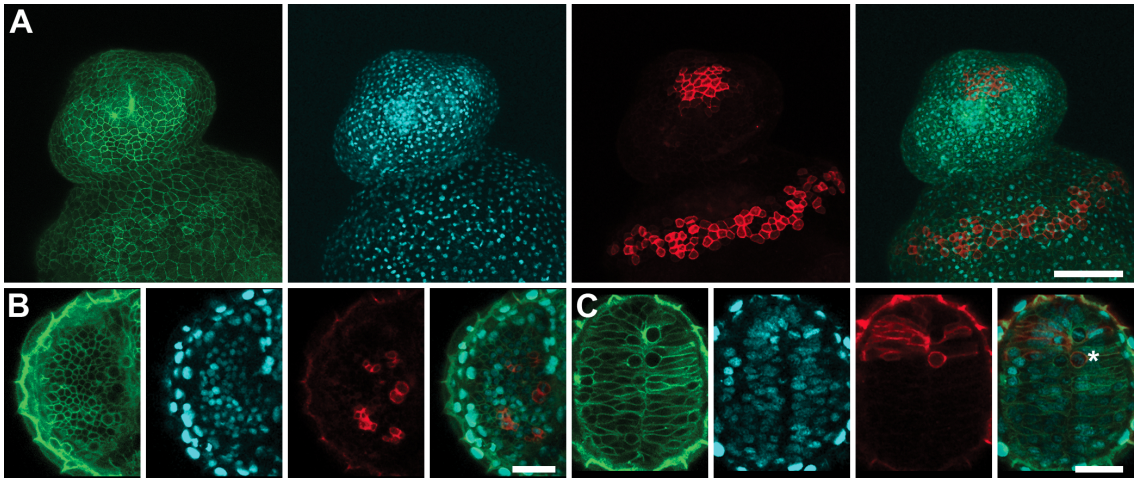

Figure 3.7: **PhOTO-M photoconversion persists in multiple cell types**. Zebrafish were photoconverted in a < 100 μm circular region of interest near the animal pole during gastrulation and were imaged the following day to visualize cell membranes at high-resolution in different tissue compartments. Even after multiple rounds of division, photoconverted membranes are still clearly visible above background. (A) Photoconverted membranes are clearly visible in the epithelium a day after photoconversion. MIPs of a ventrally mounted zebrafish (anterior top) embryo 1 day post fertilization. Left to right: unconverted memb-Dendra2 (green), H2B-Cerulean (blue), photoconverted memb-Dendra2 (red) and a merged image of the three channels. (B) Photoconverted membranes are visible and are separated by unconverted membranes in the eye a day after photoconversion. Single focal plane images of the developing eye in a ventrally mounted zebrafish (anterior top) embryo 1 day post fertilization. Left to right: unconverted memb-Dendra2 (green), H2B-Cerulean (blue), photoconverted memb-Dendra2 (red) and a merged image of the three channels. (C) Photoconverted membranes are visible in the developing forebrain a day after photoconversion. Single focal plane images of the developing forebrain in a ventrally mounted zebrafish (anterior top) embryo 1 day post fertilization. The star indicates an individual photoconverted cell in mitosis during prometaphase. Left to right: unconverted memb-Dendra2 (green), H2B-Cerulean (blue), photoconverted memb-Dendra2 (red) and a merged image of the three channels. (This figure is reproduced from [57].) Scale bars: ~ 150 μm in (A) and ~ 30 μm in (B, C)

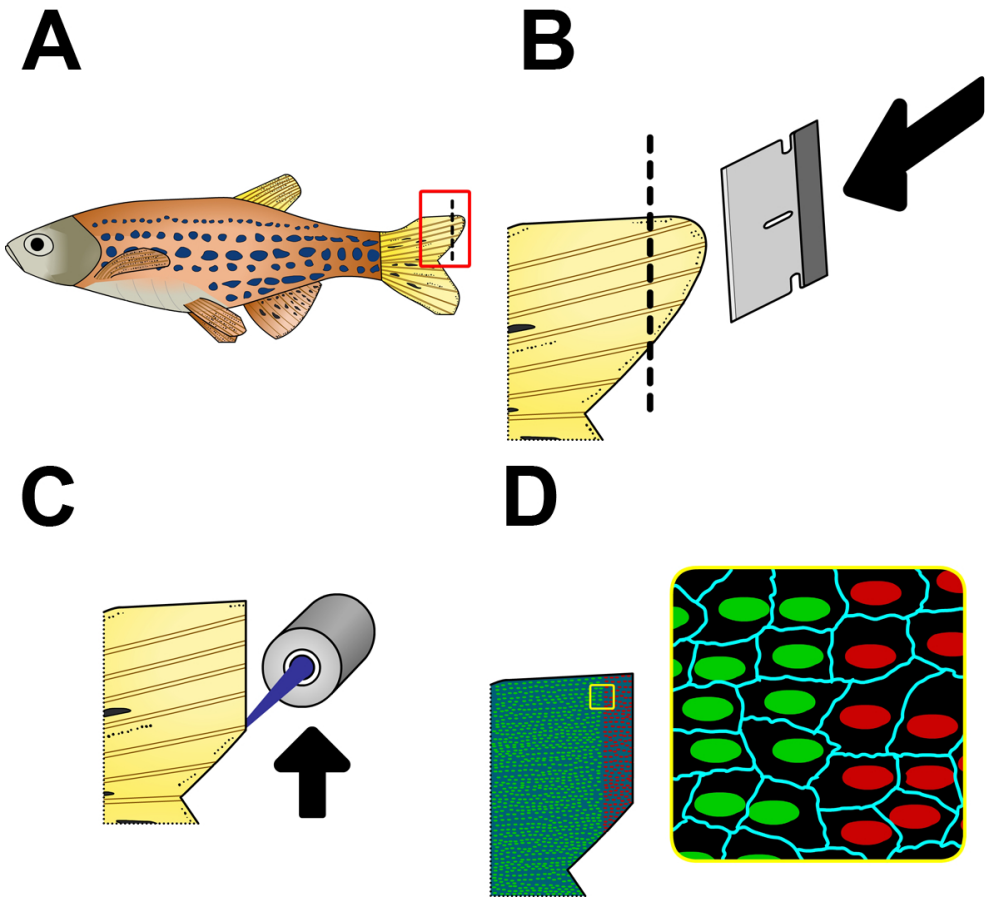

Figure 3.8: **Overview of the PhOTO-N fin regeneration protocol**. (A) An adult zebrafish is anesthetized and kept in a bath of anesthetized 30x Danieau's solution. The gills are monitored constantly so that the fish remains alive and anesthetized. (B) The tail is amputated using a razor blade (dotted line refers to amputation plane). (C) Photoconversion is achieved by fluorescent illumination of a line of cells adjacent to the amputation plane. (D) In addition to the H2B-Dendra2 (green) and memb-Cerulean (blue) signal, there is now a line of photoconverted H2B-Dendra2 nuclei (red). The inset shows a magnified view of the tail fin to appreciate the multi-channel signal. These cartoons are not to scale. (This figure is reproduced from [57].)

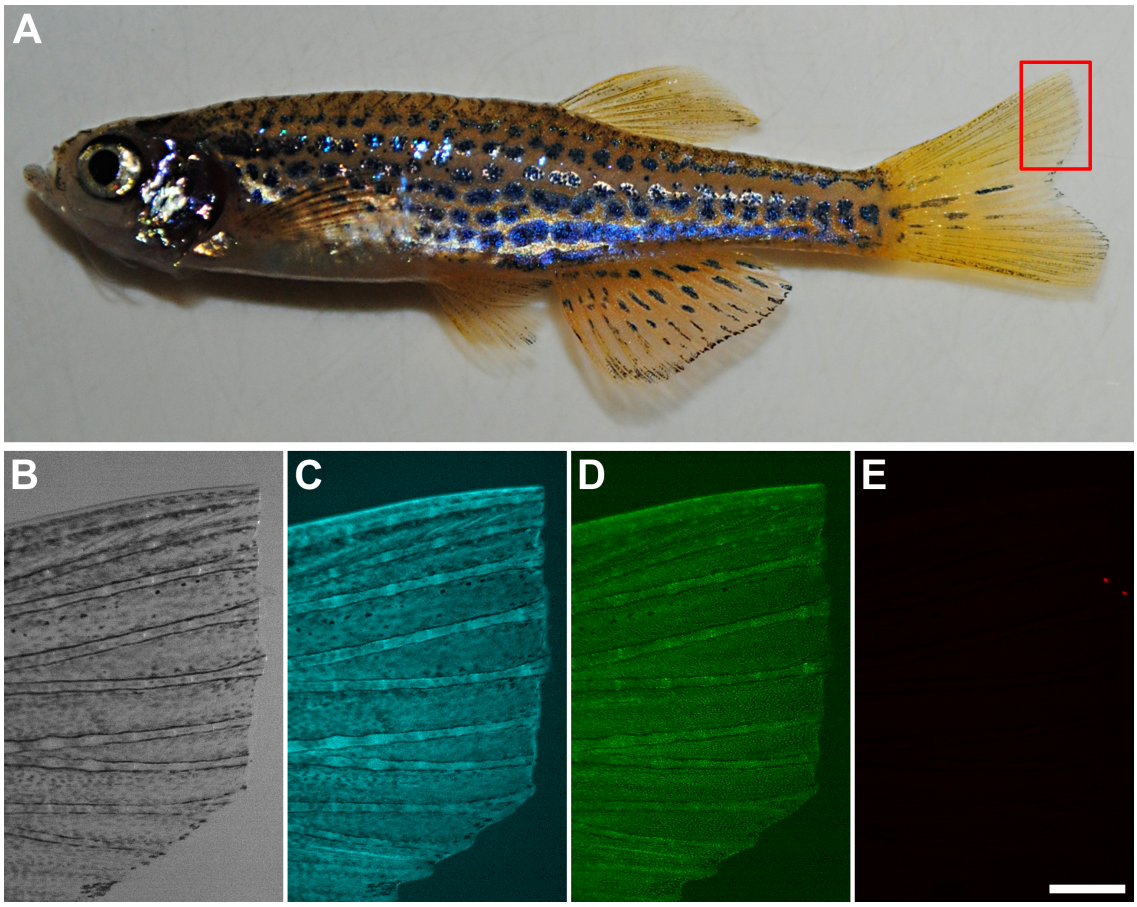

Figure 3.9: **Amputation of adult PhOTO-N zebrafish before photoconversion**. (A) A digital camera photo of the anesthetized PhOTO-N zebrafish after amputating a small portion of the upper half of the tail fin. (B–E) A fluorescent stereomicroscope image of the amputated tail fin (anterior left, ventral down) showing (B) bright field, (C) memb-Cerulean (blue), (D) unconverted H2B-Dendra2 (green), and (E) background signal when imaging with the same fluorescence emission filter as photoconverted H2B-Dendra2 (red). Note that there is almost no background fluorescent signal in panel E, except for a small bit of detritus in the water that is picked up in the red fluorescence channel. (This figure is reproduced from [57].) Scale bar: ~ 300 μm in (B–E)

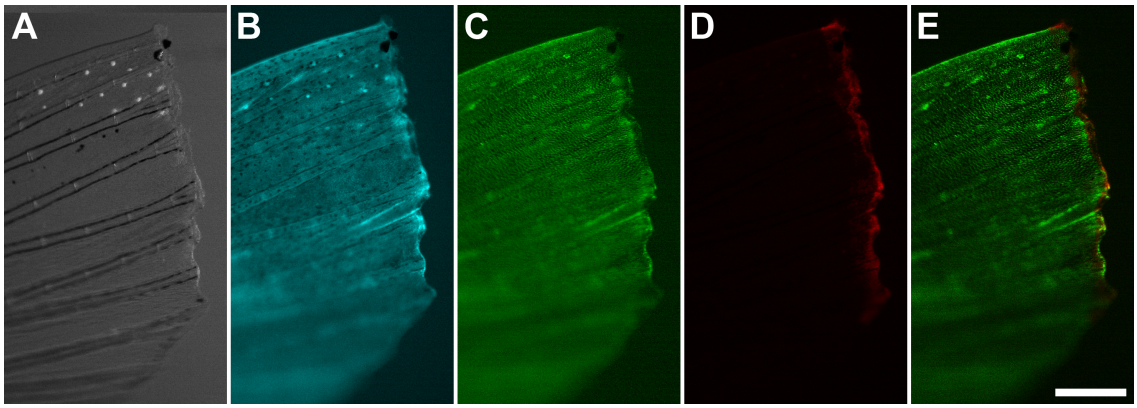

Figure 3.10: **Amputated adult PhOTO-N zebrafish tail fin after photoconversion**. A fluorescent stereomicroscope image of the photoconverted amputated tail fin (anterior left, ventral down) showing (A) bright field, (B) memb-Cerulean (blue), (C) unconverted H2B-Dendra2 (green), (D) photoconverted H2B-Dendra2 (red), and (E) a merged image of panels C and D. Note that almost all of the H2B-Dendra2 fluorescence has been photoconverted in the $\sim$ 50–100 μm region along the amputation plane, as is indicated by the lack of green signal in the photoconverted stripe in panel C. (This figure is reproduced from [57].) Scale bar: $\sim$ 300 μm

3.2.4 PhOTO-N enables identification of cell contributions to zebrafish epimorphic tail fin regeneration

Since distinct, constitutive FP expression continues throughout the lifetime of PhOTO zebrafish, these lines can be extended to approaching problems such as live imaging of epimorphic tissue regeneration. Building upon previous studies of heart [66, 17] and tail fin [19] regeneration, we used the PhOTO-N line to probe cell contributions to the regenerating tail fin (Fig. 3.8). We amputated the caudal portion of an adult ($\sim$ 7 months old) PhOTO-N zebrafish tail fin (Fig. 3.9), photoconverted all nuclei within an $\sim$ 100 μm stripe along the amputation plane (see materials and methods) (Fig. 3.10), and allowed the fin to regenerate for 7 days. Tissue birefringence in the bright field channel was a useful marker of the initial amputation plane (yellow dashed line in 3.11A). Ubiquitous memb-Cerulean and unconverted H2B-Dendra2 expression was re-established in the regenerating tissue (Fig. 3.11B, C), indicating little, if any, down-regulation of the β-*actin2* promoter driving FP expression. Using the photoconverted nuclei (Fig. 3.11D), we obtained localization and

intensity data that act as a readout for the extent of cell migration and division, respectively. We observed a large subset of cells with bright photoconverted nuclei that sit just rostral to the amputation plane (Fig. 3.11E), presumably maintaining structural integrity of the fin during regeneration. Signal from these bright photoconverted nuclei does not colocalize with unconverted H2B-Dendra2 (Fig. 3.11E'), indicating that these cells did not divide, since the H2B protein has a long half-life [156] in non-dividing cells.

Within the regenerated portion of the tail fin, we segmented all of the photoconverted H2B-Dendra2 nuclei that remained above background using an automated script (Fig. 3.12, see materials and methods) and discovered three distinct intensity populations (Fig. 3.13). Cells with no red signal over background — presumably from the contribution of unconverted cells more rostral to the amputation plane [19] — and those with slight increases over background made up the majority of cells throughout the newly regenerating region, indicating that most of the cells in the new territory result from extensive proliferation as the fin structure is re-established. As expected, a subset of bright cells were located at the distal edge of the tail fin, consistent with previous studies [157] (Fig. 3.11G). However, we also see bright cells in the middle of the regenerate (Fig. 3.11F) that continue to stay visible for over 14 days (Fig. 3.14). The lack of colocalized unconverted H2B-Dendra2 (green) signal with the brightest photoconverted (red) nuclei (Fig. 3.11F', G') suggests that these particular photoconverted cells managed to populate the regenerate without dividing at all. Notably, a subset of these cells was aligned and evenly spaced along the growth axis of the regenerating tissue (Fig. 3.15 and arrowheads in Fig. 3.11D).

3.3 Discussion

The PhOTO lines enable non-invasive, non-random mosaic labeling of the membranes or nuclei of any subset of cells at any time during development by use of the photoconvertible property of

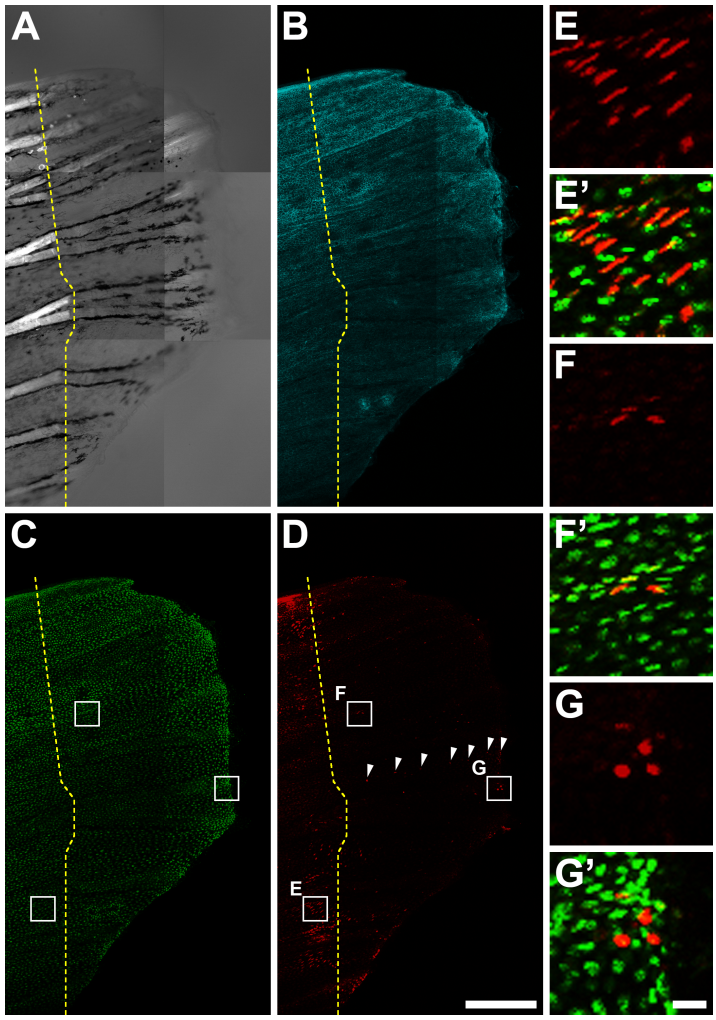

Figure 3.11: **Photoconverted cells migrate into and populate the newly regenerating fin**. Lateral view (anterior left, ventral down) MIP images of the regenerating tail fin of a live, anesthetized adult zebrafish 7 days post amputation. The dotted yellow line indicates the approximate amputation plane. (A) Bright field channel. Bright signal to the left of the dotted line arises from tissue birefringence. The terminal end of this signal indicates the amputation plane. (B) Memb-Cerulean (blue) and (C) unconverted H2B-Dendra2 (green) channels indicate that expression is still consistent as the tail fin regenerates. (D) Many of cells with fluorescence above background appear both before and after the plane of amputation in the photoconverted H2B-Dendra2 (red) channel. Cells in the central region of the tail show the least expression, suggesting extensive cell division contributing to regeneration in this area. However, certain cells to the right of the amputation plane are bright, aligned, and evenly spaced (arrowheads). (E–G) Zoomed boxed regions from C and D of photoconverted H2B-Dendra2 (red) alone. (E'–G') Merged unconverted H2B-Dendra2 (green) and photoconverted H2B-Dendra2 (red) within the zoomed boxed regions from C and D. (E, E') Many photoconverted cells in the ventral and dorsal portions of the amputated fin stayed behind the amputation plane during the regeneration process. (F, F') Surprisingly, a subset of brightly photoconverted cells were found in the central portion in addition to (G, G') other bright cells at the distal edge of the regenerate. (This figure is reproduced from [57].) Scale bars: 300 μm in (A–D) and $\sim$ 10 μm in (E–G)

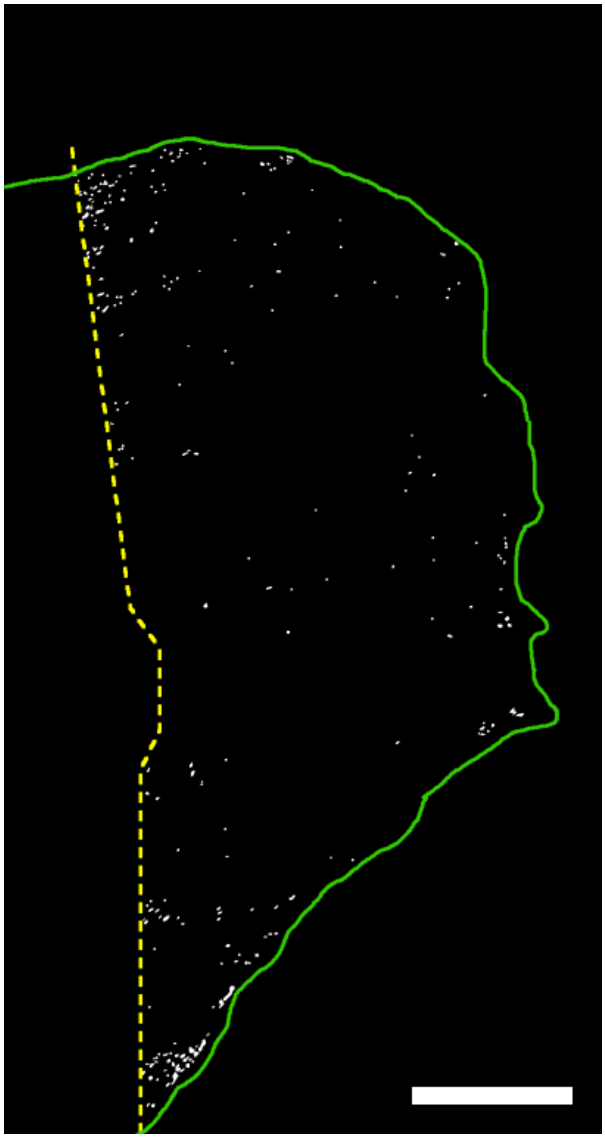

Figure 3.12: **Isolating bright, photoconverted nuclei within the regenerate**. Using an automatic thresholding script in Matlab, the nuclei from Fig. 3.11D that were sufficiently over background autofluorescent (or low-level photoconverted) signal were segmented. In this image, the approximate fin boundaries are marked with a green line, and the approximate amputation plane is marked with a yellow dotted line. Intensity from the segmented nuclei was binarized (white) to provide a mask for the original image. The mask was applied to the original image and an area-normalized intensity measurement was taken for each of the masked nuclei. Note that this image only shows cells that migrated into the regenerate (cells posterior to the amputation plane). Scale bar: $\sim$ 300 μm

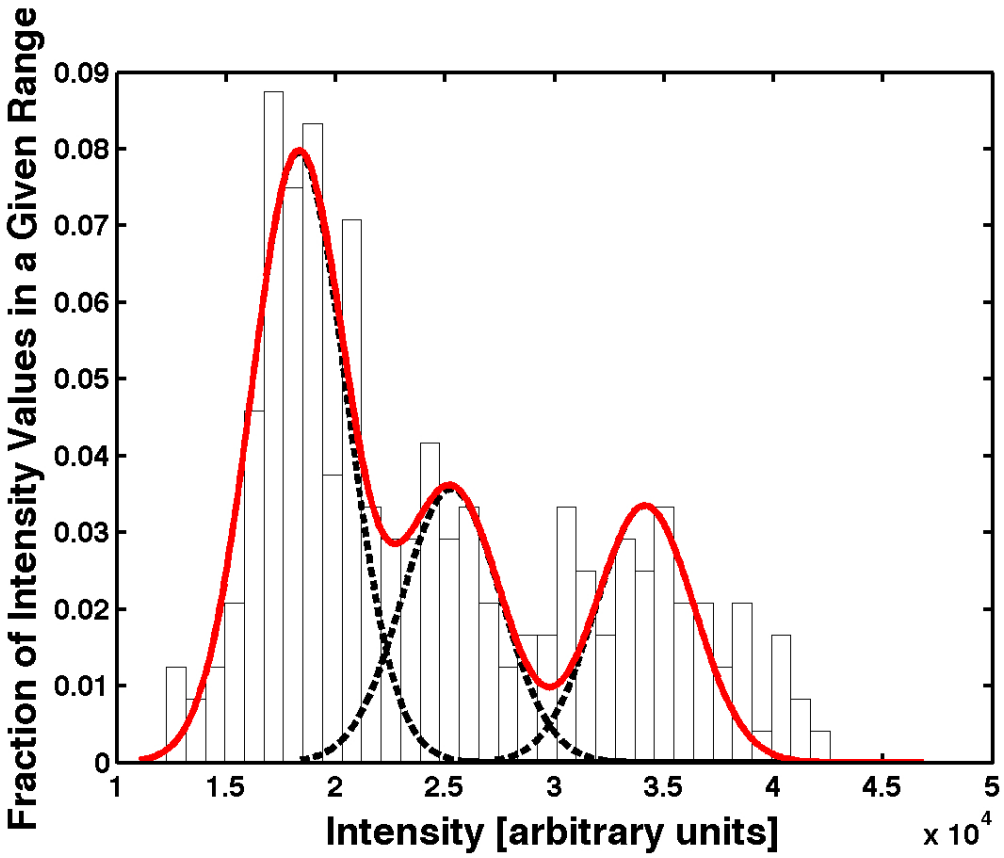

Figure 3.13: **Histogram readout for the extent of cell division after 7 days of regeneration**. Intensity data from individual nuclei within the regenerated region (posterior to the amputation plane) of the tail fin in the photoconverted H2B-Dendra2 channel (Fig. 3.11D) was segmented (Fig. 3.12). The average intensity of each segmented nucleus was recorded and this data was plotted as a histogram. The data was fit to a sum of 3 Gaussian curves, suggesting at least three distinct levels of fluorescence in the photoconverted cells above background. These three levels are indicative of the extent of divisions undergone during the re-establishment of the tail fin: the population with the highest average intensity underwent the fewest divisions, while the other two populations divided more often during the 7 day regeneration period. (This figure is reproduced from [57].)

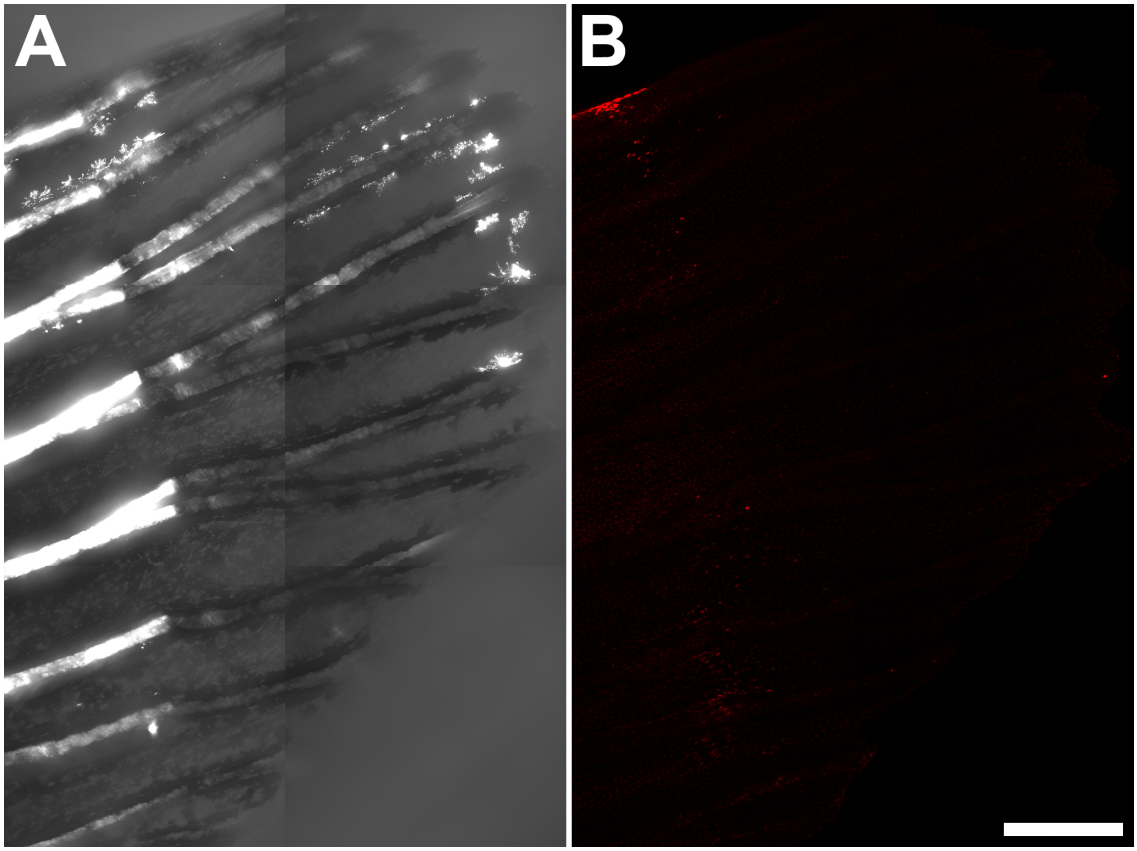

Figure 3.14: **Slowly/non-dividing nuclei within the regenerate persist until the end of the regeneration period**. (A) Bright field channel showing a nearly healed tail fin, 15 days post amputation. (B) Even 15 days post amputation — at the end of the regeneration period for caudal fin regeneration [158] — a number of cells within the fin still have signal above background, though this number is much fewer than after day 7 (compare to Fig. 3.11D). Scale bar: ~ 300 μm

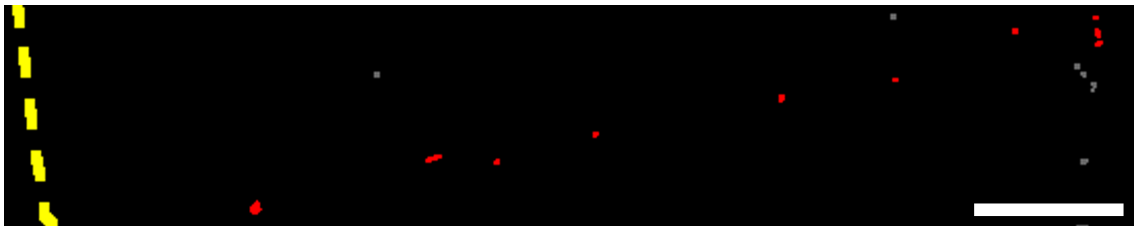

Figure 3.15: **Certain slowly dividing cells align along the longitudinal axis within the regenerated region**. Zoomed binary image of a subset of the segmented nuclei from the photoconverted H2B-Dendra2 channel in Fig. 3.11D. Among the scattered cells with photoconverted signal over background (gray), certain cells (red) seem aligned and evenly spaced along the anterior-posterior axis of the tail fin within the regenerating region. Note that the yellow dashed line in the image refers to the position of the amputation plane as in Fig. 3.11. (This figure is reproduced from [57].) Scale bar: ~ 100 μm

mDendra2, combining the strengths of global and sparse/partial lineage tracing techniques and enabling selective lineage tracing during adult regeneration. The photoconversion is immediate and nontoxic, circumventing experimental shortcomings seen with heat shock or drug inducible promoters for mosaic labeling, which require significant incubation time before expression and have possible cytotoxic effects during temperature or drug treatment. An additional feature is that the multi-compartment labeling in the PhOTO lines eliminates the need for exogenous counterstains.

3.3.1 PhOTO zebrafish and recent lineage tracing methods

Current analyses of early tissue specification are often facilitated by the use of tissue specific promoters driving FP expression [59]. In many situations, tissue specific transgenic lines expressing FP reporters exist and represent attractive tools for quick identification of a region of interest to focus on for lineage analysis. To target subpopulations of tissue specific promoter driven sequences, clever methodologies have been devised, including combining tissue specific FP expression with clonal mosaic analysis [62] or with mutant analysis [159]. As a complementary approach, when tissue specificity and instantaneous targeting of subpopulations of cells within labeled tissues for lineage analysis is desired, either PhOTO transgenic line may be incrossed with the tissue specific line of interest. The sole constraint for applying this PhOTO incross method for lineage analysis is that the expressed FP from the tissue specific transgenic should not have significant spectral overlap with the photoconverted mDendra2 channel.

Additionally, a useful non-transgenic labeling approach for zebrafish lineage tracing has been described recently, the so-called SNAP-Tag [160]. Like the PhOTO lines, SNAP-Tags can be targeted to different cell compartments (e.g., nuclei and membranes) and may be designed for photouncaging experiments. It is unclear, however, how long injected SNAP-Tag fluorescent conjugates will remain visible within the zebrafish, which may preclude lineage tracing past early develop-

mental time windows. Thus, SNAP-Tags and PhOTO zebrafish are both valuable tools for early developmental lineage tracing, while the PhOTO zebrafish also has the advantage of lineage tracing during any stage in the lifetime of the zebrafish.

3.3.2 Implications of PhOTO zebrafish for large-scale, systems-level analyses of cell behavior

Considerable efforts have been made to segment and track dense cell populations during development using nuclear labeling [5, 7, 67, 161], though density and spacing of segmentable features as well as time resolution between frames increase uncertainty of these cell tracking experiments [162]. Regional reduction in segmentation and tracking complexity, which is possible with the PhOTO lines, can decrease computational effort required for large-scale embryo reconstruction, especially when selecting out areas of high cell density and mobility, as in the shield of early developing embryos. Since both the membrane and nuclear compartments are labeled, segmentation errors that occur when nuclei are in close proximity with each other can be avoided [163]. Finally, data taken within separate photoconverted regions from different embryos — especially in the case of the PhOTO-M line where small scale membrane dynamics are visible in photoconverted subsets — can ultimately be superimposed to get a sum-of-parts view of cellular dynamics during particular stages of development or regeneration, effectively eliminating uncertainty from any given region in a whole-embryo context.

Additionally, technological advances in imaging may be applied to improve resolution in both time and space for cell tracking (e.g., a recent lateral line lineage tracing study [164]). As mentioned, the PhOTO zebrafish have the advantage of targeted regional specificity when a specific transgenic line is unavailable, and they may also be used in conjunction with sophisticated imaging modalities — such as with modified selective plane illumination microscopy techniques [165, 166]

— to enhance cell tracking.

3.3.3 Revealing the extent of cell division using PhOTO-N zebrafish

Segmentable signal from a subset of photoconverted nuclei in the PhOTO-N line persists for at least 14 days, which makes the line an optimal tool for tracking of cells during organ formation as well as major regenerative processes in multiple tissue types (e.g., tail fin [19], heart [66, 17, 18] and maxillary barbel [167]). Thus, any cell and its progeny can be traced from its origin before amputation to newly established regions within the regenerate, giving insight into the contributions of individual cells when repopulating a damaged area. For instance, having non-dividing cells within the regenerating region of the tail fin may suggest that cells important for guidance during the tissue regeneration process are maintained at some frequency throughout the re-established region and not solely at the leading edge. This observation seems even more plausible when considering the alignment of cells in the regenerating tissue. Such an organization seems reminiscent of the evenly spaced arrangement of cells during posterior lateral line development, where the establishment and maintenance of certain signaling cues — some of which are integral to fin regeneration [158] — guide cell migration and deposition [168]. It will be interesting to explore whether similar spatially restricted signaling contributes to the establishment of the regenerating fin.

3.3.4 PhOTO zebrafish — further applications

The complexity of cell behaviors during other cell process may be ultimately unraveled due to the high signal-to-noise ratio of photoconverted fluorescence in the context of global labeling when using the PhOTO lines. Recall that three distinct cell populations could be distinguished in the regenerate, and, surprisingly, the PhOTO-N zebrafish proved to be especially suited to identify cells that did not divide during the regeneration period. As a potential extension, slowly dividing stem

cells and possibly even cancer stem cells may be selected from the general population of cells in a similar manner in the adult PhOTO zebrafish; photoconversion of a region of interest within a tissue followed by a several day recovery period should allow the identification and subsequent time-lapse imaging of cells within the photoconverted tissue that have divided the least.

With the combination of targeted cell tracking and global cell monitoring, the effects of therapeutics on cell behavior may also be monitored in real time. For example, since cancer stem cells have been suggested to resist traditional chemotherapies [169], photoconversion of a zebrafish tumor followed by chemotherapeutic treatment may enable time-lapse visualization of tumor regrowth from a subset of tumor cells unaffected by the treatment. Similarly, tracking cells of interest after any drug treatment that results in cell behavior changes at the single cell level (e.g., loss-of-function studies using retinoic acid [69] or morpholino oligonucleotides [170] for manipulating zebrafish regeneration) is also possible using the PhOTO zebrafish lines. Thus, the PhOTO lines are a tool that address the need for combined global and targeted partial cell labeling to approach a variety of biologically relevant problems at multiple life stages within the zebrafish.

3.4 Materials and methods

3.4.1 PhOTO constructs

The DNA constructs were generated based on a zebrafish expression vector containing a minimal β-*actin2* promoter [125], flanking *Tol2* transposable elements [126], and a polyadenylation sequence. The TaV *2A* sequence was generated using polymerase chain reaction primer extension and further subcloned with PacI and SnaBI restriction sites. A glycine-serine-glycine spacer, which has been demonstrated to ensure high cleavage efficiency of the *2A* [46], was inserted immediately upstream of the *2A* sequence. Restriction sites were subcloned into the original zebrafish expression vector

to facilitate easy modification of any element. The bicistronic template vector was generated using this vector by first incorporating a TaV *2A* sequence between the promoter and polyA sequences by subcloning. The FP mDendra2 [26] or Cerulean [135] was localized to the membrane using two repeats of a myristoylated and palmitoylated N-terminal MGCIKSKRKDNLNDDE signal sequence from Lyn kinase [37]. For nuclear localization, the C-terminus of the H2B protein was fused with either mDendra2 or Cerulean as previously described [154]. The fused mDendra2 and Cerulean constructs were subcloned with restriction sites for insertion into the PhOTO vector (sites shown in Fig. 3.1A).

3.4.2 Zebrafish husbandry

Zebrafish were raised, hatched, injected, and maintained in a house colony as previously described [151].

3.4.3 Zebrafish transgenics

To establish transgenic zebrafish lines (*Tg(βactin2:memb-Cerulean-2A-H2B-Dendra2)*^{pw1} and *Tg(βactin2:memb-Dendra2-2A-H2B-Cerulean)*^{pw2}), WT zebrafish were first injected with either 20 ng PhOTO-N or PhOTO-M plasmid DNA and 80 ng *Tol2* transposase mRNA at the zygote stage. Translated Tol2 transposase proteins recognize *Tol2* elements flanking the coding region of the construct during the early developmental phases of the zebrafish, and the coding region may be inserted randomly into a cell's genome by one of these transposase proteins [126]. Injected fish were raised at 28°C until 7 days post fertilization, when they were screened for fluorescence. Healthy-looking, brightly expressing mosaic embryos/larvae from the injected population were selected and raised to adulthood. Fish that survived to adulthood were crossed to WT adults, and the resulting embryos were screened for fluorescence. Founders positive for germline transmission and for strong, ubiq-

uitous expression were crossed with WT zebrafish to continue to propagate the line. Embryos from these founder crosses were also used for imaging.

3.4.4 Western blotting

Screened larval zebrafish from each PhOTO line as well as WT control fish were collected and homogenized in ice-cold lysis buffer (150 mM NaCl, 10 mM Tris-HCl at $\sim$ pH 7.55, 1 mM EDTA, 1% Triton X-100) with a protease inhibitor (Complete Protease Inhibitor Cocktail Tablets, Roche). Extracts from $\sim$ 2 fish per lane underwent SDS-PAGE (5% stacking gel/12% running gel) electrophoresis using a Mini-Protean Gel Doc (BioRad). The resulting bands were transferred to a PVDF membrane (Immobilon P, Millipore) after wet electroblotting (transfer buffer: 25 mM Tris, 192 mM glycine, 20% Methanol, 0.1% SDS, pH 8.1–8.5) using the Mini-Protean Gel Doc (Bio-Rad). Rabbit anti-Dendra2 polyclonal antibodies (1:5000, Evrogen) and mouse anti-α-Tubulin monoclonal antibodies (1:10000, Sigma Aldrich, loading control) were used to probe the western blots. Horseradish peroxidase linked goat anti-rabbit was used as a secondary antibody (1:10000, Jackson ImmunoResearch Laboratories, Inc.). Western blots were visualized using an ECL Plus chemiluminescence kit (GE Healthcare).

3.4.5 Imaging and mDendra2 photoconversion

After crossing founder PhOTO zebrafish with WT adults, embryos were raised in egg water [151] at 28°C until they were ready to be imaged. Prior to imaging, embryos were screened for fluorescence using an Olympus MVX10 fluorescence microscope. Positive embryos were embedded in 1% low melting point agarose (Invitrogen) in 30x Danieau's solution [4] within Lab-Tek 2-well imaging chambers with #1 coverslip bottoms (Nalge Nunc International). Embryos past 16 hpf were anesthetized using 0.015%–0.03% Tricaine methanesulfonate (Finquel/MS-222, Argent Labs) and

were maintained in anesthetic at the same concentration when embedded in the 1% agarose/30x Danieau's solution for imaging. We obtained live images in space and time using a 20x/0.8NA Plan-Apochromat air objective (Zeiss) using a Zeiss LSM 710 confocal microscope. Embryos were maintained at a temperature between 28°C and 32°C during time-lapse experiments. The tiled image in Fig. 3.2 was taken with a Leica True Confocal Scanner SP5 Spectral High-Speed Confocal System with AOBS (Acoustical Optical Beam Splitter) (Leica Microsystems Inc., Deerfield, IL) using a 20x/0.7NA objective (Leica). Photoconversion was achieved by prolonged ($>$ 30 sec) illumination of a region of interest within the zebrafish sample with a scanned 405 nm laser on the Leica confocal microscope. Images and time-lapse data from embryos were processed and cell segmentation and tracking was performed in a semi-automated manner using the spot tracking tool (for PhOTO-N nuclei) and the surface segmentation tool (PhOTO-N membranes and PhOTO-M membranes and nuclei) within Imaris software (Bitplane AG).

Adult zebrafish ($\sim$ 7 months old) were anesthetized as mentioned above and tail fins were amputated using a razor blade. Only zebrafish with short caudal fins were considered for this analysis. Fast photoconversion within an hour of amputation was achieved using a 405 nm excitation filter cube in the path of an X-cite mercury source (Zeiss) on a Zeiss 510 inverted confocal microscope. Photoconversion was confined using an iris in the path of the fluorescent light, and the stage was moved so that the confined conversion area was scanned along the plane of amputation [13]. Images in Fig. 3.9 and 3.10 were taken with an Olympus MVX10 fluorescence microscope. After imaging, the fish was immediately revived using a method reported previously [20] and was then put back on the fish husbandry system (Aquaneering). For confocal imaging of the tail after 7 days, the tail was restrained under anesthesia using 2% low melting point agarose (Invitrogen) in 30x Danieau's solution. To keep the fish alive during imaging, either system water or 30x Danieau's solution containing 0.03% Tricaine methanesulfonate was flowed across the gills of the anesthetized fish, and

gill motion was monitored constantly. Confocal images were taken using the same Zeiss LSM 710 confocal microscope. All images and videos were processed and compiled using Adobe Photoshop CS3 (Adobe Systems).

3.4.6 PhOTO-N nuclei segmentation and cell division analysis after 7 days of regeneration

Photoconverted H2B-Dendra2 MIP data from Fig. 3.11D was first processed in Photoshop CS3 (Adobe Systems) to isolate the regenerated tail fin portion from the tail fin region rostral to the amputation plane using the magnetic lasso tool. Using a custom Matlab (Mathworks) script, nuclei were segmented that had intensity above background, and the segmented mean intensity data from each nucleus was fit to a sum of three Gaussians in a manner similar to one described previously [72] to generate Fig. 3.13. The segmented data was converted to a binary image (Fig. 3.12) and modified in Adobe Photoshop CS3 (Adobe systems) (i.e., changing color of the binary nuclei from white to red and gray) in order to generate Fig. 3.15. The approximate outlined fin region (Fig. 3.12) was drawn with the bright field channel as a guide using the pencil tool in Adobe Photoshop CS3 (Adobe Systems).

Chapter 4

Dissection of an intriguing optical artifact seen with endogenous striated muscle SHG

4.1 Introduction

Although FP labeling is an effective method for studying protein expression, dynamics, and function in cells, researchers — especially recently — have used endogenous contrast from SHG-capable protein arrays as a tool to dissect structural changes that result from disease progression, such as in muscular dystrophy [171, 172] and cancer [22]. As demonstrated in a recent study documenting the first ten cell divisions in the zebrafish embryo using solely endogenous contrast (microtubule-derived SHG, and membrane-facilitated THG) [87], endogenous SHG imaging requires no exogenous agent (e.g., a fluorescent dye, etc.). Of course, the caveat is that only a few different protein structures have this SHG-capable property, as mentioned in Section 1.3.3.

Originally, I wished to apply this endogenous SHG imaging tool in the embryonic zebrafish to act as a diagnostic for early stage neuromuscular disorders (some of which have been reported in zebrafish [173, 174, 175]), since other SHG-based approaches for diagnosing muscular dystrophy focused on later stage progression of the disorder [171, 172]. My initial efforts — images from which can be seen in Fig. 4.1 as well as Videos A.3.1 and A.3.2 — were focused on developing a

system for imaging zebrafish muscle compartments with high contrast as the muscle cells, or myofibers, are first differentiating within the segmentation period [51, 176]. With this information, I wanted to compare muscle development in the WT with mutant phenotypes mimicking neuromuscular disorders, such as the zebrafish *sapje* mutant [173]. Unfortunately, the regular banding structure is sparse early in development, and the detection setup on the laser scanning microscope was not optimized for SHG signal collection in the transmitted direction.

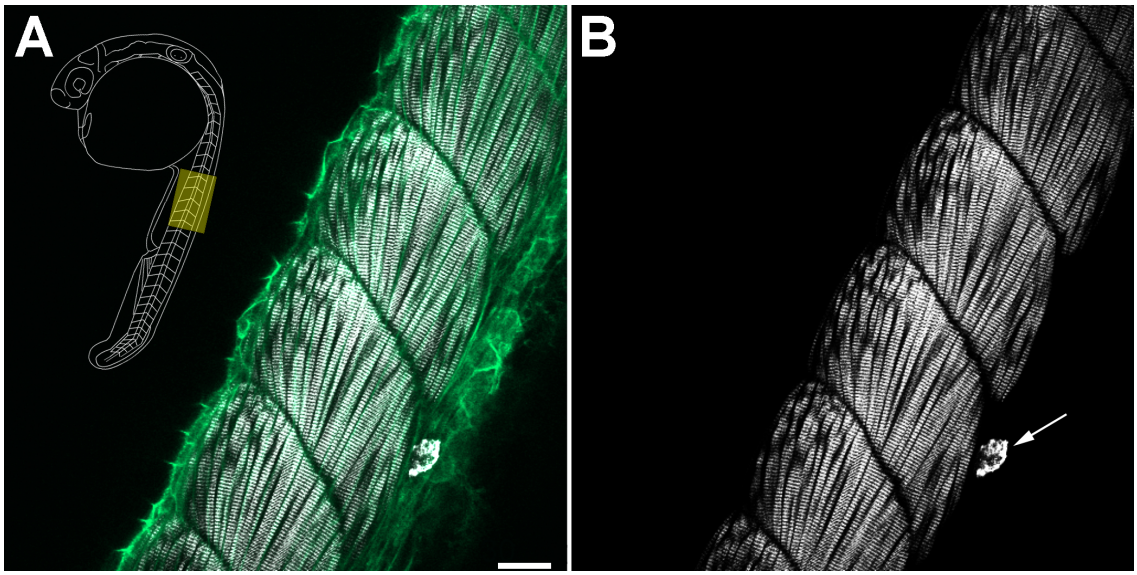

Figure 4.1: **SHG provides a means to monitor muscle organization with subcellular resolution**. These panels show a single optical section image of a trunk somite region (see highlighted area on inset cartoon of zebrafish) within a laterally mounted, live memb-Dendra2 expressing zebrafish embryo at 2 dpf. (A) A merged image of SHG signal (white) and memb-Dendra2 fluorescence (green), showing that the striated SHG pattern originates from endogenous sarcomeric structures (the myosin bundles) within muscle cells. (B) In the SHG signal channel alone, the striated SHG pattern can be appreciated more clearly. Additionally, even without additional contrast, the somite boundaries (vertical myosepta, which are the dark boundaries seen here separating the longitudinal muscle fibers) are clearly visible in the image. Even after 1x PTU treatment, certain iridophores are still visible as broad-band signal overlapping with the SHG channel (arrow) at this stage of development. Note that this signal can be isolated using a multi-channel spectral detector, if desired. Scale bar: 30 μm

Interestingly, while I was working on this problem, I had several fruitful discussions with a physics graduate student in the lab, Nathan Hodas, and he and I began collaborating, studying prop-

erties of endogenous SHG in embryonic and larval zebrafish skeletal muscle. Whenever we were imaging whole zebrafish, we noticed many interesting patterns in the SHG signal (Fig. 4.2), and we decided to look into these structures more closely. As it turns out, these so-called "verniers" or "herringbones" — 'Y'-shaped patterns and curved distortions in the place of what would normally be expected to be parallel banded SHG signal — have been seen in muscle tissue since the 1950s, when Huxley and Taylor studied the electrical stimulation of isolated frog muscle fibers [177]. More recent studies using SHG [172, 178, 179, 180] have pondered the source of this signal without any rigorous characterization, attributing it to myofiber remodeling and regeneration [172].

In this chapter, I will discuss how we determined that these vernier patterns of SHG in intact, fixed zebrafish skeletal muscle are most likely an optical artifact of SHG imaging. We hope to submit our results to a peer-reviewed journal in the near future. This work was performed in collaboration with Nathan Hodas, Periklis Pantazis, and Scott E. Fraser. Importantly, Nathan Hodas focused mainly on the theory of SHG to characterize this optical artifact, while I prepared the zebrafish samples for imaging. Additionally, Nathan Hodas and I each performed imaging experiments using these samples in an effort to find evidence for the elusive nature of the verniers.

4.2 Results

4.2.1 Theory suggests that verniers are "optical illusions"

By going through the theory of SHG, Nathan Hodas was able to determine that the vernier pattern in zebrafish skeletal muscle was most likely an "optical illusion". This comprehensive theoretical analysis can be best appreciated by looking at Chapter 4 of Nathan Hodas' thesis [181] (especially Fig. 4.3 on p. 92), and I will not dwell on it in detail here, since it was completely his effort in the project. After performing this exhaustive analysis, Nathan Hodas was able to discern some rules

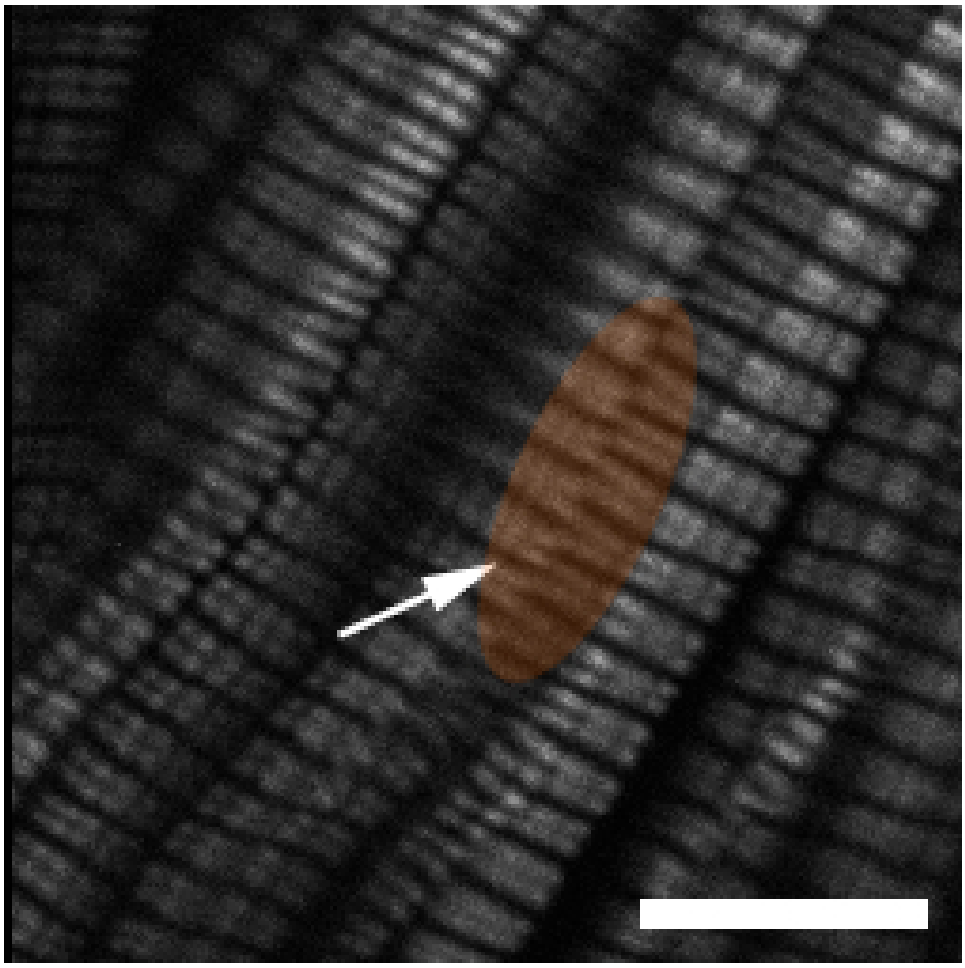

Figure 4.2: **Verniers are distorted SHG signals visible deep inside the somite**. In this image from a 5 dpf, laterally mounted fixed WT embryo, clear distortions can be appreciated in the SHG signal (curvature toward the edges of the SHG bands in much of the image), including verniers (white arrow indicating orange highlighted region). This particular highlighted region has SHG bands that link adjacent myofibers, suggesting that these subcellular structures might be connected between cells across their membrane boundaries in some fashion. Scale bar: 10 μm

that govern the visualization of these vernier patterns. Most importantly, Nathan Hodas realized that as the laser passes through the tissue sample, the Gouy shift at the focus (i.e., where the phase of the light shifts by π [55]) can cause varying patterns of intensity, depending on the orientation of the individual muscle fibers in a tissue. In his model, when two muscle fibers are arranged such that the myosin bands in repeating sarcomere units are staggered with respect to one another (Fig. 4.3A), this phase shift can cause an illusory increase in intensity between the fibers, leading one to believe that myosin exists between or connects the fibers themselves (schematic representation in Fig. 4.3B).

4.2.2 Verifying the theoretical model of verniers

We determined that the easiest way to prove whether these verniers are "optical illusions" would be to image the SHG within zebrafish skeletal muscle with fluorescent counterstains in addition to endogenous SHG imaging. If we could show that the spectral signatures are similar to the theory, then we would prove that the verniers are a result of the SHG process and not a physical state of the sarcomeric myosin. As a first successful example, we labeled (using memb-Dendra2 and H2B-Cerulean mRNA injections, see materials and methods) and visualized the membrane fluorescence in the somite compartments of 5 day post fertilization (dpf) zebrafish larvae. We hypothesized that if verniers are indeed a result of staggered muscle fibers, we would see SHG signal crossing the fluorescently labeled membranes. We obtained clear images — both in single focal plane sections ('xy' longitudinal images) as well as orthogonal optical cross sections ('xz' images) through the depth of the zebrafish — indicating that verniers did in fact cross membrane boundaries, though there was no indication that there were any breaks in the membrane in the fluorescence channel (refer to Fig. 3.17 and 3.18 in [181]). This was our first indication that these verniers were non-physical connections between adjacent myofibers.

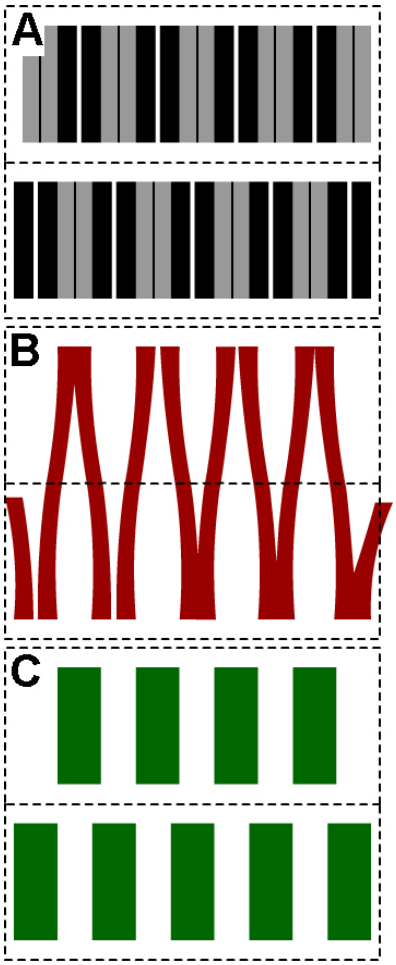

Figure 4.3: **Verniers appear when myosin bands are staggered in adjacent myofibers**. (A) In this simplified two-dimensional cartoon, two myofibers are depicted next to one another (sarcolemma plasma membranes are labeled as dotted lines surrounding the actin/myosin bundles), and their individual myosin (black) and actin (gray) sarcomere bands have offset sarcomere banding patterns with respect to each other. Note that the Z-lines of each sarcomere in the myofiber are depicted as black lines in the actin bands, while the M-lines are depicted as gaps at the center of the myosin bands.(B) In the SHG channel, theory predicts that the myosin signal (red) may form verniers and could even seem to link the adjacent myofibers in some regions. (C) In contrast, when the myosin is fluorescently tagged, TPEF signal emanating from labeled myosin (green) would remain basically rectangular in shape, with no gaps in fluorescence at the M-lines. Note that in panels B and C, the actin bands are assumed to be unlabeled, which is why they are not shown in the images. Tropomyosin 3 from the ct5a line [15] labels the actin thin filaments in the sarcomere, and the MF20 antibody labels the myosin thick filaments in the sarcomere, so TPEF fluorescence should be striated accordingly — (1) ct5a experiments represented in Fig. 4.4: dark bands where there is no actin, and (2) MF20 immunostaining experiments represented in Fig. 4.5 and 4.6: dark bands where there is no myosin. This cartoon is not to scale, and 2P illumination is assumed to be in the direction from the top to the bottom of each panel. This figure is for illustrative purposes only and does not represent actual results from the theoretical simulations, as depicted in Fig. 4.3 of [181].

In the theoretical analysis, Nathan Hodas determined that TPEF signal would be vastly different than SHG in many circumstances: in the case of staggered muscle fibers (when myosin is labeled within the sarcomeres), no herringbone signal should be present with TPEF, and there should be no increase in intensity between the myofibers [181] (as in Fig. 4.3C). So, we postulated that if verniers are artifacts of the SHG process, we should see differing signal in staggered muscle fibers — TPEF emission from fluorescently labeled sarcomere components would show no increased fluorescence between fibers and would not have curvature or bifurcations in the signal, while SHG curvature and verniers would be prominent in the same imaging plane.

To accomplish this, we performed two different whole-mount immunostaining experiments. In the first, we used one of the so-called "flip-trap" transgenic lines established by Trinh et al. [15]; this line in particular has trapped the endogenous locus of the *tpm3* gene (ct5a allele). In this line, the tropomyosin 3 protein is labeled with the yellow FP Citrine [182], which is a regulatory protein for actin-myosin contraction and is a component of the so-called thin filaments (for a review of the structure of the striated muscle sarcomere, refer to [183]). Consequently, in this case, the Citrine TPEF signal emanates approximately between the SHG signal bands in the sarcomeres of each myofiber, in this case only labeling the slow muscle, which is a thin superficial muscle layer beneath the epidermis in zebrafish [184]. Unfortunately, the slow muscle seems well aligned in zebrafish, so verniers were difficult to find. Luckily, in one case, when the muscle in a somite was slightly distorted (perhaps as a consequence of zebrafish twitching that was frozen in time after fixation), we noticed the vernier pattern as a slight deflection in the SHG signal (Fig. 4.4A). As expected, the fluorescence channel shows no such deflection (Fig. 4.4B, C).

To complement our thin filament fluorescence experiment, we performed a second test in WT embryos, labeling the thick filaments. 7 dpf embryos were fixed and immunostained with an anti-myosin antibody (MF20) and probed with an AF488 conjugated goat anti-mouse secondary anti-

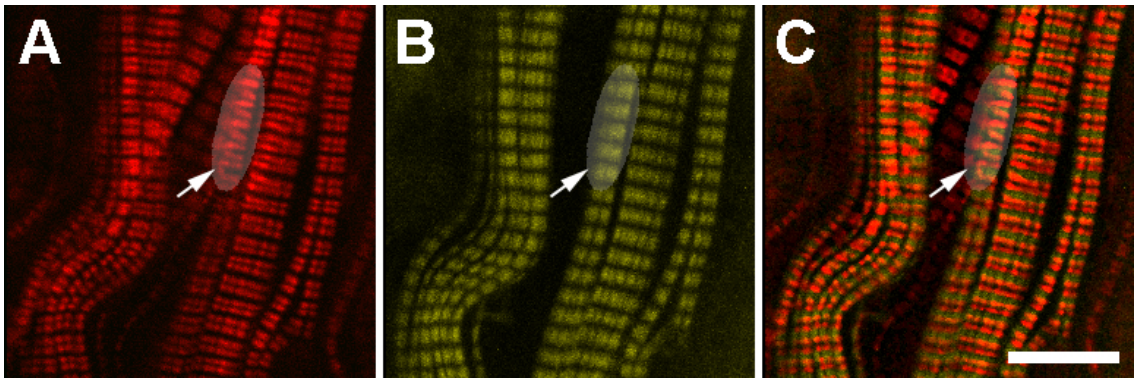

Figure 4.4: **Apparent curvature in the sarcomere structure is only visible within the SHG channel in fluorescently labeled zebrafish embryos**. In this single optical section of the superficial slow muscle layer of a laterally mounted, fixed 5 dpf ct5a [15] zebrafish embryo, the thick filaments are visible from the SHG signal (red), and the thin filaments are visible due to the fact that endogenous tropomyosin 3 is fluorescently tagged (yellow). Wavy muscle tissue is indicative of twitching movements that occurred before fixation was complete. The arrows in each panel indicate the highlighted region where the verniers appear in the SHG channel alone (A) In the SHG channel (red), verniers can be seen as local curvature in the normally straight bands. (B) In the fluorescence channel, there is no curvature in the banding pattern, indicating that the sarcomeres are not actually physically bent in this region. (C) This is demonstrated further in the merge of panels A and B, where the distorted SHG vernier signal seems to overlap with the adjacent fluorescence band within the same muscle fiber. Scale bar: 10 μm

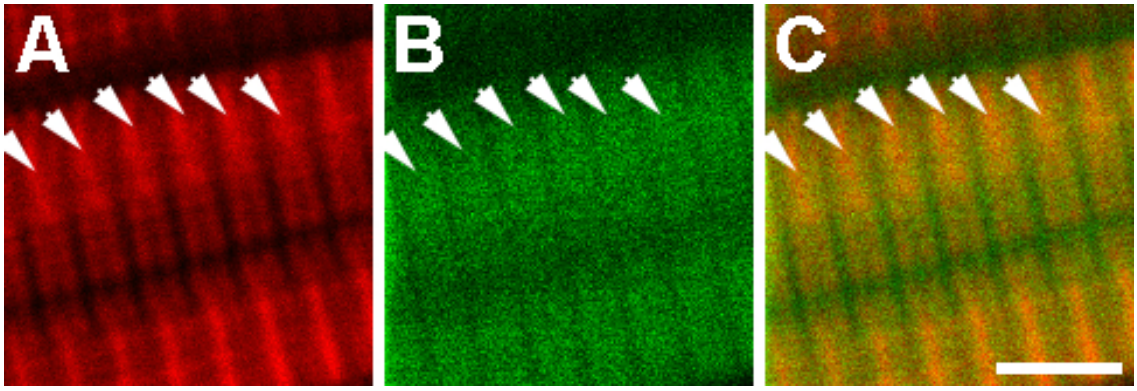

Figure 4.5: **A longitudinal 'xy' optical section through the zebrafish somite shows myosin band verniers in the SHG channel only**. A zebrafish embryo at 7 dpf was fixed and immunostained with anti-myosin MF20 primary and goat-anti-mouse-AF488 secondary antibodies (see materials and methods) before being imaged using a C-Apochromat 63x/1.2 NA water immersion objective at $\sim$ 3.18 zoom in the software. This image shows two adjacent labeled myofibers within the trunk of the embryo (anterior left, ventral down). (A) SHG signal (red) shows clear 'Y'-shaped verniers (arrows) that result from adjacent, slightly staggered myofibers. (B) This vernier pattern is not present (see arrows pointing to the same region as in panel A) in the evenly banded signal from the Citrine channel (green), which depicts the antibody-derived TPEF emission. The signal is even and almost rectangular in shape, with discernible gaps between the bands (indicating the I bands of the sarcomere [183]). Importantly, as expected, the fluorescence channel has no break at the center of the myosin band, which would correspond to the M-line. (C) The merged image shows that the signal co-localizes between the labeled myofiber fluorescence and the SHG channels, but the actual signal pattern is dramatically different in each case. Scale bar: 5 μm

body (Invitrogen, see materials and methods). In this case, the thick filaments are labeled, so the SHG co-localizes with the TPEF from the AF488 on the secondary antibody (Fig. 4.5 and 4.6). Again, we observed that although the herringbone pattern is present in the SHG signal in both longitudinal (Fig. 4.5) and optical cross sections (Fig. 4.6), the fluorescence signal remains perfectly straight.

4.3 Discussion

4.3.1 Confirmation of verniers as an "optical illusion" using combined TPEF and SHG microscopy

In this study, we used a combination of TPEF and SHG as a tool to analyze a peculiarity of endogenous SHG signal in the striated skeletal muscle of zebrafish larvae. Previously, Nathan Hodas showed through theory that SHG and TPEF signal from simplified sarcomeres can be dramatically different in staggered striated muscle fibers, and we were able to show that verniers that looked like they linked adjacent muscle fibers in membrane- and nuclear-labeled zebrafish larvae were actually separated by unbroken membrane fluorescence [181]. In the case of the flip trap zebrafish example in Fig. 4.5, if the sarcomere components actually had a physical distortion in their structure, the fluorescence would have had a comparable curvature to the signal seen in the SHG channel. Instead, we see perfectly straight fluorescent signal, while SHG signal seems to be asymmetrically contracted and overlaps with the fluorescence.

Further confirmation was seen in the MF20-labeled larval fish, where TPEF-labeling showed a regular, periodic, and evenly labeled thick filament organization, while SHG displayed a variety of vernier-like patterns in the same optical section. This was apparent in the longitudinal optical section (Fig. 4.5), where the 'Y'-shaped vernier patterns showed up in most myosin bands of the

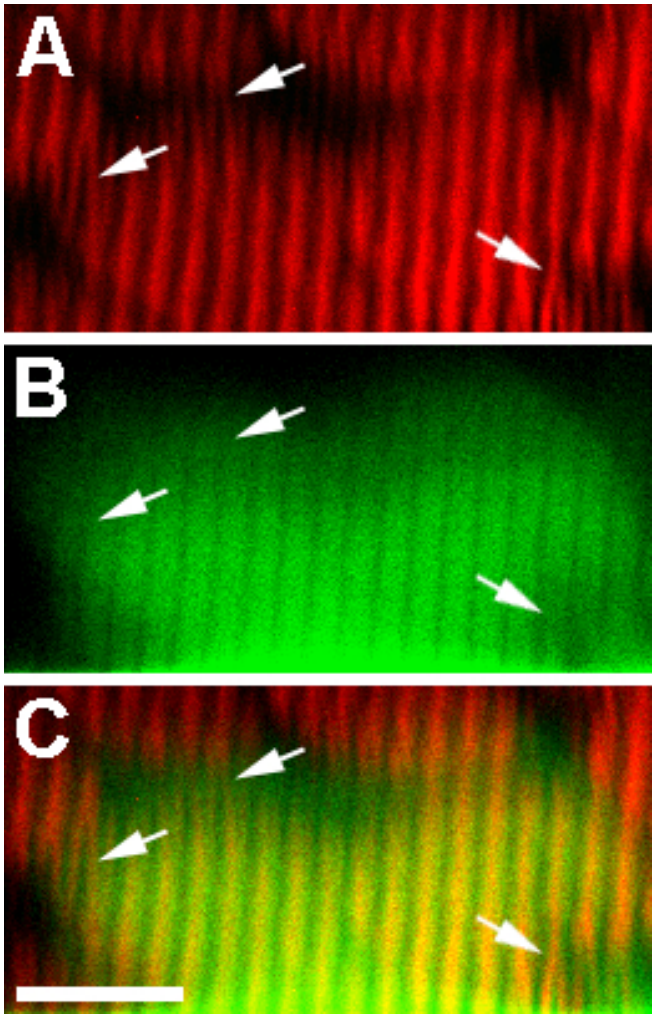

Figure 4.6: **Optical 'xz' sections in depth show additional evidence that myosin band verniers exist solely in the SHG channel**. In a different 7 dpf zebrafish embryo sparsely immunostained with MF20 (anterior right, dorsal into the plane), an optical cross section through the depth of the tissue was taken using the same conditions as in Fig. 4.5 (1.76 zoom in this case). (A) In the SHG channel, adjacent myofibers seem to be linked by myosin verniers (arrows). (B) In the Citrine fluorescence channel, the banding pattern does not bifurcate at all (see the arrows pointing to the same regions as in panel A). (C) In the merged image, the SHG signal and the fluorescent signal overlap within the labeled myofiber but do not show the same vernier signal pattern (arrows). Thus, the vernier patterns are only present in the SHG channel. If there were true physical connections between adjacent myofibers, this pattern would have also shown up in the fluorescence channel. The fluorescence signal is much more diffuse than the tight banding pattern in the SHG, but the straight, aligned striated structure can still be appreciated. This diffuse signal could have arisen from the incubation conditions — such as high detergent — or from the fixation, leading to some tissue distortion. Note that we chose to label the muscle tissue sparsely in this manner by using a more stringent fix (i.e., 4% instead of 2% formaldehyde) so that we would be able to label single isolated muscle fibers and would be able to discern better the muscle boundaries in the fluorescence channel. Scale bar: 10 μm

sarcomeres while the fluorescent signal remained consistently (nearly) rectangular in shape. This bifurcated pattern in the SHG can be attributed to the orientation of the muscle fibers, where some areas have enhanced SHG at the M-line while other M-line regions have no SHG signal, creating a vernier shape. Corroborating evidence for this lies in the fact that the TPEF signal from each of the AF488-labeled myosin bands is evenly fluorescent with no changes at the M-line, as expected.

In addition, the sparse MF20 staining (labeling only a few myofibers due to a low penetration rate of the MF20 into the sample) was advantageous to prove that verniers are an artifact of SHG imaging, especially in the cross section image (Fig. 4.6): if two cells were in fact connected via physical myosin verniers, the fluorescence would have been able to label the adjacent cell as clearly, at least regionally where the connection occurred. In our examples, no fluorescence was seen in adjacent cells in addition to the fact that no curvature was seen in the fluorescence channel. We saw SHG verniers that extended past the fluorescence signal outside of a particular myofiber, giving a misleading indication that two myofibers might be linked. However, the fluorescence does not cross into adjacent myofibers even when SHG verniers are present and supposedly link them, which is a strong indication that the theory is correct.

4.3.2 Taking advantage of verniers when characterizing muscle tissue

Recently, there was a theoretical report documenting the optical patterns that can be generated in isolated striated muscle fibers that seems to agree with Nathan Hodas' theoretical model [185]. Unlike our study, this group focused mostly on single-band versus double-band patterns of muscle SHG verniers (similar to Fig. 4.5) and did not explicitly consider the curved distortions in the signal that may be seen in verniers between staggered adjacent muscle cells. Importantly, their assertion provides corroborating evidence with our independently developed model and our successive experiments.

Interestingly, verniers have been proposed as a measurement of tissue health in dystrophic mouse tissue [172]. Unlike fluorescent means for labeling the muscle tissue, SHG has the capability to not only provide structural information about the muscle fibers but can also be a clear indication of muscle organization. As muscles become more disordered as a result of the tearing and damage even seen in dystrophic disease progression, these SHG "optical illusions" appear more often [172]. So, these optical artifacts might actually be useful as a quantitative means for analyzing disease progression. This may even be a tractable approach for analyzing disease progression in humans, as new minor invasive SHG microendoscopy protocols are formulated and refined (as in [80]), potentially eliminating the need for invasive tissue biopsies and fixed histochemical staining.

4.3.3 Limitations of endogenous SHG microscopy

The application of SHG imaging for visualizing endogenous structures has remained limited[1]. A major challenge that must be considered is that most endogenous SHG signal intensities are typically much weaker than TPEF [72]. Thus, higher laser power may be needed to gain sufficient contrast when imaging endogenous muscle myosin. In this case, close attention must be paid to ensure that the increased power does not damage the tissue. Additionally, when SHG and fluorescence are imaged in tandem, higher-powered 2P laser light used to visualize muscle SHG may quickly bleach a fluorophore, if the 2P illumination is within the absorption band of the fluorescent probe. In this case, care must be taken to choose appropriate fluorescent materials and 2P wavelengths for SHG collection.

An additional issue when using epi-detection for endogenous SHG imaging is that the forward-directed SHG signal needs to get scattered in the backward direction [72]. Thus, in the future, I will need to use a better-optimized setup (similar to [23, 87]) to continue my work in using endoge-

[1] Some of the text in Section 4.3.3 was first reported a publication in *Bioessays* that was written in collaboration with Periklis Pantazis, Scott E. Fraser, and myself [1].

nous SHG as a diagnostic tool for understanding the progression of muscular dystrophy early in development, especially if I move into higher vertebrate systems (e.g., mice).

4.3.4 Suggested improvements to make endogenous SHG an effective early stage diagnostic tool for neuromuscular disease

The potential for endogenous SHG as an early diagnostic for neuromuscular disease is still attractive, but we will require certain future improvements to the imaging conditions. A recent study detailed a so-called "photo-conversion" effect of sarcomeric SHG patterns after illumination with a femtosecond pulsed laser source, suggesting that the structure of the sarcomere could be disrupted by chronic exposure of the 2P laser, even at powers well below the tissue damage threshold [180]. The lack of contrast in the sarcomeric striations that we have seen in early attempts at long-term SHG imaging in zebrafish (Video A.3.2, 850 nm illumination) may be explained by this phenomenon. This study mentions that the use of longer wavelength illumination dramatically reduces this effect [180], so in the future, we will consider pushing illumination further into the near infrared regime, while remaining within the tissue "transparency window" between 600 nm and 1300 nm [186]. Two ways to accomplish this are as follows: (1) an optical parametric oscillator can be placed in series with a commercial 2P laser to extend the tunable range, or (2) a femtosecond pulsed Cr:forsterite laser [187] could be used as an alternative to standard, commercially available Ti/Sapphire 2P tunable laser sources (also touched upon in [1]).

As mentioned in Section 4.3.3, a variety of conditions must be met in order to obtain significant SHG at the detector, especially if epi-directed signal is used instead of transmitted detection. In the case of the zebrafish, which is optically clear at early stages (especially when treated with 1x PTU, see materials and methods), transmitted detection is still the optimal choice. Collimation adjustments, the use of a different condenser to optimize SHG signal collection, and the addition

of better transmitting/reflection lenses and mirrors in the transmitted direction could improve signal collection, possibly reducing the required laser power to achieve appreciable signal. Additionally, more sensitive detectors could be placed in the transmitted direction, such as the so-called GaAsP detectors, which may have up to $\sim$ 30–45% collection efficiency between 400 and 600 nm, which is in the range of possible SHG produced within the tunable range of Ti/Sapphire laser sources. If the tunable range can be extended, so-called avalanche photodiode detectors may have up to $\sim$ 75% collection efficiency between 600 nm and 700 nm (personal correspondence, Zeiss representatives).

4.4 Materials and methods

4.4.1 Zebrafish husbandry

Zebrafish were raised, hatched, injected, and maintained in a house colony as previously described [151].

4.4.2 Immunohistochemistry

Zebrafish embryos (WT or ct5a allele [15] transgenic zebrafish) were obtained by incrossing males and females from the same genetic background. These embryos were allowed to develop for $\sim$ 18–20 hr before being treated with 1x 1-phenyl 2-thiourea (PTU, Sigma Aldrich) to inhibit pigment formation for the following few days of development. PTU medium was exchanged once every day or two. In the days before imaging, the embryos were kept in egg water [151] in a Petri dish and kept in a 28°C incubator.

To fix the zebrafish, the embryos/larvae were first anesthetized in 0.015–0.03% MS-222 (Finquel) and then placed in 4% methanol-free formaldehyde (Thermo Scientific) on ice. After $\sim$ 5 min, embryos were allowed to continue to fix at room temperature on a nutator (BD Diagnostics)

for 1 hr before being washed in Ca^{2+}/Mg^{2+}-free 1x PBS 3 times (15 min, each). ct5a zebrafish (Fig. 4.4) and the WT zebrafish that was used to generate Fig. 4.2 were immediately prepared for imaging. Embryos that were stained with MF20 antibody were first blocked overnight at 4°C in 1x PBS (Ca^{2+}/Mg^{2+}-free) + 1% dimethyl sulfoxide (DMSO) + 1% bovine serum albumin (BSA) + 1.5% Triton X-100 detergent (referred to as PBSTB). Anti-myosin MF20 supernatant (gift of Max Ezin at Caltech) was obtained from the Developmental Studies Hybridoma Bank at the University of Iowa. MF20 was incubated on a nutator at room temperature in PBSTB with the whole-mount zebrafish for 2.25 hr (1:3 dilution). Embryos were washed 3 times (15 min each) in PBSTB before being suspended in PBSTB and treated with goat anti-mouse-AF488 IgG secondary antibodies (Invitrogen) (1:200 dilution). The embryos were incubated with the secondary antibody protected from light at room temperature on a nutator for 2.5 hr. After 3 washes (10 min each), the embryos were prepared for imaging.

4.4.3 Zebrafish imaging

Fish for the live imaging experiments from Section 4.1 of this chapter were treated as follows before imaging. Embryos were injected — with either (1) $\sim$ 200 ng/μl memb-Dendra2 mRNA (from the pMTB construct described in [61], prepared with mMESSAGE, mMACHINE kit, Ambion) alone (Fig. 4.1 and Video A.3.1) or (2) $\sim$ 200 ng/μl each of memb-Dendra2 and H2B-Cerulean mRNA (Fig. A.3.2) — at the zygote stage as described in Appendix B, Section B.2.7.

For all imaging experiments (live and fixed), zebrafish were embedded in 1% low melting point agarose (agarose for the living samples contained 0.015–0.05% MS-222 (Finquel) to anesthetize the embryos) as detailed in Appendix B, Section B.2.8 and imaged on a Zeiss LSM 510 or 710 system with 2P capabilities (Coherent, Chameleon Ti/Sapphire laser source). The living zebrafish embryos (Fig. 4.1 as well as Videos A.3.1 and A.3.2) were imaged within a Zeiss incubation chamber on the

microscope, maintained at 28°C. Custom filters (kindly provided by Semrock, Inc.) placed in the transmitted light path on the microscope enabled detection of SHG signal. 2P wavelengths between 850 nm and 900 nm were used in these experiments, since they seem to produce optimal SHG in zebrafish striated muscle. Fluorescence signal was detected in the epi-direction using standard detection filter settings for each fluorophore. Successive optical sections were taken using the Zeiss LSM to cover large volumes of the muscle compartments and to locate vernier patterns from staggered muscle fibers. Images were processed in Imaris (Bitplane, AG) as well as ImageJ (NIH) and Adobe Photoshop CS3 (Adobe Systems), where minor brightness/contrast adjustments and filtering (small area median filter) were performed.

Chapter 5

Improving biological applicability of SHG nanoprobes by testing and applying a robust functionalization routine

5.1 Introduction

Over the past ten years, second harmonic generation (SHG) imaging has been utilized for a variety of *in vivo* imaging applications, with applications ranging from label-free imaging during embryonic development [87] to early stage cancer detection [22]. As mentioned, until recently, biologically relevant SHG imaging has been focused on imaging exogenous dye markers [90, 94, 89, 91, 93, 92] or endogenous protein structures that enable weak second harmonic generation [87, 22, 88, 188, 85, 83, 86], such as muscle myosin as in Chapter 4. In comparison to the relatively weak SHG in these organized protein arrays, a variety of inorganic crystalline materials have been shown to exhibit strong SHG signatures, including barium titanate [189] ($BaTiO_3$, referred to here as BT). Recently, a colleague of mine in the lab, Periklis Pantazis, took advantage of the superior optical properties of these inorganic materials, referred to as SHG nanoprobes, at the nanoscale, where he labeled and imaged live, intact zebrafish embryos and larvae and was lead author on the publication demonstrating these materials [72].

I appreciated that possible applications for SHG nanoprobes in biology are wide-ranging. Potentially the most important feature of these nanocrystals is that they offer a compatible spectral signature to any fluorescent protein or dye currently used in biological imaging — unlike the absorption band that is an inherent property of fluorescent probes, the anti-Stokes shift that is characteristic of SHG signal can be tuned for any application. Generally, by choosing a proper 2P illumination wavelength and proper emission filter sets, both SHG signal and fluorescent emission can be simultaneously collected and spectrally separated. In addition, given the distinct wavelength dependence of SHG signal in different SHG nanoprobes, multiple varieties of SHG nanoprobes may be combined to achieve a spectrally separable signal [72]. Thus, SHG nanoprobes may be used in conjunction with traditional fluorescent labels as an additional unique spectral label for multi-marker imaging, such as is necessary for long-term cell tracking at the level of a single cell in culture [190] and *in vivo* [191].

In working with the PhOTO zebrafish lines, described in Chapter 3, I came to realize the difficulty of deep-tissue fluorescent imaging within an adult zebrafish. Even with transgenics expressing as strongly as the PhOTO lines, live imaging deep within the adult is made nearly intractable by the incredible tissue autofluorescence, opacity, and heterogeneity (i.e., optical-aberration inducing conditions), which is why our focus on regeneration has been initially in the fin, which is a much easier tissue compartment to visualize in a living, intact system. In contrast, SHG nanoprobes can be imaged in optically challenging tissue environments, deep within living tissue [72]. So, I came to understand that one of the major benefits of the SHG nanoprobe labeling is that these materials may be especially attractive for applications in older zebrafish or higher-order vertebrate (e.g., mouse) cell tracking experiments, as their bright, high SNR signal can be captured in absorptive and scattering tissue as development proceeds past any early tissue transparency time period. Consequently, I began working with these nanomaterials in the hopes that they will one day be used hand-in-hand

with the fluorescence-based tools and endogenous SHG imaging approaches that I have worked on in my thesis project. I will briefly touch upon these ideas for the future in Chapter 6.

Initially, I wanted to ensure that the inherent toxicity of BT was negligible in a biological context. This issue of labeling probe toxicity cannot be stressed enough; nanoparticles of varying sizes have been shown to be sequestered in the body for long periods of time in the reticuloendothelial system [192, 193], so decreasing the likelihood of nanoparticle-induced toxicity is of paramount importance to allow these materials to be clinically relevant [194]. To carry out these initial toxicity tests, I worked in collaboration with my colleague (who happens to be my brother), Christopher Dempsey. We injected zygote stage zebrafish embryos with commercially available quantum dots (Invitrogen), BT, and a 1x PBS control solution to gauge whether early development is affected. We expected this to be a sensitive toxicity test, because we applied these nanomaterials directly into the developing zebrafish and monitored whether injected embryos could proceed past the gastrula period, which is a dynamic stage in the zebrafish lifetime where coordinated cell movements, division, and signaling are regulated to set up the initial body plan of the organism [51]. Any dramatic changes in these processes as a result of the injections or the introduction of these nanomaterials could lead to developmental aberrations and embryo lethality[1]. Data from these preliminary tests suggested that SHG nanoprobe injections are no more detrimental than the control saline injections (Fig. 5.1). We most often attribute increased lethality arising from saline injections over uninjected controls as resulting from unintentional trauma to the fragile and small (< 1 mm) zygote stage embryos stemming from the injection needle or bolus of injected material. Thus, we concluded that any lethality in the SHG nanoprobe injected embryos probably stemmed from this same unintentional trauma at the time of injection, which was in marked contrast to the highly toxic quantum dots.

With the knowledge that BT nanoparticles are sufficiently nontoxic even under stringent condi-

[1]These previous two sentences were adapted from a review publication in *Bioessays* that was written in collaboration with Periklis Pantazis, Scott E. Fraser, and myself [1].

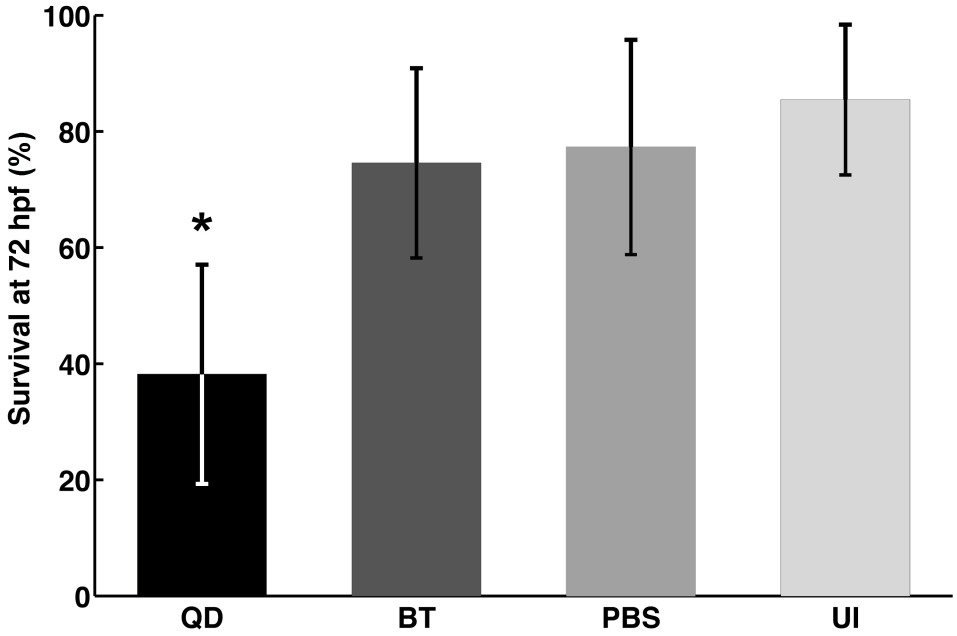

Figure 5.1: **BT nanoparticles are nontoxic after zygote stage injections**. In this experiment, zebrafish were injected at the zygote stage with $\sim$ 2.3 nl of the following: quantum dots (QD), barium titanate nanoparticles (BT), 1x phosphate buffered saline control (PBS, Thermo Scientific), or uninjected control (UI). Embryo lethality was assessed at $\sim$ 72 hpf for each injection condition. This experiment was performed 4 times so that a total of N = 110 embryos were analyzed for each injection condition. An average of 85% of the total embryos were alive from the uninjected control group at 72 hpf, while the BT and FSG group had slightly lower survival percentages of 75% and 77%, respectively. The quantum dots had marked reduction in embryo survival, with an average survival percentage of 38%. P values were calculated using an unequal variance, two-tailed t-test. QDs had statistically significant reduction in embryo survival (asterisk) after 72 hpf with respect to all other conditions ($p \approx 10^{-4}$ with respect to BT and PBS and $p \approx 10^{-6}$ with respect to UI). BT did not have a significant reduction in survival compared to the PBS injection ($p \approx 0.7$) or the uninjected control ($p \approx 0.1$), indicating that BT toxicity is negligible, even when the material is bare (i.e., not surface functionalized) and injected before a crucial period of early embryo development.

tions, we determined that we could make SHG nanoprobes more clinically relevant by designing a broadly applicable surface functionalization routine [195], similar to those described with BT [196] and other nanoparticles [194, 113, 197, 198, 199, 200, 25] in the literature. Also, one important consideration in favor of functionalization was that our starting materials are commercially derived and are heterogeneous in size. This heterogeneity is twofold: (1) the process of production of these nanomaterials through the commercial source results in a broad distribution of nanoparticle sizes, ranging from $\sim$ 50–200 nm; and (2) the nanoparticles are sold in dry powder form, leading to significant aggregation of the particles. Proper functionalization could at least limit the latter of the two size heterogeneity issues by creating a barrier around each individual nanoparticle (or smaller cluster that cannot be broken apart from sonication), preventing further aggregation. This size issue is of particular relevance for targeting in an *in vivo* system, where efficient uptake and diffusion into tissue extracellular spaces (e.g., with gold nanoparticles [201, 24]) as well as eventual clearance from the body (e.g., with quantum dots [193]) has been shown to be strongly dependent on the size of the nanoparticle itself. This, along with other considerations for designing clinically relevant nanoparticles for biological applications (described well in a recent review [195]), led us to design a functionalization scheme for BT. Note that much of the text and data from this chapter was performed in collaboration with Jelena Čulić-Viskota, Periklis Pantazis, and Scott E. Fraser and has been submitted as a manuscript to *Nature Protocols*, where Jelena Čulić-Viskota and I share equal contribution first authorship (where I am second position)[2].

In this chapter, we describe how we prepared BT nanoparticles for biologically relevant imaging by surface functionalization (using standard chemical techniques as can be found in common linkage chemistry textbooks [202]). The advantage of our BT functionalization routine is that

[2]I performed all of the zebrafish-related steps of the procedure, performed the imaging, prepared the graphs, and analyzed the data for the imaging steps. Jelena Čulić-Viskota performed all chemical functionalization steps in this procedure and performed the chemical analyses (e.g., IR, EDS, TEM, DLS). Much of the text reflects our initial submission to *Nature Protocols*, before the text was shortened as a result of requests from the editor.

the intermediate step of surface exposed amine-terminal groups acts as a platform for a variety of chemistries, including non-reactive surface coatings (e.g., PEG), bio-orthogonal linkages (i.e., copper-free click chemistry), and protein targeting moieties (IgG antibodies, in this case). Importantly, a majority of the methods used in this functionalization protocol are easily attempted at room temperature (RT) and moderate conditions.

After functionalization, we demonstrate a unique imaging-based approach to test for proper functionalization. Following this assay, we demonstrate how to incorporate these nanoprobes in an *in vivo* setting using zygote stage injection of dispersed, PEG functionalized SHG nanoprobes. Over time, the dramatic cell divisions and migration that are hallmarks of early development, cause the SHG nanoprobes to distribute within a large number of cells, and we show how to image these nanoparticles within the developing embryo. Our *in vivo* example illustrates the utility of the SHG nanoprobes: because of the high signal-to-noise ratio (SNR), appreciable brightness, and absence of bleaching/blinking, SHG nanoprobe labeling of cells within a biological tissue of interest will allow for long-term imaging even within challenging (i.e., highly scattering and absorbing) tissue environments. Finally, we demonstrate applications of our antibody (Ab) functionalization in fixed zebrafish samples and live isolated primary cells.

5.2 Results

5.2.1 Diagrammatic overview of functionalization procedure and zebrafish imaging

In order to prepare the SHG nanoprobes for biological imaging, functionalization is necessary to achieve sufficient particle separation and to prevent aggregation before introduction into biological tissues [3]. Excessive aggregation could lead to reduced biocompatibility, even though the materials themselves are non-toxic. To prepare the surface of the BT nanoparticles for a silanization reaction,

[3]For a detailed list of materials, reagents, and procedures used for this chapter, refer to Appendix B.

the surface is first exposed to an aqueous solution of hydrogen peroxide (H_2O_2) for 4 hr at 110°C with stirring. These conditions have been optimized to saturate the surface with hydroxyl (–OH) groups [203] (hydroxylated BT, referred to as BT-OH). A beneficial consequence of the H_2O_2 treatment is that it will strip any surface adsorbed carbonates on the BT surface, similar to the action of weak aqueous acetic acid solutions [204]. Vacuum drying of the BT-OH powder using a Schlenk line will prevent any carbonate from being re-adsorbed to the surface of BT. After hydroxylation, a 24 hr surface silanization reaction with N-aminoethyl-2,2,4-trimethyl-1-aza-2-silacyclopentane is performed at RT in anhydrous toluene (Fig. 5.2). Surface functionalization is achieved as a result of a ring-opening reaction made possible by hydroxyl groups on the oxide surface. This reaction forms a high-density monolayer on the BT surface without any byproducts [205]. The terminal ends of the silane layer are exposed amine functional groups (the product is now referred to as BT-NH_2) that are convenient for use in a variety of bioconjugation reactions [202].

After initial trouble with reproducibility of the functionalization routine, we determined that we needed a simple test for proper functionalization. To achieve this, we designed a procedure to coat the BT nanoparticles with a fluorescent conjugate. Importantly, we ensured that this procedure required multiple chemical steps — our stringent test would verify whether multstep functionalization reactions would result in appreciable surface coverage. The initial step in this reaction (after surface silanization) is the addition of an azide functionalized surface via 1-ethyl-3-(3-dimethylaminopropyl) carbodiimide (EDC)/ N-hydroxysuccinimide (NHS) coupling of 6-azidohexanoic acid to the surface amines in anhydrous dichloromethane (DCM) for 4 hr [202]. The azido-modified BT-NH_2 is then reacted overnight at RT in a copper-free click chemistry reaction with biotin-PEO-cyclooctyne [206], producing biotin coated BT nanoparticles (referred to as biotin-BT, Fig. 5.3). Finally, the washed biotin-BT nanoparticle dispersion is reacted for 1 hr at RT in the dark with 488 AlexaFluor (AF488) conjugated streptavidin (referred to as BT-streptavidin-AF488,

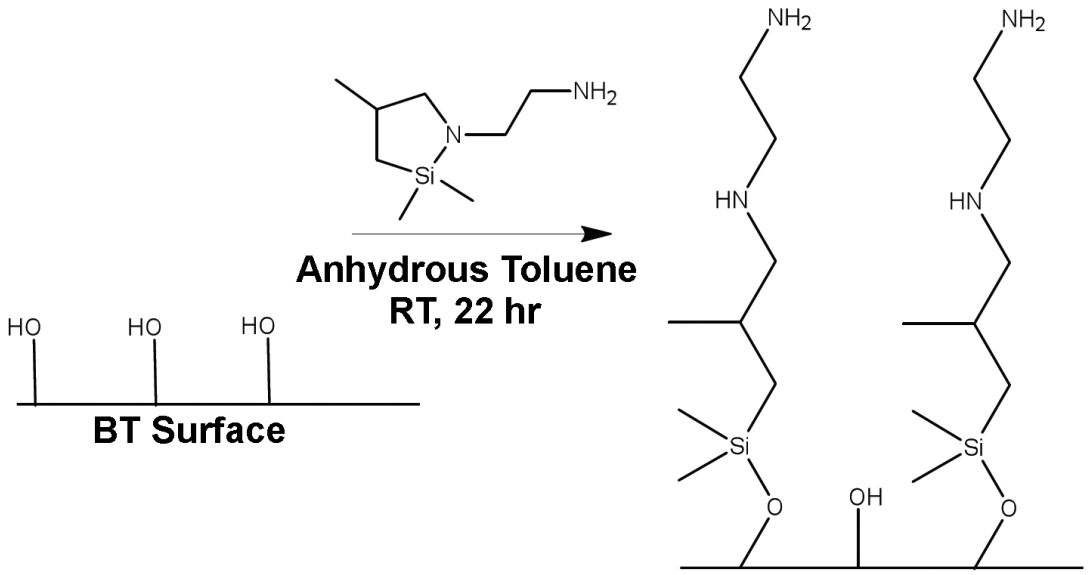

Figure 5.2: **BT surface hydroxylation and silanization**. After the surface of BT is hydroxylated by H_2O_2 treatment, N-aminoethyl-2,2,4-trimethyl-1-aza-2-silacyclopentane is reacted, exposing terminal NH_2 groups. Note that no deleterious byproducts are formed during the reaction that could compromise the biocompatibility of the particles when introduced into a sample. The terminal amines on the BT surface as a result of this silanization reaction act as a versatile platform for a variety of other surface modifications.

Fig. 5.4). Although many applications of biotin-BT are possible, our preparation of biotin-BT is used in this protocol as a means for qualifying proper functionalization of the nanoprobes via SHG and 2P imaging (see Section 5.2.3), which is a straightforward control for troubleshooting the functionalization protocol.

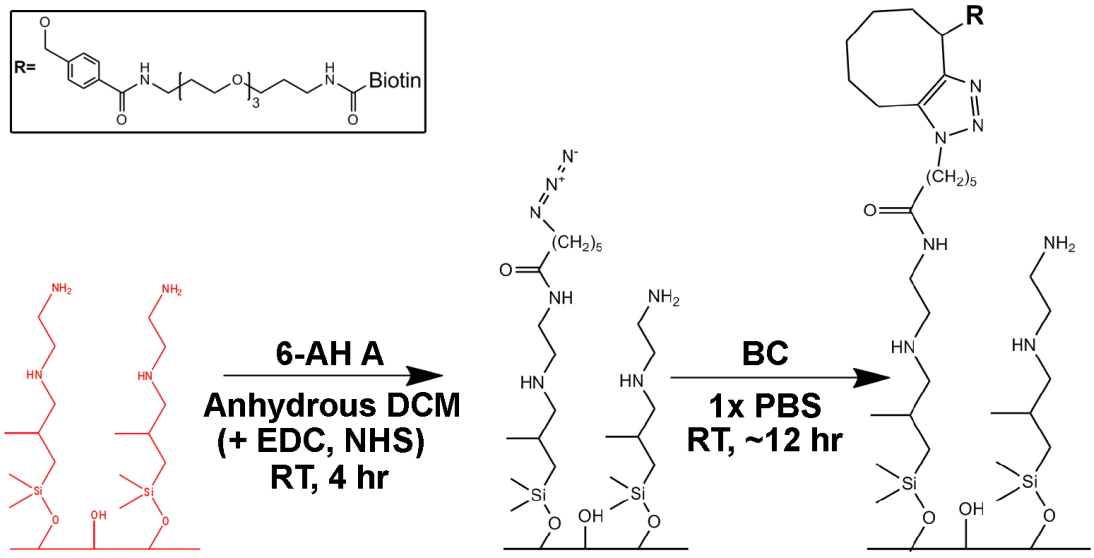

Figure 5.3: **BT-streptavidin functionalization with a multistep click chemistry linkage**. 6-azidohexanoic acid (6-AH A) is reacted and covalently attached to the terminal amines on BT-NH_2 in the presence of EDC and NHS. Biotin-PEO-cyclooctyne (BC) is then reacted to achieve a biotin covered surface on the BT nanoparticles. Streptavidin can then be incubated with biotin-BT, resulting in high-affinity surface binding. This represents a 4 total step synthesis, including surface silanization. We use this streptavidin linkage as a control to ensure that proper coating has occurred.

Taking the functionalization a step further to coat the SHG nanoprobes with a non-reactive surface group, amine functionalized BT was linked with poly(ethylene glycol) (PEG) in anhydrous DCM with a similar EDC/NHS coupling reaction (Fig. 5.5). Importantly, PEG is a biocompatible polymer that effectively suppresses non-specific binding of proteins to nanoparticles and should prevent significant particle aggregation [207]. In the future, other biocompatible polymers could also be used to provide widespread binding to the BT surface, if necessary.

After PEG functionalization, we introduced the particles into the living zebrafish embryo. We

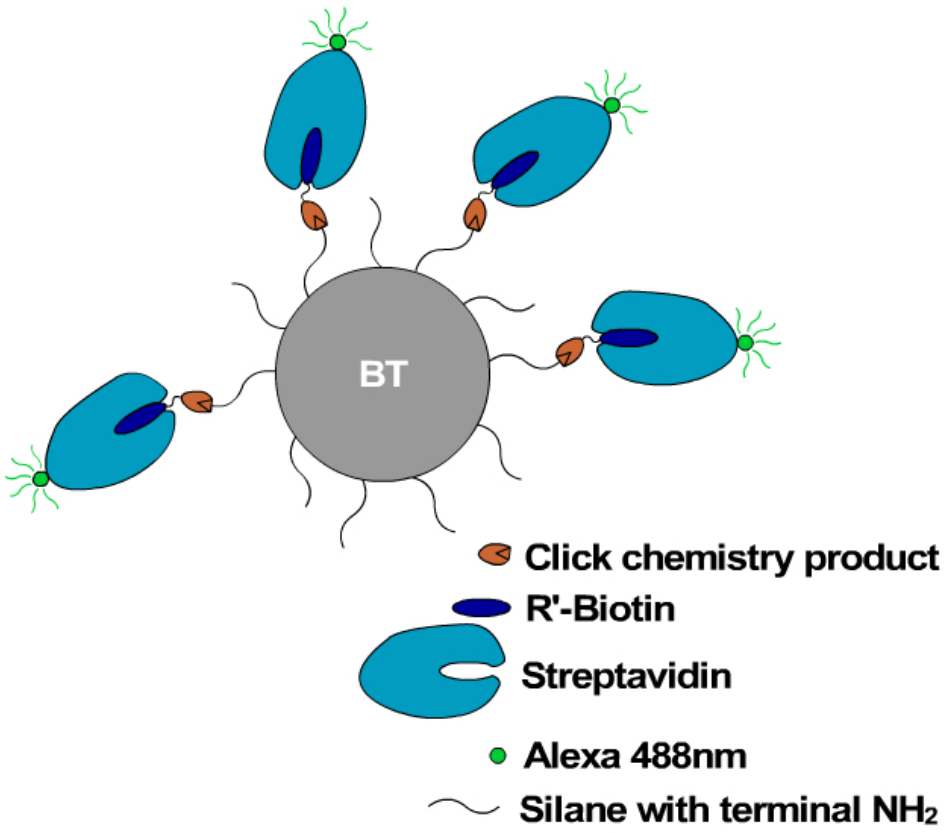

Figure 5.4: **Cartoon of BT-streptavidin-AF488**. After functionalization, several groups are attached to the surface of BT, including the initial silane, the 6-AH A, the BC, and the AF488-conjugated streptavidin. Though it is possible that not all terminal amines are reacted with 6-AH A, the high yield of click chemistry should ensure that any terminal azides will be reacted with BC. Co-localization of AF488 fluorescence and SHG signal from the BT can be used to verify that the multistep functionalization was successful. Note that each element is not to scale.

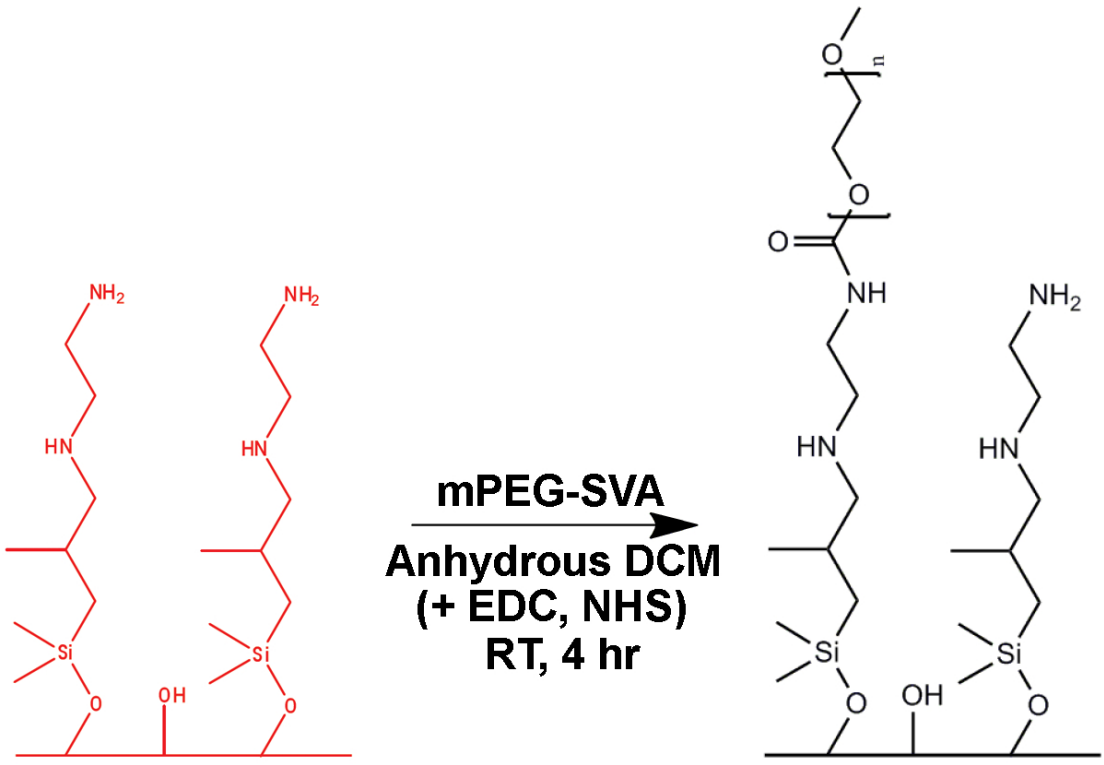

Figure 5.5: **PEG-BT functionalization**. mPEG-SVA is reacted with the terminal amines on the surface of BT-NH_2 in the presence of EDC and NHS. The product is washed in ethanol and water by centrifugation and the liquid supernatant is discarded. Properly functionalized PEG-BT nanoparticles have reduced aggregation in solution, even after sedimentation (resuspension requires flicking the vial containing the nanoparticle solution).

first sonicated the PEG-BT diluted in deionized water for 30 min within a bath sonicator so that the nanoparticles are well dispersed before injection. Within 5 min of sonication, zebrafish embryos were injected with PEG-BT by inserting a borosilicate needle into the yolk cell of the embryo near to or inside of the zygote cell. Though direct cell injection may be preferable to ensure that a large number of particles is distributed into the organism, yolk cell injection has a decreased chance of embryo lethality due to imperfect use of the injector. After yolk cell injection, cytoplasmic streaming and cell cytoplasmic connections maintained with the yolk during cleavage stages [51] allows the nanoparticles to be taken into the embryonic cells. After allowing the embryo to develop at 28°C for as long as 24 hr — depending on the desired stage of development — embryos were embedded in 0.1–1% low melting point agarose within coverslip chambers before imaging.

To enable cell-specific targeting, we utilized a functionalization routine to link glycosylated Abs (e.g., of mammalian origin) to the platform terminal amines on BT-NH_2 [202]. First, the Ab of choice is reacted with sodium periodate ($NaIO_4$) in 0.1 M $NaPO_4$ buffer at RT for 1 hr, which oxidizes certain sugars on the characteristic glycosylated moieties linked to the F_c region of the Ab itself. Meanwhile, BT-NH_2 is reacted with Succinimidyl 6-hydrazinonicotinate hydrochloride (SHNH), also in 0.1 M $NaPO_4$ buffer at RT for 1 hr. After these initial reactions, the treated antibody is added to the SHNH-reacted BT, linking the aldehydes from the oxidation to the NHS ester terminal groups now on the surface of BT (Fig. 5.6).

5.2.2 Chemical methods to verify the surface coating of BT nanoparticles

To verify the presence of different functional groups incorporated on the BT surface, we performed a rapid spectroscopic technique, FT-IR analysis, on BT, BT-OH, and BT-NH_2 samples using the KBr pellet method. A few drops deposited on an IR polymer film card of the N-aminoethyl-2,2,4-trimethyl-1-aza-2-silacyclopentane solution were used as a hydrolyzed reagent control for referenc-

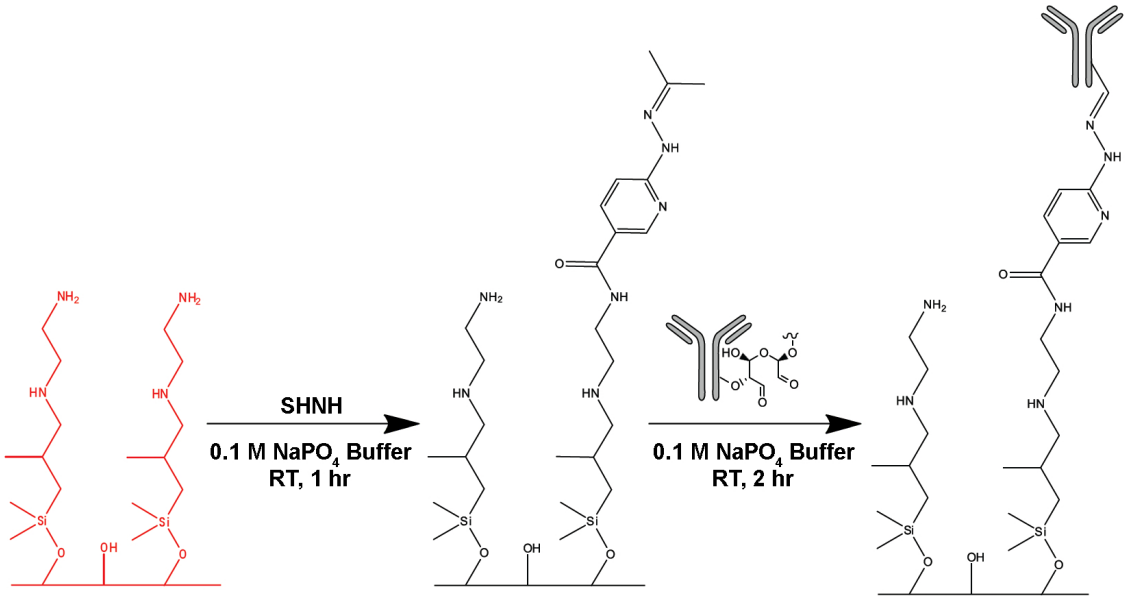

Figure 5.6: **Ab-BT functionalization**. This two-step reaction requires the reaction of SHNH with the terminal amines on BT-NH_2 first. Next, a sodium periodate-treated glycosylated IgG antibody is reacted with the exposed NHS ester groups on BT, linking the F_c region of the antibody to the nanoprobe. The Ab-BT nanoprobes enable cell and tissue targeting by high affinity antibody linkages to an epitope (e.g., cell surface marker) of choice.

ing the IR absorption peaks in the BT-NH_2 sample (Fig. 5.7A). The dominant peaks in the three BT spectra correspond to Ti-O [208] (around 550 cm^{-1}) as well as the Ti-O bend [209] (around 425 cm^{-1}). The wide stretch around 3000 cm^{-1} in the inset of Fig. 5.7B (blue line) indicates that H_2O_2 treatment hydroxylates the BT surface (as in e.g., [210]) and — in conjunction with subsequent vacuum drying — is successful in eliminating the adsorbed carbonate layer that is present in the commercial BT powder spectrum (Fig. 5.7B, asterisk, the weak peak at $\sim$ 1435 cm^{-1} disappears after hydroxylation). The BT-NH_2 sample spectrum (Fig. 5.7B, red line) has Si-CH_3 bands at 1260 cm^{-1} and 800 cm^{-1} from the –O-Si$(CH_3)_2$– group, along with the overlapping bands at 1130–1000 cm^{-1} that are characteristic of Si-O-Si groups introduced in the surface silanization reaction [211].

In addition to the FT-IR analysis, TEM images of the BT and BT-NH_2 samples are shown in Fig. 5.8 along with the respective EDS analysis for each. Differing surface morphology is apparent when comparing the bare commercial BT (Fig. 5.8A) and the silane functionalized BT surface (Fig. 5.8B).

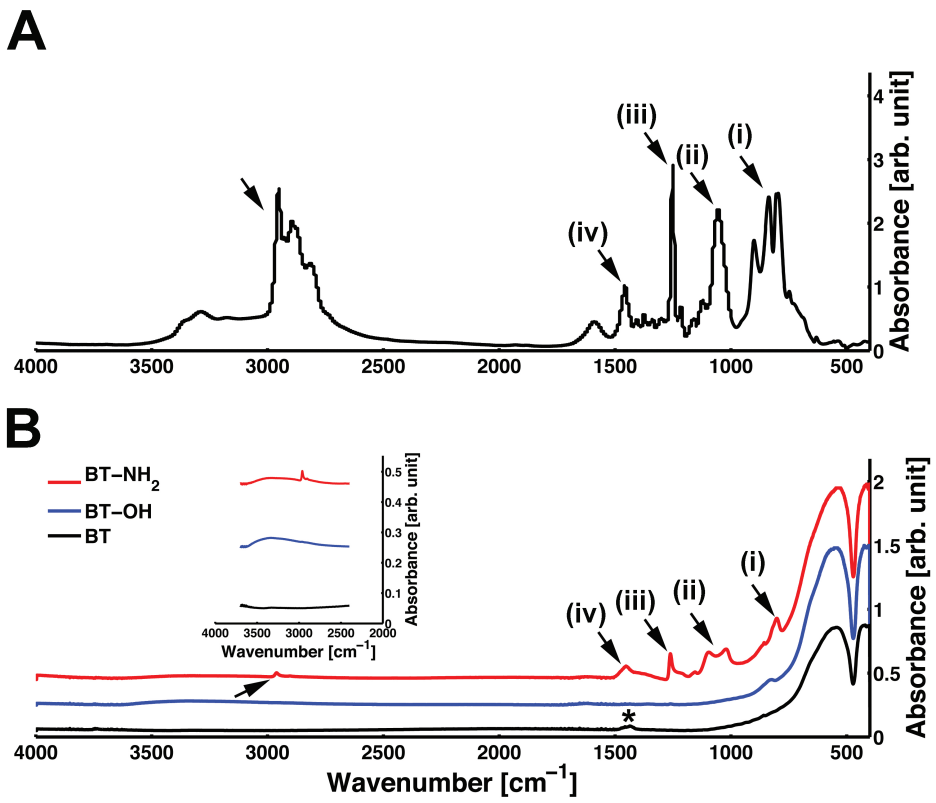

Figure 5.7: **IR spectral analyses confirm the surface hydroxylation and silanization reactions**. IR analyses characterizing the BT and BT-OH powder samples at a concentration of 2 mg within a 47.5 mg KBr matrix, and a BT-NH_2 sample at a concentration of 3 mg within a 49 mg KBr matrix. (A) As a standard for comparison to BT-NH_2 an IR spectrum was taken of a few drops of N-aminoethyl-2,2,4-trimethyl-1-aza-2-silacyclopentane coating the surface of an IR film card. (B) IR spectra for bare commercial BT (black line), BT-OH after hydroxylation (blue line) and BT-NH_2 (red line). Note that the stretch for Ti-O (around 550 cm^{-1}) and the Ti-O bend (around 425 cm^{-1}) dominate the spectra. Focusing on the region of the spectrum between 780 cm^{-1} and 1500 cm^{-1} enables appreciation of the peaks representing proper silane coating of the surface of BT-NH_2 (red line) including: (i) the 800 cm^{-1} and (iii) 1260 cm^{-1} stretches corresponding to Si-CH_3 bands in –O-Si$(CH_3)_2$– group within the silane chemical structure as well as (ii) the double-overlapping peak between 1130 and 1100 cm^{-1}, corresponding to Si-O-Si absorption. (iv) The peak in the BT-NH_2 data (red line) near $\sim$ 1450 cm^{-1} corresponds to contributions from the alkane groups in the chemical structure. In addition, the 1435 cm^{-1} stretch (asterisk, black line) that corresponds to to the adsorbed carbonate groups is eliminated after surface hydroxylation with H_2O_2 (blue line). The inset graph shows a zoom of the graphed data to better appreciate the –OH stretch, which appears after hydroxylation of the BT (blue and red lines, around 3450 cm^{-1}). In the BT-NH_2 data (red line), a weak peak near 2960 cm^{-1} can also be seen (this feature is also present in the silane control spectrum in panel A) and is due to the alkane groups stretching. In order to better appreciate the nuances of each graph, a global offset factor of 0.05 was added to all absorbance data and an offset factor of 0.2 and 0.4 was added to the absorbance values of the BT-OH and BT-NH_2 data, respectively.

The surface of BT-NH_2 is characterized by the presence of an amorphous layer around tetragonal-crystalline functionalized BT (inset in Fig. 5.8B, dotted yellow line). Additionally, control BT tends to cluster more tightly than the functionalized BT-NH_2, where there are clear gaps in between nearby particles. Thus, functionalization of the BT surface reduces aggregation of the particles, achieving a more disperse solution that can be used for introduction into biological samples. As another control, energy-dispersive X-ray spectroscopy (EDS) analysis of the samples (Fig. 5.8C) clearly indicates the presence of silicon atoms only in silane-reacted BT-NH_2.

5.2.3 Imaging-based approach for judging the success of multistep functionalization

To test for successful functionalization using the NH_2-coated BT surface as a platform, it is desirable to have a straightforward method to compare control and functionalized samples. The biotin-BT generated from this protocol is a functionalization routine that can accomplish this goal, when bound to fluorescent AF488-conjugated streptavidin. After extensive washing, we combined TPEF and SHG imaging to show whether SHG from BT and fluorescent signal from AF488 would co-localize in solely the properly functionalized BT-streptavidin sample (illustrated in Fig. 5.4). From a single spectral scan at the coverslip after significant sedimentation (a zoomed portion of these scans can be seen in Fig. 5.9), 465 SHG nanoprobe clusters in the functionalized well and 53 SHG nanoprobe clusters in the control well of an 8-well coverslip imaging chamber were segmented using the SHG channel data with a simple Matlab script. Note that even from the spectral scan image, the functionalized BT-streptavidin looks much less clustered than the bare BT control (Fig. 5.9A, B), which is an initial indication of successful functionalization. Indeed, fewer crystals in the control well met the criterion for segmentation (below a certain size threshold near the diffraction limit, which would be relevant to SHG imaging *in vivo*). The average intensity for photons collected within each wavelength band (10 nm increments in this case) was normalized to the size of each of

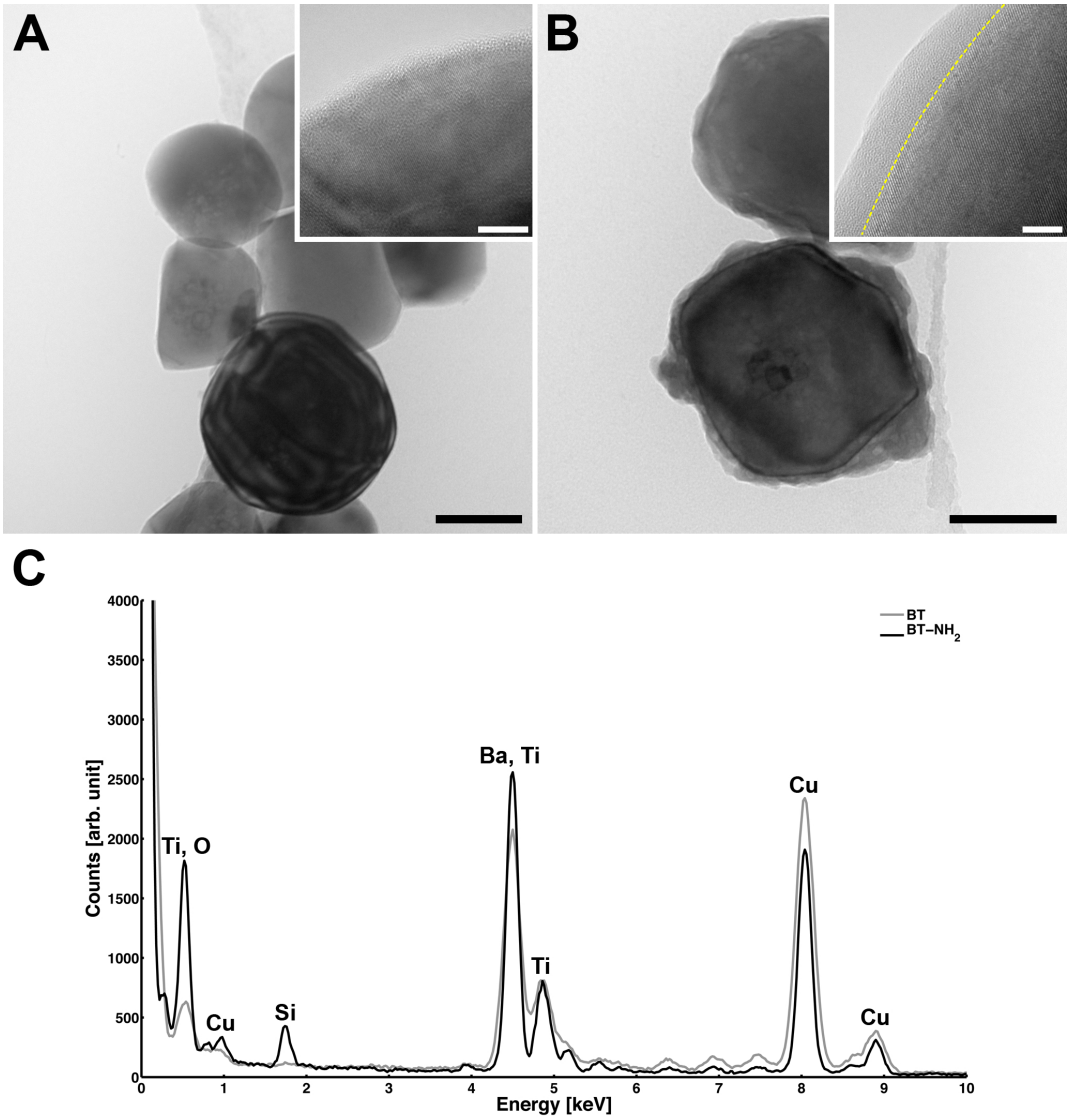

Figure 5.8: **TEM images and EDS analyses provide additional confirmation of hydroxylation and silanization on the surface of BT**. (A) TEM image of non-functionalized BT control at 178 600x magnification as well as at 4 753 000x magnification (inset). Note the lattices representing the crystallinity of the material, which is an essential requirement to be met for SHG. (B) BT-NH_2 at 136 300x magnification and at 3 724 000x magnification (inset) showing the presence of an amorphous layer (of variable thickness, usually $\sim$ 5 nm) around the crystal particle. Note that the N-aminoethyl-2,2,4-trimethyl-1-aza-2-silacyclopentane coating is an invisible single layer (too thin to be seen even at high magnification) at the outermost edge of the amorphous coat and that the thickness of the amorphous coating may be attributed to barium leaching during hydroxylation. (C) EDS spectra indicating the atomic composition of non-functionalized BT nanocrystals (gray line) and functionalized BT-NH_2 (black line). In addition to the characteristic peaks for BT, there is a new peak in the BT-NH_2 data that is specific to the presence of Si atoms in the sample. The Cu that is detected in each of the atomic composition histograms arises from the TEM grid itself. Scale bars: 100 nm (main figures) and 5 nm (insets)

the SHG nanoprobe clusters and was plotted in Fig. 5.10. Clearly, SHG from properly functionalized BT-streptavidin-AF488 co-localizes with AF488 emission. Thus, amine surface coating should be a successful platform for further functionalization methods — even those that are multistep — that generate dispersed BT nanoprobes for long-term *in vivo* imaging, such as with PEG-BT.

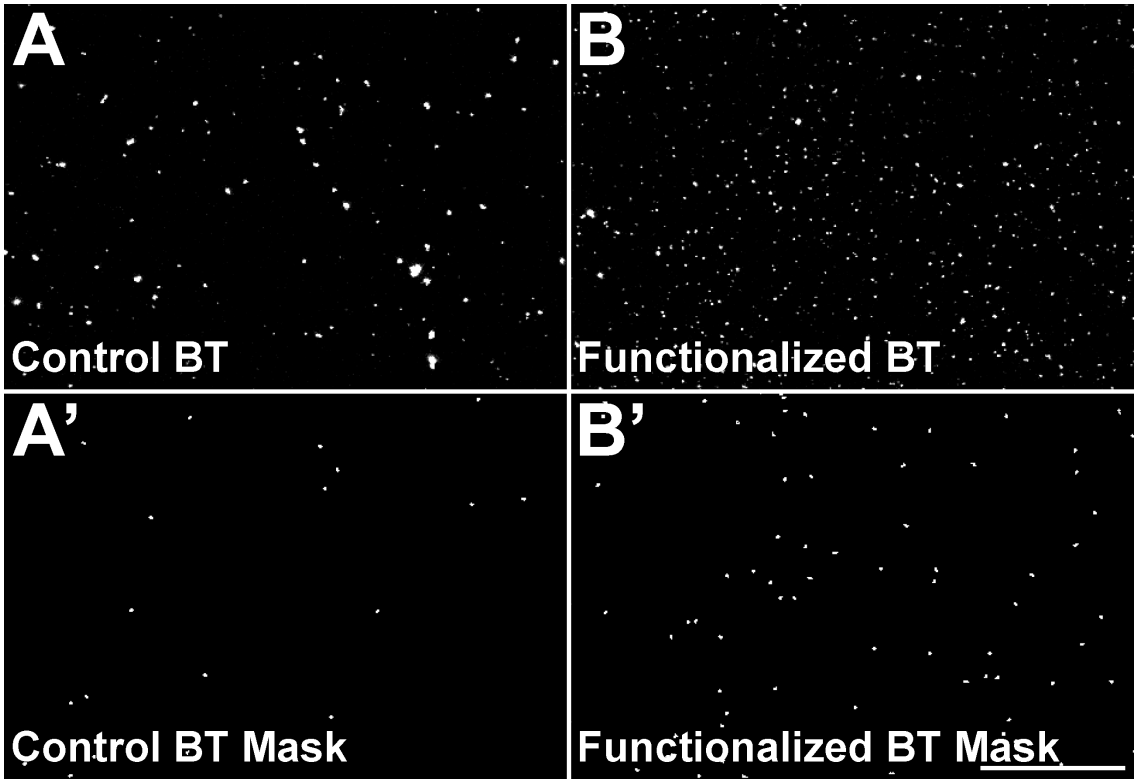

Figure 5.9: **Bare BT and BT-streptavidin-AF488 imaging and segmentation as a means to assess the success of surface functionalization**. Bare BT and biotin-BT were incubated in separate vials with AF488-conjugated streptavidin for 1 hr before being washed and centrifuged three times. 200 μl aliquots of the solutions were placed in separate wells of an 8-well coverslip chamber and the solution was allowed to sediment for several minutes. Using a Zeiss C-Apochromat 40x/1.2NA W Corr M27 objective and the 34 channel spectral detector on an LSM 710 microscope in "lambda mode", signal was obtained from particle clusters — from 421 nm to 587 nm in $\sim$ 10 nm increments — at the surface of the coverslip upon illumination with 965 nm light from a 2P laser source. Using an automated script, the SHG nanoprobe clusters from each well were segmented using the (A, B) SHG signal channel data, since these crystals will have this characteristic signal at 482.5 nm regardless of whether an AF488-conjugated streptavidin coating exists or not. (A', B') A mask was created from segmented crystal data that had an area between 6 and 10 pixels (characteristic of larger than diffraction limited particles, which would have greater non-saturated AF488 signal, if the signal is present). Note that these are zoomed in images of the original data. Scale bar: 50 μm

5.2.4 PEG-BT has reduced aggregation when compared to bare BT samples

After surface functionalization of BT-NH_2 with PEG using a similar EDC/NHS coupling reaction scheme (Fig. 5.5), salt stability size measurements of the PEG-BT were performed at RT. For this analysis, the hydrodynamic radius of the nanoparticles was measured in UltraPure water as well as in 1x PBS solution. Particles not properly polymer coated should display an increase in nanoparticle size when in salt solution due to the shielding of the surface charge by the buffer ions. Dynamic light scattering analysis showed that the PEG-BT samples have no appreciable increase in the hydrodynamic size radius of the particles upon the addition of 11 μl of 10x PBS in 100 μl of solution of PEG-BT in water. Importantly, non-functionalized BT displayed widely varying size ranges (up to $\sim$ 1 μm) when performing dynamic light scattering analysis even in water, indicating a much wider range of particle aggregate sizes, which is in sharp contrast to the more consistent cluster sizes of PEG-BT samples. This is also consistent with the wider range of sizes of nanoparticle aggregates seen in the control versus functionalized images seen in Fig. 5.9. As expected, a properly functionalized BT solution is more stable than BT alone in solution.

5.2.5 Imaging intracellularly localized PEG-BT within live zebrafish embryos

Several examples of BT imaging within living zebrafish embryos can be seen in Fig. 5.11–5.13 and Videos A.4.1–A.4.4. In each of these cases, zygote stage embryos were injected with PEG-BT and allowed to develop unhindered in a 28°C incubator before imaging. To show that SHG nanoprobes are localized within cells of the zebrafish after yolk cell injection, various dye markers can be used to label the cells within the embryo. 10,000 MW Dextran-AF546 is a dye that can be co-injected with the PEG-BT during the zygote injections. This is an effective troubleshooting tool to ensure that zygote injections are successful before attempting to image on the laser scanning microscope: after injection, embryos that have been properly manipulated will have blastomeres that fluoresce

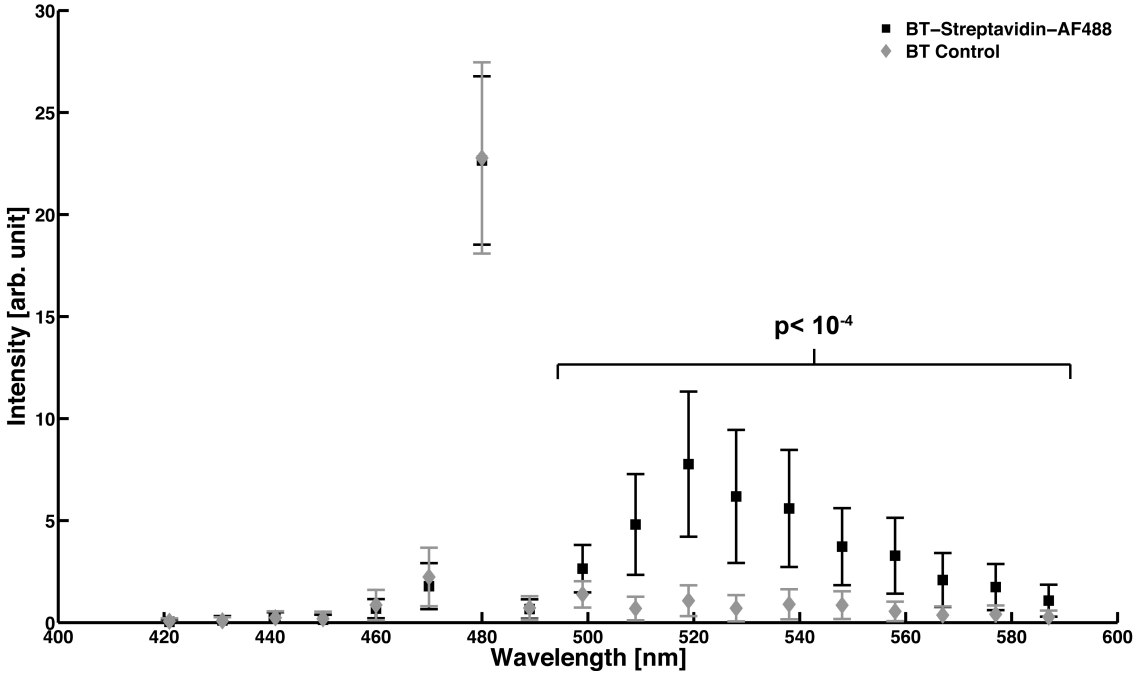

Figure 5.10: **Multistep streptavidin conjugation is verified using 2P imaging**. Imaging-based method of assessing proper BT functionalization by visualization of fluorescent streptavidin bound to biotin-BT. The masks in Fig. 5.9A', B' were used to obtain the average intensity for each wavelength increment within the spectral band (421 nm to 587 nm). This value for average intensity for a given SHG nanoprobe cluster was then normalized to its respective area in pixels. Average normalized intensity and standard deviation (error bars) from 53 BT (gray diamonds) and 465 BT-streptavidin-AF488 (black squares) SHG nanoprobe clusters at each wavelength increment was plotted using Matlab. In each case, SHG signal occurs within the 480 nm wavelength bin for both non-functionalized and functionalized BT. However, unlike the spectra for bare BT, which is negligible other than the SHG peak, signal from the BT-streptavidin-AF488 spectrum has SHG signal that co-localizes with the characteristic spectra of AF488. A pairwise T-test with unequal sample size and unequal variance confirms that the BT and BT-streptavidin-AF488 have different spectra for the wavelength range from 489 nm to 587 nm ($\sim$ 10 nm increments) with high confidence (p-value $< 10^{-4}$). Thus, this is a reasonable imaging-based method to judge proper surface functionalization of the BT surface.

under a mercury lamp when using an appropriate filter cube (e.g., Zeiss filter set 43 Cy 3, Article No: 000000 1114 101). Additionally, Bodipy TR Methyl Ester or Bodipy FL C5 ceramide dyes can be incubated with a dechorionated zebrafish embryo prior to imaging to label the cell interior or cell membranes, respectively. Alternative methods that can also provide cellular context to PEG-BT localization include ubiquitous or tissue-specific fluorescent protein expression by means of either simultaneous nucleic acid (e.g., DNA encoding a fluorescent protein of interest) injection with the PEG-BT at the zygote stage or by using a fluorescent transgenic zebrafish line (such as the PhOTO lines from Chapter 3 [57]).

By the late blastula period into early gastrulation, a number of SHG nanoprobes are scattered within the blastodisc, the pile of cells sitting atop the yolk cell that will eventually form the body of the zebrafish (Fig. 5.11A, Video A.4.1). In this case, 10 000 MW Dextran-AF546 was co-injected with PEG-BT at the zygote stage at a concentration of $\sim$ 0.02 mg/ml to give contrast to the cells sitting atop the yolk. On a separate occasion, PEG-BT was injected into zebrafish zygote stage embryos once again, this time without the addition of Dextran-AF546 (Fig. 5.11B, Video A.4.2). Fig. 5.11B depicts a zoomed in single optical section of one of the embryos at the blastula stage after a 1 hr incubation in 100 μM Bodipy TR, showing the clear intracellular localization of the SHG nanoprobes. A second PEG-BT injected embryo was allowed to develop into the early segmentation period before staining with 100 μM Bodipy FL C5 ceramide for 1 hr to visualize SHG nanoprobes inside membrane boundaries within the developing somites and notochord (Fig. 5.11C, Video A.4.3). Even after $\sim$ 12 hr of development, the SHG nanoprobes are still localized and visible inside of cells of the embryo: the nanoparticles have not been ejected but are retained within the confines of the cell, which is an important requirement for applications involving *in vivo* cell tracking using these probes. SHG nanoprobes can be seen throughout the zebrafish embryo even $\sim$ 24 hr after injection at the zygote stage (Fig. 5.12). Importantly, this 24 hpf embryo does

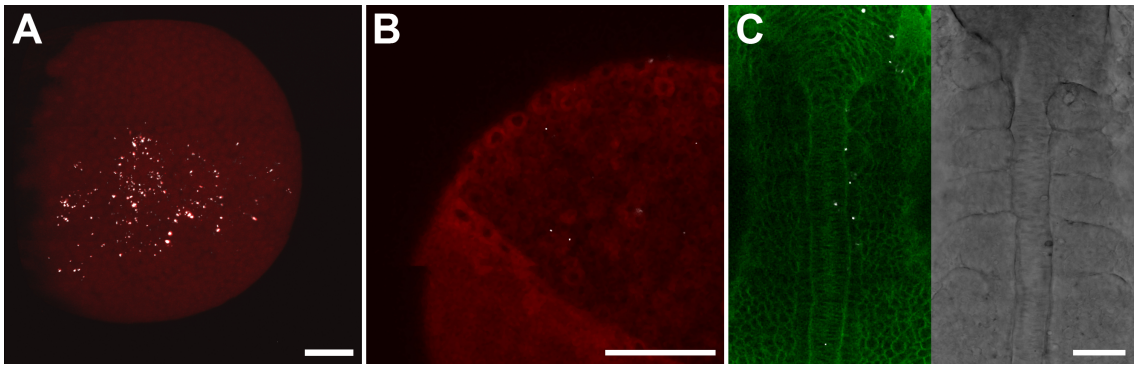

Figure 5.11: **PEG-BT localizes and persists within cells of the developing zebrafish embryo after zygote stage microinjection**. In each of the following, 2.3 nl of PEG-BT solution was injected into zygote stage zebrafish embryos, and the embryos were kept in a 28°C incubator before they were prepared for imaging some number of hours after injection. (A) By the sphere stage of development, scattered PEG-BT (white) can be seen within a great number of cells in the blastodisc in this surface reconstruction projection ($\sim$ 88 μm in depth) of a slightly tilted (animal pole is more towards the right of the embryo) animal pole mounted zebrafish embryo using a Zeiss LD C-Apochromat 40x/1.1 W Korr UV-VIS-IR M27 objective. In this case, 10,000 MW Dextran-AF546 was co-injected with the PEG-BT at the zygote stage to act as an injection control: properly injected embryo cells fluoresce when illuminated with a laser around the peak excitation of the AF546 dye (red channel in the surface reconstruction). (B) In a single optical slice image of a laterally mounted sphere stage zebrafish embryo (animal pole is toward the top right, $\sim$ 40 μm into the embryo in depth), PEG-BT (white) can be seen within 6 Bodipy TR methyl-ester-labeled cells (red). Note that Bodipy TR methyl-ester was incubated with dechorionated embryos at a concentration of 100 μM for 1 hr before washing three times in egg water followed by imaging. (C) Staining with 100 μM Bodipy FL C5 ceramide for 1 hr followed by 3 washes in egg water during the early segmentation period allows visualization of cell membrane boundaries within the embryo to better appreciate the intracellular localization of the PEG-BT. Here, the zebrafish was imaged at the 5 somite stage ($\sim$ 12 hr post fertilization) in a dorsal orientation (anterior toward the top), which can be best appreciated in the bright field channel (right image). In the left image, PEG-BT (white) can be seen within the Bodipy-labeled membrane boundaries (green) of 9 cells in various tissue compartments (notochord, somites, and neural territories of the developing brain) within a single optical slice $\sim$ 72 μm deep within the embryo with respect to the dorsal surface. Images in panels B and C were taken using a Zeiss LD LCI Plan-Apochromat 25x/0.8 Imm Korr DIC objective. (D) Scale bars: 100 μm in (A, B) and 50 μm in (C)

not have conflicting spectral signal (e.g., iridophores) at this stage, but later stage embryos would need to be imaged using a spectral scan to rule out small regions of broad-band pigment signal.

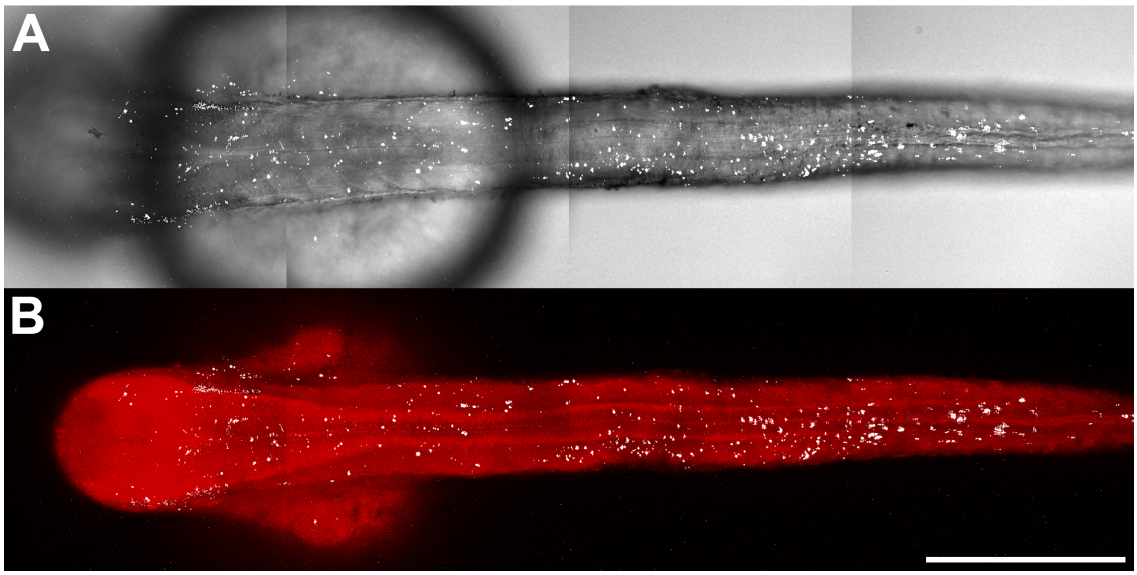

Figure 5.12: **PEG-BT localization throughout the body of a 24 hpf embryo**. In this panel, a PEG-BT injected zebrafish was transferred from egg water to egg water containing 1x PTU at $\sim$ 16 hr post fertilization to limit pigment formation. Before imaging, the embryo was anesthetized with 0.015% Tricaine methanesulfonate and dorsally mounted (anterior to the left, bright field in top image) using forceps in 1% agarose with 0.015% tricaine methanesulfonate and 1x PTU. PEG-BT (white, top and bottom images) persists within cells throughout the body of the zebrafish even after 24 hr of development, as can be seen in this $\sim$ 48 μm MIP (starting $\sim$ 50 μm in depth from the dorsal surface) of a 100 μM Bodipy TR methyl-ester stained zebrafish embryo (red, bottom image). A Zeiss Plan-Apochromat 20x/0.8 M27 was used in this panel. Scale bar: 300 μm

To demonstrate *in vivo* time-lapse imaging of the SHG nanoprobes within living zebrafish embryos, fluorescent protein and SHG nanoprobe imaging was employed in tandem (Fig. 5.13, Video A.4.4). At the zygote stage, simultaneous injections of 20 ng/μl plasmid memb-Dendra2 DNA with 80 ng/μl Tol2 transposase mRNA were performed to label the embryo in a mosaic manner as previously described (Chapter 2 [61]) along with PEG-BT. Fig. 5.13 shows snapshots from an $\sim$ 48 min time-lapse during late stage gastrulation, where single SHG nanoprobe clusters can be seen within at least three memb-Dendra2-labeled epiblasts as the cells migrate across the surface of the embryo. Importantly, the two labels work well together — mosaic memb-Dendra2 fluorescence allows vi-

sualization of membrane dynamics and morphology while SHG from the SHG nanoprobes enables interrogation of intracellular dynamics and cytosolic fluidity. Additionally, several non-fluorescent cells are presumably labeled with SHG nanoprobes and can be seen during the time-lapse, since these SHG nanoprobes move across the surface of the embryo at rates similar to the other labeled cells in the image. Perhaps most importantly, these SHG nanoprobes are high-contrast labels that will not overlap in space when labeling even adjacent cells (unlike ubiquitous cytosolic fluorescence, for example), so they will be especially useful for tracking co-labeled cells in time in three dimensions as the embryo develops, as well. Even at illumination wavelengths below the tissue damage threshold ($\sim$ 10 mW for cell culture [212]), SHG nanoprobes can be seen in time with high contrast without the worry of bleaching or blinking.

5.2.6 Immunohistochemical staining using secondary Ab-conjugated BT nanoprobes in fixed zebrafish embryos

In an effort to make the Ab-BT appropriate for a variety of immunohistochemical applications, we initially chose a secondary antibody (Invitrogen) as an ideal candidate for surface functionalization. Thus, any properly chosen primary antibody (i.e., derived from a compatible host for the secondary antibody) could be used to probe the tissue sample, followed by incubation with the secondary Ab-BT to achieve high-contrast labeling. Initially, we chose to probe the GFP protein in GFP-labeled endothelial cells from *Tg(flk1:EGFP)* transgenic zebrafish [213]. This way, we could simultaneously view the fluorescence from the GFP-labeled cells along with the SHG from Ab-BT to see whether the immunohistochemical labeling was specific or not. So, Ab-BT functionalization was tested in fixed vibratome sections of $\sim$ 1.5 dpf embryos (Fig. 5.14). Interestingly, there was some co-localized SHG and GFP signal (Fig. 5.14, arrows) a few tens of microns into the tissue. However, penetration into the tissue was limited after 1.5 hr incubation, which resulted in incomplete

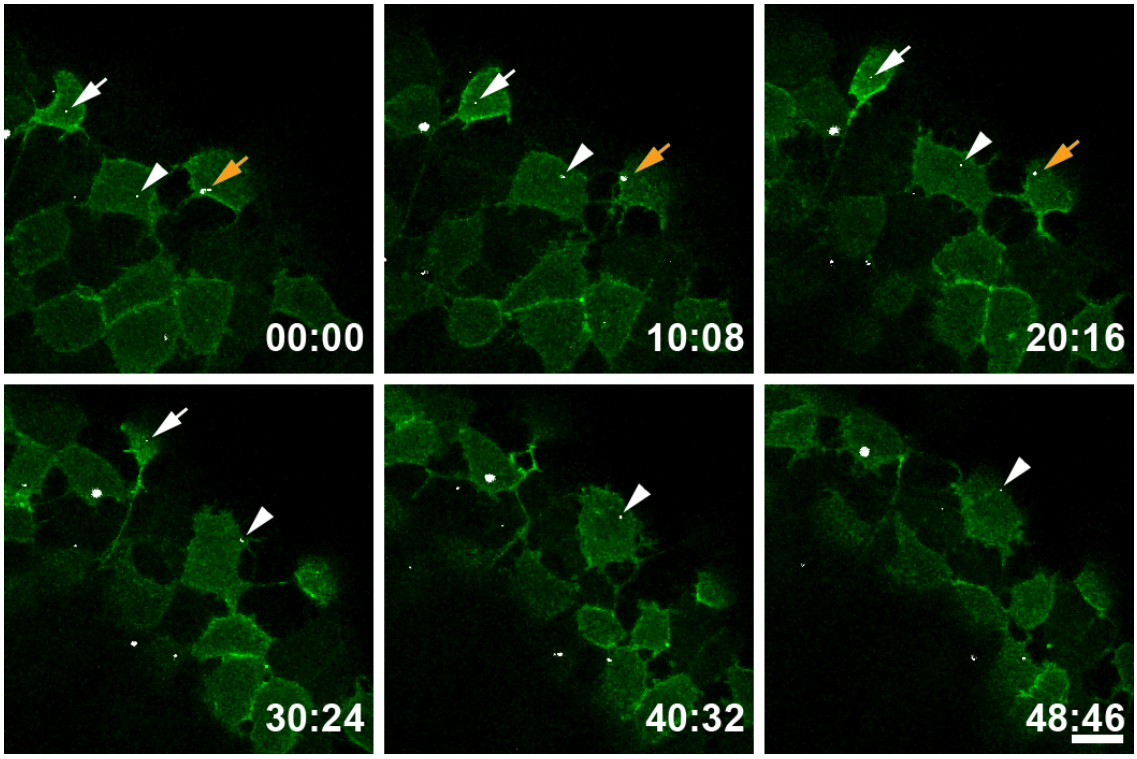

Figure 5.13: **Monitoring subcellularly localized PEG-BT *in vivo* at the gastrula stage**. The following are images from a time-lapse movie of a mid-gastrula period zebrafish embryo mounted in an animal pole orientation using a Zeiss C-Apochromat 40x/1.20 W Korr M27 objective (see Video A.4.4). First, 20 ng/μl plasmid membrane-targeted photoconvertible fluorescent protein *mDendra2* DNA and 80 ng/μl *Tol2* transposase mRNA were injected along with PEG-BT nanoprobes at the zygote stage. This DNA/mRNA injection enables the embryo to be labeled in a mosaic manner — that is, only a subset of the total cells in the embryo will have a proper insertion of the plasmid DNA into the genome by the expressed transposase protein, enabling expression of the membrane-targeted mDendra2 protein. Three images $\sim$ 2.5 μm apart in the z-direction were taken of the embryo for each time-point with no delay between frames, and approximately 38 sec were needed to capture each time point. The resulting image stacks were maximum intensity projected in the z-direction. PEG-BT (white) nanoprobes can be seen in several memb-Dendra2-labeled (green) as well as unlabeled cells. One diffraction limited SHG nanoprobe can be seen within one memb-Dendra2-labeled cell throughout the time-lapse during epiboly migration (arrowhead), while other cells containing single SHG nanoprobe clusters move out of the plane of view over time (white and orange arrows). Note that the varying sizes of the nanoprobes within the video presumably stem from anomalous subdiffusion and molecular crowding within cell compartments (e.g., endocytic compartments). Time-stamps: min:sec. Scale bar: 20 μm

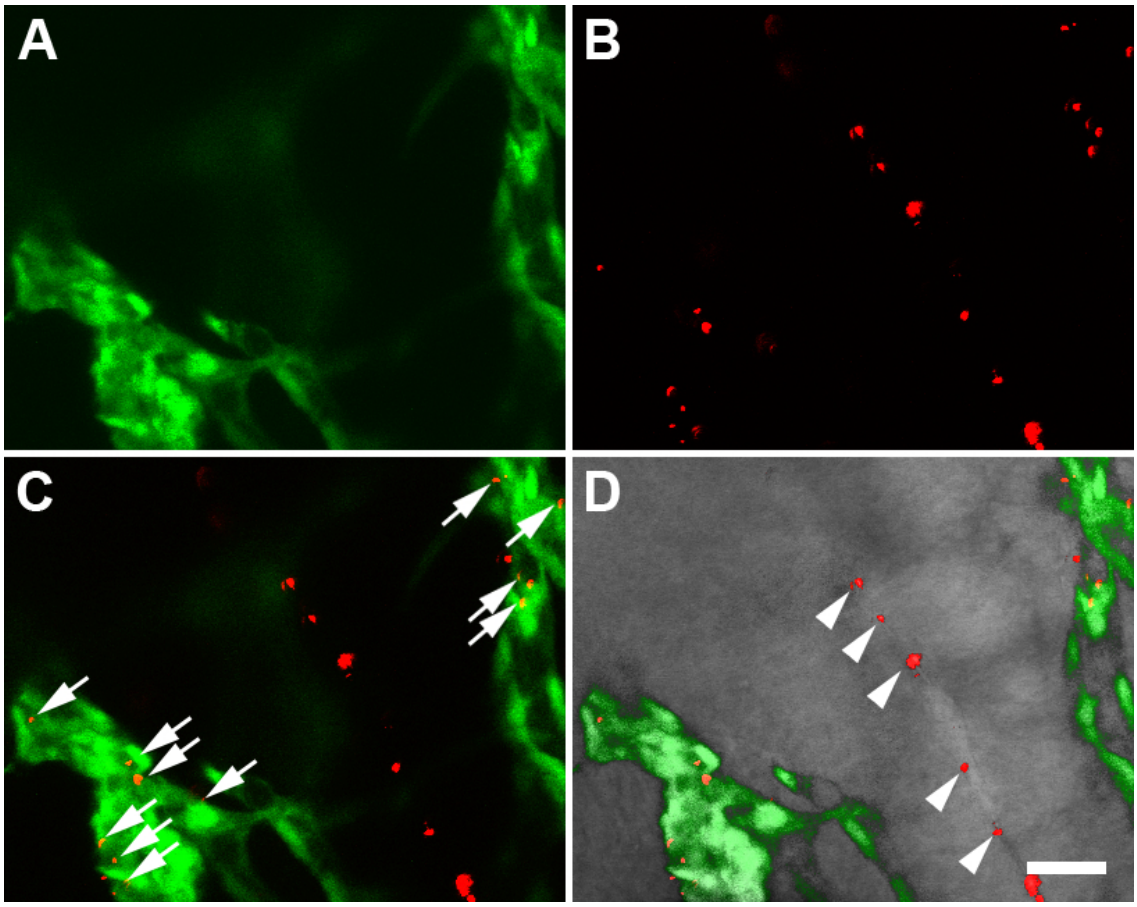

Figure 5.14: **Co-localized GFP and Ab-BT signals in tissue sections show incomplete staining of Ab-BT**. 36 hpf *Tg(flk1:EGFP)* [213] zebrafish were fixed in 4% paraformaldehyde (PFA) for 1 hr at RT and were washed three times, followed by vibratome (Vibratome Series 1000, The Vibratome Co.) sectioning ($\sim$ 200 μm thickness) after embedding in 4% agarose (Invitrogen). Primary rabbit anti-GFP antibody (1:500 dilution) was incubated with the sections for 1.5 hr at RT, followed by washing and subsequent (goat anti-rabbit-AF568, Invitrogen) secondary Ab-BT incubation (1:4 dilution) for 1.5 hr at RT. Note that the incubation solution was 1x PBS + 0.1% Triton X-100 + 0.5% BSA. (A) GFP fluorescence (green) and (B) SHG (red, contrast enhanced in Photoshop CS3) from the Ab-BT could be seen within the zebrafish tissue after fixation and immunostaining, in this example in the developing forebrain of the zebrafish (anterior mount). (C) Ab-BT and GFP had co-localized signal (arrows), though the labeling of the secondary Ab-conjugated BT was sparse after the 1.5 hr incubation. (D) A subset of large ($>$ 1 μm) Ab-BT clusters appeared stuck within folds of the developing forebrain (bright field in grayscale), even after washing (arrowheads). Scale bar: 25 μm

staining. Additionally, certain exceedingly large (> 1 μm) Ab-BT clusters could be trapped within folds of the tissue, such as in the developing forebrain of the zebrafish (Fig. 5.14D, arrowheads). Thus, initial attempts at Ab-BT staining were somewhat positive but inefficient, at best.

Subsequently, an alternative epitope was labeled (mouse anti-dystrophin MANDRA1, Developmental Studies Hybridoma Bank, as used in [72]), which we hoped would be an easier target for the Ab-BT: the protein target, dystrophin, is localized to cell periphery at the vertical myosepta within zebrafish somites (Fig. 5.15) and these protein levels are not nearly as excessive as with promoter-induced overexpression, as in the *Tg(flk1:EGFP)* transgenic line. After a 3 day incubation with the secondary Ab-BT, significant accumulation of the nanoparticles could be seen within the tissue (Fig. 5.16A, B), especially at the vertical myosepta (red outlines in Fig. 5.16A', B'). However, near the surface, there was significant nonspecific binding within the somites, presumably due to Ab-BT aggregates getting stuck within pores created by the PBSTB (see Fig. 5.16) incubation solution.

Zooming into the tissue and visualizing the AF488 signal conjugated to the secondary Abs atop the BT provides more context into why nonspecific binding may occur (Fig. 5.17). BT that has co-localized AF488 fluorescence and SHG predominately localizes at the vertical myosepta (see AF488 signal on SHG nanoprobes in Fig. 5.17A), while BT without appreciable AF488 signal can be seen in other portions of the muscle compartment and the yolk (toward the left side of the image in Fig. 5.17). This separation between specific and non-specific labeling can be more clearly appreciated in Fig. 5.18A, where SHG nanoprobes along the vertical myosepta are labeled in red and the nonspecific binding BT is labeled in gray. Interestingly, a rough calculation of this particular image shows that approximately half of the BT seems to localize at the three visible myosepta, while the remaining half accumulates nonspecifically, especially within the yolk (towards the left side of the image). It is important to mention that yolk accumulation is somewhat expected, because of the the high lipid content in this tissue compartment.

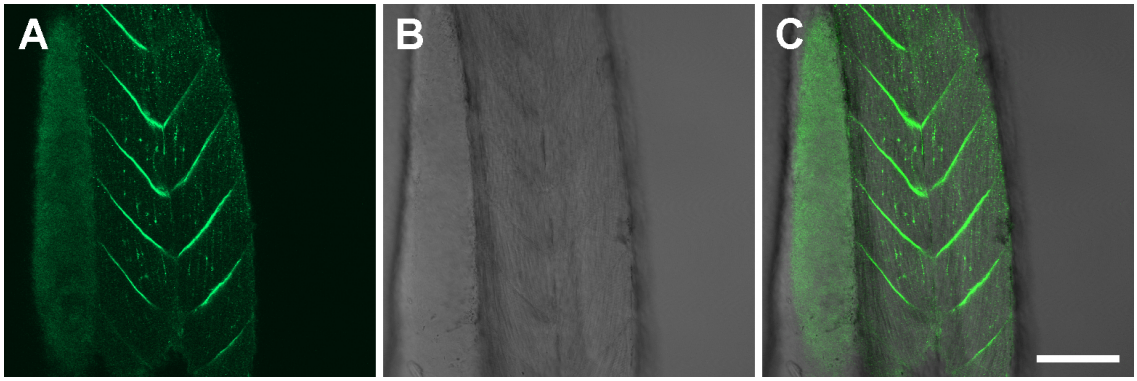

Figure 5.15: **Dystrophin localizes primarily to vertical myosepta within zebrafish muscle compartments**. This is a whole-mount staining of an $\sim$ 2.5 dpf WT zebrafish embryo treated with 1x PTU (lateral image, anterior down, ventral left). After 4% PFA fixation and subsequent washing in 1x PBS, whole embryos were blocked overnight at 4°C in 1x PBS (without Ca^{2+}/Mg^{2+}) + 0.5% Triton X-100 + 1% DMSO + 1% BSA (referred to as PBSTB). The primary antibody (mouse anti-dystrophin MANDRA1, Developmental Studies Hybridoma Bank) was added at a 1:500 dilution for 1.5 hr at RT, followed by subsequent washes. The secondary Ab (goat anti-mouse-AF488, Invitrogen) was added to embryos in PBSTB for 1.5 hr at RT (1:250 dilution) before washing and imaging. (A) Fluorescence (of a single optical section) from the AF488 (green) conjugated to the secondary Ab shows a chevron shaped pattern. (B) The bright field (grayscale) shows the characteristic chevron shape of the somites at this stage of development. (C) Merge of panels A and B showing that AF488 signal localizes to muscle boundaries at the vertical myosepta, as expected. Scale bar: 100 μm

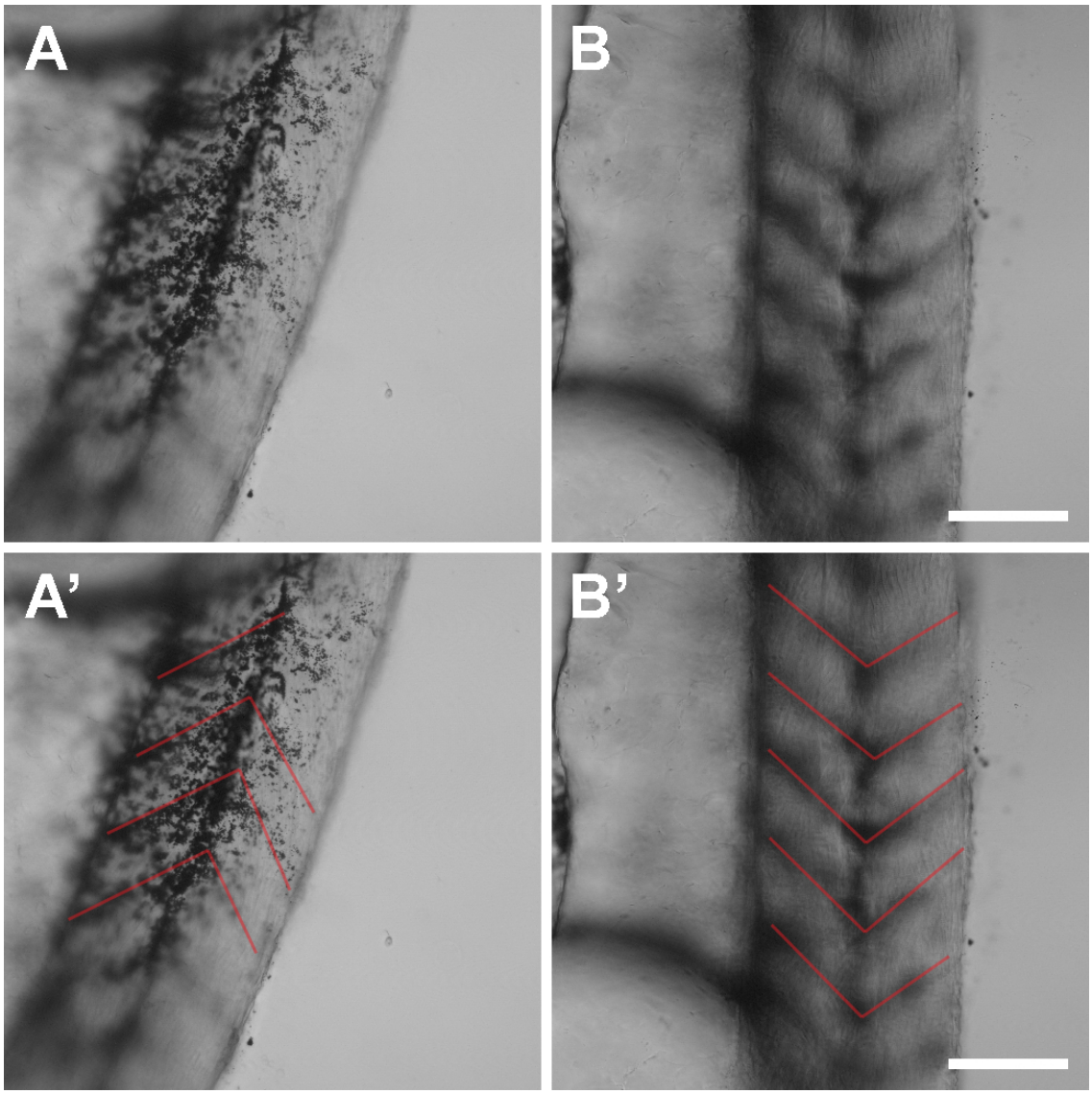

Figure 5.16: **Ab-BT accumulates at the vertical myosepta when probing for the dystrophin protein**. These bright field images show a single fixed, $\sim$ 2.5 dpf embryo in two different lateral orientations. Embryos from this trial were prepared as in Fig. 5.15, except that the secondary Ab-BT incubation was a 1:3 dilution in PBSTB and went for 3 days in an orbital shaker at 4°C before minimal washing. (A, A') In this orientation towards the surface of the tissue (anterior top, ventral left), significant accumulation of the nanoprobes can be seen within the vertical myosepta (red lines, A') as well as in other nonspecific areas of the somites (especially towards the center, at the horizontal myoseptum). (B, B') In this orientation deep in the tissue (anterior bottom, ventral left), significant accumulation can be seen predominantly in the vertical myosepta (red lines, B'). Scale bar: 100 μm

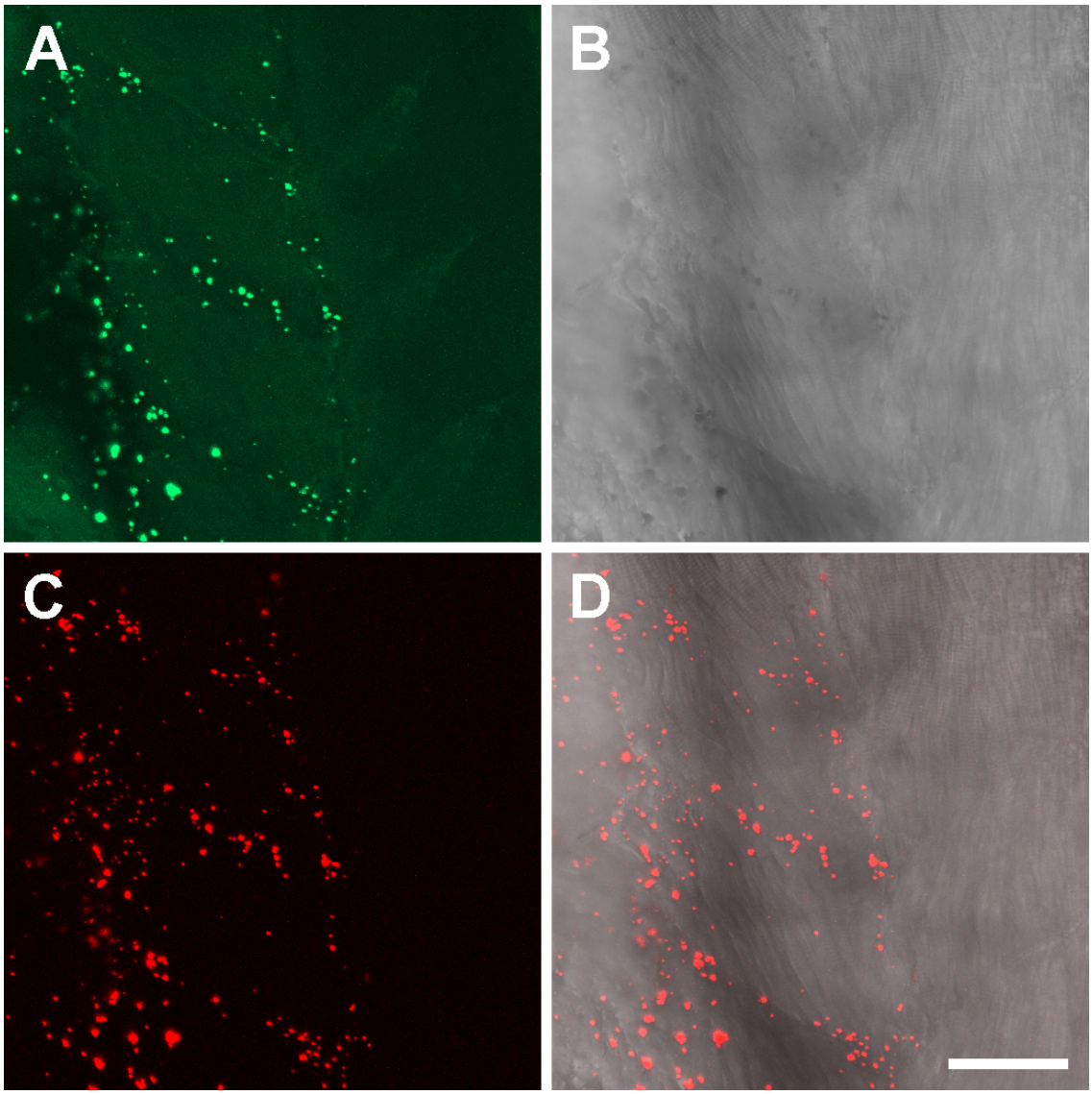

Figure 5.17: **Higher magnification visualization of a whole-mount stained zebrafish using Ab-BT**. This is an MIP image (consisting of $\sim$ 17.6 μm in depth) of a different $\sim$ 2.5 dpf embryo than in Fig. 5.16 but prepared in the same manner (anterior down, ventral left). This is a zoomed in image (effective 40x: zoom of 2 using a 20x 0.8NA air objective, Zeiss) showing the accumulation of Ab-BT within fixed zebrafish tissue. (A) AF488 signal from the Ab-BT (green) shows significant accumulation of properly functionalized Ab-BT at the vertical myosepta. (B) The bright field (grayscale), showing the vertical myosepta more clearly. (C) SHG (red, contrast enhance in Adobe Photoshop CS3) from the Ab-BT showing SHG nanoprobes both inside and outside of the expected localization region at the vertical myosepta. Taking data from panels A and C into account, visible nonspecific accumulation could be due to the fact that some BT may not have significant Ab coverage after functionalization. (D) Merge of panels B and C. Scale bar: 50 μm

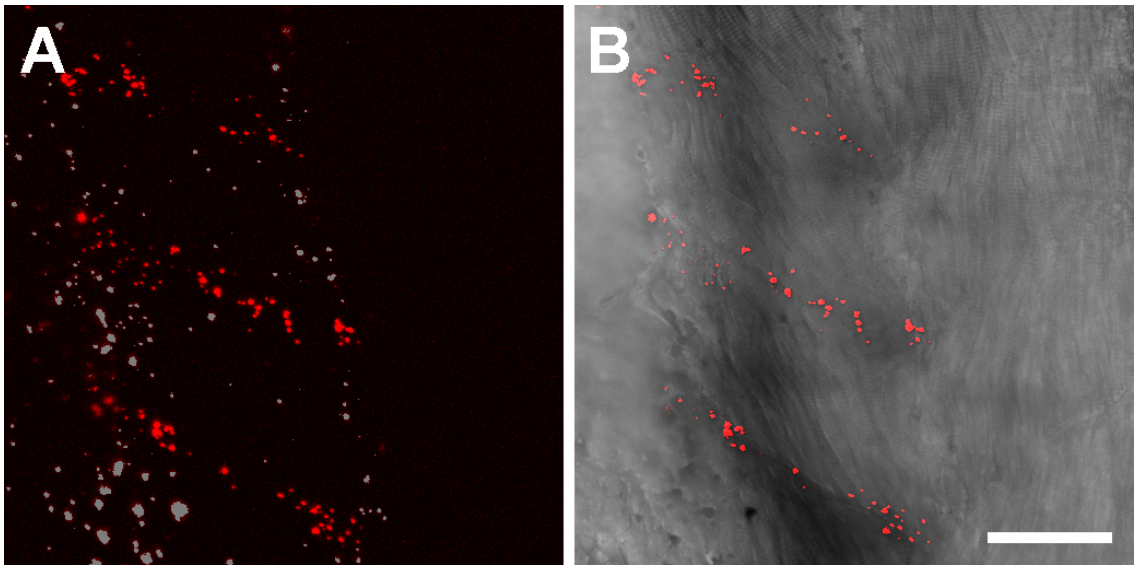

Figure 5.18: **Ab-BT accumulates mainly in the vertical myosepta and the yolk**. This figure is a more processed version of the zoomed image seen in Fig. 5.17. (A) SHG from Ab-BT within the vertical myosepta (red) was isolated from signal from those that were nonspecifically bound (gray). Most of the nonspecific binding seen in these images occurs within the yolk (towards the left side of the image), where nonspecific binding is often significant and difficult to block with BSA. This rough segmentation was done by eye with the magic wand tool in Adobe Photoshop CS3. (B) Red-labeled Ab-BT from panel A was isolated from the rest of the SHG signal in the tissue and superimposed on the grayscale bright field image from Fig. 5.17B to appreciate co-localization at the three visible vertical myosepta. Scale bar: 50 μm

5.2.7 Targeting live mouse bone marrow cells with Ab-BT

Following the fixed Ab-BT tests, we attempted to target live primary cells in suspension. This particular protocol was performed in collaboration with Gregor Adams and Sapna Shah at the University of Southern California. To accomplish this, whole bone marrow was isolated from two freshly killed mice by flushing the marrow from the humerus and tibia bones from each mouse with media (using a syringe). Then, the cells were affinity purified for the cKit (CD117) marker, which has been shown to target hematopoietic stem and progenitor cell populations [214], by running cells incubated with anti-CD117-conjugated magnetic beads through a column. Cells were then split into two equal volumes and were incubated with either BT-OH solution in 1x Hank's balanced salt solution (HBSS, Invitrogen) or Ab-BT (monoclonal IgG, FITC rat anti-mouse Ly-6A/E, BD Biosciences) solution in 1x HBSS for 15 min on ice; flicking of the tube every 3 minutes kept the particles and cells in suspension during the incubation. After incubation, cells were separated from unbound SHG nanoprobes by centrifugation. Briefly, cells in medium ($\sim$ 4 mL of HBSS) were carefully layered over lymphocyte separation medium ($\sim$ 4 mL, Cellgro by Mediatech, Inc.) and were centrifuged at 400 *g* for 5 min. After centrifugation, excess BT pellets at the bottom of the tube, while cells remain at the media interface. Cells were carefully pipetted and resuspended in 4% formalin followed by imaging the same day in 8-well coverslip chambers [4].

We expected that the Ab-BT should be able to target approximately 10% of the cKit enriched population (personal correspondence with Gregor Adams based on his experience with FACS sorting of cells using this marker). To test this, we imaged 11 independent regions for each sample (BT-OH and Ab-BT). In each of the 11 regions for each sample, cells associated with BT were counted along with the total number of cells in the region to determine an average fraction of BT-

[4]Note that the cell isolation and incubation protocol described here was performed by Sapna Shah in the laboratory of Gregor Adams at the University of Southern California. I was present during each of the steps and assisted in the incubation steps. I performed all of the subsequent imaging and analysis.

bound cells. A picture of zoomed portions of individual regions for BT-OH and Ab-BT can be seen in Fig. 5.19 and 5.20. After counting over 10^4 total cells, we determined that Ab-BT binds more effectively to the primary cells than the BT-OH control (Fig. 5.21).

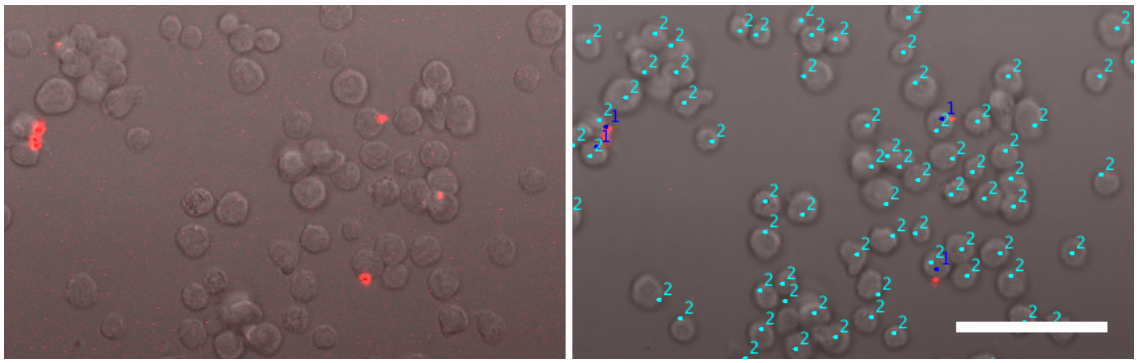

Figure 5.19: **Binding of BT-OH to isolated primary mouse marrow cells**. In this experiment, bone marrow cells were isolated from freshly killed mice and cKit enriched using an affinity column (for a full list of materials for this protocol, see Section B.1.4), resulting in a population of predominately mononuclear cells [214]. Half of these cells were incubated for 15 min on ice (to limit fluid phase endocytosis) with BT-OH before being spun down for 5 min at 400 *g* in lymphocyte separation medium (Cellgro by Mediatech, Inc.) to isolate the cells from unbound BT-OH. Cells were then immediately fixed in 4% formalin and imaged in an 8-well coverslip chamber (Nalge Nunc International) on a laser scanning microscope (Zeiss) with an LD C-Apochromat 40x/1.1 NA water objective (Zeiss). Left panel: this is a zoomed portion of a merged image of SHG from BT-OH (red) and a bright field image of the cKit enriched primary cells (grayscale). Right panel: cells were counted (labeled with "2") using the "cell counter" plugin for ImageJ. Additionally, some cells were associated with BT-OH (labeled with "1") even after centrifugation in lymphocyte separation medium. Scale bar: 50 μm

5.3 Discussion

SHG nanoprobes are a class of materials that have great potential in biological applications since they have a tight spectral signal that is compatible with fluorescence-based approaches, can be inherently nontoxic (as is the case with BT), and can be seen deep within highly refractive tissues [72, 1]. We have refined BT as a biologically relevant imaging probe by creating a robust functionalization protocol, where stable terminal amines serve as a platform for a variety of chemical additions to the nanoparticle surface. Additionally, we introduced a combined fluorescence/SHG imaging-based

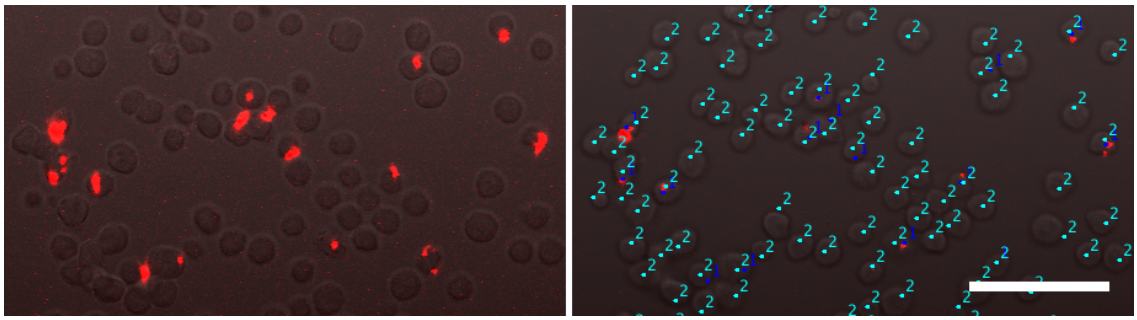

Figure 5.20: **Binding of Ab-BT to isolated primary mouse marrow cells**. An equal aliquot of cKit enriched cells from those prepared in Fig. 5.19 were incubated for 15 min on ice (to limit fluid phase endocytosis) with Ab-BT. In this case, the Ab was a primary Ab directed toward the Sca1 antigen on the surface of a subset of the cKit enriched cells (monoclonal IgG, FITC rat anti-mouse Ly-6A/E, BD Biosciences). This incubation was followed by a 5 min centrifugation step at 400 *g* in lymphocyte separation medium to isolate the cells from unbound Ab-BT. Cells were fixed in 4% formalin, placed in a well of an 8-well coverslip chamber (Nalge Nunc International) and imaged as in Fig. 5.19. Left panel: this is a zoomed portion of a merged image of SHG from Ab-BT (red) and a bright field image of the cKit enriched primary cells (grayscale). Right panel: cells were counted (labeled with "2") using the "cell counter" plugin for ImageJ. Additionally, Ab-BT was bound to a number of the cells on the plate (labeled with "1") even after centrifugation in lymphocyte separation medium. Scale bar: 50 μm

method to test future functionalization chemistries, in this case with BT-streptavidinAF488, where we showed that this click chemistry-mediated routine results in efficient and significant surface coating of BT. Furthermore, we introduced well-dispersed PEG-BT into live zebrafish embryos and observed their subcellular localization, taking advantage of the high-contrast, non-bleaching, and non-blinking spectral properties of SHG nanoprobes. Finally, we targeted Ab-BT to specific epitopes in both fixed and live samples, giving preliminary insight into how these nanoparticles could be used for specific labeling experiments in the future.

5.3.1 Current limitations

Our protocol is a general method for successfully preparing functionalized BT SHG nanoprobes, introducing the nanoprobes into the zebrafish, and imaging the nanoprobes within cells of the zebrafish early in development. This protocol should be easily modifiable for other functionalization

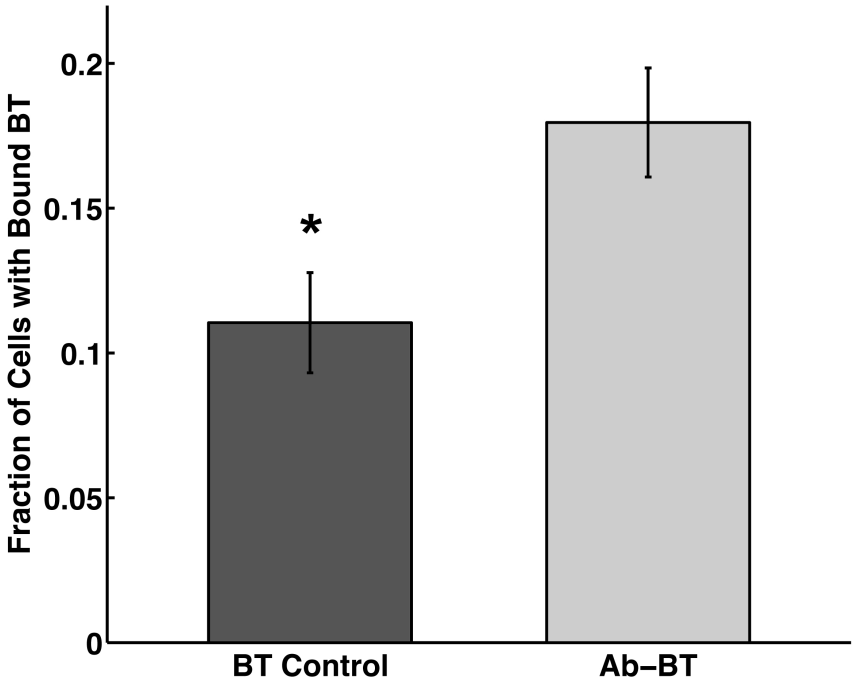

Figure 5.21: **Ab-BT shows increased binding to enriched cKit$^+$ primary cells**. cKit enriched cells isolated to generate Fig. 5.19 and 5.20 were imaged in the following manner: 11 (450 μm x 450 μm) independent regions from each well (BT-OH and Ab-BT) were imaged as z-Stacks such that the entire cell height was accounted for ($\sim$ 20 to 30 μm, 0.5 μm increments). In each region, each of the cells were counted (4008 cells from the BT-OH control well in total from 11 regions, 6756 cells from the Ab-BT well in total from 11 regions), and each of the cells associated with SHG nanoprobe clusters were counted using the "cell counter" plugin for ImageJ, as depicted in the right panels of Fig. 5.19 and 5.20. Regions where too many cells were clumped together — where it was difficult to count the total number of cells in the cluster with the bright field channel — were ignored from the quantification. The average fraction of cells associated with SHG nanoprobes was calculated for each of the regions, and a paired, two-tailed t-test with unequal variance was performed to test whether a statistically significant difference in BT association could be calculated for the two conditions. BT-OH had significantly reduced binding as compared to Ab-BT (p value: $\sim 2\text{x}10^{-8}$), suggesting that in addition to general nonspecific binding to cells in suspension, Ab-BT has specific binding to a subset of cKit enriched cells, as well.

chemistries (including targeted chemistries such as antibody linkages), and SHG nanoprobe introduction into — as well as imaging within — other organisms (e.g., chick, amphibian, mouse) should be an easy adaptation. The major limitation of the SHG nanoprobes in biological imaging applications is straightforward: in contrast to fluorescent proteins, these probes cannot be used in applications requiring genetically encoded labeling.

Importantly, since commercially available $\sim$ 50–200 nm BT nanocrystals are the starting material for functionalization in this protocol, applications for single molecule analysis or efficient cell or protein targeting are limited, even when extending the protocol to targeted labeling such as with the proposed biotin linking chemistry. In the future, production of monodisperse BT at sizes under 10 nm will be important for single cell labeling and to allow efficient renal clearing within the body [193], while sizes between 10 and 100 nm may enable more long-term targeting of the particles to desirable targets, such as cancer [24]. BT nanoparticle synthesis methods have already been described for the cubic crystal structure variety (i.e., centrosymmetric lattice) [215], but we will need tetragonal particles (i.e., noncentrosymmetric lattice) in order to use these materials as SHG-capable labels [72].

5.3.2 Streptavidin as a source for high-affinity protein tagging

Recently, there has been a significant focus in the literature to create robust chemical labeling strategies for cells in an effort to overcome limitations of traditional genetically encoded fluorescent approaches [216]. In this protocol, we generated BT-streptavidin nanoparticles using a multistep chemical synthesis approach. Although we did not explore the possibility, we could potentially use the BT-streptavidin to target cells labeled specifically with biotin. Site-specific biotin incorporation into recombinant proteins has been established using the bacterial biotin ligase enzyme BirA [217]. Subsequent research has been focused on specific cell targeting of biotinylated proteins on

the surface of live cells (e.g., with fluorescent dye conjugation [218] and quantum dots [219]). Thus, using similar protocols for cell-surface labeling with BirA [220], we can target BT-streptavidin to the surface, enabling high-fidelity tracking of proteins within the cell membrane.

5.3.3 Non-reactive surface coating and long-term cell and tissue labeling

Since PEG-BT has long-term stability within cells of the zebrafish and does not disrupt normal tissue development, these functionalized nanoparticles can be used for long-term cell tracking, even in highly scattering tissue environments. One unexplored avenue for the PEG-BT lies in its potential to be an alternative lineage tracing maker that could be used in combination with traditional techniques [59]. In a lineage tracing experiment, a bolus of dispersed PEG-BT could be used as an indelible marker within even relatively opaque (e.g., *Xenopus*, mouse, etc.) living organisms [221], since these probes should presumably redistribute within some number of subsequent daughter cells after successive divisions during development or regeneration. Redistribution of PEG-BT after mitosis is an interesting topic to explore on its own; these probes could be used to study cell subcompartment (e.g., endosomes, lysosomes) partitioning during division with high contrast and unparalleled time resolution, because of the advantageous photophysical properties of SHG (i.e., no blinking, bleaching) [1, 72].

Additionally, PEG functionalization of other nanomaterials decreases clearance through the kidneys and reduces bio-reactivity *in vivo* [195, 222]. Consequently, PEG-BT may be used in combination with nanoparticle drug delivery vectors for the study of cancer and cancer therapeutics. Co-introduction of a properly designed and synthesized PEG-BT — taking into consideration how the efficiency of nanoparticle retention and tumor association varies with size and surface chemistry [201, 24] — with a cancer therapeutic could enable *in vivo* imaging of tumor-associated SHG nanoprobes as the tumor is attacked by the therapeutic agent. Additionally, alternative multistep

functionalization protocols (such as a modified binary functionalization routine as demonstrated in [198]) could allow BT to be a visualizable delivery vector itself. However, one possible concern is that although certain PEG conjugated materials are FDA approved for use in biocompatible therapeutics [222], there is a possibility that PEG may still cause an immune response in some cases [223]. If PEG bioreactivity becomes an issue, alternative polymer coatings may need to be tested in the future (e.g., as in [196]).

5.3.4 Considerations for antibody targeting applications of Ab-BT

In this chapter, we observed several potential issues with the current Ab-BT. Clearly, Ab-BT is especially limited by the current size distribution and aggregation state of the nanoprobes. One major concern is that penetration into thick (e.g., whole-mount) tissues requires extensive incubation times (days, instead of hours with Ab immunohistochemistry) and seems to be characterized by significant background nonspecific binding, even at high concentrations of BSA. However, as tetragonal BT production protocols are refined in the future, these worries should be allayed. Additionally, we showed that perhaps as many as half of the BT that is functionalized with this Ab functionalization method does not achieve enough Ab coverage to ensure primarily specific labeling. Improvements or modifications to the Ab-BT synthesis protocol could enhance the surface coverage to limit nonspecific binding. A possible alternative functionalization could take advantage of our produced BT-streptavidin, which should allow selective attachment to biotinylated molecules for specific cell targeting — biotinylated antibodies, in this case — as was described previously for quantum dots [200]. In addition, the protocol can potentially be extended to directly conjugate antibodies to the surface through covalent means atop our amine-terminal platform [202].

In response to the issues raised above, we intentionally chose difficult cases for proof-of-principal analyses of the Ab-BT probes to gauge their potential in targeted biological imaging

applications. For example, efficient whole-mount staining can even be difficult with antibodies alone (note the incomplete staining in Section 4.2.2). Although a subset of crystals were not functionalized well enough to achieve complete immunostaining, small (< 1 μm) well-coated Ab-BT localized specifically within thick sections of *Tg(flk1:EGFP)* embryos and at the vertical myosepta within whole-mount dystrophin-targeted WT embryos. This suggests that more refined BT synthesis and adjustment of the Ab:BT ratio in the functionalization protocol may provide even better labeling in future experiments. However, Ab-BT labeling for immunohistochemical applications seems limited, practically speaking: SHG nanoprobe labeling is best suited for imaging deep within challenging tissue environments. Since most immunostaining can be performed in thin tissue sections, Ab-BT may provide a negligible improvement in contrast and might require excessive incubation times to achieve sufficient labeling of an epitope of interest.

Instead, Ab-BT will be highly suited for live cell imaging approaches. In this chapter, we showed that Ab-BT can be used to target specific cells within a heterogeneous population. Interestingly, approximately 10% of cells in the population were able to nonspecifically interact with the BT-OH control (referred to as promiscuous binding cells). If Ab-BT also bound to these promiscuous binding cells as effectively, we can estimate that the Ab-BT was able to specifically target $\sim 8\%$ of the total population, which is in close agreement with the aforementioned expectation that 10% of cKit$^+$ cells express Sca1 on their surface. This result is of great significance — certain specifically labeled Sca1-displaying cells (such as hematopoietic stem cells) can be reintroduced into the bloodstream of a mouse and can home to the bone marrow [214]. Importantly, nonspecific binding to promiscuous binding cells could be avoided altogether by isolating a pure population of cells by FACS sorting (as performed previously to isolate hematopoietic stem and progenitor cells [224]) before the Ab-BT incubation. Thus, Ab-BT-labeled cKit$^+$, Sca1$^+$ cells could potentially be tracked in the highly refractory bone marrow environment or within the vasculature of recipient mice in the

future.

5.3.5 Extension to other SHG nanoprobes

We expect that other SHG capable nanomaterials could be substituted for BT in this protocol, assuming they are capable of exposing hydroxyl groups on their surface. Candidate SHG nanoprobes with this property are inorganic oxides (such as those mentioned in Section 1.3.4 in Chapter 1) with high second-order susceptibility. For example, nanoparticles of one of these alternatives, ZnO, have been shown to have significant hydroxyl coverage when suspended in water [225, 226]. Achieving monodisperse synthesis and efficient functionalization of a variety of SHG nanoprobes will enable multi-SHG labeling (as demonstrated as a proof-of-principal in [72]) and will make these nanomaterials even more attractive as nontoxic, high-contrast labels in thick, optically challenging tissue environments.

Chapter 6

Conclusions and perspectives

Inspired by recent beautifully described accomplishments in the field of bioimaging ([5, 6, 17, 20, 66, 72, 87], to list a few), I strove to refine a toolbox of compatible elements that can be applied to a variety of biological imaging applications relevant to any stage in the life of an organism, with a focus on the zebrafish model system. Tools taking advantage of both Stokes (fluorescence) and anti-Stokes (SHG, in this case) imaging modalities were the main thrust of my endeavors. The fluorescent imaging approaches that I worked on in collaboration with researchers at the California Institute of Technology in the Biological Imaging Center provide unique advantages for lineage tracing analyses: (1) membrane-targeted mosaic analysis illuminates cell morphology that cannot be appreciated with ubiquitous imaging alone [61]; and (2) the PhOTO transgenic lines facilitate the global as well as targeted dissection of cell dynamics, division, and cell morphology throughout the lifetime of the zebrafish [57]. Additionally, I took advantage of both endogenous and exogenous SHG imaging modalities in collaboration with individuals at the California Institute of Technology, (1) asserting that certain endogenous structural SHG signatures are taken for granted in biological tissues (i.e., verniers, in Chapter 4), and (2) improving upon an exogenous imaging probe by establishing a robust functionalization protocol and biological imaging routine (i.e., SHG nanoprobes, in Chapter 5).

In the future, I would like to apply these tools hand-in-hand with one another in a variety of

biological applications. Because of its flanking *Tol2* [126] elements, the PhOTO vector [57] can be used for mosaic analysis in future experiments probing the function of intracellular bridges [61], for example. With the choice of a spectrally separable second label (one that does not conflict with Cerulean or mDendra2), different protein (e.g., actin using LifeAct; ibidi GMBH) or organelle components (e.g., mitochondria with MitoTracker; Invitrogen) could be visualized in parallel with the plasma membrane and nuclei, which could give insight into the contents that are allowed to pass through these intracellular bridges. Additionally, visualization of the after-effects of photoablation experiments — testing the possible function of the intracellular bridges in maintaining blastodisc support — would be assisted using a multi-compartment and targeted labeling approach.

Since anti-Stokes SHG can always be tuned away from any fluorescence emission band, endogenous SHG imaging can be used to provide additional subcellular context to transgenic PhOTO zebrafish. For example, endogenous contrast from myosin in the heart/skeletal musculature or from collagen in the fins could be imaged in parallel with global and photoconverted fluorescence in the PhOTO lines when studying adult epimorphic tissue regeneration. Importantly, endogenous SHG contains both structural and functional information; in a regenerating tissue containing substantial SHG-capable protein content, the reappearance of order in the tissue can give insight into the timeline of regeneration. Initially in the regeneration process, it might be predicted that collagen or myosin organization would be lacking and would refine over time. Thus, targeted, photoconverted cells can be monitored using fluorescence while the appearance of SHG can be monitored simultaneously, in appropriately selected tissue types (muscle, fin, etc.).

SHG nanoprobes could also be integrated into fluorescence/SHG-based imaging experiments *in vivo* in the PhOTO zebrafish. SHG nanoprobe-labeled cells can be tracked for any extended period of time, since they neither bleach nor blink. As a result, a well-thought-out, long-term experiment might use a custom algorithm to take SHG images of SHG nanoprobe-labeled cells at increments

with high time resolution while taking accompanying images of fluorescently labeled surrounding tissue (to provide cell and tissue context) much less often to limit bleaching of the fluorescence. Additionally, since endogenous SHG is mostly forward directed [1, 72], SHG nanoprobe signal should always be able to be distinguished from endogenous SHG — except possibly in highly scattering tissue environments with highly speckled SHG — so both exogenous and endogenous SHG imaging can be performed in parallel with fluorescence.

One possible avenue of study could link the SHG nanoprobes and PhOTO zebrafish tools together — tracking lateral line development using photoconversion and Ab-BT labels. The lateral line is a well-characterized set of simple, external organs involved in touch sensation in zebrafish, making it an ideal candidate system for study. With appropriate antibody creation and functionalization, specific cell surface receptor epitopes (e.g., chemokine receptors [227]) could be targeted by the Ab-BT nanoprobes, and the progression of cells as they migrate and specify along the anterior-posterior axis could be tracked with high fidelity, while the PhOTO lines could monitor global cell migration and morphology (potentially with similar selective plane illumination methods as in [164]). These studies could help researchers define how cells separate from an initially migrating cluster of cells to form the differentiated lateral line elements and could also be translated to experiments involving secondary lateral line development in the adult [168].

As I continue my career in research, I hope to add to this growing imaging toolbox in order to address this and other clinically relevant applications, and I look forward to seeing how these tools will benefit other researchers in the field.

Bibliography

[1] W. P. Dempsey, S. E. Fraser, and P. Pantazis. Shg nanoprobes: Advancing harmonic imaging in biology. *Bioessays*, 2012.

[2] D. C. Prasher, V. K. Eckenrode, W. W. Ward, F. G. Prendergast, and M. J. Cormier. Primary structure of the aequorea victoria green-fluorescent protein. *Gene*, 111(2):229–33, 1992.

[3] N. C. Shaner, P. A. Steinbach, and R. Y. Tsien. A guide to choosing fluorescent proteins. *Nat Methods*, 2(12):905–9, 2005.

[4] K. Woo and S. E. Fraser. Order and coherence in the fate map of the zebrafish nervous system. *Development*, 121(8):2595–609, 1995.

[5] P. J. Keller, A. D. Schmidt, J. Wittbrodt, and E. H. Stelzer. Reconstruction of zebrafish early embryonic development by scanned light sheet microscopy. *Science*, 322(5904):1065–9, 2008.

[6] W. Supatto, D. Debarre, B. Moulia, E. Brouzes, J. L. Martin, E. Farge, and E. Beaurepaire. In vivo modulation of morphogenetic movements in drosophila embryos with femtosecond laser pulses. *Proc Natl Acad Sci U S A*, 102(4):1047–52, 2005.

[7] A. McMahon, W. Supatto, S. E. Fraser, and A. Stathopoulos. Dynamic analyses of drosophila gastrulation provide insights into collective cell migration. *Science*, 322(5907):1546–50, 2008.

[8] J. Lippincott-Schwartz, N. Altan-Bonnet, and G. H. Patterson. Photobleaching and photoactivation: following protein dynamics in living cells. *Nat Cell Biol*, Suppl:S7–14, 2003.

[9] A. K. Hadjantonakis and V. E. Papaioannou. Dynamic in vivo imaging and cell tracking using a histone fluorescent protein fusion in mice. *BMC Biotechnol*, 4:33, 2004.

[10] B. N. Giepmans, S. R. Adams, M. H. Ellisman, and R. Y. Tsien. The fluorescent toolbox for assessing protein location and function. *Science*, 312(5771):217–24, 2006.

[11] R. Y. Tsien. The green fluorescent protein. *Annu Rev Biochem*, 67:509–44, 1998.

[12] R. H. Berg and R. N. Beachy. Fluorescent protein applications in plants. *Methods Cell Biol*, 85:153–77, 2008.

[13] P. Pantazis and M. Gonzalez-Gaitan. Localized multiphoton photoactivation of pagfp in drosophila wing imaginal discs. *J Biomed Opt*, 12(4):044004, 2007.

[14] N. Plachta, T. Bollenbach, S. Pease, S. E. Fraser, and P. Pantazis. Oct4 kinetics predict cell lineage patterning in the early mammalian embryo. *Nat Cell Biol*, 13(2):117–23, 2011.

[15] L. A. Trinh, T. Hochgreb, M. Graham, D. Wu, F. Ruf-Zamojski, C. S. Jayasena, A. Saxena, R. Hawk, A. Gonzalez-Serricchio, A. Dixson, E. Chow, C. Gonzales, H. Y. Leung, I. Solomon, M. Bronner-Fraser, S. G. Megason, and S. E. Fraser. A versatile gene trap to visualize and interrogate the function of the vertebrate proteome. *Genes Dev*, 25(21):2306–20, 2011.

[16] K. D. Poss. Advances in understanding tissue regenerative capacity and mechanisms in animals. *Nat Rev Genet*, 11(10):710–22, 2010.

[17] C. Jopling, E. Sleep, M. Raya, M. Marti, A. Raya, and J. C. Belmonte. Zebrafish heart regeneration occurs by cardiomyocyte dedifferentiation and proliferation. *Nature*, 464(7288):606–9, 2010.

[18] K. Kikuchi, V. Gupta, J. Wang, J. E. Holdway, A. A. Wills, Y. Fang, and K. D. Poss. tcf21+ epicardial cells adopt non-myocardial fates during zebrafish heart development and regeneration. *Development*, 138(14):2895–902, 2011.

[19] F. Knopf, C. Hammond, A. Chekuru, T. Kurth, S. Hans, C. W. Weber, G. Mahatma, S. Fisher, M. Brand, S. Schulte-Merker, and G. Weidinger. Bone regenerates via dedifferentiation of osteoblasts in the zebrafish fin. *Dev Cell*, 20(5):713–24, 2011.

[20] K. D. Poss, L. G. Wilson, and M. T. Keating. Heart regeneration in zebrafish. *Science*, 298(5601):2188–90, 2002.

[21] S. W. Perry, R. M. Burke, and E. B. Brown. Two-photon and second harmonic microscopy in clinical and translational cancer research. *Ann Biomed Eng*, 40(2):277–91, 2012.

[22] E. Brown, T. McKee, E. diTomaso, A. Pluen, B. Seed, Y. Boucher, and R. K. Jain. Dynamic imaging of collagen and its modulation in tumors in vivo using second-harmonic generation. *Nat Med*, 9(6):796–800, 2003.

[23] X. Chen, O. Nadiarynkh, S. Plotnikov, and P. J. Campagnola. Second harmonic generation microscopy for quantitative analysis of collagen fibrillar structure. *Nat Protoc*, 7(4):654–69, 2012.

[24] S. D. Perrault and W. C. Chan. In vivo assembly of nanoparticle components to improve targeted cancer imaging. *Proc Natl Acad Sci U S A*, 107(25):11194–9, 2010.

[25] Ximei Qian, Xiang-Hong Peng, Dominic O Ansari, Qiqin Yin-Goen, Georgia Z Chen, Dong M Shin, Lily Yang, Andrew N Young, May D Wang, and Shuming Nie. In vivo tumor targeting and spectroscopic detection with surface-enhanced raman nanoparticle tags. *Nat Biotechnol*, 26(1):83–90, 2008.

[26] N. G. Gurskaya, V. V. Verkhusha, A. S. Shcheglov, D. B. Staroverov, T. V. Chepurnykh, A. F. Fradkov, S. Lukyanov, and K. A. Lukyanov. Engineering of a monomeric green-to-red photoactivatable fluorescent protein induced by blue light. *Nat Biotechnol*, 24(4):461–5, 2006.

[27] D. O. Wang, S. M. Kim, Y. Zhao, H. Hwang, S. K. Miura, W. S. Sossin, and K. C. Martin. Synapse- and stimulus-specific local translation during long-term neuronal plasticity. *Science*, 324(5934):1536–40, 2009.

[28] D. A. Stark and P. M. Kulesa. An in vivo comparison of photoactivatable fluorescent proteins in an avian embryo model. *Dev Dyn*, 236(6):1583–94, 2007.

[29] M. Hofmann, C. Eggeling, S. Jakobs, and S. W. Hell. Breaking the diffraction barrier in fluorescence microscopy at low light intensities by using reversibly photoswitchable proteins. *Proc Natl Acad Sci U S A*, 102(49):17565–9, 2005.

[30] E. Betzig, G. H. Patterson, R. Sougrat, O. W. Lindwasser, S. Olenych, J. S. Bonifacino, M. W. Davidson, J. Lippincott-Schwartz, and H. F. Hess. Imaging intracellular fluorescent proteins at nanometer resolution. *Science*, 313(5793):1642–5, 2006.

[31] T. Sato, M. Takahoko, and H. Okamoto. Huc:kaede, a useful tool to label neural morphologies in networks in vivo. *Genesis*, 44(3):136–42, 2006.

[32] S. Nowotschin and A. K. Hadjantonakis. Use of kikgr a photoconvertible green-to-red fluorescent protein for cell labeling and lineage analysis in es cells and mouse embryos. *BMC Dev Biol*, 9:49, 2009.

[33] S. J. Caron, D. Prober, M. Choy, and A. F. Schier. In vivo birthdating by baptism reveals that trigeminal sensory neuron diversity depends on early neurogenesis. *Development*, 135(19):3259–69, 2008.

[34] H. Tsutsui, S. Karasawa, H. Shimizu, N. Nukina, and A. Miyawaki. Semi-rational engineering of a coral fluorescent protein into an efficient highlighter. *EMBO Rep*, 6(3):233–8, 2005.

[35] J. Wiedenmann, S. Ivanchenko, F. Oswald, F. Schmitt, C. Rocker, A. Salih, K. D. Spindler, and G. U. Nienhaus. Eosfp, a fluorescent marker protein with uv-inducible green-to-red fluorescence conversion. *Proc Natl Acad Sci U S A*, 101(45):15905–10, 2004.

[36] D. M. Chudakov, S. Lukyanov, and K. A. Lukyanov. Tracking intracellular protein movements using photoswitchable fluorescent proteins ps-cfp2 and dendra2. *Nat Protoc*, 2(8):2024–32, 2007.

[37] D. A. Zacharias, J. D. Violin, A. C. Newton, and R. Y. Tsien. Partitioning of lipid-modified monomeric gfps into membrane microdomains of live cells. *Science*, 296(5569):913–6, 2002.

[38] Y. A. Labas, N. G. Gurskaya, Y. G. Yanushevich, A. F. Fradkov, K. A. Lukyanov, S. A. Lukyanov, and M. V. Matz. Diversity and evolution of the green fluorescent protein family. *Proc Natl Acad Sci U S A*, 99(7):4256–61, 2002.

[39] V. Adam, K. Nienhaus, D. Bourgeois, and G. U. Nienhaus. Structural basis of enhanced photoconversion yield in green fluorescent protein-like protein dendra2. *Biochemistry*, 48(22):4905–15, 2009.

[40] B. H. Robertson, M. J. Grubman, G. N. Weddell, D. M. Moore, J. D. Welsh, T. Fischer, D. J. Dowbenko, D. G. Yansura, B. Small, and D. G. Kleid. Nucleotide and amino acid sequence coding for polypeptides of foot-and-mouth disease virus type a12. *J Virol*, 54(3):651–60, 1985.

[41] P. de Felipe, G. A. Luke, L. E. Hughes, D. Gani, C. Halpin, and M. D. Ryan. E unum pluribus: multiple proteins from a self-processing polyprotein. *Trends Biotechnol*, 24(2):68–75, 2006.

[42] M. L. Donnelly, L. E. Hughes, G. Luke, H. Mendoza, E. ten Dam, D. Gani, and M. D. Ryan. The 'cleavage' activities of foot-and-mouth disease virus 2a site-directed mutants and naturally occurring '2a-like' sequences. *J Gen Virol*, 82(Pt 5):1027–41, 2001.

[43] E. Provost, J. Rhee, and S. D. Leach. Viral 2a peptides allow expression of multiple proteins from a single orf in transgenic zebrafish embryos. *Genesis*, 45(10):625–9, 2007.

[44] G. Trichas, J. Begbie, and S. Srinivas. Use of the viral 2a peptide for bicistronic expression in transgenic mice. *BMC Biol*, 6:40, 2008.

[45] W. Tang, I. Ehrlich, S. B. Wolff, A. M. Michalski, S. Wolfl, M. T. Hasan, A. Luthi, and R. Sprengel. Faithful expression of multiple proteins via 2a-peptide self-processing: a versatile and reliable method for manipulating brain circuits. *J Neurosci*, 29(27):8621–9, 2009.

[46] A. L. Szymczak, C. J. Workman, Y. Wang, K. M. Vignali, S. Dilioglou, E. F. Vanin, and D. A. Vignali. Correction of multi-gene deficiency in vivo using a single 'self-cleaving' 2a peptide-based retroviral vector. *Nat Biotechnol*, 22(5):589–94, 2004.

[47] M. J. Osborn, A. Panoskaltsis-Mortari, R. T. McElmurry, S. K. Bell, D. A. Vignali, M. D. Ryan, A. C. Wilber, R. S. McIvor, J. Tolar, and B. R. Blazar. A picornaviral 2a-like sequence-based tricistronic vector allowing for high-level therapeutic gene expression coupled to a dual-reporter system. *Mol Ther*, 12(3):569–74, 2005.

[48] J. Fang, J. J. Qian, S. Yi, T. C. Harding, G. H. Tu, M. VanRoey, and K. Jooss. Stable antibody expression at therapeutic levels using the 2a peptide. *Nat Biotechnol*, 23(5):584–90, 2005.

[49] M. Li, Y. Wu, Y. Qiu, Z. Yao, S. Liu, Y. Liu, J. Shi, and D. Zheng. 2a peptide-based, lentivirus-mediated anti-death receptor 5 chimeric antibody expression prevents tumor growth in nude mice. *Mol Ther*, 20(1):46–53, 2012.

[50] S. B. Hedges. The origin and evolution of model organisms. *Nat Rev Genet*, 3(11):838–49, 2002.

[51] C. B. Kimmel, W. W. Ballard, S. R. Kimmel, B. Ullmann, and T. F. Schilling. Stages of embryonic development of the zebrafish. *Dev Dyn*, 203(3):253–310, 1995.

[52] G. J. Lieschke and P. D. Currie. Animal models of human disease: zebrafish swim into view. *Nat Rev Genet*, 8(5):353–67, 2007.

[53] G. W. Stuart, J. V. McMurray, and M. Westerfield. Replication, integration and stable germ-line transmission of foreign sequences injected into early zebrafish embryos. *Development*, 103(2):403–12, 1988.

[54] W. B. Amos and J. G. White. How the confocal laser scanning microscope entered biological research. *Biol Cell*, 95(6):335–42, 2003.

[55] J.B. (Ed.) Pawley. *Handbook of Biological Confocal Microscopy*. Springer Science, New York, 3rd edition, 2006.

[56] Barry R. Masters and Peter T. C. So. *Biomedical Nonlinear Optical Microscopy*. Oxford UP, New York, 2008.

[57] W. P. Dempsey, S. E. Fraser, and P. Pantazis. Photo zebrafish: A transgenic resource for in vivo lineage tracing during development and regeneration. *PLoS One*, 7(3):e32888, 2012.

[58] C. D. Stern, J. Charite, J. Deschamps, D. Duboule, A. J. Durston, M. Kmita, J. F. Nicolas, I. Palmeirim, J. C. Smith, and L. Wolpert. Head-tail patterning of the vertebrate embryo: one, two or many unresolved problems? *Int J Dev Biol*, 50(1):3–15, 2006.

[59] M. E. Buckingham and S. M. Meilhac. Tracing cells for tracking cell lineage and clonal behavior. *Dev Cell*, 21(3):394–409, 2011.

[60] K. Woo, J. Shih, and S. E. Fraser. Fate maps of the zebrafish embryo. *Curr Opin Genet Dev*, 5(4):439–43, 1995.

[61] L. Caneparo, P. Pantazis, W. Dempsey, and S. E. Fraser. Intercellular bridges in vertebrate gastrulation. *PLoS One*, 6(5):e20230, 2011.

[62] R. C. Tryon, C. W. Higdon, and S. L. Johnson. Lineage relationship of direct-developing melanocytes and melanocyte stem cells in the zebrafish. *PLoS One*, 6(6):e21010, 2011.

[63] C. Guo, W. Yang, and C. G. Lobe. A cre recombinase transgene with mosaic, widespread tamoxifen-inducible action. *Genesis*, 32(1):8–18, 2002.

[64] R. Ramachandran, A. Reifler, J. M. Parent, and D. Goldman. Conditional gene expression and lineage tracing of tuba1a expressing cells during zebrafish development and retina regeneration. *J Comp Neurol*, 518(20):4196–212, 2010.

[65] R. T. Collins, C. Linker, and J. Lewis. Maze: a tool for mosaic analysis of gene function in zebrafish. *Nat Methods*, 7(3):219–23, 2010.

[66] K. Kikuchi, J. E. Holdway, A. A. Werdich, R. M. Anderson, Y. Fang, G. F. Egnaczyk, T. Evans, C. A. Macrae, D. Y. Stainier, and K. D. Poss. Primary contribution to zebrafish heart regeneration by gata4(+) cardiomyocytes. *Nature*, 464(7288):601–5, 2010.

[67] Z. Bao, J. I. Murray, T. Boyle, S. L. Ooi, M. J. Sandel, and R. H. Waterston. Automated cell lineage tracing in caenorhabditis elegans. *Proc Natl Acad Sci U S A*, 103(8):2707–12, 2006.

[68] R. M. Warga and C. B. Kimmel. Cell movements during epiboly and gastrulation in zebrafish. *Development*, 108(4):569–80, 1990.

[69] N. Blum and G. Begemann. Retinoic acid signaling controls the formation, proliferation and survival of the blastema during adult zebrafish fin regeneration. *Development*, 139(1):107–16, 2012.

[70] E. Nacu and E. M. Tanaka. Limb regeneration: a new development? *Annu Rev Cell Dev Biol*, 27:409–40, 2011.

[71] M. Kragl, D. Knapp, E. Nacu, S. Khattak, M. Maden, H. H. Epperlein, and E. M. Tanaka. Cells keep a memory of their tissue origin during axolotl limb regeneration. *Nature*, 460(7251):60–5, 2009.

[72] P. Pantazis, J. Maloney, D. Wu, and S. E. Fraser. Second harmonic generating (shg) nanoprobes for in vivo imaging. *Proc Natl Acad Sci U S A*, 107(33):14535–40, 2010.

[73] R.W. Boyd. *Nonlinear Optics*. Academic Press, San Diego, 2nd edition, 2003.

[74] Richard Lee Sutherland, Daniel Garth McLean, and Sean Kirkpatrick. *Handbook of Nonlinear Optics*. Marcel Dekker, Inc., New York, 2nd edition, 2003.

[75] Y. R. Shen. Surface properties probed by second-harmonic and sum-frequency generation. *Nature*, 337(6207):519–525, 1989.

[76] P. A. Franken, A. E. Hill, C. W. Peters, and G. Weinreich. Generation of optical harmonics. *Physical Review Letters*, 7(4):118, 1961.

[77] T. H. Maiman. Stimulated optical radiation in ruby. *Nature*, 187(4736):493–494, 1960.

[78] L. Moreaux, O. Sandre, M. Blanchard-Desce, and J. Mertz. Membrane imaging by simultaneous second-harmonic generation and two-photon microscopy. *Opt Lett*, 25(5):320–2, 2000.

[79] J. Mertz and L. Moreaux. Second-harmonic generation by focused excitation of inhomogeneously distributed scatterers. *Optics Communications*, 196(1–6):325–330, 2001.

[80] M. E. Llewellyn, R. P. Barretto, S. L. Delp, and M. J. Schnitzer. Minimally invasive high-speed imaging of sarcomere contractile dynamics in mice and humans. *Nature*, 454(7205):784–8, 2008.

[81] K. R. Parameswaran, J. R. Kurz, R. V. Roussev, and M. M. Fejer. Observation of 99generation in a periodically poled lithium niobate waveguide. *Opt Lett*, 27(1):43–5, 2002.

[82] Victor Mizrahi and J. E. Sipe. Phenomenological treatment of surface second-harmonic generation. *J. Opt. Soc. Am. B*, 5(3):660–667, 1988.

[83] I. Freund, M. Deutsch, and A. Sprecher. Connective tissue polarity. optical second-harmonic microscopy, crossed-beam summation, and small-angle scattering in rat-tail tendon. *Biophys J*, 50(4):693–712, 1986.

[84] R. M. Williams, W. R. Zipfel, and W. W. Webb. Interpreting second-harmonic generation images of collagen i fibrils. *Biophys J*, 88(2):1377–86, 2005.

[85] P. J. Campagnola, A. C. Millard, M. Terasaki, P. E. Hoppe, C. J. Malone, and W. A. Mohler. Three-dimensional high-resolution second-harmonic generation imaging of endogenous structural proteins in biological tissues. *Biophys J*, 82(1 Pt 1):493–508, 2002.

[86] V. Nucciotti, C. Stringari, L. Sacconi, F. Vanzi, L. Fusi, M. Linari, G. Piazzesi, V. Lombardi, and F. S. Pavone. Probing myosin structural conformation in vivo by second-harmonic generation microscopy. *Proc Natl Acad Sci U S A*, 107(17):7763–8, 2010.

[87] N. Olivier, M. A. Luengo-Oroz, L. Duloquin, E. Faure, T. Savy, I. Veilleux, X. Solinas, D. Debarre, P. Bourgine, A. Santos, N. Peyrieras, and E. Beaurepaire. Cell lineage reconstruction of early zebrafish embryos using label-free nonlinear microscopy. *Science*, 329(5994):967–71, 2010.

[88] Jr. Brown, R. M., A. C. Millard, and P. J. Campagnola. Macromolecular structure of cellulose studied by second-harmonic generation imaging microscopy. *Opt Lett*, 28(22):2207–9, 2003.

[89] A. C. Millard, L. Jin, M. D. Wei, J. P. Wuskell, A. Lewis, and L. M. Loew. Sensitivity of second harmonic generation from styryl dyes to transmembrane potential. *Biophys J*, 86(2):1169–76, 2004.

[90] D. A. Dombeck, L. Sacconi, M. Blanchard-Desce, and W. W. Webb. Optical recording of fast neuronal membrane potential transients in acute mammalian brain slices by second-harmonic generation microscopy. *J Neurophysiol*, 94(5):3628–36, 2005.

[91] M. Nuriya, J. Jiang, B. Nemet, K. B. Eisenthal, and R. Yuste. Imaging membrane potential in dendritic spines. *Proc Natl Acad Sci U S A*, 103(3):786–90, 2006.

[92] L. Sacconi, D. A. Dombeck, and W. W. Webb. Overcoming photodamage in second-harmonic generation microscopy: real-time optical recording of neuronal action potentials. *Proc Natl Acad Sci U S A*, 103(9):3124–9, 2006.

[93] J. E. Reeve, H. A. Collins, K. De Mey, M. M. Kohl, K. J. Thorley, O. Paulsen, K. Clays, and H. L. Anderson. Amphiphilic porphyrins for second harmonic generation imaging. *J Am Chem Soc*, 131(8):2758–9, 2009.

[94] J. Jiang, K. B. Eisenthal, and R. Yuste. Second harmonic generation in neurons: electro-optic mechanism of membrane potential sensitivity. *Biophys J*, 93(5):L26–8, 2007.

[95] A Kachynski, A Kuzmin, M Nyk, I Roy, and P Prasad. Zinc oxide nanocrystals for non-resonant nonlinear optical microscopy in biology and medicine. *The journal of physical chemistry C, Nanomaterials and interfaces*, 112(29):10721–10724, 2008.

[96] T. R. Kuo, C. L. Wu, C. T. Hsu, W. Lo, S. J. Chiang, S. J. Lin, C. Y. Dong, and C. C. Chen. Chemical enhancer induced changes in the mechanisms of transdermal delivery of zinc oxide nanoparticles. *Biomaterials*, 30(16):3002–8, 2009.

[97] Chia-Lung Hsieh, Rachel Grange, Ye Pu, and Demetri Psaltis. Three-dimensional harmonic holographic microcopy using nanoparticles as probes for cell imaging. *Opt Express*, 17(4):2880–91, 2009.

[98] Jerome Extermann, Luigi Bonacina, Enrique Cuña, Christelle Kasparian, Yannick Mugnier, Thomas Feurer, and Jean-Pierre Wolf. Nanodoublers as deep imaging markers for multi-photon microscopy. *Opt. Express*, 17(17):15342–15349, 2009.

[99] Y Pu, M Centurion, and D Psaltis. Harmonic holography: a new holographic principle. *Applied Optics*, 47(4):103–110, 2008.

[100] Ernesto V. Rodriguez, Cid B. de Araújo, Antonio M. Brito-Silva, V. I. Ivanenko, and A. A. Lipovskii. Hyper-rayleigh scattering from batio3 and pbtio3 nanocrystals. *Chemical Physics Letters*, 467(4–6):335–338, 2009.

[101] Justin C. Johnson, Haoquan Yan, Richard D. Schaller, Poul B. Petersen, Peidong Yang, and Richard J. Saykally. Near-field imaging of nonlinear optical mixing in single zinc oxide nanowires. *Nano Lett*, 2(4):279–283, 2002.

[102] L Bonacina, Y Mugnier, F Courvoisier, R Le Dantec, J Extermann, Y Lambert, V Boutou, C Galez, and JP Wolf. Polar fe (io 3) 3 nanocrystals as local probes for nonlinear microscopy. *Applied Physics B: Lasers and Optics*, 87(3):399–403, 2007.

[103] L. Le Xuan, S. Brasselet, F. Treussart, J. F. Roch, F. Marquier, D. Chauvat, S. Perruchas, C. Tard, and T. Gacoin. Balanced homodyne detection of second-harmonic generation from isolated subwavelength emitters. *Applied Physics Letters*, 89(12):121118–3, 2006.

[104] N Sandeau, L Le Xuan, D Chauvat, C Zhou, J-F Roch, and S Brasselet. Defocused imaging of second harmonic generation from a single nanocrystal. *Opt Express*, 15(24):16051–60, 2007.

[105] Loc Le Xuan, Chunyuan Zhou, Abdallah Slablab, Dominique Chauvat, Cédric Tard, Sandrine Perruchas, Thierry Gacoin, Philippe Villeval, and Jean-François Roch. Photostable second-harmonic generation from a single ktiopo4 nanocrystal for nonlinear microscopy. *Small*, 4(9):1332–1336, 2008.

[106] P. Wnuk, L. L. Xuan, A. Slablab, C. Tard, S. Perruchas, T. Gacoin, J. F. Roch, D. Chauvat, and C. Radzewicz. Coherent nonlinear emission from a single ktp nanoparticle with broadband femtosecond pulses. *Opt Express*, 17(6):4652–8, 2009.

[107] ME Rodríguez, A Speghini, F Piccinelli, F Nodari, M Bettinelli, D Jaque, and J García Solé. Multicolour second harmonic generation by strontium barium niobate nanoparticles. *Journal of Physics D: Applied Physics*, 42(10):102003, 2009.

[108] Y. Nakayama, P. J. Pauzauskie, A. Radenovic, R. M. Onorato, R. J. Saykally, J. Liphardt, and P. Yang. Tunable nanowire nonlinear optical probe. *Nature*, 447(7148):1098–101, 2007.

[109] D. N. Nikogosyan. *Nonlinear optical crystals : a complete survey*. Springer Science, New York, 1st edition, 2005.

[110] Y. R. Chang, H. Y. Lee, K. Chen, C. C. Chang, D. S. Tsai, C. C. Fu, T. S. Lim, Y. K. Tzeng, C. Y. Fang, C. C. Han, H. C. Chang, and W. Fann. Mass production and dynamic imaging of fluorescent nanodiamonds. *Nat Nacommentchnol*, 3(5):284–8, 2008.

[111] Chi-Cheng Fu, Hsu-Yang Lee, Kowa Chen, Tsong-Shin Lim, Hsiao-Yun Wu, Po-Keng Lin, Pei-Kuen Wei, Pei-Hsi Tsao, Huan-Cheng Chang, and Wunshain Fann. Characterization and application of single fluorescent nanodiamonds as cellular biomarkers. *Proc Natl Acad Sci U S A*, 104(3):727–732, 2007.

[112] Shu-Jung Yu, Ming-Wei Kang, Huan-Cheng Chang, Kuan-Ming Chen, and Yueh-Chung Yu. Bright fluorescent nanodiamonds: no photobleaching and low cytotoxicity. *J Am Chem Soc*, 127:17604–17605, 2005.

[113] Yun Xing, Qaiser Chaudry, Christopher Shen, Koon Yin Kong, Haiyen E Zhau, Leland W Chung, John A Petros, Ruth M O'Regan, Maksym V Yezhelyev, Jonathan W Simons, May D Wang, and Shuming Nie. Bioconjugated quantum dots for multiplexed and quantitative immunohistochemistry. *Nature Protocols*, 2(5):1152–1165, 2007.

[114] X. Wang, X. Ren, K. Kahen, M. A. Hahn, M. Rajeswaran, S. Maccagnano-Zacher, J. Silcox, G. E. Cragg, A. L. Efros, and T. D. Krauss. Non-blinking semiconductor nanocrystals. *Nature*, 459(7247):686–9, 2009.

[115] Michael Kasha. Characterization of electronic transitions in complex molecules. *Discussions of the Faraday Society*, 9:14–19, 1950.

[116] Y. Pavlyukh and W. Hübner. Nonlinear mie scattering from spherical particles. *Physical Review B*, 70(24):245434, 2004.

[117] J. Shan, J. I. Dadap, I. Stiopkin, G. A. Reider, and T. F. Heinz. Experimental study of optical second-harmonic scattering from spherical nanoparticles. *Physical Review A (Atomic, Molecular, and Optical Physics)*, 73(2):023819–4, 2006.

[118] L. Solnica-Krezel. Conserved patterns of cell movements during vertebrate gastrulation. *Curr Biol*, 15(6):R213–28, 2005.

[119] M. L. Concha and R. J. Adams. Oriented cell divisions and cellular morphogenesis in the zebrafish gastrula and neurula: a time-lapse analysis. *Development*, 125(6):983–94, 1998.

[120] B. Kilian, H. Mansukoski, F. C. Barbosa, F. Ulrich, M. Tada, and C. P. Heisenberg. The role of ppt/wnt5 in regulating cell shape and movement during zebrafish gastrulation. *Mech Dev*, 120(4):467–76, 2003.

[121] J. P. Trinkaus. Surface activity and locomotion of fundulus deep cells during blastula and gastrula stages. *Dev Biol*, 30(1):69–103, 1973.

[122] F. Ulrich, M. L. Concha, P. J. Heid, E. Voss, S. Witzel, H. Roehl, M. Tada, S. W. Wilson, R. J. Adams, D. R. Soll, and C. P. Heisenberg. Slb/wnt11 controls hypoblast cell migration and morphogenesis at the onset of zebrafish gastrulation. *Development*, 130(22):5375–84, 2003.

[123] D. S. Sepich, C. Calmelet, M. Kiskowski, and L. Solnica-Krezel. Initiation of convergence and extension movements of lateral mesoderm during zebrafish gastrulation. *Dev Dyn*, 234(2):279–92, 2005.

[124] R. K. Ho and C. B. Kimmel. Commitment of cell fate in the early zebrafish embryo. *Science*, 261(5117):109–11, 1993.

[125] S. Higashijima, H. Okamoto, N. Ueno, Y. Hotta, and G. Eguchi. High-frequency generation of transgenic zebrafish which reliably express gfp in whole muscles or the whole body by using promoters of zebrafish origin. *Dev Biol*, 192(2):289–99, 1997.

[126] K. Kawakami and A. Shima. Identification of the tol2 transposase of the medaka fish oryzias latipes that catalyzes excision of a nonautonomous tol2 element in zebrafish danio rerio. *Gene*, 240(1):239–44, 1999.

[127] K. M. Kwan, E. Fujimoto, C. Grabher, B. D. Mangum, M. E. Hardy, D. S. Campbell, J. M. Parant, H. J. Yost, J. P. Kanki, and C. B. Chien. The tol2kit: a multisite gateway-based construction kit for tol2 transposon transgenesis constructs. *Dev Dyn*, 236(11):3088–99, 2007.

[128] C. W. Liaw, R. Zamoyska, and J. R. Parnes. Structure, sequence, and polymorphism of the lyt-2 t cell differentiation antigen gene. *J Immunol*, 137(3):1037–43, 1986.

[129] N. C. Shaner, R. E. Campbell, P. A. Steinbach, B. N. Giepmans, A. E. Palmer, and R. Y. Tsien. Improved monomeric red, orange and yellow fluorescent proteins derived from discosoma sp. red fluorescent protein. *Nat Biotechnol*, 22(12):1567–72, 2004.

[130] F. A. Ramirez-Weber and T. B. Kornberg. Cytonemes: cellular processes that project to the principal signaling center in drosophila imaginal discs. *Cell*, 97(5):599–607, 1999.

[131] J. Miller, S. E. Fraser, and D. McClay. Dynamics of thin filopodia during sea urchin gastrulation. *Development*, 121(8):2501–11, 1995.

[132] Y. Gong, C. Mo, and S. E. Fraser. Planar cell polarity signalling controls cell division orientation during zebrafish gastrulation. *Nature*, 430(7000):689–93, 2004.

[133] E. Quesada-Hernandez, L. Caneparo, S. Schneider, S. Winkler, M. Liebling, S. E. Fraser, and C. P. Heisenberg. Stereotypical cell division orientation controls neural rod midline formation in zebrafish. *Curr Biol*, 20(21):1966–72, 2010.

[134] C. Houart, M. Westerfield, and S. W. Wilson. A small population of anterior cells patterns the forebrain during zebrafish gastrulation. *Nature*, 391(6669):788–92, 1998.

[135] M. A. Rizzo, G. H. Springer, B. Granada, and D. W. Piston. An improved cyan fluorescent protein variant useful for fret. *Nat Biotechnol*, 22(4):445–9, 2004.

[136] F. A. Ramirez-Weber and T. B. Kornberg. Signaling reaches to new dimensions in drosophila imaginal discs. *Cell*, 103(2):189–92, 2000.

[137] E. S. Schulze and S. H. Blose. Passage of molecules across the intercellular bridge between post-mitotic daughter cells. *Exp Cell Res*, 151(2):367–73, 1984.

[138] M. P. Greenbaum, W. Yan, M. H. Wu, Y. N. Lin, J. E. Agno, M. Sharma, R. E. Braun, A. Rajkovic, and M. M. Matzuk. Tex14 is essential for intercellular bridges and fertility in male mice. *Proc Natl Acad Sci U S A*, 103(13):4982–7, 2006.

[139] Tetsuo Kageyama. The occurrence of elongated intercellular bridges in deep cells of oryzias embryos during blastula and gastrula stages. *Journal of Experimental Zoology*, 248(3):306–314, 1988.

[140] R. C. Buck, P. T. Ohara, and W. H. Daniels. Intercellular bridges of chick blastoderm studied by scanning and transmission electron microscopy. *Experientia*, 32(4):505–7, 1976.

[141] G. C. Schoenwolf and I. S. Alvarez. Role of cell rearrangement in axial morphogenesis. *Curr Top Dev Biol*, 27:129–73, 1992.

[142] J. C. Tapia, N. Kasthuri, K. J. Hayworth, R. Schalek, J. W. Lichtman, S. J. Smith, and J. Buchanan. High-contrast en bloc staining of neuronal tissue for field emission scanning electron microscopy. *Nat Protoc*, 7(2):193–206, 2012.

[143] J. Livet, T. A. Weissman, H. Kang, R. W. Draft, J. Lu, R. A. Bennis, J. R. Sanes, and J. W. Lichtman. Transgenic strategies for combinatorial expression of fluorescent proteins in the nervous system. *Nature*, 450(7166):56–62, 2007.

[144] Y. A. Pan, J. Livet, J. R. Sanes, J. W. Lichtman, and A. F. Schier. Multicolor brainbow imaging in zebrafish. *Cold Spring Harb Protoc*, 2011(1):pdb prot5546, 2011.

[145] T. A. Weissman, J. R. Sanes, J. W. Lichtman, and J. Livet. Generating and imaging multicolor brainbow mice. *Cold Spring Harb Protoc*, 2011(7):763–9, 2011.

[146] H. Hama, H. Kurokawa, H. Kawano, R. Ando, T. Shimogori, H. Noda, K. Fukami, A. Sakaue-Sawano, and A. Miyawaki. Scale: a chemical approach for fluorescence imaging and reconstruction of transparent mouse brain. *Nat Neurosci*, 14(11):1481–8, 2011.

[147] A. Rustom, R. Saffrich, I. Markovic, P. Walther, and H. H. Gerdes. Nanotubular highways for intercellular organelle transport. *Science*, 303(5660):1007–10, 2004.

[148] S. Sowinski, C. Jolly, O. Berninghausen, M. A. Purbhoo, A. Chauveau, K. Kohler, S. Oddos, P. Eissmann, F. M. Brodsky, C. Hopkins, B. Onfelt, Q. Sattentau, and D. M. Davis. Membrane

nanotubes physically connect t cells over long distances presenting a novel route for hiv-1 transmission. *Nat Cell Biol*, 10(2):211–9, 2008.

[149] S. C. Watkins and R. D. Salter. Functional connectivity between immune cells mediated by tunneling nanotubules. *Immunity*, 23(3):309–18, 2005.

[150] Jr. Cartwright, J. and J. M. Arnold. Intercellular bridges in the embryo of the atlantic squid, loligo pealei. i. cytoplasmic continuity and tissue differentiation. *J Embryol Exp Morphol*, 57:3–24, 1980.

[151] Monte Westerfield. *The zebrafish book. A guide for the laboratory use of zebrafish (Danio rerio)*. Univ. of Oregon Press, Eugene, 4th edition, 2000.

[152] A. Urasaki, G. Morvan, and K. Kawakami. Functional dissection of the tol2 transposable element identified the minimal cis-sequence and a highly repetitive sequence in the subterminal region essential for transposition. *Genetics*, 174(2):639–49, 2006.

[153] D. Balciunas, K. J. Wangensteen, A. Wilber, J. Bell, A. Geurts, S. Sivasubbu, X. Wang, P. B. Hackett, D. A. Largaespada, R. S. McIvor, and S. C. Ekker. Harnessing a high cargo-capacity transposon for genetic applications in vertebrates. *PLoS Genet*, 2(11):e169, 2006.

[154] T. Kanda, K. F. Sullivan, and G. M. Wahl. Histone-gfp fusion protein enables sensitive analysis of chromosome dynamics in living mammalian cells. *Curr Biol*, 8(7):377–85, 1998.

[155] K. Kawakami. Tol2: a versatile gene transfer vector in vertebrates. *Genome Biol*, 8 Suppl 1:S7, 2007.

[156] M. A. D'Angelo, M. Raices, S. H. Panowski, and M. W. Hetzer. Age-dependent deterioration of nuclear pore complexes causes a loss of nuclear integrity in postmitotic cells. *Cell*, 136(2):284–95, 2009.

[157] A. Nechiporuk and M. T. Keating. A proliferation gradient between proximal and msxb-expressing distal blastema directs zebrafish fin regeneration. *Development*, 129(11):2607–17, 2002.

[158] K. D. Poss, J. Shen, and M. T. Keating. Induction of lef1 during zebrafish fin regeneration. *Dev Dyn*, 219(2):282–6, 2000.

[159] R. Sood, M. A. English, C. L. Belele, H. Jin, K. Bishop, R. Haskins, M. C. McKinney, J. Chahal, B. M. Weinstein, Z. Wen, and P. P. Liu. Development of multilineage adult hematopoiesis in the zebrafish with a runx1 truncation mutation. *Blood*, 115(14):2806–9, 2010.

[160] C. Campos, M. Kamiya, S. Banala, K. Johnsson, and M. Gonzalez-Gaitan. Labelling cell structures and tracking cell lineage in zebrafish using snap-tag. *Dev Dyn*, 240(4):820–7, 2011.

[161] S. Preibisch, S. Saalfeld, J. Schindelin, and P. Tomancak. Software for bead-based registration of selective plane illumination microscopy data. *Nat Methods*, 7(6):418–9, 2010.

[162] M. Chertkov, L. Kroc, F. Krzakala, M. Vergassola, and L. Zdeborova. Inference in particle tracking experiments by passing messages between images. *Proc Natl Acad Sci U S A*, 107(17):7663–8, 2010.

[163] B. Rizzi and A. Sarti. Region-based pdes for cells counting and segmentation in 3d+time images of vertebrate early embryogenesis. *Int J Biomed Imaging*, 2009:968986, 2009.

[164] J. Swoger, M. Muzzopappa, H. Lopez-Schier, and J. Sharpe. 4d retrospective lineage tracing using spim for zebrafish organogenesis studies. *J Biophotonics*, 4(1–2):122–34, 2010.

[165] T. A. Planchon, L. Gao, D. E. Milkie, M. W. Davidson, J. A. Galbraith, C. G. Galbraith, and E. Betzig. Rapid three-dimensional isotropic imaging of living cells using bessel beam plane illumination. *Nat Methods*, 8(5):417–23, 2011.

[166] T. V. Truong, W. Supatto, D. S. Koos, J. M. Choi, and S. E. Fraser. Deep and fast live imaging with two-photon scanned light-sheet microscopy. *Nat Methods*, 8(9):757–60, 2011.

[167] E. E. LeClair and J. Topczewski. Development and regeneration of the zebrafish maxillary barbel: a novel study system for vertebrate tissue growth and repair. *PLoS One*, 5(1):e8737, 2010.

[168] E. Y. Ma and D. W. Raible. Signaling pathways regulating zebrafish lateral line development. *Curr Biol*, 19(9):R381–6, 2009.

[169] Y. Zhao, Q. Bao, A. Renner, P. Camaj, M. Eichhorn, I. Ischenko, M. Angele, A. Kleespies, K. W. Jauch, and C. Bruns. Cancer stem cells and angiogenesis. *Int J Dev Biol*, 55(4–5):477–82, 2011.

[170] R. Thummel, S. Bai, Jr. Sarras, M. P., P. Song, J. McDermott, J. Brewer, M. Perry, X. Zhang, D. R. Hyde, and A. R. Godwin. Inhibition of zebrafish fin regeneration using in vivo electroporation of morpholinos against fgfr1 and msxb. *Dev Dyn*, 235(2):336–46, 2006.

[171] S. V. Plotnikov, A. M. Kenny, S. J. Walsh, B. Zubrowski, C. Joseph, V. L. Scranton, G. A. Kuchel, D. Dauser, M. Xu, C. C. Pilbeam, D. J. Adams, R. P. Dougherty, P. J. Campagnola, and W. A. Mohler. Measurement of muscle disease by quantitative second-harmonic generation imaging. *J Biomed Opt*, 13(4):044018, 2008.

[172] O. Friedrich, M. Both, C. Weber, S. Schurmann, M. D. Teichmann, F. von Wegner, R. H. Fink, M. Vogel, J. S. Chamberlain, and C. Garbe. Microarchitecture is severely compromised but

motor protein function is preserved in dystrophic mdx skeletal muscle. *Biophys J*, 98(4):606–16, 2010.

[173] D. I. Bassett, R. J. Bryson-Richardson, D. F. Daggett, P. Gautier, D. G. Keenan, and P. D. Currie. Dystrophin is required for the formation of stable muscle attachments in the zebrafish embryo. *Development*, 130(23):5851–60, 2003.

[174] J. J. Dowling, A. P. Vreede, S. E. Low, E. M. Gibbs, J. Y. Kuwada, C. G. Bonnemann, and E. L. Feldman. Loss of myotubularin function results in t-tubule disorganization in zebrafish and human myotubular myopathy. *PLoS Genet*, 5(2):e1000372, 2009.

[175] M. J. Parsons, I. Campos, E. M. Hirst, and D. L. Stemple. Removal of dystroglycan causes severe muscular dystrophy in zebrafish embryos. *Development*, 129(14):3505–12, 2002.

[176] C. J. Snow, M. Goody, M. W. Kelly, E. C. Oster, R. Jones, A. Khalil, and C. A. Henry. Time-lapse analysis and mathematical characterization elucidate novel mechanisms underlying muscle morphogenesis. *PLoS Genet*, 4(10):e1000219, 2008.

[177] A. F. Huxley and R. E. Taylor. Local activation of striated muscle fibres. *J Physiol*, 144(3):426–41, 1958.

[178] M. Both, M. Vogel, O. Friedrich, F. von Wegner, T. Kunsting, R. H. Fink, and D. Uttenweiler. Second harmonic imaging of intrinsic signals in muscle fibers in situ. *J Biomed Opt*, 9(5):882–92, 2004.

[179] G. Recher, D. Rouede, P. Richard, A. Simon, J. J. Bellanger, and F. Tiaho. Three distinct sarcomeric patterns of skeletal muscle revealed by shg and tpef microscopy. *Opt Express*, 17(22):19763–77, 2009.

[180] G. Recher, D. Rouede, E. Schaub, and F. Tiaho. Skeletal muscle sarcomeric shg patterns photo-conversion by femtosecond infrared laser. *Biomed Opt Express*, 2(2):374–84, 2011.

[181] Nathan O. Hodas. *Nonlinear dynamics of nanoscale systems*. PhD thesis, California Institute of Technology, 2011.

[182] O. Griesbeck, G. S. Baird, R. E. Campbell, D. A. Zacharias, and R. Y. Tsien. Reducing the environmental sensitivity of yellow fluorescent protein. mechanism and applications. *J Biol Chem*, 276(31):29188–94, 2001.

[183] Bruce Alberts, Alexander Johnson, Julian Lewis, Martin Raff, Keith Roberts, and Peter Walter. *Molecular Biology of the Cell*. Garland Science, New York, 4th edition, 2002.

[184] H. L. Stickney, M. J. Barresi, and S. H. Devoto. Somite development in zebrafish. *Dev Dyn*, 219(3):287–303, 2000.

[185] D. Rouede, G. Recher, J. J. Bellanger, M. T. Lavault, E. Schaub, and F. Tiaho. Modeling of supramolecular centrosymmetry effect on sarcomeric shg intensity pattern of skeletal muscles. *Biophys J*, 101(2):494–503, 2011.

[186] B J Tromberg, N Shah, R Lanning, A Cerussi, J Espinoza, T Pham, L Svaasand, and J Butler. Non-invasive in vivo characterization of breast tumors using photon migration spectroscopy. *Neoplasia*, 2(1–2):26–40, 2000.

[187] Shih-Hsuan Chia, Tzu-Ming Liu, Anatoly A. Ivanov, Andrey B. Fedotov, Aleksey M. Zheltikov, Ming-Rung Tsai, Ming-Che Chan, Che-Hang Yu, and Chi-Kuang Sun. A sub-100fs self-starting cr:forsterite laser generating 1.4w output power. *Opt Express*, 18(23):24085–24091, 2010.

[188] P. J. Campagnola and L. M. Loew. Second-harmonic imaging microscopy for visualizing biomolecular arrays in cells, tissues and organisms. *Nat Biotechnol*, 21(11):1356–60, 2003.

[189] R. C. Miller, D. A. Kleinman, and A. Savage. Quantitative studies of optical harmonic generation in cds, batio3, and kh2po4 type crystals. *Physical Review Letters*, 11(4):146–149, 1963.

[190] D. Staedler, T. Magouroux, R. Hadji, C. Joulaud, J. Extermann, S. Schwung, S. Passemard, C. Kasparian, G. Clarke, M. Gerrmann, R. L. Dantec, Y. Mugnier, D. Rytz, D. Ciepielewski, C. Galez, S. Gerber-Lemaire, L. Juillerat-Jeanneret, L. Bonacina, and J. P. Wolf. Harmonic nanocrystals for biolabeling: A survey of optical properties and biocompatibility. *ACS Nano*, 2012.

[191] T. Schroeder. Long-term single-cell imaging of mammalian stem cells. *Nat Methods*, 8(4 Suppl):S30–5, 2011.

[192] B. Ballou, L. A. Ernst, S. Andreko, T. Harper, J. A. Fitzpatrick, A. S. Waggoner, and M. P. Bruchez. Sentinel lymph node imaging using quantum dots in mouse tumor models. *Bioconjug Chem*, 18(2):389–96, 2007.

[193] H. S. Choi, W. Liu, P. Misra, E. Tanaka, J. P. Zimmer, B. Itty Ipe, M. G. Bawendi, and J. V. Frangioni. Renal clearance of quantum dots. *Nat Biotechnol*, 25(10):1165–70, 2007.

[194] H. S. Choi, W. Liu, F. Liu, K. Nasr, P. Misra, M. G. Bawendi, and J. V. Frangioni. Design considerations for tumour-targeted nanoparticles. *Nat Nacommentchnol*, 5(1):42–7, 2010.

[195] M. E. Davis, Z. G. Chen, and D. M. Shin. Nanoparticle therapeutics: an emerging treatment modality for cancer. *Nat Rev Drug Discov*, 7(9):771–82, 2008.

[196] P. Kim, S. C Jones, P. J Hotchkiss, J. N Haddock, B. Kippelen, S. R Marder, and J. W Perry. Phosphonic acid-modified barium titanate polymer nanocomposites with high permittivity and dielectric strength. *Advanced Materials*, 19(7):1001–1005, 2007.

[197] H. M. Xiong, Y. Xu, Q. G. Ren, and Y. Y. Xia. Stable aqueous zno@polymer core-shell nanoparticles with tunable photoluminescence and their application in cell imaging. *J Am Chem Soc*, 130(24):7522–3, 2008.

[198] Guo Liang Li, Dong Wan, K. G. Neoh, and E. T. Kang. Binary polymer brushes on silica@polymer hybrid nanospheres and hollow polymer nanospheres by combined alkyne-azide and thiol-ene surface click reactions. *Macromolecules*, 43(24):10275–10282, 2010.

[199] Xingyong Wu, Hongjian Liu, Jianquan Liu, Kari N. Haley, Joseph A. Treadway, J. Peter Larson, Nianfeng Ge, Frank Peale, and Marcel P. Bruchez. Immunofluorescent labeling of cancer marker her2 and other cellular targets with semiconductor quantum dots. *Nat Biotechnol*, 21:41–46, 2003.

[200] J. K. Jaiswal, E. R. Goldman, H. Mattoussi, and S. M. Simon. Use of quantum dots for live cell imaging. *Nat Methods*, 1(1):73–8, 2004.

[201] S. D. Perrault, C. Walkey, T. Jennings, H. C. Fischer, and W. C. Chan. Mediating tumor targeting efficiency of nanoparticles through design. *Nano Lett*, 9(5):1909–15, 2009.

[202] Greg T. Hermanson. *Bioconjugate Techniques*. Academic Press, Amsterdam, 2nd edition, 2008.

[203] S. J. Chang, W. S. Liao, C. J. Ciou, J. T. Lee, and C. C. Li. An efficient approach to derive hydroxyl groups on the surface of barium titanate nanoparticles to improve its chemical modification ability. *J Colloid Interface Sci*, 329(2):300–5, 2009.

[204] Y. V. Kolen'ko, K. A. Kovnir, I. S. Neira, T. Taniguchi, T. Ishigaki, T. Watanabe, N. Sakamoto, and M. Yoshimura. A novel, controlled, and high-yield solvothermal drying route to nanosized barium titanate powders. *Journal of Physical Chemistry B*, 111(20):7306–7318, 2007.

[205] Barry Arkles, Youlin Pan, Gerald L. Larson, and Donald H. Berry. Cyclic azasilanes: volatile coupling agents for nacommentchnology. *Silanes and Other Coupling Agents*, 3:179–191, 2004.

[206] N. J. Agard, J. A. Prescher, and C. R. Bertozzi. A strain-promoted [3 + 2] azide-alkyne cycloaddition for covalent modification of biomolecules in living systems. *J Am Chem Soc*, 126(46):15046–7, 2004.

[207] A. S. Karakoti, S. Das, S. Thevuthasan, and S. Seal. Pegylated inorganic nanoparticles. *Angew Chem Int Ed Engl*, 50(9):1980–94, 2011.

[208] K. S. Mazdiyasni, R. T. Dolloff, and J. S. Smith. Preparation of high-purity submicron barium titanate powders. *Journal of the American Ceramic Society*, 52(10):523–526, 1969.

[209] J. T. Last. Infrared-absorption studies on barium titanate and related materials. *Physical Review*, 105(6):1740–1750, 1957.

[210] T. Lee. Nanoscale patterning of barium titanate on block copolymers. *Langmuir*, 13(14):3866, 1997.

[211] Philip J. Launer. Infrared analysis of organosilicon compounds: spectra-structure correlations. *Silicone Compounds Register and Review (reprint)*, pages 100–103, 1987.

[212] A. Hopt and E. Neher. Highly nonlinear photodamage in two-photon fluorescence microscopy. *Biophys J*, 80(4):2029–36, 2001.

[213] S. W. Jin, D. Beis, T. Mitchell, J. N. Chen, and D. Y. Stainier. Cellular and molecular analyses of vascular tube and lumen formation in zebrafish. *Development*, 132(23):5199–209, 2005.

[214] S. Okada, H. Nakauchi, K. Nagayoshi, S. Nishikawa, Y. Miura, and T. Suda. Enrichment and characterization of murine hematopoietic stem cells that express c-kit molecule. *Blood*, 78(7):1706–12, 1991.

[215] T. Ould-Ely, M. Luger, L. Kaplan-Reinig, K. Niesz, M. Doherty, and D. E. Morse. Large-scale engineered synthesis of batio nanoparticles using low-temperature bioinspired principles. *Nat Protoc*, 6(1):97–104, 2011.

[216] K. M. Marks and G. P. Nolan. Chemical labeling strategies for cell biology. *Nat Methods*, 3(8):591–6, 2006.

[217] A. O'Callaghan C, M. F. Byford, J. R. Wyer, B. E. Willcox, B. K. Jakobsen, A. J. McMichael, and J. I. Bell. Bira enzyme: production and application in the study of membrane receptor-ligand interactions by site-specific biotinylation. *Anal Biochem*, 266(1):9–15, 1999.

[218] I. Chen, M. Howarth, W. Lin, and A. Y. Ting. Site-specific labeling of cell surface proteins with biophysical probes using biotin ligase. *Nat Methods*, 2(2):99–104, 2005.

[219] M. Howarth, K. Takao, Y. Hayashi, and A. Y. Ting. Targeting quantum dots to surface proteins in living cells with biotin ligase. *Proc Natl Acad Sci U S A*, 102(21):7583–8, 2005.

[220] M. Howarth and A. Y. Ting. Imaging proteins in live mammalian cells with biotin ligase and monovalent streptavidin. *Nat Protoc*, 3(3):534–45, 2008.

[221] B. E. Cohen. Biological imaging: Beyond fluorescence. *Nature*, 467(7314):407–8, 2010.

[222] R. Duncan. Polymer conjugates as anticancer nanomedicines. *Nat Rev Cancer*, 6(9):688–701, 2006.

[223] S. M. Moghimi, A. J. Andersen, S. H. Hashemi, B. Lettiero, D. Ahmadvand, A. C. Hunter, T. L. Andresen, I. Hamad, and J. Szebeni. Complement activation cascade triggered by peg-pl engineered nanomedicines and carbon nanotubes: the challenges ahead. *J Control Release*, 146(2):175–81, 2010.

[224] C. Lo Celso, H. E. Fleming, J. W. Wu, C. X. Zhao, S. Miake-Lye, J. Fujisaki, D. Cote, D. W. Rowe, C. P. Lin, and D. T. Scadden. Live-animal tracking of individual haematopoietic stem/progenitor cells in their niche. *Nature*, 457(7225):92–6, 2009.

[225] M. Przybyszewska, A. Krzywania, M. Zaborski, and M. I. Szynkowska. Surface properties of zinc oxide nanoparticles studied by inverse gas chromatography. *J Chromatogr A*, 1216(27):5284–91, 2009.

[226] N. Asakuma, T. Fukui, M. Toki, K. Awazu, and H. Imai. Photoinduced hydroxylation at zno surface. *Thin Solid Films*, 445(2):284–287, 2003.

[227] A. Ghysen and C. Dambly-Chaudiere. The lateral line microcosmos. *Genes Dev*, 21(17):2118–30, 2007.

[228] Jerry R. Mohrig, Christina Noring Hammond, and Paul F. Schatz. *Techniques in Organic Chemistry*. W.H. Freeman and Company, New York, 2nd edition, 2006.

[229] R. M. White, A. Sessa, C. Burke, T. Bowman, J. LeBlanc, C. Ceol, C. Bourque, M. Dovey, W. Goessling, C. E. Burns, and L. I. Zon. Transparent adult zebrafish as a tool for in vivo transplantation analysis. *Cell Stem Cell*, 2(2):183–9, 2008.

Appendix A

Supplementary video legends

A.1 Chapter 2 supplementary videos

A.1.1 Video 1: Intercellular bridges persist during the gastrula period

This is a maximum intensity projection (MIP) time-lapse video near the animal pole of a memb-Dendra2 mosaic, where an intercellular bridge (red arrows) connect two epiblast cells from the mid to the late gastrula period. Notice how even as the intercellular bridge elongates, it still remains unbroken even at the end of the timecourse. The top right portion of the intercellular bridge disappears beneath the field of view over time due to the curvature of the embryo. This particular embryo was especially sparsely labeled, allowing a high-resolution view of this particular intercellular bridge without significant overlap from the fluorescence of most other labeled cells. (This video is reproduced from [61].) Scale bar: major gridlines are in 25 μm increments.

A.1.2 Video 2: Intercellular bridges are still present during the segmentation period

This is a volume projection time-lapse video near the animal pole of a memb-Dendra2 mosaic, showing the time period between 90% epiboly and the 10 somite stage of development. Intercellular bridges can still be appreciated within the unlabeled areas of the mosaic embryo, though they are so thin that higher power (which is why the cell bodies are saturated in intensity) is required to see

them clearly. Note how many of the intercellular bridges are fragmenting and disintegrating during this period. This intercellular bridge fragmentation may be the reason for all of the cell membrane detritus seen within the embryo as the video progresses. (This video is reproduced from [61].) Scale bar: 50 μm

A.1.3 Video 3: Intercellular bridges are formed as a result of an incomplete mitotic event

This is a volume projection time-lapse video near the animal pole of a memb-Dendra2 mosaic (green) in the late blastula period, where all nuclei are labeled with H2B-mCherry (red) from an mRNA co-injection at the zygote stage. As the cells divide, a thin membrane tether is maintained between the two daughter cells. Note that the nuclear label is a useful means to verify that the intercellular bridges do in fact connect two intact cells. Each of the daughters are still capable of producing membranous filapodia as they crawl within the blastodisc. Interestingly, this intercellular bridge seems to have a bifurcation point (closer to the leftmost cell of the pair). (This video is reproduced from [61].) Scale bar: 25 μm

A.1.4 Video 4: Cells connected by intercellular bridges are able to undergo normal oriented cell division

This is an MIP time-lapse video near the animal pole of a photoconverted cell within a memb-Dendra2 mosaic during gastrulation. The cell was photoconverted to isolate it even further from surrounding labeled cells in a targeted manner using a near-UV laser source, which is a benefit of using this tool of combined mosaicism and photoconvertible protein expression. During the time-lapse, photoconverted memb-Dendra2 proceeds along the intercellular bridge (emanating from the top of the cell in the image). Additionally, the cell undergoes a normal division event, leaving the

intercellular bridge intact. Interestingly, the two daughter cells may have created a new intercellular bridge, suggesting that cells that the cell machinery necessary to ensure intercellular bridge formation is maintained as long at least as long as the original intercellular bridge remains intact. (This video is reproduced from [61].) Scale bar: 25 μm

A.1.5 Video 5: Membrane-associated proteins can be trafficked along the intercellular bridges

This is an MIP time-lapse video near the animal pole of a photoconverted cell within a memb-Dendra2 mosaic during early gastrulation. Two cells are connected by an intercellular bridge (arrows), which can be seen clearly in the unconverted channel (green, left panel). Before the onset of this time-lapse, the lower connected cell was photoconverted using a near-UV laser source, and progression of the photoconverted memb-Dendra2 protein was monitored along the intercellular bridge (red, right panel). The leading edge of the photoconverted memb-Dendra2 signal is indicated at each time-point with an arrow (right panel). Clearly, the membrane associated protein mDendra2 can progress into even the thinnest of intercellular bridges. The memb-Dendra2 leading edge moved approximately 22 μm in 18 min (approximated using the segmented line tool in ImageJ (NIH)). Interestingly, this intercellular bridge has a bifurcation point (closer to the lowermost cell), and photoconverted memb-Dendra2 can also be seen to migrate to the end of this bifurcated segment. Scale bar: 50 μm

A.1.6 Video 6: Intercellular bridges may allow connected epiblast cells to communicate across long distances during gastrulation

This is an MIP time-lapse video near the animal pole of a memb-Dendra2 mosaic during the middle of gastrulation. Two cells (arrowheads in frame 1) are connected by an intercellular bridge (arrows

in frame 1). 38 minutes after the start of the movie, the lower cell begins to divide (arrow). The upper cell divides $\sim$ 43 min later (arrow at 1 hr, 21 min), and as the upper cell divides, the intercellular bridge begins to fragment (arrows at 1 h4, 26 min). This raises the possibility that the intercellular bridges may connect cells so that each can divide once before the membrane tether is no longer needed between them, or it at least suggests that cell division information can be shared across vast ($\sim$ 145 μm in this case, measured using the segmented line tool in ImageJ (NIH)) distances during gastrulation. Scale bar: 50 μm

A.2 Chapter 3 supplementary videos

A.2.1 Video 1: Time-lapse data for PhOTO-N development during late gastrulation

This video shows each frame of the time-lapse summarized in Fig. 3.5. (A) Memb-Cerulean intensity data (blue), (B) unconverted H2B-Dendra2 intensity data (green), (C) and segmented photoconverted H2B-Dendra2 intensity data (red). Initially, 3 cells were photoconverted (2 EVL cells and one epiblast). Both EVL cells divide between the first and second time point, and the epiblast cell divides between 1 hour, 19 minutes and 2 hours. (D) Merged image of panels A–C. (This video is reproduced from [57].) Scale bar: 50 μm

A.2.2 Video 2: Segmented time-lapse of PhOTO-N development during late gastrulation

This video shows segmented data for each frame of the time-lapse summarized in Fig. 3.5. The nuclei were segmented: the red and orange spheres represent the EVL nuclei and the white spheres represent the migrating epiblast nuclei. The membrane of the orange-labeled EVL nucleus was segmented and is highlighted in all three panels of the image in enhanced contrast blue. (A) Segmented

and photoconverted H2B-Dendra2 data (red) as well as the segmented EVL membrane data (blue) with the bright field data (grayscale) from the time-lapse video. The developing head and optic primordia can be seen during the time-lapse. (B) Segmented and photoconverted H2B-Dendra2 data as well as the enhanced contrast segmented EVL membrane data along with the merged animal pole images as seen in Video A.2.1. (C) Isolated zoomed images of the segmented nuclei and membranes during the time-lapse. (This video is reproduced from [57].) Scale bars: 50 μm

A.2.3 Video 3: Time-lapse data for PhOTO-M membrane dynamics visualization during late gastrulation

This video shows each frame of the time-lapse summarized in Fig. 3.6 in the text. (A) H2B-Cerulean intensity data (blue), (B) unconverted memb-Dendra2 intensity data (green), (C) segmented photoconverted memb-Dendra2 intensity data (red). Cells are dynamic throughout the time-lapse, starting as a tight cluster of cells and eventually moving apart laterally and away from the developing head toward the ventral side of the embryo as the time-lapse progresses. (D) Merged image of panels A–C, which also includes segmented nuclear data (multi-colored surfaces) within each of the photoconverted membranes. (This video is reproduced from [57].) Scale bar: 50 μm

A.2.4 Video 4: Segmented time-lapse data for PhOTO-M membrane dynamics visualization during late gastrulation

This video shows segmented data for each frame of the time-lapse summarized in Fig. 3.6 in the text. First, the photoconverted membranes were segmented in 3D. Then, using the segmented data, nuclei within the surrounding photoconverted membranes were identified and represented as colored surfaces. The nuclei were tracked starting with the final frame, moving backward in time. (A) Segmented and photoconverted memb-Dendra2 (red) as well as the segmented H2B-Cerulean

channel (multi-colored surfaces) along with the bright field (grayscale) from the time-lapse video. Note that the developing head and optic primordia can be seen during the time-lapse. (B) Segmented and photoconverted memb-Dendra2 (red) as well as the segmented H2B-Cerulean (multi-colored surfaces) along with the merged animal pole images as seen in Video A.2.3. (C) Isolated zoomed images of the segmented nuclei and membranes during the time-lapse. (This video is reproduced from [57].) Scale bars: 50 μm

A.3 Chapter 4 supplementary videos

A.3.1 Video 1: Striated SHG signal can be seen with high contrast throughout the somite compartment within a zebrafish embryo

This video shows the same laterally mounted zebrafish embryo as in Fig. 4.1. This is a merged image of both memb-Dendra2 fluorescence (green) and SHG signal from the muscle myosin (white). Initially, a volume projection representation of 120 μm in depth is rotated, giving a sense of the thickness of the tissue and the tight bundling of the muscle fibers, which is clear in the SHG signal. Next, each optical section (2 μm between each) is stepped through the tissue in succession. Note that only memb-Dendra2 signal can be seen in the developing neural territories towards the left side of the embryo in the deeper optical sections, indicating that myosin is the only readily visible SHG-capable material in the trunk of the zebrafish at this stage. Large non-striated clusters of signal towards the periphery of the tissue can be attributed to broad-band tissue pigment spectra that overlaps with the SHG channel. Scale bar: 30 μm

A.3.2 Video 2: Imaging the earliest muscle differentiation and organization events during the segmentation period using SHG imaging

This is a time-lapse volume rendering visualizing the development of the somites within a laterally mounted $\sim$ 15 hpf WT zebrafish embryo ($\sim$ 60 μm total depth in the z direction). (A) This is a merged time-lapse image of the developing zebrafish musculature after zygote stage mRNA injections, where membranes are labeled with memb-Dendra2 (green), nuclei are labeled with H2B-Cerulean (blue), and developing muscle myosin has endogenous SHG contrast (white) due to 2P illumination (850 nm, in this case). This gives cellular context to the developing organism — zebrafish muscle will arise within the labeled area. (B) This is a time-lapse image of the SHG channel (white) alone. Note that appreciable SHG appears around the 04:21 time point ($\sim$ 18 hpf), indicating the first differentiated muscle fibers. Interestingly, the striated pattern often lacks contrast in long-term time-lapse videos, indicating possible perturbations to the tissue from the 2P laser source. Scale: major gridlines are in 20 μm increments.

A.4 Chapter 5 supplementary videos

A.4.1 Video 1: Surface projection rotation of a PEG-BT-labeled zebrafish embryo

This is a rotation of the surface projection image seen in Fig. 5.11A. This video illustrates the extent of PEG-BT labeling within a sphere stage zebrafish embryo after successful zygote stage injection. 10,000 MW Dextran-AlexaFluor546 labels the cell interior of each of the blastomeres within the embryo (red), while the yolk cell appears dark. SHG nanoprobes (white) can be seen even as deep as $\sim$ 70 μm (in the z direction) within the cells of the blastodisc during the rotation. Scale bar: 100 μm

A.4.2 Video 2: Optical sections through a PEG-BT-labeled blastula stage zebrafish embryo

This video shows PEG-BT within Bodipy TR methyl-ester-labeled blastomeres during the sphere stage of development (see Fig. 5.11B for one of the optical sections). The video progresses through 40 optical sections (2 μm between each in the z-direction, $\sim$ 76 μm total depth) within an animal pole mounted zebrafish embryo co-labeled with Bodipy TR methyl-ester (red) to visualize cell cytoplasmic contents (nuclei appear dark). PEG-BT clusters (white) of varying size can be seen with high contrast throughout the depth and remain within the cells of the embryo. Scale bar: 100 μm

A.4.3 Video 3: Optical sections through a PEG-BT-labeled segmentation period zebrafish embryo

This video highlights PEG-BT within a live, early segmentation period embryo (see Fig. 5.11C for one of the optical sections). This video progresses through 12 optical sections (2 μm between each in the z-direction, $\sim$ 20 μm total depth) within a dorsally mounted (anterior top) zebrafish embryo at the 5 somite stage co-labeled with Bodipy FL C5 ceramide (green) to visualize cell boundaries (cell contents appear dark). PEG-BT clusters (white) of varying size are seen within the boundaries of cells in the somites, the notochord (center midline extending from top to bottom), and neural territories. Since the embryo is $<$ 16 hr post fertilization, it does not need to be anesthetized during imaging, so Tricaine methanesulfonate is unnecessary. PTU treatment is also unnecessary since pigment is not present at this stage. Scale bar: 50 μm

A.4.4 Video 4: Time-lapse of PEG-BT-labeled cells during the gastrula period

in vivo time-lapse video of an animal pole mounted zebrafish embryo (seen as static time-points in Fig. 5.13). This video depicts an MIP of cells ($\sim$ 7.5 μm projected in depth) labeled with

PEG-BT (white) and mosaically expressed, membrane-targeted Dendra2 (green). The first frame shows the three PEG-BT nanoprobes that were labeled in Fig. 5.13 that can be followed in time by eye, because of the high contrast of the SHG signal. Note that the two SHG nanoprobes labeled with arrows move beneath the plane of focus during the time-lapse. Interestingly, several PEG-BT nanoprobes seem to mark cells that are not labeled with memb-Dendra2, because they seem to move at approximately the same rate as other cells in the image while not being inside any of the labeled cells themselves. Note that the varying sizes of the nanoprobes within the video presumably stem from anomalous subdiffusion and molecular crowding within cell compartments (e.g., endocytic compartments). Time-stamps: min:sec. Scale bar: 20 μm

Appendix B

Detailed materials and methods from Chapter 5

The following is a detailed procedure in list format for the silanization, streptavidin, and PEG functionalization routines described in Chapter 5 to appreciate the steps required to properly functionalize the SHG nanoprobes to improve their applicability in *in vivo* imaging. This procedure list was included with the manuscript submitted to Nature Protocols in collaboration with Jelena Čulić-Viskota, Periklis Pantazis, and Scott E. Fraser, where I shared equal contribution first author (second position) with Jelena Čulić-Viskota. The SHNH conjugation to BT and subsequent Ab linkage follow standard protocols (*e.g., Bioconjugate Techniques*, reference [202] in the text).

B.1 Materials and equipment

Note that all of the materials and equipment used in this procedure were readily available in the laboratory, so appropriate alternatives could be used, if necessary.

B.1.1 Reagent list

- Barium titanate (BT, Nanostructured & Amorphous Materials, Inc., 99.9% (wt/vol), 200 nm tetragonal, Cat. No. 1148DY, http://www.nanoamor.com/inc/sdetail/20905) CRITICAL: Though this protocol may be applicable to other nanomaterials, we have only tested this rou-

tine for BT in particular. CAUTION: Handle dry nanoparticles with extreme care under a ventilated hood with adequate personal protective equipment (gloves, protective eyewear and clothing).

- N-aminoethyl-2,2,4-trimethyl-1-aza-2-silacyclopentane (Gelest, Cat. No. SIA0592.0, www.gelest.com) CAUTION: Reagent is reactive with water and moisture. Store in sealed containers under inert gas.

- Hydrogen peroxide solution (H_2O_2, Aldrich, 30% (wt/vol), in H_2O, Cat. No. 216763, www.sigmaaldrich.com) CAUTION: Hydrogen peroxide is an irritant and a corrosive, and should be handled with caution under a ventilated hood with adequate personal protective equipment (gloves, protective eyewear and clothing). H_2O_2 is a strong oxidizing agent and should be properly stored in a solvent refrigerator.

- Anhydrous toluene (Aldrich, 99.8% (vol/vol), Cat. No. 244511, www.sigmaaldrich.com)

- 6-azido-hexanoic acid (gift from J. Szychowski, California Institute of Technology), which may be be purchased at EMD Novabiochem, Cat. No. 851097, http://www.emdchemicals.com).

- Biotin-PEO-cyclooctyne (gift from J. Szychowski, California Institute of Technology), which may be synthesized as reported previously [206]. CAUTION: Refrigerate the reagent.

- Alexa Fluor 488 (referred to as AF488) conjugated streptavidin (Invitrogen, 2 mg/ml, Cat. No. S-11223, www.invitrogen.com) CAUTION: Refrigerate the reagent and protect from light.

- Anhydrous dichloromethane (DCM, Aldrich, 99.8% (vol/vol), Cat. No. 270997, www.sigmaaldrich.com)

- 1-ethyl-3-(3-dimethylaminopropyl) carbodiimide (EDC, Thermo Scientific, Cat. No. 22980, www.thermoscientific.com) CAUTION: EDC should be stored at temperatures below -20°C.
- N-hydroxysuccinimide (NHS, Thermo Scientific, Cat. No. 24500, www.thermoscientific.com) CAUTION: NHS should be stored at temperatures below -20°C.
- Methoxy-Poly(Ethylene Glycol)- succinimidyl valerate (mPEG$_{2k}$-SVA, Laysan Bio, MW 2,000, Cat. No. MPEG-SVA-2000-1g, www.laysanbio.com) CAUTION: PEG should be stored at temperatures below -20°C.
- 1x phosphate buffered saline (1xPBS, Thermo Scientific, www.thermoscientific.com)
- Cellgro 1x PBS (Mediatech, Inc., Cat. No. 21-030-CV, cellgro.com)
- 10x PBS (pH 7.2, Invitrogen, www.invitrogen.com)
- Ethanol abs (Koptec, VWR, us.vwr.com)
- Distilled and double deionized water from laboratory distillation column from the Mark Davis laboratory at Caltech (note that any other purified water can be substituted)
- UltraPure, Gibco water (Invitrogen, Cat. No. 10977, www.invitrogen.com)
- Agarose, UltraPure Low melting point (Invitrogen, Cat. No. 16520-050, www.invitrogen.com)
- Agarose, UltraPure (Invitrogen, Cat. No. 16500-100, www.invitrogen.com)
- 30x Danieau solution (or Embryo Medium [151])
- Egg water (the medium in which early embryos are incubated before imaging experiments)
- Tricaine methanesulfonate (Finquel/MS-222, Argent Labs, http://www.argent-labs.com) CRITICAL STEP: In order to adhere to ARRIVE guidelines, an approved anesthetic (MS-222 for zebrafish) must be used for embryo anesthesia and euthanasia.

- 1-phenyl 2-thiourea (Sigma Aldrich, Cat. No. P7629, www.sigmaaldrich.com) to inhibit pigment formation in $>$ 24 hr post fertilization embryos/larvae CAUTION: PTU is toxic, so use appropriate personal protective equipment when handling.

- Embryo tested mineral oil (Sigma Aldrich, Cat. No. 8042-47-5, www.sigmaaldrich.com)

- Optional: Phenol red (Sigma Aldrich, Cat. No. P0290, www.sigmaaldrich.com) diluted to 0.1 to 0.3% (wt/vol) in water

- Optional: 10,000 MW Dextran-AF546 (Invitrogen, Cat. No. D22911, www.invitrogen.com) CAUTION: Store in the dark at -20C and minimize exposure to light.

- Optional: Bodipy TR Methyl Ester (Invitrogen, Cat. No. C34556, www.invitrogen.com) CAUTION: Store in the dark at -20C and minimize exposure to light.

- Optional: Bodipy FL C5 ceramide (Invitrogen, Cat. No. D-3521, www.invitrogen.com) CAUTION: Store in the dark at -20C and minimize exposure to light.

B.1.2 Equipment list

- Heating oil bath (RET Basic, IKA WERKE) with temperature controller (ETS-D4 fuzzy, IKA WERKE)

- DuoSeal Vacuum Pump (Welds 1399)

- Vacuum gauge

- Cold trap

- Teflon 50 ml round bottom flask

- Silicone High Vacuum Grease (Dow Corning, Cat. No. 100504-358, us.vwr.com)

- Teflon magnetic stir bars
- Schlenk line (also referred to as vacuum gas manifold)
- Argon tank connected to the inert gas manifold line (CAUTION: Any inert gas can be substituted.)
- MEGAPURE 6A water still with demineralizer fed with deionized water (Barnstead International, Series 676, Cat. No. A440518, www.thermoscientif.com)
- Centrifuge (Eppendorf, 5417C)
- Centrifuge (Eppendorf, 5810 R, 15 amp version)
- Freeze dryer
- Dialysis membrane made from regenerated cellulose with a molar mass cutoff of 1 kDa
- 10 ml disposable syringes and needles
- Greiner 50 ml centrifuge tube
- 20 ml glass vial
- 1.5 ml tube (Eppendorf, Cat. No. 0030 120.086, www.eppendorf.com)
- Parafilm M Barrier Film (Structure Probe Inc., Cat. No. 01853, www.2spi.com)
- Equipment necessary to perform solid IR analysis with KBr pellet method (refer to an analytical chemistry book [228])
- Sonicator (Branson 5510, 60 Watts)
- FT-IR (Nicolet Nexus 470) with Omnic Software 8.1 (Thermo Fisher Scientific Inc.)

- Drying oven (Yamato DX300)
- Brookhaven ZETA Pals (Brookhaven Instruments Corporation) with ZetaPALS Particle Sizing Software for the nanoparticle hydrodynamic radius salt stability test
- Transmission electron microscope (TEM) (Technai TF30) with energy-dispersive X-ray spectroscopy (EDS) capability with INCA software.
- C-flat Holey Carbon TEM grids (EMS, Cat. No. CF213-50, www.emsdiasum.com)
- Nanoject II nanoliter injector (Drummond Scientific Company, Cat. No. 3-000-204, www.drummondsci.com) for embryo injections
- 3.5 inch borosilicate glass capillary tubes (Drummond Scientific Company, 3-000-203-G/X, www.drummondsci.com) CRITICAL: This or a comparable microinjection apparatus is necessary for proper early stage injections of zebrafish embryos.
- Needle puller (Sutter Instrument, P-2000 Laser Based Micropipette Puller, www.sutter.com)
- Intertek Listed ultrasonic cleaner (Model: CD-4800) for nanoparticle dispersion before zygote injection
- LSM 510/710 (Carl Zeiss AG, www.zeiss.com) with 2-photon capabilities (Chameleon Ultra II, Coherent Inc., www.coherent.com) for SHG microscopy
- Equipment for raising zebrafish and maintaining zebrafish (refer to [151])
- Zebrafish breeding tanks and equipment for collecting zebrafish embryos. Breeding tanks are plastic chambers that either have a divider that allows eggs to settle to the bottom or have marbles at the bottom of the tank to prevent fish from eating their embryos before collection (refer to [151]).

- Labtek multi-well chambered coverglass/coverslip chambers (Nunc International, #1 coverslip thickness, 2- and 8-well: Cat. No. 155380 and 155411, www.nuncbrand.com) CRITICAL STEP: This or a comparable coverslip chamber is necessary for easy embryo manipulation and preparation for imaging. Note that we are implicitly assuming the use of an inverted geometry microscope in this case. The protocol would need to be modified if an upright geometry confocal microscope was to be used.

- Forceps (Student Dumont #5: Fine Science Tools, Inc., Cat. No. 91150-20, www.finescience.com)

- Hair loop (piece of hair looped and taped or glued to the end of a 2–3 mm diameter plastic or metal rod) to orient embryos

- Glass transfer pipettes/disposable Pasteur pipettes (Corning Inc., Cat. No. 7095B-5X, catalog2.corning.com)

- Petri dishes of varying size (35 x 10 mm Falcon Easy Grip Petri dishes: Becton, Dickinson and Company, Cat. No. 351008, http://www.bdbiosciences.com and 100 x 15 mm polystyrene disposable Petri dishes: VWR International LLC, Cat. No. 25384-302, https://us.vwr.com)

- Microscope objectives with sufficient transmittance ($> 80\%$) in the UV-VIS-IR range (Carl Zeiss AG objectives: Plan-Apochromat 20x/0.8 M27 for lower magnification applications, LD LCI Plan-Apochromat 25x/0.8 Imm Korr DIC, C-Apochromat 40x/1.2NA W Corr M27 for superficial SHG imaging within the sample, or LD C-Apochromat 40x/1.1 W Korr UV-VIS-IR M27 for deeper imaging within the sample, www.zeiss.com) CRITICAL STEP: The microscope objective used in experiments with SHG nanoprobes should have a wide transmittance range to allow for efficient illumination of the sample and collection of the resulting SHG signal.

- Fluorescence dissection stereomicroscope with appropriate filter sets to visualize any fluorescent labels (fluorescent dyes, etc.) that were introduced along with the SHG nanoprobes (Olympus America, Inc., MVX10 Macroview, www.olympusamerica.com)

- Dissecting Microscope (Leica Microsystems, MZ9.5 modular high-performance stereomicroscope, http://www.leica-microsystems.com)

B.1.3 Reagent preparation

- Silanes are moisture sensitive. It is recommended to store opened silane containers under inert gas, by purging the container. Additionally, they can be stored over indicating Drierite absorbent (Hammond, VWR Cat No. 22890-900, vwrlabshop.com) in a secondary container.

- PEG polymers are also moisture sensitive. These compounds should be stored at the manufacturer recommended temperature and under inert gas to prevent the PEG NHS ester from hydrolyzing. Ensure that the powders of PEG, EDC and NHS are warmed to room temperature before weighing the required amount.

- Danieau Solution Stock: To make a 300x stock solution (that should be diluted to 30x in water before using with embryos), add 34.8 ml of 5 M NaCl, 2.1 ml of 1M KCl, 1.2 mL of 1M $MgSO_4$, 1.8 ml of 1M $Ca(NO_3)_2$, and 15 ml of 1M HEPES buffer to 945.1 ml water. Adjust the pH between 7.0 and 7.6 with low molarity NaOH or HCl. Store at room temperature for several months.

- Egg water: To make a solution of egg water, add 4.5 g NaCl powder, 1.125 g $CaSO_4$ powder, and 1 mL methylene blue to 18.9 L of deionized water. Store at 28°C (optimal zebrafish embryo incubation temperature) for several months.

- Tricaine Stock: Make a 0.1% (wt/vol) stock solution as follows. Dissolve 50 mg of tricaine

powder in 50 ml 30x Danieau solution (or egg medium). Adjust the pH between 7.0 and 7.6 with low molarity NaOH or HCl. Store at -20°C in 10 ml aliquots for months. Dilute to 0.01–0.02% (wt/vol) when anesthetizing embryos. Tricaine may also be stored at 4°C for up to a week if kept out of the light.

- PTU Stock: For a 25x stock solution, dilute 0.15 g PTU powder in 200 ml 30x Danieau solution (or egg water, for embryos that are not being prepared for imaging) and stir for several hours until the powder completely dissolves. Store and protect from light at 4°C for several months. Dilute to 1x (0.003% (wt/vol)) when incubating with embryos.

- Agarose: For either regular or low melting point agarose, make a 1% (wt/vol) stock solution in a heat-safe (microwave-safe) flask by adding 1 g agarose powder into 100 ml 30x Danieau solution and dissolving uncovered on high in the microwave using $\sim$ 10 s time intervals. Agarose may be stored at room temperature or within an appropriate incubator (37°C for low melting point, 65°C for regular melting point) for at least a year as long as no fungal or bacterial growth is seen within the gel. (CAUTION: Do not allow the solution to bubble over in the microwave. The solution should dissolve within 2–3 min, depending on the microwave.)

B.1.4 Reagent list for cKit enrichment and cell separation for the Ab-BT tests in Section 5.2.7

- CD117 MicroBeads (Miltenyi Biotec, Cat No. 130-091-224, http://www.miltenyibiotec.com/) to incubate with freshly isolated whole bone marrow cells

- MS Columns (Miltenyi Biotec, Cat No. 130-042-201, http://www.miltenyibiotec.com/), the magnetic column used to separate out the cKit (CD117) expressing population

- Pre-Separation Filters, 30 μm (Miltenyi Biotec, Cat No. 130-041-407,

http://www.miltenyibiotec.com/) to remove large cell aggregates/ particulates before entering the column to ensure efficient cKit expressing cell enrichment

- OctoMACS Separator (Miltenyi Biotec, Cat No. 130-042-108, http://www.miltenyibiotec.com/)
- Hank's balanced salt solution, 1x (HBSS, Cat No. 21-020, cellgro.com), media with which to resuspend and incubate freshly prepared whole bone marrow cells
- Lymphocyte separation medium (Cellgro by Mediatech, Inc, Cat No. 25-072, cellgro.com) to isolate cells from excess BT via centrifugation (a density gradient separation medium)

B.2 Detailed procedure

B.2.1 Hydroxylation of BT to expose hydroxyl groups for enhanced efficiency of silanization; timing: 14 hr total (including drying overnight)

1. Disperse 400 mg of BT in 25 ml of hydrogen peroxide solution for 20 min within a 50 ml sealed Teflon flask by sonication. CAUTION: Handle H_2O_2 and dry nanoparticles with extreme care under a ventilated hood with adequate personal protective equipment (gloves, protective eyewear and clothing). CRITICAL STEP: Substitution of the Teflon flask with a glass flask will result in silicon contamination from silicon leaching from the glass.

2. Fit the Teflon flask with a water condenser and an adapter connected to a Schlenk line. Place the Teflon flask in an oil bath fitted with a thermocouple temperature controller. Keep at 110°C for 4 hr under reflux in an argon environment with stirring at 750 min^{-1}. CAUTION: Utilize an outlet to prevent pressure build-up in the flask from released oxygen from the reaction.

3. Cool the solution to room temperature (RT) by removing the flask from the oil bath and wiping the excess oil with an acetone soaked paper towel.

4. Clean the silicon joint grease off of the neck of the Teflon flask using a Kimwipe soaked with acetone or hexane.

5. Place the contents of the flask into a 50 ml Greiner tube.

6. Pellet the powder in solution by centrifugation at 3220 *g* for 5 min in distilled and double deionized water at RT, and discard the supernatant. Redisperse the solid pellet in the solvent and repeat the wash step eight times, until no bubbles are detected. The bubbling is due to the decomposition of any leftover H_2O_2 into water and oxygen gas.

7. Dry the hydroxylated BT (referred to now as BT-OH) overnight under vacuum (1 mbar) at RT. CAUTION: Handle dry nanoparticles with extreme care under a ventilated hood with adequate personal protective equipment (gloves, protective eyewear and clothing).

B.2.2 Silanization of BT-OH as an amine terminal platform for further functionalization; timing: 30 hr

8. Heat 100 mg of BT-OH in a Teflon flask to 150°C for 4 hr under vacuum (1 mbar) to eliminate all traces of adsorbed water. CAUTION: Handle dry nanoparticles with extreme care under a ventilated hood with adequate personal protective equipment (gloves, protective eyewear and clothing). CRITICAL STEP: The use of a Teflon flask will eliminate unwanted silicon contamination that may arise from the use of a glass flask.

9. Cool the flask to RT and purge with argon by opening the inert gas manifold on the Schlenk line to fill the flask. CRITICAL STEP: Water can be easily re-adsorbed after the vacuum drying. Do not store the dried powder, but use immediately.

10. Quickly detach the flask from the Schlenk line and close with a rubber septum, securing it with parafilm to prevent significant water re-adsorption.

11. Purge the flask with argon by inserting a syringe needle that is connected to the argon manifold line.

12. Add 9.9 ml anhydrous toluene with a 10 ml syringe and purge with argon.

13. Disperse BT-OH by sonication for 1 min using the bath sonicator.

14. Add 0.1 ml (1% (vol/vol)) of N-aminoethyl-2,2,4-trimethyl-1-aza-2-silacyclopentane to the solution and stir for 25 hr in an inert environment at RT.

15. Transfer the solution to a 50 ml Griener tube.

16. Wash the powder with ethanol by centrifugation (3220 *g*, 5 min, RT). Perform the final wash with water instead of ethanol. This compound will be referred to as BT-NH_2, since the terminal functional group after this reaction is a primary amine.

B.2.3 Synthesis of biotin-BT and streptavidin conjugation as a control for proper functionalization; timing: 16.5 hr

17. Disperse 30 mg of BT-NH_2 in 1 ml of DCM within a 1.5 ml tube and sonicate for 20 min.

18. Add 10 mg of EDC, 10 mg of NHS and 75 mg of 6-azido-hexanoic acid to the solution.

19. Stir the solution with a Teflon magnetic stir bar for 4 hr at RT.

20. Wash twice with ethanol by centrifugation (8000 *g*, 2 min, RT). Wash the product — azido modified barium titanate (referred to as BT-N_3) — one final time with water.

21. Disperse 5 mg of BT-N_3 in 1.5 ml of 1x PBS by sonication for 40 min.

22. Add 3 μl of 10 mM biotin-PEO-cyclooctyne solution to the solution and stir overnight at RT.

23. Wash the product (referred to as biotin-BT) by centrifugation (3220 g, 5 min, RT) in 1x PBS three times.

24. To test for proper/sufficient functionalization of BT nanoparticles, add 10 μl of 2 mg/ml AF488-conjugated streptavidin stock solution to the 1x PBS dispersed biotin-BT solution.

25. Stir the solution for 1 hr at RT in the dark by covering the vial with aluminum foil.

26. Wash the powder three times by centrifugation (8000 g, 2 min, RT) with water. Discard the supernatant.

27. Resuspend the streptavidin conjugated biotin-BT, referred to as BT-streptavidin-AF488, in 1x PBS within a 1.5 ml tube.

B.2.4 Synthesis of mPEG-COOH by hydrolysis of mPEG-SVA; timing: 3 d

28. React mPEG$_{2k}$-SVA for 4 hr in aqueous solution with constant stirring at RT. CRITICAL STEP: Note that PEG-SVA or any NHS ester-conjugated PEG may be used instead of synthesized mPEG-COOH, but this method utilizes the same effective EDC/NHS conjugated reaction as in the biotin-BT control. Similarly, any molecular weight of PEG can be used for the modification, keeping in mind that the most suitable molecular weights of PEG have been reported in the range of 1.5–5 kDa [207].

29. Rinse the dialysis membrane in water prior to use.

30. Wash the mPEG$_{2k}$-COOH solution by dialysis with a 1 kDa floating regenerated cellulose membrane against distilled water for one day. Change the water after 2 hr, after 4 hr, and the

next morning. CRITICAL STEP: Make sure that the last water change takes place at least 2 hr prior to stopping the dialysis procedure.

31. Transfer the dialysis solution into a vial.

32. Freeze the solution by slowly lowering the vial into liquid nitrogen and freeze-dry the frozen product under vacuum (0.01 torr, -17°C) for 2 days.

B.2.5 Synthesis of PEG-BT for introduction into biological samples; timing: 4.5 hr

33. Disperse 10 mg of BT-NH_2 in 1 ml of anhydrous DCM by sonication for 20 min in a 1.5 ml tube. CAUTION: Handle dry nanoparticles with extreme care under a ventilated hood with adequate personal protective equipment (gloves, protective eyewear and clothing).

34. Add 10 mg of EDC and 10 mg of NHS along with 30 mg of $mPEG_{2k}$-COOH to the solution. CRITICAL STEP: As noted previously in step 28, $mPEG_{2k}$-SVA may be used directly with the amine coated BT-NH_2 powder. However, if autohydrolysis of PEG NHS ester is suspected, a small amount of EDC and NHS should be added to ensure that the reaction takes place efficiently.

35. Allow the reaction to proceed for 4 hr by stirring with a Telfon magnetic stir bar at RT.

36. Wash the solution by centrifugation against ethanol twice and finally with water at 8000 *g* for 2 min at RT. The resulting product is PEG functionalized BT (referred to as PEG-BT).

B.2.6 Imaging-based confirmation of proper functionalization; timing: 2 hr

37. Prepare a control BT solution to compare to BT-streptavidin-AF488 by dispersing 5 mg of BT-OH in 1x PBS by sonication (40 min) followed by repeating steps 24–27 with BT-OH alone (referred to as BT-control) in a 1.5 ml tube. This will act as a control for the extent

of nonspecific binding of streptavidin-AF488 on non-functionalized particles. CAUTION: Handle dry nanoparticles with extreme care under a ventilated hood with adequate personal protective equipment (gloves, protective eyewear and clothing).

38. Flick the 1.5 ml tubes several times to redisperse any sedimented BT-streptavidin-AF488 and BT-control. Each of the solutions should be rather concentrated, so remove 10–100 μl of the supernatant from each and dilute 1:10–1:100 in 1x PBS so that the solution is milky but not completely opaque when the particles are dispersed.

39. Pipette $\sim$ 200–400 μl of each solution into separate wells of an 8-well coverslip chamber (#1 coverslip bottom). Note that 200 μl will be just enough for a droplet within the well, which may make focusing to the sample easier by focusing to the edge of the droplet, while 400 μl will fill the entire bottom of the well in solution.

40. Place the coverslip chamber on the stage of a confocal laser scanning microscope with 2P capabilities and a spectral scanning capability (e.g., the so-called "lambda mode" in the Zeiss Zen 2009/2010 software).

41. Focus to the coverslip surface with a high numerical aperture water objective (since the sample is in PBS) at 40x magnification.

42. Using the two-photon (2P) laser (set at 820 nm, for example) at low power ($\sim$ 1% in the software), scan single optical sections of the sample continuously — using a band-pass emission filter that contains the SHG peak (peak at 410 nm, in this case) — focusing up and down in the z direction until a plane is found with the most SHG signal (especially from the smallest SHG nanoprobes). CRITICAL STEP: SHG signal is narrow in spectrum, so for confocal microscopes that allow direct selection of emission wavelength ranges, choose a narrow band (5–10 nm) centered around the peak of SHG emission (e.g., 405–415 nm or 400–420 nm,

when the illuminating beam is 820 nm). The choice of a narrow bandwidth filter is critical to minimize autofluorescence, especially when imaging in biological tissues.

43. Choose a 2P wavelength that will excite the dye conjugated to streptavidin. Regardless of the wavelength, SHG signal should be visible from the nanoprobes. For BT-streptavidin-AF488, $\sim$ 965 nm is a reasonable choice to excite the AF488 dye.

44. Prepare an appropriate light path on the microscope software to detect a wide-band of spectral information from each pixel within the image (e.g., "lambda scan" of a 34 channel detector in the Zeiss Zen software). Breaking up the spectral data into 10 nm increments is sufficient, since the SHG signal will be blue-shifted and spectrally separated with respect to the dye emission.

45. Take a single spectral scan of the plane of maximal SHG signal in the BT-control as well as the BT-streptavidin-AF488 well.

46. Observe the intensity profile of the spectral data surrounding each nanoprobe cluster within the well. The BT-streptavidin-AF488 nanoprobes should have peaks for both SHG and AF488 emission, while the BT-control will only have the SHG peak.

B.2.7 Zebrafish zygote stage injections with PEG-BT; timing: 1.5 hr

47. The night before embryo injections, set up male/female crosses in breeding tanks. Separate males from females by dividers so that the fish will not breed before the injection setup is prepared the next day. CAUTION: Appropriate institutional regulatory board guidelines must be followed when performing animal experiments. In this protocol, animal experiments conducted were covered under the animal license protocol number 1227 'Zebrafish Developmental Biology' approved by Caltech's Institutional Animal Care and Use Committee (IACUC).

48. Use a needle puller to prepare several injection needles made from borosilicate glass capillary tubes. Break the end of the tip off on a bias using forceps when viewing the tip of the needle under a dissection microscope. CAUTION: The glass pipettes should not have an internal fiber.

49. On the day of injection (one day after step 47), prepare PEG-BT solution for injection into zebrafish embryos. Depending on the application, several preparations can be attempted: PEG-BT alone (option (a)), PEG-BT co-injected with dye (option (b)), or PEG-BT co-injected with DNA encoding a fluorescent protein along with transposase mRNA (option (c)). PEG-BT localizes within cells of the embryo and can be tracked for any extended period of time alone. Often, it is desirable to have cell context to the localization of PEG-BT within zebrafish cells, which can be achieved by co-labeling with PEG-BT using options (b) or (c). Note that mRNA encoding a fluorescent protein may be co-injected instead of fluorescent protein DNA plus transposase mRNA, though this will not be discussed in this protocol. The animal experiments conducted were covered under the animal license protocol number 1227 'Zebrafish Developmental Biology' approved by Caltech's Institutional Animal Care and Use Committee (IACUC).

    (a) PEG-BT alone

        i. Sonicate PEG-BT for 1 min in a bath sonicator. Allow sedimentation of largest clusters for 2 min.

        ii. Dilute 10–50 μl supernatant of the PEG-BT in water (UltraPure) such that it is milky but not completely opaque (between 1:50 and 1:100).

        iii. Sonicate for 1 min in a bath sonicator.

        iv. Wait 2 minutes and then proceed with injections as described below.

(b) PEG-BT co-injected with dye

i. Prepare PEG-BT as in steps i.–iii. in option (a).

ii. Dilute dye to proper stock concentration using manufacturer's instructions. For the case of 10 000 MW Dextran conjugated to an AF (in our case, AF546), dilute to a 0.1 mg/ml injection solution in 1x PBS.

iii. Add 1 μl of dye injection solution into 4 μl prepared PEG-BT solution and proceed with injections as described below.

(c) PEG-BT co-injected with fluorescent protein DNA

i. Prepare PEG-BT as in steps i.–iii. in option (a).

ii. Prepare a plasmid by cloning the cDNA encoding a fluorescent protein of interest into an appropriate vector containing transposable elements flanking the coding region of the plasmid (e.g., pMTB vector [57, 61]). CRITICAL STEP: DNA injection will allow mosaic fluorescent protein expression within a zebrafish embryo. Tissue-specific promoter-driven expression may be used, if labeling of particular tissue types with fluorescence is of interest. Additionally, ubiquitous promoters (e.g., β-actin promoter [125]) may be employed if cell specific labeling is not needed.

iii. Generate mRNA encoding the sequence for the transposase that recognizes the transposable elements in the plasmid (e.g., Tol2 [126] for the pMTB vector) by following the manufacturers instructions on an mRNA expression kit (e.g., mMESSAGE mMACHINE from Ambion).

iv. Combine the mRNA and DNA into a single stock solution for preparation for injection. The fluorescent protein DNA concentration should be $\sim$ 100 ng/μl and the transposase mRNA concentration should be $\sim$ 400–500 ng/μl.

v. Add 1 μl of DNA/mRNA stock to 4 μl prepared PEG-BT solution on ice and proceed with injections as described below.

50. It is often useful to visualize the injection into the embryo. If this is desired, ensure that the 5 μl injection solution contains 0.1–0.3% (wt/vol) phenol red. A red-colored bolus of liquid containing the injection solution should be seen in the injected embryos when phenol red is used.

51. Remove dividers from the fish crosses that were set up the previous day so that they will mate. Wait $\sim$ 15–30 min for fish to mate before collecting embryos.

52. Prepare the injector setup (e.g., Nanoject II) so that the injection needle will be within the viewing platform of a dissection microscope and fill pipette needle with embryo tested mineral oil before placing it on the injector itself.

53. Collect the embryos and transfer to a Petri dish filled with egg water.

54. Using a plastic transfer pipette, move the zebrafish embryos over to an agarose injection chamber. Orient the zygote stage embryos into the grooves of the injection chamber using a forceps. The chamber may be made by pouring hot 1–1.5% (wt/vol) agarose into a Petri dish and dropping a plastic injection chamber mold (as described in [151]) into the center of the hot agarose until the agarose solidifies. Remove as much liquid as possible from around the embryos.

55. Eject some mineral oil from the injector onto a small piece of parafilm under a dissection microscope. Pipette the 5 μl of PEG-BT solution nearby on the parafilm. Fill the needle with $\sim$ 2–5 μl of solution (depending on the number of embryos). Test that the injector ejects even (2.3 nl) amounts by injecting into the mineral oil on top of the parafilm.

56. Move the injection chamber with mounted embryos under the dissection microscope. Inject 2.3 nl of PEG-BT solution into each of the zygote stage embryos, piercing the chorion with the needle and inserting the needle into the yolk cell just beneath the developing zygote cell.

57. Transfer the injected embryos back into a Petri dish filled with egg water and move the Petri dish to a 28°C incubator.

B.2.8 Preparation of injected zebrafish for imaging; timing: up to 2 hr

58. Zebrafish at different stages must be treated slightly differently to prepare for imaging. We will discuss how to prepare samples for stages before the end of gastrulation ($<$ 10 hr post fertilization, option (a)), stages after gastrulation but before the onset of muscle twitching ($\sim$ 16 hr post fertilization, option (b)), and stages after the onset of muscle twitching ($>$ 16 hr post fertilization up through early larval stages, option (c)).

    (a) $<$ 10 hr post fertilization

        i. Transfer the embryos to a Petri dish that has been coated at the bottom with solidified 1–2% (wt/vol) agarose and filled with egg medium or 30x Danieau solution.

        ii. Using sharp forceps, remove the chorion from the embryos. CRITICAL STEP: To best remove the chorion without destroying the embryo at these early stages, it is best to tear an ever-widening hole from a single spot (using forceps in each hand) without coming near the embryo itself. Once the hole is wide enough, rotate the open chorion until the embryo drops out onto the surface of the agarose. Do not allow any part of the embryo to touch the water surface or else it will be destroyed by the surface tension.

        iii. If the embryos were prepared as in option (a) of step 49, staining by means of an

exogenous dye may be desirable at this stage. Prepare a labeling chamber: coat the bottom of a small Petri dish with 1–2% (wt/vol) agarose and let it solidify. Dilute the desired dye to manufacturers specifications (if Bodipy TR methyl-ester or Bodipy FL C5 ceramide, the concentration should be $\sim 100\ \mu$M) in 30x Danieau solution or egg medium, and fill the labeling chamber with this solution. Carefully transfer the embryos to the labeling Petri dish using a glass transfer pipette, again not letting the embryos touch the water surface at any point. Stain the embryos for ~ 1 hr before transferring them back into the large agarose-coated Petri dish filled with egg medium or 30x Danieau solution. Leave them in this solution for at least 10–15 min before the next step.

iv. Add 1.5 ml 0.1% (wt/vol) low melting point agarose in egg medium or 30x Danieau solution into one well of a 2-well coverslip chamber (#1 coverslip thickness).

v. So that the embryos are not destroyed by the heat, let the agarose cool down within the chamber for $\sim$ 1–5 min or until no condensation forms on the side of the coverslip chamber, depending on how it was stored to keep from solidifying.

vi. Using a glass transfer pipette, carefully transfer the embryos into the imaging chamber, ejecting as little medium as possible along with the embryos. Under a dissection microscope and using a hair loop (or a forceps, if you are careful), orient the embryos so that their animal pole is touching the surface of the coverslip or such that they are laterally mounted and sitting just above the surface of the coverslip. CAUTION: If the yolk cell touches the coverslip, the embryo may be damaged, which could interfere with proper development.

vii. Let the agarose solidify around the embryos for ~ 5 min before imaging.

(b) $\sim$ 10–16 hr post fertilization

i. After bud stage, the embryos are much easier to manipulate without destroying them. Within a Petri dish filled with egg water, dechorionate the injected embryos with sharp forceps.

ii. If an exogenous counterstain is desired, repeat step iii. of option (a), though this time much less volume is necessary. Just incubate the embryos within a 1.5 ml tube at 28°C in dye solution for $\sim$ 1 hr. Wash the embryos several times in egg water. CRITICAL STEP: Regardless of the stage, once the embryos have been dechorionated, only transfer them to the various solutions using a glass transfer pipette. The embryos will stick to plastic transfer pipettes.

iii. Add 1.5 ml 0.5–1% (wt/vol) low melting point agarose in 30x Danieau solution or egg medium into one well of a 2-well coverslip chamber (#1 coverslip thickness). Allow the agarose to cool as in step v. of option (a).

iv. Using a glass transfer pipette, transfer the embryos into the imaging chamber, ejecting as little medium as possible along with the embryos. Under a dissection microscope and using forceps (or hair loop, if desired), orient the embryos in any desired orientation (e.g., dorsal or lateral).

v. Let the agarose solidify around the embryos for $\sim$ 5 min before imaging.

(c) $>$ 16 hr post fertilization

i. If imaging will be performed after 16 hr post fertilization, transfer the embryos to a Petri dish with egg water containing 1x PTU and replace this solution at least once daily to prevent significant pigment formation. CAUTION: PTU is a toxic chemical, so wear appropriate personal protective equipment (gloves, protective eyewear) and handle with caution.

ii. Dechorionate injected embryos with sharp forceps. Avoid accidental trauma to the

embryo as it twitches within the chorion.

iii. If an exogenous counterstain is desired, repeat option (b), step iii., though make sure there is 1x PTU in the solution to prevent pigment formation during staining. Just incubate the embryos within a 1.5 ml Eppendorf tube at 28°C in dye solution containing 1x PTU for $\sim$ 1 hr. Wash the embryos several times in egg water containing 1x PTU.

iv. Anesthetize the zebrafish by transferring the embryos to a Petri dish with egg water containing 0.015% (wt/vol) tricaine methanesulfonate along with 1x PTU.

v. Add 1.5 ml 0.5–1% (wt/vol) low melting point agarose — with 0.015% (wt/vol) tricaine methanesulfonate and 1x PTU — in 30x Danieau or egg medium solution into one well of a 2-well coverslip chamber (#1 coverslip thickness). Allow the agarose to cool as in step v. of option (a).

vi. Using a glass transfer pipette, transfer the embryos into the imaging chamber, ejecting as little medium as possible along with the embryos. Under a dissection microscope and using a forceps (or hair loop, if desired), orient the embryos in any desired orientation (e.g., dorsal or lateral).

vii. Let the agarose solidify around the embryos for $\sim$ 5 min before imaging.

B.2.9 Imaging SHG nanoprobes within living zebrafish embryos; timing: 15 min (setup)

59. Place the coverslip chamber on the stage of a confocal laser scanning microscope with 2P capabilities and a spectral scanning capability (e.g., “lambda mode” in the Zeiss Zen software).

60. Focus into the sample using the oculars of the microscope in visual mode using an objective of appropriate magnification and — preferably to maximize SHG signal collection — high

numerical aperture (≥ 0.8).

61. Prepare imaging settings for SHG signal collection, referred to as the SHG channel. Prepare the emission filter band as in Step 42.

62. Depending on the counterstain used, prepare imaging settings for those particular dyes/fluorescent probes in a separate channel from the SHG collection. Note that a single channel may be used with the 2P laser alone in certain cases: many newer laser scanning microscopes allow direct selection of emission wavelength ranges (e.g., Zeiss QUASAR detectors), which is ideal for SHG imaging in conjunction with fluorescent markers, since the illuminating beam for SHG can be tuned to a particular wavelength (using a tunable 2P laser), allowing collection of 2P fluorescence emission simultaneously with SHG signal in two separate detectors.

63. Using low power ($\sim$ 1% of maximum in the software), scan an optical section within the tissue using the SHG channel. Larger particle clusters should be saturated even at low power, whereas smaller clusters may require higher illuminating power, especially if the illuminating beam is off resonance (i.e., significantly red-shifted from 800 nm, in the case of BT).

64. Increase the power until the smallest SHG nanoprobe clusters are visible while ensuring that there is no phototoxicity to the tissue. Set up time-lapse imaging settings with sufficient time resolution so that each of the SHG nanoprobes can be tracked in time and space within the embryo. For example, during the gastrula period, cells are very dynamic, so a relatively short time (on the order of a few minutes) between frames will be necessary to track the SHG nanoprobes, assuming they are concentrated within the embryo.

65. If multiple imaging times are desired between different stages of development, the embryo may be removed from the agarose carefully with forceps and kept in a 28°C incubator in egg water until the next imaging period. Note that during the larval stages of development and

later, significant pigment formation can occur even in the presence of PTU. Spectral detection (e.g., with the "lambda mode" software) can be used to separate SHG signal from broad-band emission from different pigments within the fish. Additionally, fish without pigment (e.g., "Casper" zebrafish [229]) may also be considered when designing an experiment using SHG nanoprobe labels.